

NORTHWESTERN UNIVERSITY

Synchrotron X-ray Studies of
Pristine, Intercalated, and Functionalized
Epitaxial Graphene on SiC(0001)

A DISSERTATION

SUBMITTED TO THE GRADUATE SCHOOL
IN PARTIAL FULFILLMENT OF THE REQUIREMENTS

for the degree

DOCTOR OF PHILOSOPHY

Field of Materials Science and Engineering

by

Jonathan D. Emery

EVANSTON, ILLINOIS

June 2013

UMI Number: 3563715

All rights reserved

INFORMATION TO ALL USERS

The quality of this reproduction is dependent upon the quality of the copy submitted.

In the unlikely event that the author did not send a complete manuscript and there are missing pages, these will be noted. Also, if material had to be removed, a note will indicate the deletion.



UMI 3563715

Published by ProQuest LLC (2013). Copyright in the Dissertation held by the Author.

Microform Edition © ProQuest LLC.

All rights reserved. This work is protected against unauthorized copying under Title 17, United States Code



ProQuest LLC.
789 East Eisenhower Parkway
P.O. Box 1346
Ann Arbor, MI 48106 - 1346

Copyright © 2013, Jonathan Emery

All Rights Reserved

ABSTRACT

Synchrotron X-ray Studies of Pristine, Intercalated, and Functionalized
Epitaxial Graphene on SiC(0001)

Jonathan D. Emery

Since its isolation in 2004, graphene has received virtually unparalleled attention from researchers in various fields. The great interest in graphene is driven in no small part by its superlative and unique electronic properties, intrinsic low dimensionality, and its potential for application in nanoelectronics. However, in order to exploit the extraordinary electronic properties of graphene, it is first necessary to develop a suitable growth method that is amenable to production at the wafer-scale. One of the most promising routes to large-scale production of graphene is via thermal extrusion of from silicon carbide. This dissertation is focused on understanding the structure of epitaxial graphene grown on the Si-terminated face of silicon carbide (EG/SiC(0001)), as well as its modified (intercalated, functionalized) forms. To do this, I employ synchrotron-based X-ray characterization techniques to investigate these structures with Å-scale resolution and chemical sensitivity.

The primary objective of this dissertation is to use a novel approach to clarify long-standing uncertainties concerning the nature of the interface between EG and the SiC substrate. This interface is highly technologically relevant, and its precise structure and chemical composition have direct influence on the properties of the graphene itself. To this end, I construct a high-resolution (sub-Å), chemically-sensitive atomic density map of the interfacial

structure using X-ray surface scattering combined with the X-ray standing wave-enhanced photoelectron spectroscopy. Next, I switch focus to engineered EG/SiC(0001) interfacial structures, which have been observed to influence the electronic properties of the overlaying graphene. Here, I present a structural investigation of the effects of hydrogen intercalation on the interfacial structure of SiC(0001), a process that has been suggested to decouple the interfacial layer from the SiC substrate. Finally, characterization efforts are extended to a series of functionalized graphene heterostructures, with the goal of understanding the consequences of graphene integration with various electronics-relevant materials. Overall, this thesis highlights the unique power of X-ray characterization techniques in the investigation of various EG/SiC(0001) systems at the ångstrom- and nanoscale. The information obtained from these measurements improves the understanding of pristine, intercalated, and functionalized EG/SiC(0001), and may help to expedite the implementation of graphene into next-generation carbon-based electronics.

Approved

Professor Michael J. Bedzyk
Department of Materials Science and Engineering
Northwestern University
Evanston, Illinois

Final Examination Committee
Prof. Michael J. Bedzyk, Chair
Prof. Mark H. Hersam
Prof. Lincoln J. Lauhon
Prof. Tobin J. Marks

Acknowledgements

To begin, I want to thank my advisor, Prof. Michael Bedzyk, for his guidance and support during my time at Northwestern. Mike is an excellent teacher and spares no effort in the training and advancement of his students. I am fortunate to have had the opportunity to study under his mentorship. Thanks also to the other members of my committee, Profs. Mark Hersam, Tobin Marks, and Lincoln Lauhon. I have been privileged to be able work with each of them on a number of fruitful collaborations in the past few years, and am better for it. I would like to specifically thank Mark Hersam, who first brought the theme of this thesis to my attention, and has, along with his group, helped to expand it from a side project to a thesis topic.

There are many collaborators who deserve acknowledgement. Among those are Hersam group members Justice Alaboson, Qing-Hua Wang, Hunter Karmel, James Johns, Chun-Hong Sham, TeYu Chien and Aparna Deshpande, each of whose work is included in this dissertation. Of these, I'd like to thank Justice in particular, who is a wonderful collaborator, great friend, and honorary Bedzyk group member. I also want to thank the Gaskill group at the Naval Research Lab, especially Virginia Wheeler, who supplied many of the samples used in these studies.

I would like to acknowledge financial support from the Northwestern Research Science and Engineering Center and the National Science Foundation. Additional thanks are necessary for the funding of two research trips to the European Synchrotron Radiation Facility in Grenoble, France, without which this work would not have been possible.

I have also been lucky enough to have had access the wonderful facilities and staff at Argonne National Lab and the Advanced Photon Source. I would like to acknowledge Paul Fenter, Sang-Soo Lee, and Tim Fister of the Chemical Sciences and Engineering Division. Paul

and his group helped jump-start me on X-ray reflectivity measurements, providing guidance, tools, and support on numerous projects. I would also like to thank the beamline staff who helped make this work possible, especially Jenia Karapetrova and Zhan Zhang of APS Sector 33 and Joe Strzalka of Sector 8. Special thanks go to Denis Keane of Sector 5. There are few as helpful, patient, hard-working, and dedicated as Denis, and he was instrumental in the success of each and every experiment at Sector 5. Lastly, I wish to thank the scientists at ID32 at the ESRF, especially Blanka Detlefs and Jörg Zegenhagen. It was a fantastic experience to work at their beamline, and one that would have been impossible without their help.

I have been privileged to work with many fantastic Bedzyk group members over the years. I am grateful for the guidance and friendship of Jeff Klug and Steven Christiansen, who helped to guide when I was a first-year, and advise me still. Thanks to Philip Lin, Y-C Tseng, and Vaibhav Kohli for help and guidance in those early years as well. Special thanks to Martin McBriarty, who is always enthusiastic to discuss new ideas, and Sumit Kewalramani, who is an excellent teacher and helped me to approach problems in new ways. I have also greatly benefited from the interactions and assistance from John Okasinski, Zhenxing Feng, Marie Zarrouati, Curtis Leung, I-Cheng Tung, Li Zeng, Bor-Rong Chen, Xiao Chen, Liane Moreau, Gavin Campbell, Parasmani Rajput, Sven Stoltz, Sudeshna Chattopadhyay, and Jerry Carsello.

Of course, I wish to acknowledge my family: my mother, Mary, my father, Dan, and my brother Matt, who have provided me with the foundation for who I am and what I do. Your love and encouragement have helped me along every step of this path, and for that I thank you.

Finally, I want to thank my wife and best friend, Renee. I cannot thank you enough for your patience, love and support during this time. I cannot imagine having done this without you.

For Renee

Table of Contents

Chapter 1: Introduction	15
1.1: Motivation.....	15
1.2: Outline	19
Chapter 2: Graphene	23
2.1: Crystal Structure Definitions	24
2.2: Graphene Fundamentals	25
2.2.1: Graphene Crystal and Electronic Structure	27
2.2.2: Graphene Electronic Properties and Applications	30
2.2.3: Graphene Synthesis Methods.....	32
2.3: Epitaxial Graphene on SiC	35
2.3.1: Silicon Carbide	35
2.3.2: Growth and Structure of EG/SiC	37
2.3.3: The EG/SiC(0001) Interface.....	40
2.4: Modifying Epitaxial Graphene	43
2.4.1: EG/SiC(0001) Intercalation	43
2.4.2: EG/SiC(0001) Functionalization	45
Chapter 3: X-ray Characterization Techniques	47
3.1: X-ray Interactions with Matter	48
3.1.1: X-ray Scattering.....	49
3.1.2: Photoelectric Absorption and Photoelectron Spectroscopy.....	55
3.2: High-resolution X-ray Reflectivity.....	59
3.2.1: Scattering from a Truncated Crystal.....	59
3.2.2: XRR Experimental: APS	68
3.3: X-ray Standing Wave.....	73
3.3.1: Dynamical Diffraction Theory.....	73
3.3.2: X-ray Standing Wave with Photoemission.....	79
3.3.3: XSW Interpretation.....	82
3.3.4: XSW Experimental: ESRF ID32	87
3.4: Supplementary Techniques.....	90
3.4.1: LEED	91
3.4.2: Low-angle X-ray Reflectivity.....	91
3.4.3: Grazing Incidence Small/Wide Angle X-ray Scattering.....	93
3.4.4: X-ray Fluorescence.....	95
Chapter 4: XSW-XPS and XRR of Pristine EG/SiC(0001)	99
4.1: Introduction.....	100

4.2: XSW on EG/SiC	102
4.3: Sample Preparation	105
4.4: Experimental.....	105
4.5: XPS Analysis	108
4.6: XSW Analysis.....	112
4.7: XRR Results	116
4.8: Discussion.....	118
4.9: Supplemental Samples.....	121
4.10: Conclusions.....	126
Chapter 5: Characterization of H-intercalated EG/SiC(0001)	127
5.1: Introduction.....	128
5.2: Experimental.....	129
5.3: X-ray Photoelectron Spectroscopy	131
5.4: X-ray Reflectivity	134
5.5: X-ray Standing Wave.....	137
5.6: Discussion/Conclusions.....	139
Chapter 6: Self-Assembled Organic Monolayer Functionalization of EG/SiC(0001)	141
6.1: PTCDA Monolayers on Epitaxial Graphene	142
6.1.1: Introduction.....	142
6.1.2: Experimental.....	144
6.1.3: Results.....	153
6.1.4: Discussion.....	160
6.2: Seeding ALD of High- κ Dielectrics on EG/SiC with Self-Assembled Monolayers	165
6.2.1: Introduction.....	165
6.2.2: AFM-derived Film Morphology	167
6.2.3: XRR-derived Film and Interface Structure.....	168
6.2.4: Discussion.....	172
Chapter 7: Templated Nanostructure Growth on EG/SiC(0001)	175
7.1: Introduction.....	176
7.2: Growth, AFM and STM of PCDA/EG/SiC(0001)	177
7.3: ZnO ALD on PCDA/EG.....	179
7.4: GIWAXS/GISAXS	181
7.5: Raman Scattering.....	187

	10
7.6: UV Polymerization	190
7.7: Summary	192
Chapter 8: Summary and Future Work	195
8.1: Summary	196
8.2: Future Work	199
8.2.1: EG on C-face and Non-Polar SiC	199
8.2.2: Intercalated EG/SiC(0001)	201
8.2.3: Other 2D Materials: MoS ₂ , BN, and Silicene	203
8.2.4: Site-specific XSW-HARPES on EG/SiC	204
References:	208
Appendix A: SWAM Analysis Routine	238
A.1: History	238
A.2: SWAM Guide	241
A.2.1: <i>cr.m</i>	242
A.2.2: <i>r0.m</i>	246
A.2.3: <i>fl.m</i>	251
A.2.4: <i>chi2.m</i>	253
A.3: Major Changes to SWAM	258
A.3.1: SWAM Extension to <i>E</i> -Scans	258
A.3.2: Convolution Correction	259
A.3.3: Data Weighting During Least-Squares Fitting	260
A.4: Function Directory and Parameter Glossary	260
A.4.1: Function Directory	261
A.4.2: Parameter Glossary	262
A.5: Future Releases	264
A.5.1: Dumond Diagram and Dispersion Surface Calculations	264
A.5.2: Model-Independent 3D Mapping and Global Fitting Routines	264
A.5.3: Standing Wave Analysis GUI (SWAG)	265
Appendix B: Alternate XSW-XPS Analysis	267
Vita	273

List of Figures

Figure 2.1: A unit cell, defined by lattice parameters a , b , c , and angles, α , β , γ	24
Figure 2.2: Graphene is the foundation of other 0D, 1D, and 3D graphitic allotropes.....	26
Figure 2.3: Physical and electronic structure of graphene.....	28
Figure 2.4: Various modes of graphene production and their potential applications.	32
Figure 2.5: Crystal structure of 6H-SiC.....	36
Figure 2.6: Schematic of a typical UHV-graphene growth procedure.	38
Figure 2.7: Comparison of surface morphology and coverage uniformity of UHV- and Ar-grown EG/SiC	39
Figure 2.8: A selection of competing models of the EG/SiC interface structure.	42
Figure 3.1: A classical depiction of scattering of an electromagnetic wave by a free electron....	49
Figure 3.2: Scattering from an isolated atom with charge distribution $\rho(\mathbf{r})$	51
Figure 3.3: Photoexcitation and subsequent relaxation processes.....	56
Figure 3.4: X-ray photoelectron spectroscopy fundamentals.	57
Figure 3.5: The source of CTRs as described using the convolution theorem , for the example of the 6H-SiC(0001) crystal.	60
Figure 3.6: A comparison of the methods used to measure CTRs.....	63
Figure 3.7: Simulations of high-resolution X-ray reflectivity curves.....	63
Figure 3.8: Examples of CCD images at various scattering conditions and the matching Ewald constructions of the intersection with the CTRs	66
Figure 3.9: Examples of scattering signals at various scattering conditions for UHV and Ar-grown EG/SiC(0001).	66
Figure 3.10: The typical setup for XRR experiments using a CCD detector at the APS.	69
Figure 3.11: Typical XRR SPEC scan macros at various beamlines.	72
Figure 3.12: A schematic of the X-ray standing wave generated by the SiC(0006) Bragg reflection.	73
Figure 3.13: Calculated reflectivity and XSW phase for the SiC(0006) reflection at $E_\gamma = 15$ keV.. ..	78
Figure 3.14: Calculated reflectivity and XSW yield curves for a series of coherent fractions and coherent positions for the SiC(0006) reflection at 2.463 keV.	84
Figure 3.15: Beamline schematic and XSW/HAXPES chamber at ESRF ID32.....	88
Figure 3.16: Principles of low-angle XRR	92
Figure 3.17: Schematic of the GIWAXS/GISAXS setup at APS 8-ID-E.....	94
Figure 3.18: Examples of allowed inter-shell transitions and Siegbahn nomenclature for X-ray emission lines.....	96

Figure 4.1: A schematic of the X-ray standing wave generated by the SiC(0006) Bragg reflection	103
Figure 4.2: Experimental geometry for XPS measurements at the ESRF.	104
Figure 4.3: LEED patterns for both UHV-grown and Ar-grown EG/SiC.	107
Figure 4.4: Survey spectra for UHV-grown and Ar-grown EG/SiC.	107
Figure 4.5: X-ray photoelectron spectra of the C 1s and Si 1s core-levels for ~1.3 ML EG/SiC.	109
Figure 4.6: Overlay of Si 1s spectra from EG/SiC taken at different emission angles for depth-sensitive studies.	109
Figure 4.7: XSW modulations of fitted XPS components for ~1.3 ML EG/SiC.	114
Figure 4.8: XRR results for ~1.3 ML UHV-grown EG/SiC.	117
Figure 4.9: 1D chemically-sensitive interface map derived from combined analysis of both XSW-XPS and XRR.	119
Figure 4.10: C 1s and Si 1s spectra from ~0.5 ML UHV-grown and ~1.7 ML Ar-grown EG/SiC.	122
Figure 4.11: XSW results for ~0.5 ML UHV-grown and ~1.7 ML Ar-grown EG/SiC.	124
Figure 4.12: XRR analysis for ~1.7 ML furnace-grown EG/SiC.	125
Figure 5.1: LEED patterns for pristine EG/SiC and H-intercalated EG/SiC at 130 eV.	129
Figure 5.2: Experimental geometry at ID32 at the ESRF.	130
Figure 5.3: Survey spectra for both pristine and H-intercalated EG/SiC(0001).	132
Figure 5.4: High-resolution XPS spectra from pristine and H-intercalated EG/SiC(0001).	132
Figure 5.5: XRR data and best fits, together with their corresponding electron-density profiles for pristine and H-intercalated EG/SiC.	135
Figure 5.6: Best-fit χ^2 values from XRR data as a function of Si-EG1 displacement for H-intercalated EG/SiC.	137
Figure 5.7: XPS-selected XSW yield curves of EG for pristine and H-intercalated EG/SiC.	138
Figure 6.1: An idealized depiction of a 1 ML PTCDA/1 ML EG/6H-SiC(0001) heterostructure.	143
Figure 6.2: UHV STM images of bare and functionalized EG/SiC sample surfaces.	146
Figure 6.3: X-ray reflectivity (XRR) data for 0 ML, 1 ML, and 2 ML PTCDA coverage.	147
Figure 6.4: Schematic of the iterative Fienup phase retrieval procedure.	150
Figure 6.5: XRR fitting results from 0 ML, 1 ML, and 2 ML PTCDA/EG/SiC.	152
Figure 6.6: Results of Fienup-based analysis for bare EG/SiC.	156
Figure 6.7: Schematic of the metal-oxide-graphene parallel-plate capacitor structure.	166
Figure 6.8: Representative AFM image of bare, functionalized and ALD-exposed EG/SiC.	168
Figure 6.9: Comparison of XRR data for bare EG/SiC, PTCDA/EG/SiC, and HfO ₂ /Al ₂ O ₃ /PTCDA/EG/SiC.	169

Figure 6.10: Low- q_z XRR data for HfO ₂ /Al ₂ O ₃ /PTCDA/EG/SiC.....	171
Figure 7.1: Self-assembled monolayer of PCDA on EG/SiC.....	178
Figure 7.2: ALD of ZnO on PCDA/EG.....	180
Figure 7.3: Schematic of the GISAXS measurements on ZnO-PCDA/EG.....	182
Figure 7.4: Scattered intensity for both DEZ-treated and as-deposited PCDA/EG/SiC.....	183
Figure 7.5: Grazing incidence small/wide angle X-ray scattering results for ZnO-PCDA/EG/SiC.	185
Figure 7.6: STM and the associated fast Fourier transforms for results for various regions on PCDA-functionalized EG/SiC(0001).....	186
Figure 7.7: AFM, Raman and XPS results for ALD-exposed PCDA/EG/SiC.....	189
Figure 7.8: Atomic layer deposition on cross-linked PCDA/EG.....	191
Figure 8.1 Elements which have shown evidence of decoupling the interfacial layer from the SiC(0001) substrate upon intercalation.....	203
Figure 8.2 ARPES data for nominally zero-layer graphene.....	206
Figure A.1: Examples of user interfaces for SWAN 2.1.2 and SWAMv2.4.....	239
Figure A.2: SWAM initialization.....	243
Figure A.3: Functional flowchart for <i>cr.m</i>	243
Figure A.4: Input and output panels for the <i>cr.m</i> routine.....	245
Figure A.5: Functional flowchart for <i>r0.m</i>	248
Figure A.6: Input and output panels and figures from the <i>r0.m</i> function.....	248
Figure A.7: Effects of detuning and Gaussian smearing of the monochromator.....	250
Figure A.8: Functional flowchart for the <i>fl.m</i> routine.....	251
Figure A.9: An example of input and output panels for the <i>fl.m</i> function.....	253
Figure A.10: Functional flow chart for <i>chi2.m</i>	255
Figure A.11: Input and output panels for the χ^2 -mapping routine, <i>chi2.m</i>	256
Figure A.12: Examples of simulated rocking curves for Si(111) and SiC(000 12) reflections at 4.925 keV.....	259
Figure A.13: The potential foundation of the SWAG program.....	266
Figure B.1: Fits to simulated data from nominal EG ₀ -only sample.....	267
Figure B.2: XPS peak-fitting and consequent XSW data and results using traditional peak-fitting parameters.....	268
Figure B.3: Goodness-of-fit maps for the Si-S ₁ distance with constrained S ₂ position.....	270

List of Tables

Table 4.1: Goodness-of-fit maps for the Si-S ₁ distance with constrained S ₂ position	111
Table 4.2: XSW results for Si 1s and C 1s components for ~1.3 ML EG/SiC.....	114
Table 4.3: XSW results for ~0.5 UHV-grown and ~1.7 ML Ar-grown EG/SiC.....	123
Table 6.1: Least-squares fitting results for XRR data.....	158
Table A.1: SWAM function directory.	261
Table A.2: SWAM parameter glossary.....	262
Table B.1: XSW results based on conventional peak-fitting parameters.	269

Chapter 1

Introduction

1.1: Motivation

THE COMMERCIAL demand for the products offered by the computing and semiconductor industry has been a powerful driving force for technological innovation since the advent of integrated circuits and microelectronic devices. This demand has stimulated huge investments into the improvement of the materials which are the foundations for the devices themselves, resulting in the rapid rate of improvement in industry figures of merit, including processor speed, memory capacity, transistor and pixel density, cost per chip, original functionality, and degree of miniaturization. The rate of improvement and growth of these properties is often conceptualized as Moore's law, which is the observation that the number of

transistors on integrated circuits doubles approximately every two years, but is now typically generalized to numerous device capabilities. To date, the industry has kept pace with the self-fulfilling prophecy of Moore's law. However, as we quickly approach the 10 nm processing regime, it is clear that it will be necessary to develop new, ultra-low-dimensional materials in order to overcome the barriers in device performance and fabrication that exist at these length scales.

A new class of 2D materials shows great promise as candidates for this next generation of thinner, faster, and more functional nanoelectronic components [1]. Of these materials, graphene, a planar sheet of carbon atoms arranged in a honeycomb configuration [2-4], has received the most attention due to its unique electronic properties [5]. Its unusually high carrier mobilities [2, 6], long-range ballistic electron transport [7, 8], room-temperature quantum Hall effect [9, 10], and low levels of $1/f$ noise [11, 12], combined with its intrinsic low dimensionality, make graphene highly attractive for implementation into nanoscale devices. While these properties may help to circumvent some of the issues that arise as the dominant silicon-based complimentary metal-oxide-semiconductor (CMOS) technology approaches the 10 nm node, graphene may have a greater role to play in flexible, analog, and unconventional electronics [4]. These applications can take advantage of graphene's unique electronic properties without being hindered by what is considered the limiting factor for graphene as a semiconducting material in digital electronics: the lack of a suitable bandgap.

Despite this promise, however, there are a myriad of challenges associated with the implementation of graphene into any electronic device. The most basic of these is production. To date, graphene has been produced using a variety of different methods, including mechanical (the

scotch-tape method) [2], liquid-phase [13] or chemical exfoliation [14] of graphite crystals, chemical vapor deposition (CVD) on various metal surfaces [15, 16], and by the thermal decomposition of silicon carbide (SiC) substrates [17, 18]. Novoselov and Geim's scotch-tape method is celebrated for its novelty and simplicity, but proves inefficient for electronic applications that require high-throughput production of high-quality graphene sheets at the wafer scale.

Of the current fabrication techniques, CVD-grown graphene and epitaxial graphene may prove to be the most viable for large-scale graphene production. CVD can be used to produce graphene of varying layer coverage, can be employed at comparatively low temperatures, and enables relatively simple transfer of graphene to arbitrary substrates. On the other hand, the small domain size and wrinkles in the graphene can limit performance. In addition, the need to transfer the CVD-grown graphene to an insulating substrate is a substantial barrier to large-scale production, and can result in higher defect concentrations and reduced yield. Epitaxial graphene (EG) grown on SiC has the distinct advantage over CVD graphene in that it can be grown directly on a semi-insulating or semiconducting single-crystal SiC wafer, eliminating the need for transfer. In addition, since the structure of the SiC substrate can be controlled, there is the potential to fabricate graphene nanoribbons by engineering the terraces and steps of the SiC crystal itself [19, 20]. However, the high substrate cost and high-temperature processing required for the growth of EG/SiC remain serious drawbacks. Regardless, the potential advantages associated with EG/SiC certainly warrant further study, and it will therefore be the graphene materials system of choice for the work in this thesis.

As is common to all new materials and technologies, obstacles to large-scale commercialization exist as researchers and engineers work to understand how to best fabricate, implement, and utilize the new material. Critical to this understanding is the development and application of the tools that enable the precise characterization of these new materials systems. Unique challenges arise in the case of graphene, as it is the first 2D material ever fabricated. However, since a 2D material is, in essence, a surface, traditional surface science tools such as scanning probe microscopy (SPM), transmission electron microscopy (TEM), low-energy electron diffraction (LEED), Auger electron spectroscopy (AES), X-ray photoelectron spectroscopy (XPS), and surface X-ray diffraction (SXRD) have all proven useful in the characterization of various types of graphenes. Ultimately, our ability to exploit the unique properties of graphene will depend on our ability to precisely produce and manipulate it in useful forms. Suitable characterization is central to this objective.

This dissertation focuses on identifying and employing appropriate structural characterization methods in effort to better understand epitaxial graphene grown on the Si-terminated face of SiC (EG/SiC(0001)). While there are a number of narratives presented in this work, the main theme of all the studies is the utilization of advanced synchrotron-based X-ray techniques to investigate EG/SiC systems of interest. The first topic is the study of the structural relationship of pristine epitaxial graphene with the underlying SiC(0001) substrate, a subject that has been intensely studied for nearly a decade but remains controversial [21-27]. The nature of the interface between the graphene and the SiC is integral to the electronic behavior of the graphene overlayers themselves and could ultimately determine whether EG/SiC is utilized in electronic devices [28, 29]. Second, we investigate the structural changes that occur upon

intercalation of hydrogen to the EG/SiC interface. This archetypical intercalated EG/SiC structure may ultimately help eliminate some of the negative caused by of the ubiquitous interfacial layer on the behavior of the overlaying graphene sheets, helping to improve their electronic properties [30, 31]. The third topic addresses the interaction of the graphene with other electronically relevant materials. This study focuses on facilitating the integration of EG/SiC with organic semiconductors and high- κ dielectric materials for the eventual utilization of graphene in real devices. Finally, we expand the functionalization study to the templated growth of nanostructures on the EG/SiC surface, a step on the path towards graphene-based nanoelectronic devices.

In essence, the objective of this dissertation is twofold:

- 1.) Gain a precise understanding of the structure of pristine, intercalated, and functionalized epitaxial graphene on SiC(0001) with the ultimate goal of facilitating the design and engineering of future graphene-based devices.
- 2.) Employ and advance current synchrotron-based X-ray techniques in the characterization of pristine, intercalated, and functionalized epitaxial graphene systems.

1.2: Outline

First, in [Chapter 2](#), I will present the essential structure and properties of graphene. I then extend the description to the special case of EG/SiC(0001). This chapter will include a brief historical review of graphene, as well as a review of subtopics specifically relevant to this dissertation, namely the nature of the EG/SiC interface, advancement in the engineering of the EG/SiC interface, and the functionalization of the graphene surface.

In [Chapter 3](#), I establish the principles central to the X-ray characterization techniques employed in this work. I begin with a basic introduction to the phenomena that occur when X-rays interact with matter. I then expand the discussion specifically to measurements used in this

work, most importantly high-resolution X-ray reflectivity (XRR) and X-ray standing wave-enhanced photoelectron spectroscopy (XSW-XPS). I also briefly address supplementary techniques used in some studies, including X-ray fluorescence (XRF) spectroscopy, grazing-incidence small/wide angle X-ray scattering (GISAXS/GIWAXS), and low-angle XRR.

[Chapter 4](#) contains the results from the combined XSW-XPS and XRR study of the EG/SiC(0001) interface, addressing long-standing uncertainties regarding the structural and chemical nature of the interface. The combined XSW-XPS and XRR analysis of the interfacial structure proves particularly powerful in resolving this highly-debated interfacial structure, ultimately allowing for the construction of a chemically-sensitive interfacial atomic density map with sub-Å resolution. We find, in agreement with some reports and contrary to others [21, 22, 24, 32], that the interfacial layer is essentially a C-only layer of graphene-like density that possesses two distinct interfacial C species which have mean positions that are slightly (~ 0.4 Å) displaced from each other along the SiC[0001] direction. One of the C species, comprising 25% of the C atoms in the interfacial layer, interacts covalently with the terminal Si atoms in the SiC(0001) substrate, while the remaining 75% adopt a graphene-like bonding configuration, although with significant sp^3 character.

In [Chapter 5](#) I present a structural study of the effect of hydrogen intercalation to the EG/SiC(0001) interface. The intercalation of various species to the EG/SiC interface has been demonstrated to greatly influence the properties of the overlaying graphene sheets [33], imparting both n - and p -type doping [30, 34, 35], as well as altering many electronic properties relevant to device behavior [31]. Here we focus on the use of XRR to investigate the structural consequences of the intercalation process and present a comparison between nominally identical

pristine and H-intercalated EG/SiC(0001) structures. These measurements reveal, as suggested by previous groups, but not quantitatively determined [30], that the intercalation of H to the interface effectively decouples the interfacial layer from the substrate and transforms it into a quasi-freestanding graphene sheet.

[Chapter 6](#) presents a set of studies on functionalized epitaxial graphene. We begin with a combined STM and XRR structural analysis of the ordering of perylene-3,4,9,10-tetracarboxylic acid (PTCDA) monolayers deposited on the EG/SiC(0001) surface [36]. We find a high degree of both lateral and vertical ordering of the PTCDA layers and show with XRR that the PTCDA monolayer possesses a weak π - π^* interaction with the EG/SiC(0001) surface, establishing it as a potential templating layer for the deposition of additional materials. Next, we realize this potential by using PTCDA as a seeding layer for subsequent atomic layer deposition (ALD) of a high- κ dielectric stack. Here, we use both high- and low-angle XRR to probe the dielectric-PTCDA/EG/SiC(0001) interface. We find that after dielectric oxide ALD the PTCDA layer remains structurally intact underneath a high conformal film, confirming its efficacy as an ALD seeding layer, and thereby opening routes for graphene integration in devices.

In [Chapter 7](#), we expand upon the planar functionalization scheme presented in Chapter 6 and use self-assembled monolayers of 0,12-pentacosadiynoic acid (PCDA) [37] to template the growth of 1D ZnO nanostructures on EG/SiC(0001). Using GISAXS/GIWAXS we are able to determine the orientational relationship of the ZnO chains with respect to the EG/SiC(0001) substrate, as well as the domain size and orientations and inter-chain spacing. The series of studies presented in [Chapter 6](#) and [Chapter 7](#) step through the natural progression from basic

functionalization to complex nanopatterning, demonstrating the fundamental steps in a fabrication scheme that may eventually lead to integration of graphene into devices.

Lastly, in [Chapter 8](#), I summarize the main findings of the thesis and suggest potential directions for future research. I highlight that the characterization techniques in this dissertation are ideally suited to the ever-expanding array of EG/SiC heterostructures and note that there exist many poorly understood structures that could benefit greatly from the methodology presented in this work.

In addition to the main text, I also include two appendices, the first of which ([Appendix A](#)) describes the overhaul and improvements made to the Bedzyk group's MATLAB-based XSW analysis software, SWAM (Standing Wave Analysis in MATLAB). This appendix includes a comprehensive guide for using SWAM. [Appendix B](#) presents an alternate analysis to that presented in [Chapter 4](#) in order to validate the models we use in that Chapter.

Chapter 2

Graphene

IN THIS CHAPTER, the basic structure, physics, properties, and applications of graphene, with specific focus on epitaxial graphene (EG) on SiC(0001) are reviewed. I begin with a description of graphene as a free-standing sheet of carbon atoms, and then continue to explain how the unique two-dimensional physical structure of graphene leads to its unusual electronic properties. I extend this review, then, to the technologically-relevant structure of epitaxial graphene on the Si-terminated face of SiC, which is central to this dissertation. Finally, I provide a brief overview of the current state of research of EG/SiC(0001) interfacial engineering and functionalization.

2.1: Crystal Structure Definitions

Before defining graphene, it is useful to establish the terminology necessary to define regular periodic structures of crystalline materials. The fundamental unit by which crystals are described is the *unit cell* (see [Figure 2.1](#)). The unit cell is defined by basis vectors \mathbf{a} , \mathbf{b} , and \mathbf{c} . Each j^{th} atom within the unit cell is positioned at

$$\mathbf{r}_j = x_j \mathbf{a} + y_j \mathbf{b} + z_j \mathbf{c}, \quad (2.1)$$

where x , y , and z are fractional positions within the unit cell. The basis vector magnitudes and relative angles define the lattice parameters,

$$|\mathbf{a}| = a, |\mathbf{b}| = b, |\mathbf{c}| = c$$

$$\alpha = \text{ArcCos} \left[\frac{\mathbf{b} \cdot \mathbf{c}}{|\mathbf{b}| |\mathbf{c}|} \right], \beta = \text{ArcCos} \left[\frac{\mathbf{c} \cdot \mathbf{a}}{|\mathbf{c}| |\mathbf{a}|} \right], \gamma = \text{ArcCos} \left[\frac{\mathbf{a} \cdot \mathbf{b}}{|\mathbf{a}| |\mathbf{b}|} \right]. \quad (2.2)$$

In addition, the concept of the *reciprocal lattice* is central to both the electronic and diffractive

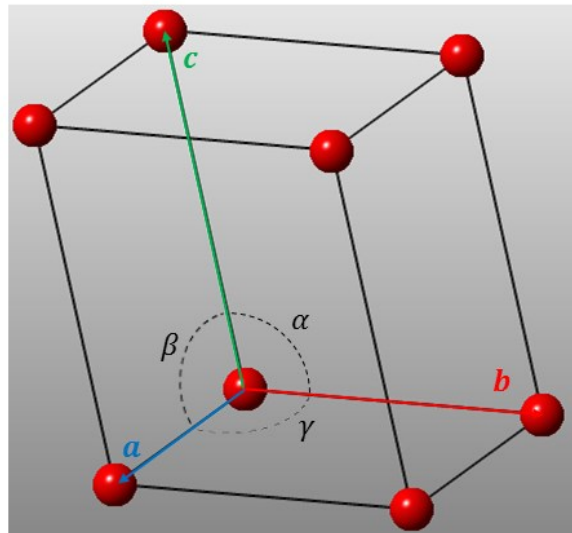


Figure 2.1: A unit cell, defined by lattice parameters a , b , c , and angles, α , β , γ .

description of periodic materials. The reciprocal lattice is simply the Fourier transform of the real space lattice, and is defined by reciprocal lattice basis vectors,

$$\mathbf{a}^* = 2\pi \frac{\mathbf{b} \times \mathbf{c}}{\mathbf{a} \cdot (\mathbf{b} \times \mathbf{c})}, \mathbf{b}^* = 2\pi \frac{\mathbf{c} \times \mathbf{a}}{\mathbf{a} \cdot (\mathbf{b} \times \mathbf{c})}, \mathbf{c}^* = 2\pi \frac{\mathbf{a} \times \mathbf{b}}{\mathbf{a} \cdot (\mathbf{b} \times \mathbf{c})}. \quad (2.3)$$

The Miller indices, h , k , and l are used to define any lattice point within the reciprocal lattice,

$$\mathbf{G}_{hkl} = h\mathbf{a}^* + k\mathbf{b}^* + l\mathbf{c}^*. \quad (2.4)$$

Each hkl lattice point in reciprocal space corresponds to a set of hkl planes in the real space lattice of the crystal, such that reciprocal lattice vector \mathbf{G}_{hkl} is perpendicular to the hkl planes and has a modulus $|\mathbf{G}_{hkl}| = 2\pi/d_{hkl}$, where d_{hkl} is the inter-planar spacing of the hkl planes. We work mostly with hexagonal crystal systems in the following sections, and will typically use the Bravais-Miller notation, where a set crystallographic planes is defined by the four indices, $hkil$, where $i = -(h+k)$.

2.2: Graphene Fundamentals

Graphene is a planar array of sp^2 -bonded carbon atoms that are arranged in a two-dimensional honeycomb lattice. Graphene is one of many allotropes of carbon, the most closely related of which are fullerenes, nanotubes, and graphite, as shown in [Figure 2.2](#). Graphene is special, however, in that it is the basic structural building block of all other graphitic materials. Stacking graphene sheets results in the familiar 3D graphite crystal, and by rolling a graphene sheet into a spherical shell or cylinder and joining the edges, it is possible to create a 0D fullerene or a 1D nanotubes, respectively. The low-dimensional graphene derivatives have each experienced periods of intense scientific attention in the years following their respective seminal works [38,

39], and research on each continues to merit thousands of publications a year. Recently, however, the rate of publication for studies of graphene has surpassed both its 0D and 1D counterparts.

Despite the recent surge in interest in graphene, its fundamental electronic structure has been known since work 1947, when Phillip Wallace presented a theoretical study of the graphite band structure [40]. In the 60 years following Wallace's work, there were a number of near-misses that may have resulted in earlier identification of 2D graphite crystals. Some specific close-calls include works by Hofmann and Boehm, who observed monolayers of reduced graphene oxide flakes in 1962 [41], and van Bommel, who reported graphite monolayers grown on SiC(0001) in 1975 [17]. Despite the modest experimental developments in the field during this period, physicists had realized that graphene was a useful condensed-matter analog of (2+1)-

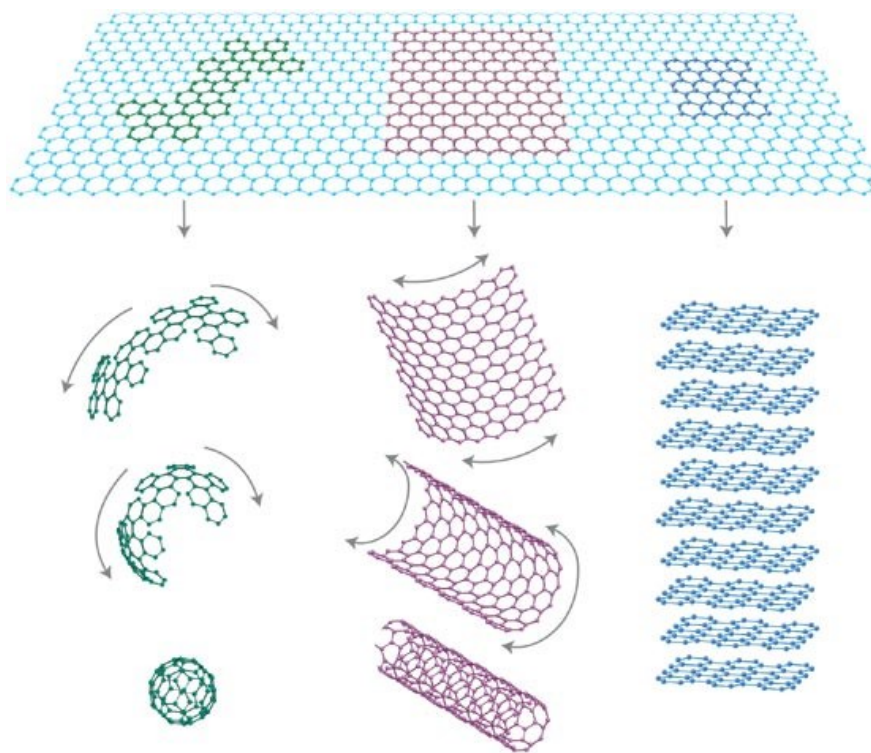


Figure 2.2: Graphene is the foundation of other 0D, 1D, and 3D graphitic allotropes. From Geim *et al.* Ref. [3].

dimensional quantum electrodynamics [42], and developed much of the theoretical foundations for graphene during this time [43, 44]. It was not until 2004, however, that graphene was isolated by using scotch tape to mechanically exfoliate individual graphene sheets from a highly-oriented pyrolytic graphite (HOPG) crystal [2]. Using this simple method, Novoselov, Geim, and coworkers were able to demonstrate some of the unique properties of graphene by isolating crystals large enough for electrical characterization. In their 2004 paper, Novoselov and Geim reported a strong ambipolar electric field effect, precise tunability of charge carrier concentrations, extremely large carrier mobilities, and surprising ambient-environment electronic quality [2]. This work inspired dozens of researchers to begin work on graphene, and has led to the discovery of a plethora of interesting electronic behaviors, such as the room-temperature quantum Hall effect [9, 10], ballistic charge transport [7, 8], and many other unique properties [5, 18]. All of these properties are derived from graphene's distinct electronic band structure, which, in turn, is derived from graphene's unique physical structure.

2.2.1: Graphene Crystal and Electronic Structure

Structurally, graphene can be described by a 2D hexagonal lattice populated with C atoms, as shown in [Figure 2.3](#). Each C atom is bound to 3 other carbons at C-C bonding distances of $d_{C-C} = 1.420 \text{ \AA}$. The primitive unit cell contains two chemically-equivalent, but symmetry-inequivalent, C atoms and is spanned by unit-cell vectors \mathbf{a}_G and \mathbf{b}_G with lengths $a_G = b_G = \sqrt{3}d_{C-C} = 2.459 \text{ \AA}$. This 2D crystal structure belongs to the $P6mm$ plane group and the origin in [Figure 2.3\(a\)](#) is placed on the highest-symmetry (6-fold) axis. The two atoms within the unit cell are positioned at $(\frac{2}{3}, \frac{1}{3})$ and $(\frac{1}{3}, \frac{2}{3})$ and the atomic areal density of the graphene sheet is 38.20 C/nm^2 . As shown in [Figure 2.3\(b\)](#), when C is arranged in this honeycomb pattern, three of the

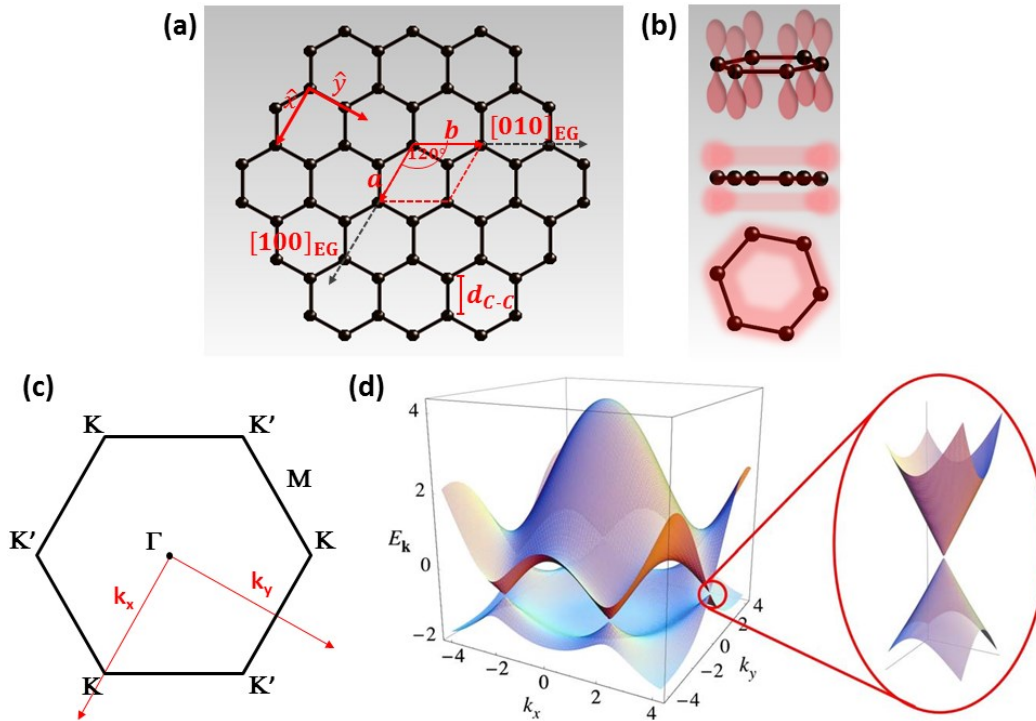


Figure 2.3: Physical and electronic structures of graphene. (a) A fragment of a graphene lattice with basis vectors \mathbf{a}_G and \mathbf{b}_G (red lines) defining the graphene unit cell (outlined by dotted lines and basis vectors). The unit cell contains two C atoms. (b) An example of the out-of-plane $2p_z$ orbitals and sp^2 hybridization of a carbon ring. The $2p_z$ orbitals interact to form a delocalized π system above and below the graphene plane, and are responsible for electron transport in graphene. (c) The first Brillouin zone for graphene, showing the critical points. (d) The electronic band structure for graphene calculated with the tight-binding model, and an enlargement of the low-energy conical dispersion relationship of graphene at the K point (from Ref. [5]).

four half-filled valence orbitals sp^2 hybridize to form localized in-plane σ -bonds, which give graphene its strong structural core. The remaining valence electron occupies the $2p_z$ orbital to generate the partially occupied out-of-plane π -bonds, which are responsible for the low-energy electronic properties of graphene. We should note that the two C atoms (denoted A and B, respectively, in [Figure 2.3\(a\)](#)) within the unit cell are inequivalent in terms of bond orientation. This leads to the alternate description of graphene as consisting of two interpenetrating sublattices; each possessing a single C atom. This approach facilitates the discussion of the

peculiarities of graphene electron transport, such as ballistic conduction [7, 45], spin transport [46], and Berry's phase of π [47, 48].

The hexagonal Brillouin zone for graphene is shown in [Figure 2.3\(c\)](#) with critical points Γ , M, and K (as well as inequivalent point K') indicated. A common way to describe the low-energy electronic band structure is to consider the π -bonds formed between the nearest-neighbor C atoms within the hexagonal lattice. [Figure 2.3\(d\)](#) shows the single-particle graphene band structure, calculated with the tight-binding model [5, 40, 49],

$$E(k_x, k_y) = \pm t \sqrt{1 + 4 \cos\left(\frac{\sqrt{3}}{2} a_G k_y\right) \cos\left(\frac{1}{2} a_G k_x\right) + 4 \cos^2\left(\frac{1}{2} a_G k_x\right)}, \quad (2.5)$$

where k_x and k_y are the components of the in-plane momentum, and $t \sim 2.8$ eV is the nearest-neighbor hopping energy [5]. The peculiar electronic properties observed in graphene are due to the structure near the K and K' points. As shown in [Figure 2.3\(c\)](#), at these six points there exists a symmetrical (about the Fermi energy, E_F) conical dispersion relationship between energy and momentum at some displacement from the K or K' point,

$$E(k_x, k_y) = \pm v_F \hbar \sqrt{\Delta k_x^2 + \Delta k_y^2} \quad (2.6)$$

where $v_F \sim \frac{1}{300} c$ is the Fermi velocity and c is the speed of light. This description of the behavior of the charge carriers near the K and K' points is similar that used to describe the behavior of chiral massless Dirac particles [5], and for this reason the K and K' points are typically referred to as *Dirac points*. While the basic electronic behavior was predicted by Wallace in 1947, it was not until 2005 that it was observed experimentally in graphene [47, 48].

2.2.2: Graphene Electronic Properties and Applications

The electronic structure and properties graphene, together with its low dimensionality, are the main sources of interest to electronics researchers and engineers. The most obvious cause for excitement is the extremely high charge carrier mobilities observed in graphene, which may find application in high-frequency field effect transistors (FETs). Graphene mobility is theoretically limited to $\sim 2.5 \times 10^5 \text{ cm}^2 \text{V}^{-1} \text{s}^{-1}$ for suspended graphene at room temperature [50, 51] and observed experimentally as high as $\sim 1 \times 10^5 \text{ cm}^2 \text{V}^{-1} \text{s}^{-1}$ for hexagonal boron-nitride-encapsulated graphene at room temperature and low (10^{11} cm^{-2}) carrier concentration [6]. These values are much larger than those typical of electronics-grade Si ($\sim 1.4 \times 10^3 \text{ cm}^2 \text{V}^{-1} \text{s}^{-1}$) and better even than those of single-crystal InSb, which has possessed the largest known room-temperature electron mobility at $7.8 \times 10^4 \text{ cm}^2 \text{V}^{-1} \text{s}^{-1}$ [52]. Graphene's high carrier mobility is complemented by its low electronic noise [11] and high current stability [53] which make it especially attractive for high-frequency transistor applications. It should be noted, however, that while cut-off frequencies in the THz regime have been reported [54] the maximum oscillation frequencies still lag behind those of conventional Si transistors by an order of magnitude [4, 55].

Currently, it is regarded that graphene will more likely find application in analog and radio-frequency applications rather than logic devices, limited by the small on-off current ratios result from the absence of a suitable bandgap. Researchers continue to explore solutions to this limitation, and possible routes for bandgap opening include nanoribbon formation [56-58], bilayer coverage control [59, 60], and chemical modification [61, 62]. However, each of these potential solutions has proven problematic, either because they do not induce a large enough gap, or because they so drastically reduce the transport properties of the graphene that it no longer

possesses the unique electronic behavior that makes it attractive in the first place [4, 63]. Regardless, the field-effect in graphene was first reported in Novoselov and Geim's original 2004 paper, and the first graphene FET was reported only in 2007 [64]. Therefore the field is less than a decade old, and will require time to mature and develop [63].

In the event that graphene does not succeed Si in FETs, it may still find a niche in applications with less stringent electronic requirements. These include, for example, flexible electronics and touch-screen electrodes, which can take advantage of graphene's low dimensionality, low sheet resistance ($30\Omega/\square$), optical transmittance (97.7% per layer and virtually wavelength-independent for visible light [65]), and mechanical robustness. In addition, graphene's 2D nature and low electronic noise make it particularly sensitive to even small-scale electronic perturbations, implying that it could be used for single-molecule sensors [11, 66]. Alternatively, graphene may be best suited for application in basic nanoscale electrical interconnection or thermal dissipation due its large electrical and thermal conductivities and 2D structure. Of all these possibilities, perhaps the most natural application for graphene is in radiofrequency and analog devices, which do not require a high on/off current ratio for operation, but would benefit greatly from increased mobility and high switching speeds [63, 67]. The potential applicability of the unique electronic properties of graphene, together with its intrinsic low-dimensionality, are what make it such an attractive candidate for implementation in future nanoscale technologies.

2.2.3: Graphene Synthesis Methods

If graphene is to be employed in large-scale electronics applications, it will be necessary to develop a production method that yields high-quality graphene while being both scalable and economical. A diagram showing the relative cost vs. quality of various graphene fabrication methods is shown in [Figure 2.4](#). Novoselov and Geim's mechanical exfoliation technique [2] produces high-quality monolayer (ML) graphene that can be transferred to arbitrary substrates, but the flakes are randomly scattered on the substrate. In addition, the process is inefficient, likely making it suitable only at the research-level application. Similarly, mass quantities of μm -sized graphene platelets can be produced through solution-phase exfoliation of graphite crystals [13] or via the chemical or thermal [14] reduction of graphene oxide, but the quality is not

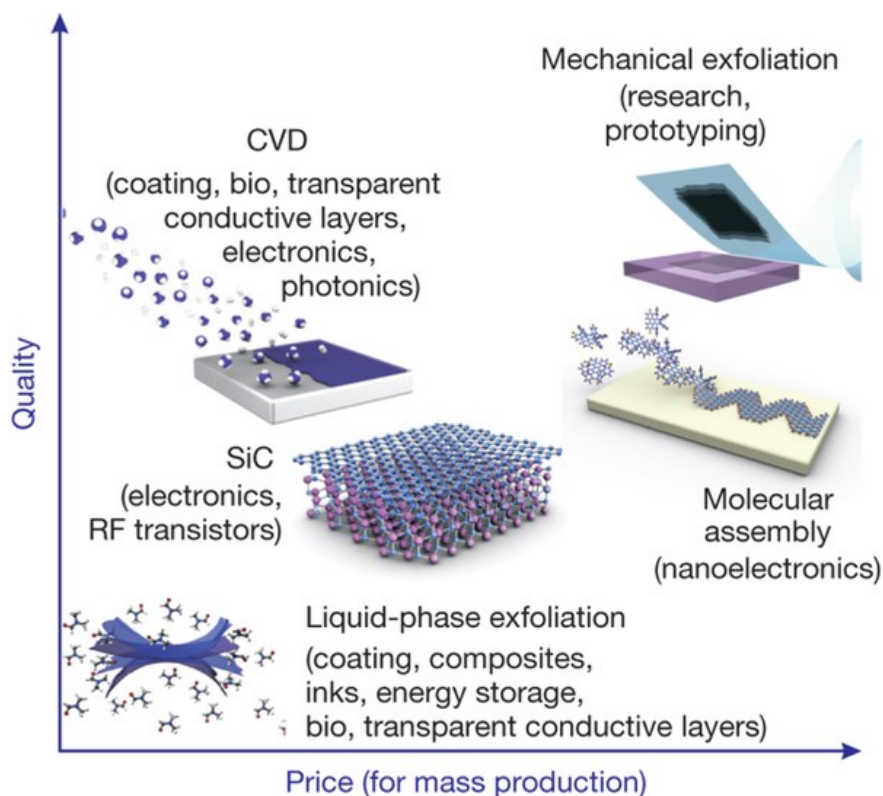


Figure 2.4: Various modes of graphene production and their potential applications. From Ref. [4]

adequate for graphene electronics applications. The two methods that appear most likely to be utilized by the electronics industry are either 1.) chemical vapor deposition (CVD) of graphene films metal surfaces, or 2.) thermal extrusion of graphene from SiC single crystals. Both of these methods produce relatively high-quality graphene sheets at the wafer scale, and each has its relative advantages and drawbacks.

The epitaxial growth of graphene with CVD has been demonstrated on numerous metal substrates and with various hydrocarbon precursors [68-70]. Each CVD-grown graphene film has distinctive (and tunable) properties that depend on the substrate type, precursor, and growth conditions. Currently, graphene growth on polycrystalline Cu films is of particular interest due its high film quality over large areas and its relatively low cost of production [16, 69-71]. After CVD growth on the metal substrate, the graphene is removed and transferred to an arbitrary substrate for subsequent device fabrication or characterization. This requisite transfer process limits the scalability of this method due to the expense and effort involved in etching the underlying metal substrate. Apart from being expensive, the transfer process limits the ultimate quality of the graphene due to etchant damage, polymeric support residue contamination, or due to the tearing, wrinkling and cracking of the graphene incurred during handling [4]. Despite these deficiencies, devices fabricated from large areas of CVD-grown graphene films have yielded state-of-the-art performance (mobilities of $1 \times 10^5 \text{ V}^2 \text{ cm}^{-1} \text{ s}^{-1}$ are possible over large areas), and this production method is becoming widespread [69]. CVD growth of graphene continues to be one of the most promising methods for producing graphene for electronic applications.

An alternate technique, the epitaxial growth of graphene on the surface of SiC [17, 18], holds a number of important advantages over CVD-grown graphene. In this growth technique,

epitaxial graphene (referred to herein as EG) is produced via the thermal decomposition of a single-crystal SiC substrate via the preferential sublimation of Si atoms from the crystal surface. At sufficiently high temperatures, the remaining C atoms will rearrange to form graphene sheets. These EG films possess many of the same properties observed in graphene produced using other techniques [18, 19, 72-74]. The foremost advantage of this method is that the graphene is formed on a ready-made electronics-grade substrate and does not require the damaging post-fabrication transfer procedures necessary for CVD-produced graphene. In addition, if graphene is to be used in nanoelectronics applications, it will need to be patterned at the nanoscale. Therefore, it is a great advantage to have an atomically well-defined substrate that can potentially be exploited for bottom-up templated graphene growth. This allows for the creation of, for example, regular arrays of ≤ 40 nm wide EG nanoribbons preferentially grown on crystal facets [75] or EG grown on step-free mesas [20]. Finally, because there exists strong structural coherence between the EG and the electronic-grade SiC substrate [17, 18] (at least for the Si-terminated face), there exists opportunities for engineering of the EG/SiC interface to influence the EG properties [30, 33]. The existence of this epitaxial relationship means that precise control of the SiC surface prior to graphitization (e.g., control of facet/step type and density, nanoscale pre-patterning, selective doping, or directed functionalization) may allow for fabrication of a myriad of engineered EG/SiC structures [76].

Of course, for the implementation of EG/SiC into nanoelectronic devices to proceed, researchers will have to first surpass a number of technological barriers. The first challenge is that the processing temperatures required to graphitize SiC are typically $>1200^\circ\text{C}$, which is incompatible with existing silicon-based semiconductor technology. Researchers are exploring

ways to circumvent this issue by employing either laser synthesis of graphene from SiC [77], or via carbon deposition directly onto the SiC surface [78, 79], but those approaches are very recent. SiC substrate quality, price, and wafer size is also often cited as a limiting factor, but the increased competition and recent development of high-quality 150-mm wafers are beginning to reduce costs, facilitating large-scale production. However, continued progress is necessary with regards to controlling the SiC surface morphology and terrace size, the graphene layer thickness and domain sizes, and, of course, it is critical to develop a clearer understanding of the influence of the substrate and interfacial layers on the behavior of the graphene film.

2.3: Epitaxial Graphene on SiC

2.3.1: Silicon Carbide

There are hundreds of known polytypes of SiC, all of which belong to the hexagonal crystal family, except one, which has cubic symmetry [80]. In EG/SiC research the most commonly studied polytypes are 4H-SiC and 6H-SiC, which belong to the same $P6_3mc$ space group (the same as wurtzite), but possess differing stacking arrangements of SiC bilayers along the c -axis. The majority of research on EG/SiC to date has been performed on the polar (0001) and (000 $\bar{1}$) surfaces of hexagonal 4H- or 6H-SiC [74]. There do exist a handful of reports on graphene grown on non-polar faces of SiC [81] and on the cubic polytype, 3C-SiC [82, 83], but these surfaces lack the hexagonal template for graphene growth provided by the basal planes of the polar surfaces, and have thus far not been a focus of study. Herein we concentrate on EG/SiC(0001) because the growth of EG films on that surface can be better controlled as

compared to $\text{SiC}(000\bar{1})$, a critical requirement to the measurements used in this work. From this point on, “EG/SiC” will denote EG grown on the Si-face of graphene, unless otherwise noted.

In this work we study EG grown only on 6H-SiC crystals (depicted in [Figure 2.5](#) and hereto referred to simply as SiC), and therefore will provide descriptions with respect to that polytype. In SiC, Si and C atoms sp^3 hybridize into a tetrahedral arrangement, shown in [Figure 2.5\(a\)](#), with a Si-C bonding distance of 1.89 Å. The difference in Pauling electronegativities between Si and C ($\chi_{\text{Si}} = 1.9$, $\chi_{\text{C}} = 2.5$), however, gives the Si-C bonds significant ionic character. In [Figure 2.5\(b\)](#), a projection along the $\text{SiC}[11\bar{2}0]$ direction shows stacked SiC bilayers. The c_{SiC} lattice parameter is 15.12 Å and the d -spacing between the SiC bilayers is d_{0006}

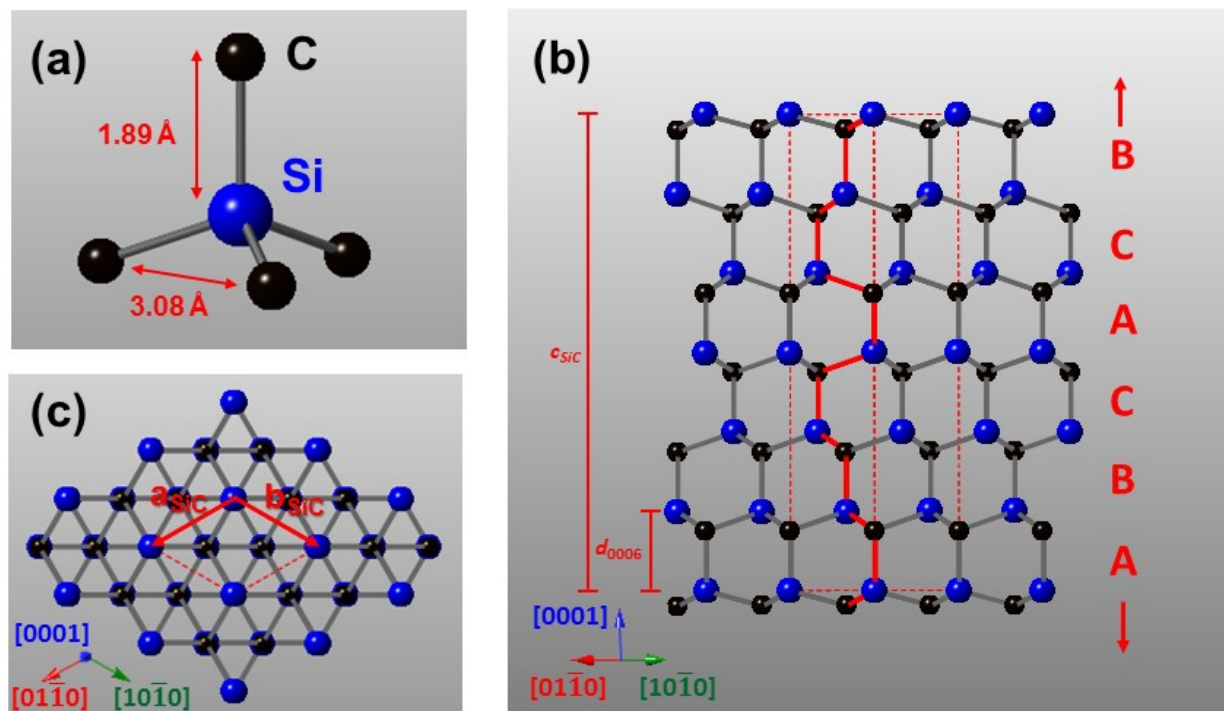


Figure 2.5: Crystal structure of 6H-SiC. (a) The basic structural element of the SiC crystal is the Si-C tetrahedral bonding arrangement. (b) A projection along the $\text{SiC}[\bar{1}\bar{1}20]$ direction, highlighting the ABCACB-type stacking arrangement. The top-view (Along the $\text{SiC}[0001]$) of the $\text{SiC}(0001)$ crystal structure. (c) The lattice vectors and unit cell are indicated with red arrows and dashed red lines, respectively. Note that to minimize surface dangling bonds the (0001) surface will be Si terminated while the $(000\bar{1})$ will be C-terminated.

≈ 2.52 Å. SiC is intrinsically a large bandgap semiconductor (3.02 eV for 6H-SiC), and is therefore defined as insulating, but can be *p*-doped or *n*-doped with various Group 13 or Group 15 elements, respectively. This insulating nature of SiC is an advantage over CVD-grown graphene on metals in terms of device fabrication. [Figure 2.5\(c\)](#) shows a view along the SiC[000 $\bar{1}$] direction, indicating the hexagonal symmetry of the ideal, unreconstructed SiC(0001) 1×1 surface. The in-plane lattice parameters are $a_{\text{SiC}} = b_{\text{SiC}} = 3.08$ Å.

2.3.2: Growth and Structure of EG/SiC

As mentioned earlier, the production of graphene via the preferential sublimation of Si from the substrate is a high-temperature ($\sim 1200^\circ$ C in UHV with direct heating or electron bombardment or $\sim 1600^\circ$ C under Ar atmosphere or low vacuum in an induction furnace) process. The step-by-step UHV growth process of EG/SiC(0001) has been well-documented. An example preparation routine (characterized using low-energy electron diffraction (LEED)) is shown in [Figure 2.6](#), and identifies the surface phase evolution as a function of anneal temperature as described by Emtsev *et al.* in Ref. [24]. It is important to note that EG/SiC(0001) preparation varies widely from laboratory to laboratory, and the methodology can affect EG coverage uniformity, thickness, and surface morphology [21, 29, 84, 85]. However, as discussed in [Section 2.3.3](#), the chemical and structural nature of the final graphitized state does not seem to vary significantly between EG/SiC(0001) growth methodologies. Indeed, the final product typically exhibits characteristic LEED patterns and XPS spectra which are associated with an interfacial $(6\sqrt{3}\times 6\sqrt{3})R30^\circ$ reconstructed layer covered by graphene [29, 85, 86].

Referring to [Figure 2.6](#), samples are generally ultrasonically solvent-cleaned to remove organic contaminants, and then etched in H_2 at high temperature ($>1000^\circ C$) before introduction to the UHV chamber in order to remove surface and polishing damage. This process produces a regular, atomic-stepped surface [88]. A native SiO_2 surface oxide forms upon exposure of the SiC surface to air [89, 90], but the oxide is unstable above $\sim 1000^\circ C$ and therefore removed naturally during the EG growth process [86]. The initial annealing steps drive off the surface oxide (which is possible at lower temperatures under Si flux), and the surface then proceeds through a series of (3×3) and $(\sqrt{3}\times\sqrt{3})R30^\circ$ reconstructions, the formation of which is dependent on whether Si flux provided to the surface. It should be noted that the practice of supplying Si flux to the surface is not universal (it was not performed on the samples presented in this thesis), and is not thought to have a significant influence on the C-rich or EG phases that form at higher temperature [21, 86].

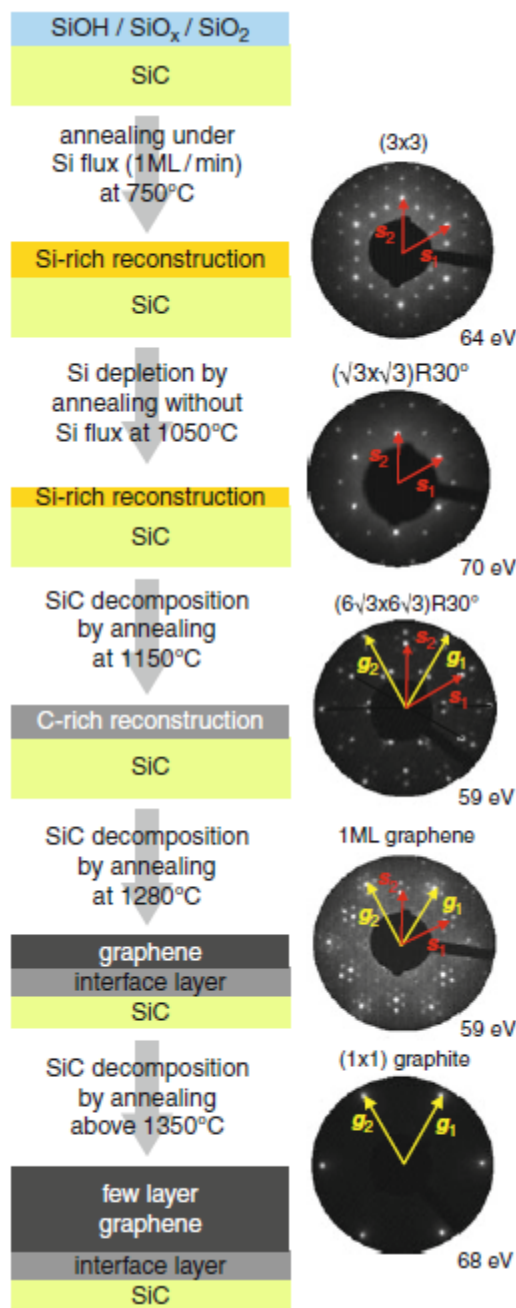


Figure 2.6: Schematic of a typical UHV-graphene growth procedure. The process is described in Ref. [24] and the diagram is from Ref. [87]

Eventually, and for the most part regardless of the nuances of the UHV preparation method, the $(6\sqrt{3}\times 6\sqrt{3})R30^\circ$ reconstructed phase is observed at $\sim 1150^\circ\text{C}$ and graphitization occurs $\sim 1250^\circ\text{C}$. Further heating results in the formation of additional graphene layers [86, 87].

Although UHV-grown graphene samples are still commonly used, this method of growth is poorly kinetically controlled and typically results in samples with poor surface morphology and broad coverage distribution (see [Figure 2.7](#)) [91, 92]. However, by providing a diffusion barrier to Si sublimation with an Ar-growth atmosphere, it is possible to effectively increase the Si vapor pressure at the SiC surface [87, 88, 93]. This increased partial pressure helps to equilibrate the EG growth process by slowing the Si evaporation rate. Because the Ar-growth

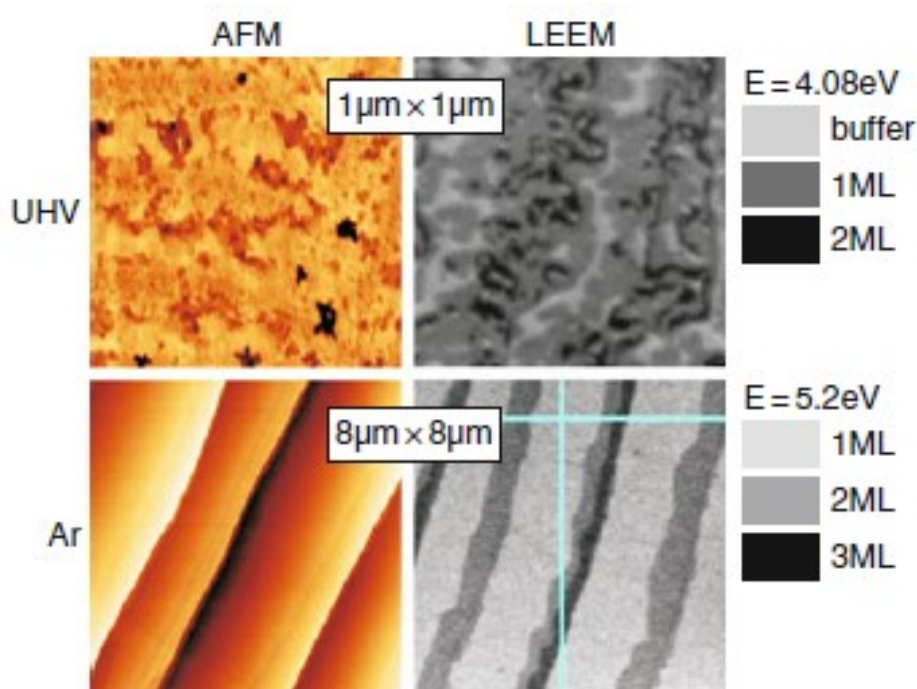


Figure 2.7: Comparison of surface morphology and coverage uniformity of UHV- and Ar-grown EG/SiC. AFM (left panel) shows that EG/SiC surface morphology is greatly improved using Ar-mediated growth. Similarly, LEEM mapping of EG coverage shows that on Ar-grown samples, EG multilayer growth is limited near the step edges, with the large terraces covered by monolayer EG, while UHV-grown samples have interspersed regions of 0, 1, and 2 ML graphene. From Refs. [87] and [88].

method requires higher temperatures to surpass the diffusion barrier, as opposed to EG grown in UHV, the growth is performed at $\sim 1600^\circ\text{C}$, enabling enhanced C surface diffusion. According to the current models describing the growth process, the balance of Si sublimation and C surface diffusion is crucial to the step-flow growth mode, and is greatly improved using Ar-assisted growth [94]. The ultimate result is an improved growth mode that produces morphologically superior EG/SiC(0001). A comparison of morphology and graphene layer coverage using atomic force microscopy (AFM) and low-energy electron microscopy (LEEM) is shown in [Figure 2.7](#). Samples produced using both UHV- and Ar-growth methods were studied in this work.

2.3.3: The EG/SiC(0001) Interface

One particularly interesting feature that arises during the growth of EG/SiC(0001) in both UHV- and Ar ambient environments is the formation and persistence of the $(6\sqrt{3}\times 6\sqrt{3})R30^\circ$ reconstructed layer. This reconstruction was first observed in the earliest studies of graphitization of SiC(0001) by van Bommel *et al.*, and it was suggested that it was caused by a weakly interacting graphite layer sitting atop the unreconstructed SiC surface [17]. Interestingly, it was found that when the UHV growth of EG/SiC(0001) was monitored *in situ* using LEED, the $(6\sqrt{3}\times 6\sqrt{3})R30^\circ$ reconstruction pattern first appears at about 1150°C and persists at higher temperatures, although the $(6\sqrt{3}\times 6\sqrt{3})R30^\circ$ LEED spot intensities decrease with increased surface coverage [29]. This observation indicates the presence of a sustained interfacial structure even after graphene formation. At sufficiently high EG coverage the LEED spots from the interfacial layer are completely attenuated by the EG overlayers (see [Figure 2.6](#)). EG coverage-dependent XPS measurements later corroborated the LEED results [24], identifying a pair of core-shifted interfacial signals that maintain constant relative intensity during graphene growth.

This interfacial layer, varyingly called the buffer layer, zero-layer graphene, EG_0 (or G_0), carbon nanomesh, $(6\sqrt{3}\times 6\sqrt{3})R30^\circ$ layer or $6R3$ layer (in this work, we use either “interfacial layer” or “ EG_0 ”), is of great interest for understanding the behavior of the electronic properties of overlaying EG sheets. This stems from the fact that, while EG grown on SiC(0001) exhibits a graphene-like band structure [24, 95], it has significantly poorer electronic properties (e.g., mobility) than either graphene grown on the C-face of SiC [19, 96, 97] or compared to CVD and exfoliated graphenes [98]. It has been suggested that the interfacial layer has pronounced influence on the behavior of the graphene, affecting its carrier type and density [8, 59, 99, 100], introducing charge scattering centers [30, 101, 102], and causing symmetry breaking and bandgap formation [25, 26, 28]. Many of these effects are highly debated in no small part due to the poorly-understood nature of the interface itself. Therefore, since the precise atomic and chemical nature of the interface may play a decisive role in the physical properties of the overlaying graphene sheets, it is critical to gain an accurate understanding of its structure [3, 5, 25, 103].

The exact structure of the interface has been debated since its first observation in 1975 [17] and has since been the main focus of a large body of work. After the first studies by van Bommel and co-workers, in which the interface layer was suggested to be a weakly-interacting graphene layer sitting atop an unreconstructed SiC surface, other groups offered an assortment of alternate structures. These included coexisting surface phase models and $(\sqrt{3}\times\sqrt{3})R30^\circ$ reconstructed SiC surfaces under commensurable graphite layers [104-107]. Later, after the discovery of the extraordinary nature of EG/SiC piqued the research community’s interest, further models were suggested (examples in [Figure 2.8](#)) including:

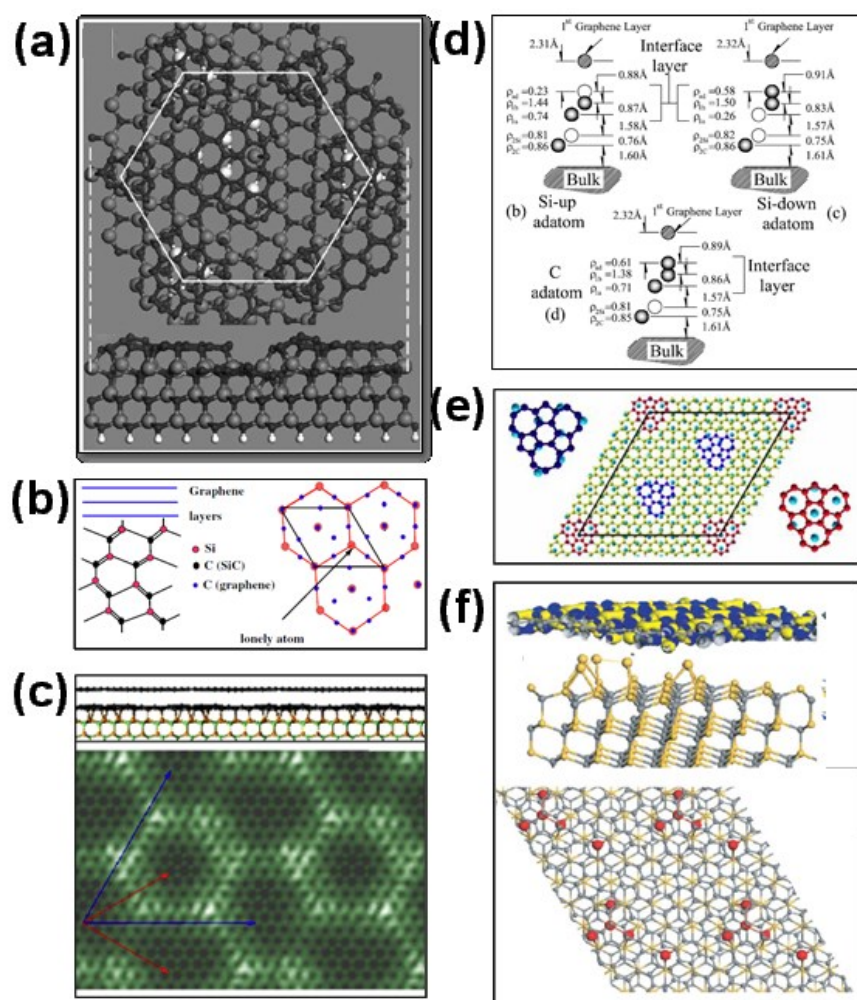


Figure 2.8: A selection of competing models of the SiC interface structure. (a) The 6×6 C nanomesh [108]; (b) The covalently-bound stretched graphene (CSG) model [109]; (c) A rippled, covalently-bound graphene-like layer [103]; (d) Complex Si- and C-adatom layered structures [21]; (e) A defected, warped, graphene-like layer [23]; and (f) A periodic cell with Si tetramer and adatom structures.

1. A 6×6 nanomesh model with isolated C nanoislands (Figure 2.8(a)) [108].
2. Covalent bound/stretched graphene models (CSG), which possess high populations of interfacial dangling Si bonds (Figure 2.8(b)) [109-111].
3. A rippled, partially covalently-bound, topologically graphene-like layer model (Figure 2.8(c)) [24, 32, 103, 112].
4. Complex Si- or C-adatom models possibly possessing of Si tetramer and adatom structures (Figure 2.8(d) and (f)) [21, 22].
5. A warped, defected layer model with hexagon-pentagon-heptagon defects (Figure 2.8(e)) [23].

These many varied models have complicated the interpretation of this interfacial structure, leaving the true nature of the EG₀ an open question. Recently, however, the consensus has begun to lean strongly towards [model 3](#), despite the occasional report to the contrary [27, 113-115]. The topic of the nature of the interface layer is revisited using a fresh experimental approach in [Chapter 4](#).

2.4: Modifying Epitaxial Graphene

As the study of graphene moves beyond the scope of basic science and into practical implementation into functional devices, it will be necessary to control the electronic properties of graphene in order to tailor the material to specific applications. For this reason, we will need to move beyond pristine EG/SiC structures and on to engineered materials. A full integration of EG/SiC into nanoelectronics will require the understanding and control of the EG/SiC band structure and charge carrier behavior as well as precise patterning and lithography for production of graphene nanostructures. Additionally, the control of the graphene surface for incorporation with other electronic materials and the engineering of the EG/SiC interface for the tailoring of the graphene properties may prove crucial. In this work we discuss two ways in which the surface and interface can be controlled: via non-covalent molecular functionalization of the EG basal plane, and by intercalation of chemical species to the interface.

2.4.1: EG/SiC(0001) Intercalation

Owing to the influence of the interface on the behavior of EG/SiC discussed in the previous section, there have recently been a number of efforts aimed at modifying the interfacial structure via the intercalation of various atomic species (see Ref. [33] and references therein). The first

and most well-studied example of this is the intercalation of hydrogen to the interface [30]. This is performed either with a high-temperature anneal of EG/SiC in the presence of ultrapure molecular hydrogen [30] or by the exposure of the EG/SiC surface to atomic hydrogen in UHV [116]. The authors contend that these treatment processes allow for the penetration of the hydrogen atoms through the graphene layers and into the interface, where they break the Si-C bonds that exist between the Si-terminated SiC (according to [model 3](#) in [Section 2.3.3](#)) and subsequently saturate the dangling Si bonds. This results in the decoupling of the covalently attached interfacial layer from the substrate, converting the graphene-like layer into a new, nominally pristine graphene sheet [30]. This process was found to be reversible, with the de-intercalation of the hydrogen occurring at $\sim 700^\circ\text{C}$ when annealed in vacuum [30]. Recently, the technological relevancy of this treatment has been emphasized with Hall mobility studies, which found improved room-temperature mobility ($\times 3$), decreased mobility dependence on temperature [117], modification of dopant type and carrier concentration [30], and improved graphene transistor behavior [31]. Additionally, this intercalation process is helping to elucidate the source of the doping of various EG/SiC systems, as recently discussed by Ristein *et al.* [99].

Following the first reports of H-intercalated EG/SiC(0001) the method has expanded to utilize a veritable zoo of new intercalants, including Li, O, F, Na, Si, Ge, and Au [34, 35, 118-122]. Each of these intercalants has the potential to impart distinct influence on the overlaying graphene sheets, providing a wealth of opportunities for the tailoring of the overlaying graphene layers [33]. While much progress has been made already, the understanding of these intercalated structures will be central to the development of these new interfacial engineering techniques.

2.4.2: EG/SiC Functionalization

If EG/SiC is to play a role in future nanoscale devices it will need to be easily incorporated with other types of materials, such as dielectrics and metals [123, 124]. The surface of pristine EG/SiC is inherently chemically inert due to its homogeneity and the delocalized sp^2 electronic hybridization of the C bonds. This means that, unlike other semiconductor materials like Si, Ge, or GaAs, there are no available surface bonding sites for the growth of dielectric films or metal contacts. For this reason, it is essential to develop various functionalization schemes to integrate EG/SiC into devices.

The main aim of the functionalization schemes presented in this work is to enable the atomic layer deposition (ALD) growth of high-quality thin films and nanostructures on the EG/SiC surface. This means that we must seek to provide specifically reactive chemical handles on the graphene surface while avoiding any deterioration of the graphene properties during the process. To do this, one needs to construct sufficiently robust functional moieties while avoiding disruption of the graphene lattice itself. The routes for functionalization the graphene surface can be split into two categories: covalent and non-covalent chemistries.

Covalent functionalization schemes rely on covalent attachment of various chemical species to the C within the graphene layer itself. The most common forms of atomic covalent functionalization use H, F, and O [125], which can provide a simple, uniformly functionalized graphene surface while exerting minimal influence on the graphene electronic behavior [126-129]. Other functionalization pathways may make use energetic organic free radicals [130-132] or acidic oxidation [133]. However, since covalent functionalization schemes rely inherently on the disruption of the graphene sp^2 hybridized structure, the possibilities for negative effects on

the graphene layer are ever-present. An alternative approach is to employ non-covalent functionalization of graphene [134, 135]. There have been a variety of approaches for this weakly-interacting functionalization, including the spin-coating of polymer films [136, 137], deposition of metals [10, 138] or metal oxides [139, 140], and the use of small inorganic [141, 142] or large aromatic molecules [36, 124, 143, 144]. Typically, the interactions of these materials with the graphene layer are sufficiently weak that the electronic properties of the graphene are largely unaffected, although situations in which doping occurs have been observed [10, 145, 146]. The non-covalent approach is a promising way to provide chemical reactivity to the graphene surface while maintaining the quality of the underlying graphene.

Chapter 3

X-ray Characterization Methods

THE EVER-INCREASING demand for compact, high-performance, and inexpensive electronic devices drives the relentless miniaturization of electronic components. This demand has now pushed manufacturers close to the ~10 nm regime, where highly precise control at the near-atomic-scale is required. To achieve this degree of control it is critical that precise, fundamental structural understanding is established for relevant materials. To achieve this, it is necessary to develop and utilize appropriate tools for the characterization of the new materials that may one day be essential to the industry. One promising class of electronic materials is that of 2D crystals [1]. These include, for example, atomically thin sheets carbon (graphene), boron nitride, and molybdenum disulfide, which are known for their semimetallic, insulating, and semiconducting properties, respectively. In principle, these materials can be used as building blocks to create the 2D electronic components of the future. The surge in interest in these low-

dimensional structures has proven a windfall for surface scientists, who have spent decades developing tools to resolve surface, interface, and nanoparticle structures with Å-scale resolution. Some of the most-used of these methods include electron-, ion-, and X-ray scattering and spectroscopy, as well as a variety of scanning probe techniques. This Chapter provides descriptions for a number of surface-sensitive X-ray techniques that are used to investigate the structure of pristine, functionalized, and intercalated forms of epitaxial graphene. This Chapter is meant to be a general introduction to the techniques of interest, but the examples provided in this chapter are derived for EG/SiC system in order to provide a perspective congruent with the experimental work of later chapters.

3.1: X-ray Interactions with Matter

The central concepts in this dissertation revolve around the interactions of X-rays with matter. It is therefore important to establish a basic conceptual foundation of the processes in which X-rays interact with matter at the atomic level: scattering and absorption. This section provides a brief introduction to the basic physical principles that are critical to the characterization techniques used in this work. Here, we largely restrict ourselves to a classical description in order to simplify the discussion. In the general description of scattering and the extension to crystal truncation rod (CTR) analysis, we use the kinematical approximation, which assumes an elastic, single-scattering mechanism, and is appropriate in low-intensity scattering regimes. In the description of X-ray standing wave, however, it will be necessary to incorporate dynamical diffraction theory, which accounts for multiple scattering effects. Thorough descriptions of the X-ray scattering can be found in books by Warren [147], Cowley [148] or Als-Nielsen and

McMarrow [149]. More in-depth discussion concerning the quantum physics of photoelectric absorption are available from Loudon [150] or Mandl and Shaw[151].

3.1.1: X-ray Scattering

X-rays are transverse electromagnetic waves comprised of perpendicular electric and magnetic fields that propagate along wavevector $\mathbf{k} = \hat{\mathbf{u}} \frac{2\pi}{\lambda}$, where λ is the wavelength and $\hat{\mathbf{u}}$ is the directional unit vector. In the approximation of a linearly polarized planewave, the electric field (E -field) component of the electromagnetic wave is described as $\mathbf{E}(\mathbf{r}, t) = \hat{\mathbf{\epsilon}} \mathcal{E}_0 e^{i(\omega t - \mathbf{k} \cdot \mathbf{r})}$, where $\hat{\mathbf{\epsilon}}$ is the unit vector describing the direction of the polarization of the E -field, \mathcal{E}_0 is the E -field amplitude, \mathbf{r} is the position vector, ω is the angular frequency, and t is time. Note here that the magnetic component of the X-ray is neglected in the following discussion because the intensity of magnetic scattering is orders of magnitude weaker than that of charge scattering.

In this section it is adequate to use the classical elastic description of X-ray scattering, in

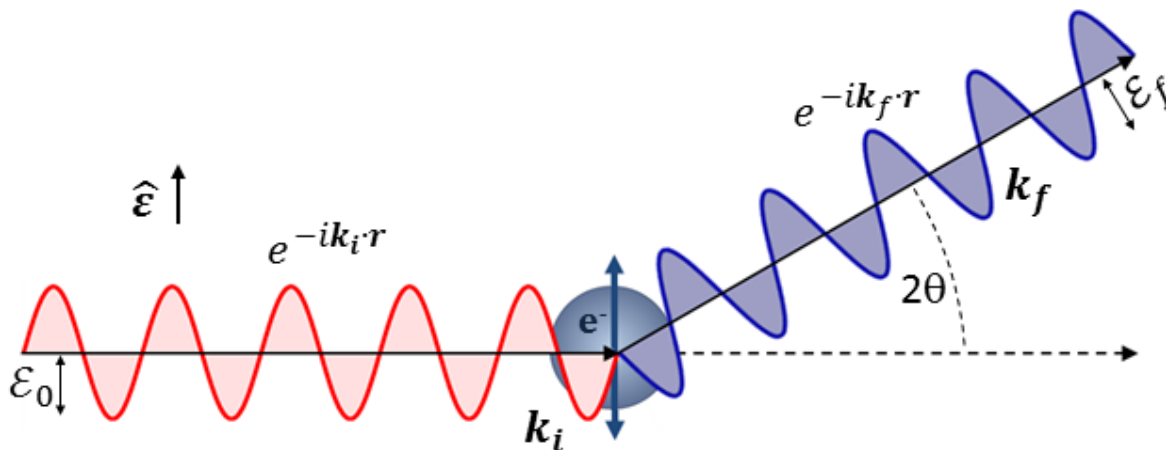


Figure 3.1: A classical depiction of scattering of an electromagnetic wave by a free electron. The outgoing wave scatters at angle 2θ with respect to the incoming wave. In this example we show a π -scattering geometry. Adapted from Schleputz [152].

which the wavelengths of the incident and scattered photons (with wavevectors \mathbf{k}_i and \mathbf{k}_f , respectively) are equal ($|\mathbf{k}_i| = |\mathbf{k}_f| = 2\pi/\lambda$), or Thomson scattering. In this process, which is depicted in [Figure 3.1](#), the E -field component of the incoming X-ray planewave ($\mathbf{E}_0 = \mathcal{E}_0 e^{-i\mathbf{k}_i \cdot \mathbf{r}}$) oscillates the free electron in a way that is conceptually analogous to the classical damped, driven, harmonic oscillator. The electron will, in turn, accelerate and anisotropically emit radiation into space. The magnitude of the emitted radiative field ($|\mathbf{E}_{rad}|$) is proportional to that of the incoming planewave, but is also inversely proportional to the radial distance from the scattering event, R , and affected by the relative orientation of the scattered beam with respect to the primary beam polarization, which is accounted for by polarization factor. The Thomson scattering equation [147, 153] relates the incident and radiated E -field amplitudes

$$\begin{aligned} \mathcal{E}_f e^{-i\mathbf{k}_f \cdot \mathbf{r}} &= \mathcal{E}_0 \frac{r_e}{R} p e^{-i\mathbf{k}_i \cdot \mathbf{r}} \\ \mathcal{E}_f &= \mathcal{E}_0 \frac{r_e}{R} p e^{i(\mathbf{k}_f - \mathbf{k}_i) \cdot \mathbf{r}} = \mathcal{E}_0 \frac{r_e}{R} p e^{i\mathbf{q} \cdot \mathbf{r}} \end{aligned} \quad (3.1)$$

where r_e is the Thomson scattering length, and $\mathbf{q} = \mathbf{k}_f - \mathbf{k}_i$ is the momentum transfer vector (see [Figure 3.2](#)). The magnitude of \mathbf{q} is $|\mathbf{q}| = q = \frac{4\pi}{\lambda} \sin(\frac{2\theta}{2})$, where 2θ is the scattering angle between \mathbf{k}_i and \mathbf{k}_f . p is the polarization factor

$$\begin{aligned} p &= \hat{\mathbf{e}}_0 \cdot \hat{\mathbf{e}}_f = 1 \text{ for } \sigma\text{-polarization and} \\ p &= \hat{\mathbf{e}}_0 \cdot \hat{\mathbf{e}}_f = \cos(2\theta) \text{ for } \pi\text{-polarization,} \end{aligned} \quad (3.2)$$

where $\hat{\mathbf{e}}_0$ and $\hat{\mathbf{e}}_f$ are the polarization vectors for the incoming and scattered waves. During X-ray measurements we are sensitive to the intensity of the scattered X-ray, which is the modulus squared of the amplitude,

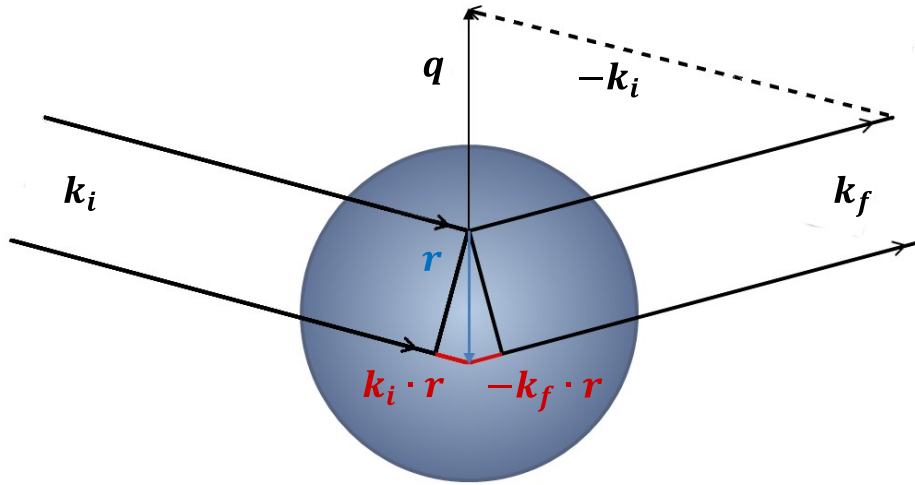


Figure 3.2: Scattering from an isolated atom with charge distribution $\rho(\mathbf{r})$. When an incoming X-ray plane wave, denoted by wavevector \mathbf{k}_i , is scattered elastically ($|\mathbf{k}_i| = |\mathbf{k}_f|$) along \mathbf{k}_f , the phase shift between the wave scattered from the origin and one at position \mathbf{r} is $(\Delta v) = \mathbf{q} \cdot \mathbf{r}$. Adapted from Als-Nielsen and McMorrow [149].

$$I = |\mathcal{E}_f|^2 = I_0 \left(\frac{r_e}{R}\right)^2 P \quad (3.3)$$

where $I_0 = \mathcal{E}_0 \cdot \mathcal{E}_0^*$ is the intensity of the incoming wave and $P = p^2$ is the polarization factor defined at the level of intensity¹. It is important to note the consequences of the cancellation of the phase terms in [Eq. 3.3](#) due to the product of the scattered plane wave with its complex conjugate. This loss of this phase information during measurement is the source of the infamous phase problem in X-ray crystallography, and is arguably the greatest obstacle in the interpretation of X-ray scattering data. Regardless, a great deal of information can still be acquired by measuring the scattered intensity, which makes X-ray scattering a powerful technique.

¹The polarization factor defined at the level of intensity:

$$P = \begin{cases} 1 & \sigma - \text{scattering geometry} \\ \cos^2(2\theta) & \pi - \text{scattering geometry} \\ \frac{1}{2}(1 + \cos^2(2\theta)) & \text{unpolarized} \end{cases}$$

This description of scattering from a single point charge can be extended to the scattering of X-rays from an atom modeled by a continuous charge distribution of density $\rho(\mathbf{r})$. Here, each individual volume fraction $d\mathbf{r}$ at position \mathbf{r} contributes a value proportional to $\rho(\mathbf{r})d\mathbf{r}$ (from this point we neglect the factor $\mathcal{E}_0 \frac{r_e}{R} p$ from [Eq. 3.1](#) for brevity) to the overall scattered amplitude. The waves contributed by each scattering volume fraction interfere and the coherent addition of these waves determines the total scattered amplitude. The interference of these waves depends on the phase differences (Δv) between waves scattered from volume elements displaced from an arbitrarily defined origin by \mathbf{r} ([Figure 3.2](#)) and is defined by their path-length difference, $\mathbf{k}_i \cdot \mathbf{r} + (-\mathbf{k}_f \cdot \mathbf{r})$. This phase difference is expressed as $\Delta v(\mathbf{r}) = \mathbf{q} \cdot \mathbf{r}$ and defines the phase factor of the scattered field, $e^{i\mathbf{q} \cdot \mathbf{r}}$, first introduced in [Eq. 3.2](#). Integration over a specific atomic charge density distribution then yields definition of the scattering amplitude,

$$f^0(\mathbf{q}) = \int \rho_a(\mathbf{r}) e^{i\mathbf{q} \cdot \mathbf{r}} d\mathbf{r}, \quad (3.4)$$

also known as the *atomic form factor*. \mathbf{q} -dependent factors for free atoms and many ions have been calculated and are typically approximated using the Cromer-Mann equation [154]. [Eq. 3.4](#) also establishes a very important concept that can be generalized to *any* electron density distribution (e.g., single crystals, stratified media, nanoparticle distributions, amorphous materials, etc.). Namely, the scattered amplitude, or *structure factor*, is proportional to the Fourier transform of any electron density distribution,

$$F(\mathbf{q}) = \int \rho(\mathbf{r}) e^{i\mathbf{q} \cdot \mathbf{r}} d\mathbf{r}. \quad (3.5)$$

The Fourier description of scattering from an electron density distribution is a central concept to many of the techniques used in this work.

The addition of dispersion corrections f' and f'' to [Eq. 3.4](#) gives the full \mathbf{q} - and E_γ - (incident beam energy) dependent atomic scattering factor,

$$f^a(\mathbf{q}, E_\gamma) = f^0(\mathbf{q}) + f'(E_\gamma) + if''(E_\gamma). \quad (3.6)$$

This equation, which defines the scattered amplitude from a single atom, can first be expanded to describe a unit cell, and then a bulk crystal. The scattering from a unit cell (*u.c.*) is expressed by the coherent addition of the scatterers, the j^{th} atoms, located within the unit cell at positions \mathbf{r}_j (see [Eq. 2.1](#)). This contribution is expressed in terms of the unit cell structure factor,

$$F_{u.c.}(\mathbf{q}) = \sum_j f_j^a(\mathbf{q}) e^{i\mathbf{q}\cdot\mathbf{r}_j} \quad (3.7)$$

and is proportional to the unit cell's total scattered amplitude. In turn, the structure factor for a small crystal of $N_1 \times N_2 \times N_3$ unit cells is the lattice sum of all unit cells at positions $\mathbf{R}_n = n_1\mathbf{a} + n_2\mathbf{b} + n_3\mathbf{c}$, where n_1, n_2, n_3 are an integers. When separated into the basis components the expression for the total structure factor for the crystal is

$$F_{crystal}(\mathbf{q}) = F_{u.c.}(\mathbf{q}) \sum_{n_1=0}^{N_1-1} e^{i\mathbf{q}\cdot(n_1\mathbf{a})} \sum_{n_2=0}^{N_2-1} e^{i\mathbf{q}\cdot(n_2\mathbf{b})} \sum_{n_3=0}^{N_3-1} e^{i\mathbf{q}\cdot(n_3\mathbf{c})}. \quad (3.8)$$

We can simplify this equation with the convergence of the geometric sum,

$$S_N(q) = \sum_{n=0}^{N-1} e^{iqan} = \frac{1 - e^{iqaN}}{1 - e^{iqa}}; \quad (3.9)$$

$$|S_N(\mathbf{q})|^2 = \frac{\sin^2\left(\frac{1}{2}N\mathbf{q}\cdot\mathbf{a}\right)}{\sin^2\left(\frac{1}{2}\mathbf{q}\cdot\mathbf{a}\right)},$$

and substitute the result into [Eq. 8](#) to calculate the \mathbf{q} -dependent intensity (using [Eq. 3.3](#))

$$I(\mathbf{q}) = |F_{u.c.}(\mathbf{q})|^2 \frac{\sin^2\left(\frac{1}{2}N_1\mathbf{q}\cdot\mathbf{a}\right)}{\sin^2\left(\frac{1}{2}\mathbf{q}\cdot\mathbf{a}\right)} \frac{\sin^2\left(\frac{1}{2}N_2\mathbf{q}\cdot\mathbf{b}\right)}{\sin^2\left(\frac{1}{2}\mathbf{q}\cdot\mathbf{b}\right)} \frac{\sin^2\left(\frac{1}{2}N_3\mathbf{q}\cdot\mathbf{c}\right)}{\sin^2\left(\frac{1}{2}\mathbf{q}\cdot\mathbf{c}\right)}. \quad (3.10)$$

This is the so-called 3D interference function, and is the basis for describing many useful diffractive phenomena. Examination of [Eq. 3.10](#) reveals the special case in which the Laue conditions are satisfied,

$$\mathbf{q}\cdot\mathbf{a} = 2\pi h, \quad \mathbf{q}\cdot\mathbf{b} = 2\pi k, \quad \mathbf{q}\cdot\mathbf{c} = 2\pi l, \quad (3.11)$$

where the integers h , k , and l are the Miller indices. At these conditions (and for $N > 1$) the diffracted intensity will be maximized. The 3 scalar equations for the Laue condition are equivalent to the single vector equation,

$$\mathbf{H} = \mathbf{q} = h\mathbf{a}^* + k\mathbf{b}^* + l\mathbf{c}^*. \quad (3.12)$$

Note here that the magnitude $|\mathbf{H}| = \frac{2\pi}{d_H}$, where d_H is the spacing between H lattice planes. The

Laue equations can be reduced to the common scalar form, Bragg's Law,

$$|\mathbf{H}| = \frac{2\pi}{d_H} = |\mathbf{q}| = \frac{4\pi}{\lambda} \text{Sin}\left(\frac{2\theta}{2}\right) \quad (3.13)$$

$$2d \text{Sin}(\theta_B) = \lambda,$$

or, through the de Broglie relation,

$$E_B = \frac{hc}{\lambda} = \frac{hc}{2d \text{Sin}(\theta_B)}.$$

These relationships define the geometrical Bragg angle, θ_B and geometrical Bragg energy (E_B). At the Bragg conditions defined in [Eq. 3.11](#), and in the $N \rightarrow \infty$ limit of a 3D crystal, [Eq. 3.10](#) describes a 3D array of δ -functions at hkl points in reciprocal space which form the *reciprocal lattice* of a specific crystal structure. The reciprocal lattice construction is extremely useful in describing diffraction, but to this point we have only established its most basic description. In [Section 3.2](#) we extend this formalism for the special case of scattering along the surface normal of a semi-infinite truncated crystal: high-resolution X-ray reflectivity (XRR). In [Section 3.3](#), however, we must precisely describe the scattered intensity in the region of single-crystal Bragg reflections. In this regime the kinematical approximation breaks down and we must employ dynamical diffraction theory for a precise description of the scattering phenomena.

3.1.2: Photoelectric Absorption and Photoelectron Spectroscopy

As mentioned earlier, X-rays can interact with matter by scattering or absorption processes. Strictly, a quantum mechanical approach for both the incoming electromagnetic field and the photoelectron are required to accurately describe the physics of X-ray absorption. However, in this work, it is typically sufficient to limit ourselves to a classical analysis. Here, X-ray absorption occurs by photoionization of electrons from their ground states. When an X-ray with sufficient energy interacts with an atom, there is a possibility that an electron will be ionized from its initial state, be it a valence or core level, and ejected into the final state above the vacuum level of the sample. This is the photoelectric effect ([Figure 3.3](#)).

In core-level photoelectron spectroscopy, a hole is generated in a core atomic shell (energy E_1) upon ejection of the photoelectron. This unfilled energy state can be filled by one of two competing decay processes: fluorescence X-ray emission or Auger electron ejection. During fluorescence emission, the core hole is filled when an electron from a higher energy state (energy E_2), and a characteristic X-ray is emitted with an energy that is equal to the difference in energy ($E_{\gamma'} = E_2 - E_1$) between the higher and lower levels. The Auger emission process is qualitatively similar, but rather than producing a photon during relaxation, an Auger electron is emitted. While the study of these excitation and relaxation processes are distinct (but related) sub-disciplines of absorption spectroscopy, the information carried by the emitted photoelectron is the most revealing for chemical and electronic states, while fluorescence and Auger spectroscopies are used primarily for elemental analysis.

In this work both X-ray photoelectron spectroscopy (XPS) and X-ray fluorescence spectroscopy (XRF) are used to gain chemical and elemental knowledge about a material of interest. These spectroscopies are well-suited for the analysis of extremely low concentrations of

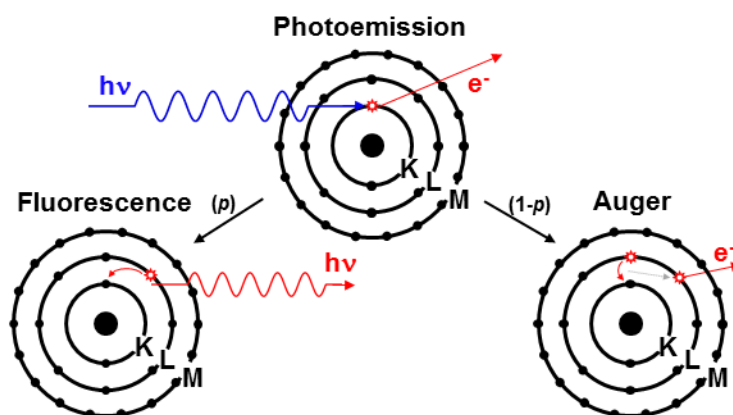


Figure 3.3: Photoexcitation and subsequent relaxation processes. An incoming photon (blue wave) ionizes an electron from the K-shell of an atom and triggers a subsequent decay cascade. After a photon ionizes the atom during the photoemission process, the hole is filled by the emission of either a.) a characteristic fluorescent X-ray or b.) an Auger electron. In the example shown, the fluorescence process is undergoing a $K\alpha$ transition and the Auger process is undergoing a KLL transition. Adapted from Zegenhagen [155].

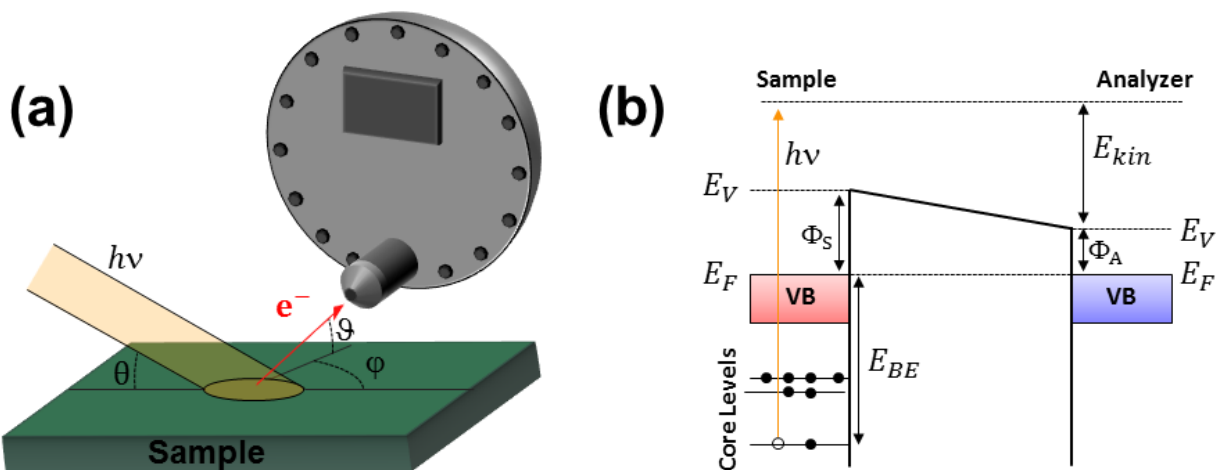


Figure 3.4: X-ray photoelectron spectroscopy fundamentals. (a) A depiction of a typical XPS experimental setup. A monochromatic X-ray beam (yellow) impinges on the sample with incident angle θ . A hemispherical photoelectron analyzer, positioned at in-plane and out-of-plane angles ϕ and Θ , analyzes the emitted photoelectrons, (b) The energy diagram representing the emission and detection of a core-level photoelectron. The Fermi levels (E_F) are aligned by a physical electrical connection between the analyzer and sample.

atoms confined to surfaces at very low (sub-monolayer) coverages. XRF is used as a probe of heavy atom elemental surface coverages, and is discussed briefly in [Section 3.4.4](#). XPS, on the other hand, is used with a greater degree of sophistication in that it is combined with the X-ray standing wave method to allow chemically-sensitive structural measurements, as discussed in detail in [Section 3.3](#).

A simple schematic of an XPS experimental setup is shown in [Figure 3.4\(a\)](#). The incoming X-ray with energy $E_\gamma = h\nu$ impinges upon the sample with some incident angle, θ . Provided that the incident beam energy is sufficiently high, an absorption event may occur, leading to the excitation of a photoelectron (e^-), which is subsequently detected by a photoelectron analyzer. The measured kinetic energy E_{kin} of the ejected photoelectrons is the incident beam photon energy minus the initial state binding energy (E_{BE}) and the work function of the analyzer, Φ_A : $E_{kin} = E_\gamma - E_{BE} - \Phi_A$, as depicted schematically in [Figure 3.4\(b\)](#). The

sample and analyzer are electrically connected to force their Fermi energies, E_F to be equal, thereby eliminating the influence of the work function of the sample, Φ_S , on the measured kinetic energy. Therefore, by measuring the photoelectron kinetic energy, it is possible to deduce the electron's initial state E_{BE} (referenced to the Fermi level of a metallic sample), and thereby obtain information about the chemical environment of the emitter atom.

Photoemission spectra provide a wealth of information about the chemical composition of the sample of interest. However, interpretation of spectra is complicated because numerous sources that can lead to the shifting, broadening, and changes in intensity of spectral components. When analyzing a photoemission spectrum, one typically attempts to interpret the core-level peak shift, peak width, lineshape, and peak intensity in order to deduce the bonding configuration of the species of interest. For example, the core-level shift is sensitive to the valence charge distribution of the emitter atom, and the magnitude of a shift can often be interpreted by comparing electronegativities of bound atoms [156]. Relative core-level shifts are also affected, for example, by band-bending (Fermi-level pinning) [30, 157], charge-transfer doping, and spontaneous substrate polarization [99, 158]. According to the Heisenberg uncertainty principle, the intrinsic energy width, Γ , of a peak is inversely proportional to the core-hole lifetime (τ) generated during the photoemission process, $\Gamma \sim \hbar/\tau$. Γ is typically on the order of few tenths of an eV for K-shell core-holes for low- Z ($Z \lesssim 15$) atoms [159]. This observed width is broadened by the finite resolution of both the analyzer and X-ray source. Other influences on the peak width include bond inhomogeneity in terms of strain (torsion and length), chemical diversity, and phonon broadening. Peak shape is influenced by the degree of inelastic scattering a photoelectron experiences, the inherent exciting X-ray and analyzer lineshapes,

specimen charging, as well as electronic structure [160, 161]. The observed intensity of a core-level signal is dependent on the experimental setup (for example, X-ray flux density, polarization and energy, detector acceptance angle and position, and sample illuminated area and geometry), the atomic photoionization cross-section, and the depth from which the photoelectrons are originating. Herein, we will take particular advantage of the sensitivity of the photoemission yield to the local intensity of an E -field standing wave, as described in [Section 3.3](#), in order to enhance conventional XPS measurements with a high degree of structural sensitivity.

The influencing factors mentioned above are of particular importance in the thesis, but are only some of the many spectral influences in XPS. For extended and more in-depth discussions of XPS, especially with respect to XPS for chemical analysis, the reader is directed to texts by Fadley [161], Barr [162], or Briggs and Seah [163].

3.2: High-resolution X-ray Reflectivity

3.2.1: Scattering from a Truncated Crystal

In [Section 3.1.1](#), the kinematical approximation is used to describe the scattered X-ray intensity from a 3D crystal. Here, we extend this formalism to the case of a truncated crystal, i.e., a non-infinite crystal which possesses a surface plane with normal along the z -direction. The consequence of the truncation is perhaps best expressed using the convolution theorem, the Fourier description of X-ray scattering, and the concepts of the real and reciprocal lattices. The convolution (denoted by operator \otimes) of two functions $f(x)$ and $g(x)$ is defined

$$(f \otimes g)(x) = \int_{-\infty}^{\infty} f(x')g(x - x') dx'. \quad (3.14)$$

The convolution of two functions produces a third function $(f \otimes g)(x)$ which, at position x , is the integrated areal overlap of the two functions original functions as $g(x')$ passes over $f(x')$. The property of the convolution function relevant to this narrative is the convolution theorem, which states that the Fourier transform of the product of two functions is equal to the convolution of the Fourier transforms (\mathcal{F}) of the individual functions,

$$\mathcal{F}(f \cdot g) = \mathcal{F}(f) \otimes \mathcal{F}(g). \quad (3.15)$$

As shown in [Figure 3.5\(a\)](#), a truncated crystal (in the z -direction) can be described as the product of an infinite three dimensional crystal (with electron density distribution, $\rho(\mathbf{r})$) with a Heaviside step function, $h(z)$. As derived in in [Section 3.1.1](#), the Fourier transform of the

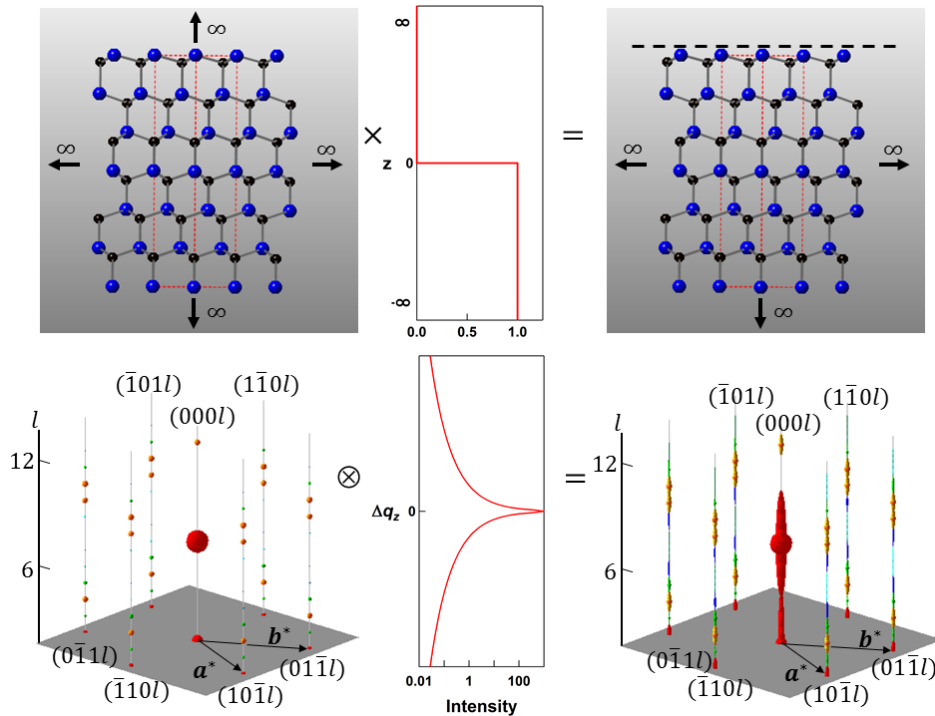


Figure 3.5: The source of CTRs as described by using the convolution theorem for the example of the 6H-SiC(0001) crystal. Adapted from Als-Nielsen [149] and Schlepütz [152].

electron density distribution of the crystal was shown to produce a periodic reciprocal lattice of δ -functions. The Fourier transform of the step function yields a function with intensity proportional to q_z^{-2} . From [Eq. 3.15](#), the reciprocal space intensity pattern is then described by the convolution of $\mathcal{F}(\rho(\mathbf{r}))$ and $\mathcal{F}(h(z))$. [Figure 3.5\(b\)](#) shows a depiction of the result of the convolution of the two functions, which produces a smearing in the intensity of the Bragg peaks in the direction normal to the surface. The continuous crystal truncation rods (CTRs) are located at integer hk indices within the surface plane, and the intensity for a perfectly truncated crystal is maximal at the Bragg peaks, but varies as Δq_z^{-2} at displacement Δq_z from the Bragg condition. A precise mathematical description of the CTR intensity as a function of q_z is found by recalling [Eq. 3.8](#) and modifying the third summation term to span a crystal truncated at $z = 0$ in the c lattice direction. This yields, after including a small absorption term ($\beta \sim 10^{-5}$),

$$F_{crystal}(\mathbf{q}) = F_{u.c.}(\mathbf{q}) \sum_{n_1=1}^{N_1} e^{i\mathbf{q}\cdot(n_1\mathbf{a})} \sum_{n_2=1}^{N_2} e^{i\mathbf{q}\cdot(n_2\mathbf{b})} \sum_{n_3=-\infty}^0 e^{i\mathbf{q}\cdot(n_3\mathbf{c})} e^{-n_3\beta}, \quad (3.16)$$

where the third term is identified as a geometric series $\sum_{n=0}^{\infty} b^n$. This sum converges to $\frac{1}{1-b}$ for $|b| < 1$ (which is true after the inclusion of the absorption term). We let $j = -n_3$, and the result yields the CTR structure factor,

$$F_{CTR}(\mathbf{q}) = \sum_{n_3=-\infty}^0 e^{i\mathbf{q}\cdot(n_3\mathbf{c})} e^{-n_3\beta} = \sum_{j=0}^{\infty} (e^{i\mathbf{q}\cdot\mathbf{c}-\beta})^j = \frac{1}{1 - e^{i\mathbf{q}\cdot\mathbf{c}-\beta}} \quad (3.17)$$

or, now neglecting absorption,

$$F_{CTR}(\mathbf{q}) \stackrel{\beta \rightarrow 0}{=} \frac{1}{1 - e^{i\mathbf{q}\cdot\mathbf{c}}} \quad (3.18)$$

In the work presented in this thesis, we limit ourselves to the special case in which $h = k = 0$ in order to probe structure along the surface normal direction, which will coincide with the c and c^* directions. The rod defined at $h = k = 0$ is called the specular rod because the angle between the incident and outgoing wavevectors and the surface normal are equal, which, in the Bragg-Brentano geometry, means that $\omega = \theta = 2\theta/2$. This measurement is referred to in this work as high-resolution XRR, or just XRR (as compared to low-angle XRR, see [Section 3.4.2](#)). Because we maintain a specular scattering condition and are therefore only measuring scattered intensity only along q_z (i.e., the in-plane components of the scattering vector, $q_x = q_y = 0$), we can combine equations [Eq. 3.16](#) and [Eq. 3.18](#) to define the total structure factor,

$$F_{Tot}(q_z) = F_{u.c.}(q_z)F_{CTR}(q_z) + F_{OL}(q_z), \quad (3.19)$$

where F_{OL} accounts for the inclusion of an overlayer of m atomic layers at positions z_m atop the truncated crystal. This additional structure factor is used to account for non-bulk surface, interface, and film layers. Each atomic layer, whether it be bulk, near-surface relaxed bulk layers, or interfacial and film overlayers, are modeled with the following equation,

$$F(q_z) = \sum_m c_m f_m^a(q_z) e^{iq_z z_m} e^{-\frac{1}{2}(q_z u_m)^2} \quad (3.20)$$

in which c_m is the fractional occupancy factor and u_m is the Debye-Waller factor distribution width.

In the last few years, the typical method for measuring CTRs has transitioned from the use of point detectors to the use of area detectors. The use of area detectors enables the simultaneous sampling of both the rocking curve and background so that the background-subtracted reflectivity signal can be acquired with a single camera shot ([Figure 3.6](#)). This has led

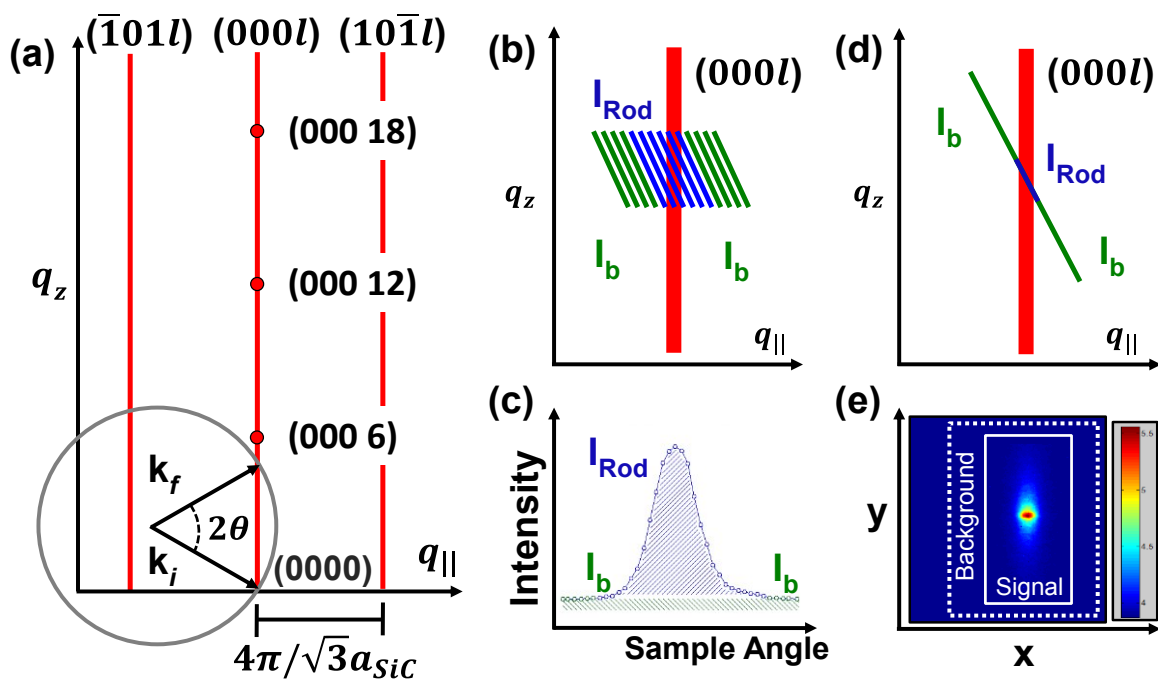


Figure 3.6: A comparison of the methods used to measure CTRs using either a point detector with fixed-detector rocking scans or an area detector. (a) The intersection of the Ewald sphere with the specular SiC(000L) rod using the Bragg-Brentano geometry. Also shown are non-specular CTRs (not to scale with respect to the Ewald sphere). (b) Representation of the rocking curve sampling method traditionally used for the measurement of CTR intensity. The slanted set of parallel line segments represent the Ewald sphere arc segments cutoff in the q_z direction by the point detector vertical slits at different points of the rocking curve scan (transverse scan). (c) The rocking curve measurement amounts to a sampling of the reflected intensity by the detector resolution function and results in a peak reflectivity (blue) superimposed on a background (green). (d) Representation of single-image sampling of the crystal truncation rod with a CCD detector. (e) Background regions and signal regions are defined within the CCD image. Adapted from Ref. [164].

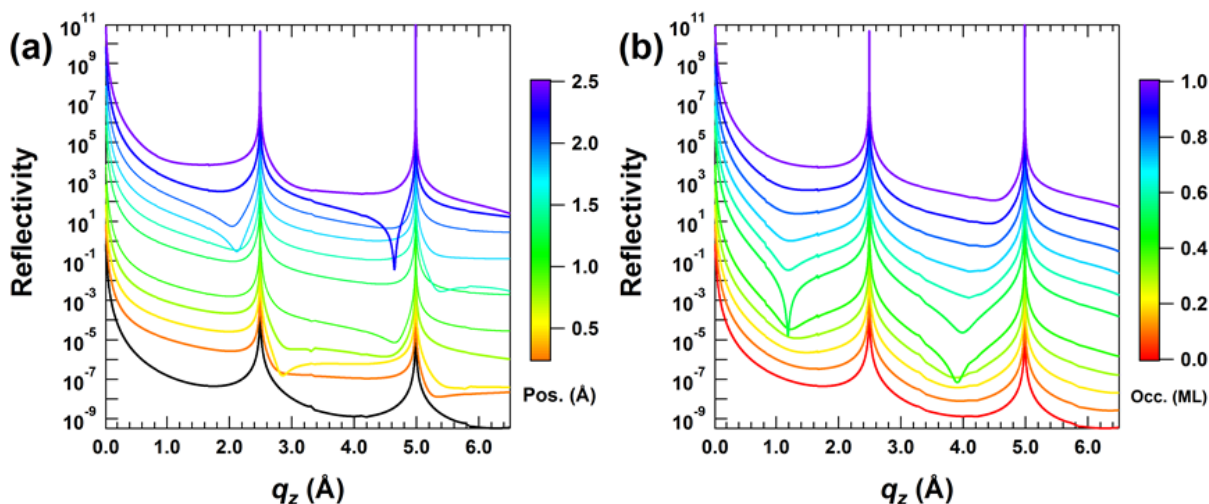


Figure 3.7: Simulations of high-resolution X-ray reflectivity curves. (a) The effect of changing the position of a hypothetical single sheet of graphene from 0.25-2.50 Å above the top-most Si layer of SiC(0001). (b) The effect of changing the occupancy of the graphene sheet between 0.0-1.0 ML coverage. The calculation for the bulk truncated crystal is shown in black in (a).

to greatly improved speed and accuracy of CTR data acquisition [164-166], increasing experimental throughput manifold. In addition, this methodology allows for the visualization of the scattered intensity, effectively enhancing the ability to identify spurious signals in the detector, and thereby improving overall data interpretation and signal integration. All XRR data presented in this work is acquired with CCD area detectors using an open-slit, σ -scattering geometry (for experimental description, see [Section 3.2.2](#)), and a monochromatic X-ray source with finite beam divergence ($\delta\theta_b$). In the condition in which the intersection of the Ewald sphere with the CTR is completely encompassed when intersected with the CCD, the absolute specular reflectivity is expressed [164, 167]

$$R(q_z) = \frac{I(q_z)}{I_0} = \left(\frac{4\pi r_e}{q_z a_{u.c.}} \right)^2 |F_{Tot}(q_z)|^2 |B(q_z)|^2, \quad (3.21)$$

where $a_{u.c.}$ is the surface unit cell area and $B(q_z)$ is the Robinson roughness factor [168],

$$|B(q_z)|^2 = \frac{(1 - \beta_R)^2}{1 + \beta_R^2 - 2\beta_R \cos(q_z c)}, \quad 0 \leq \beta_R \leq 1. \quad (3.22)$$

The derivation of [Eq. 3.21](#) includes correction factors associated with the Lorentz factor, $L = 1/\sin(2\theta)$, and detector resolution $\Delta q_z = 2k \cos(\theta)\delta\theta_b$, but the values have been reduced into the prefactor [167]. A step-by-step analysis of these factors and their forms in the open-slit CCD detector geometry can be found in the work by Fenter *et al.* [164, 167]. Also, as discussed in Ref. [164], the full acceptance of the scattered intensity into the detector will, in principle, eliminate the need for active area correction, greatly simplifying the analysis.

To convey the sensitivity of this measurement to minute changes in surface structure we refer to [Figure 3.7](#). Here, we demonstrate the effects of the presence of a single graphene-like layer (denoted EG, carbon areal density is $\sim 38.20 \text{ C/nm}^2$) on the scattering profile by changing its occupancy (c_{EG}) or position (z_{EG}). In both figures the strong peaks located at $q_z = \sim 2.5 \text{ \AA}$ and $\sim 5.0 \text{ \AA}$ are due to diffraction from the bulk 6H-SiC single crystal substrate. In [Figure 3.7\(a\)](#), the position of an ideal (flat) graphene sheet located above the Si-terminated SiC surface is varied by a displacement of 0.25 \AA to 2.5 \AA . The simulated intensity is extremely sensitive to the position of this sheet, especially at values near ~ 2.0 , ~ 2.9 and $\sim 5.5 \text{ \AA}$, where intensity variations of ~ 2 orders of magnitude are caused by $\sim 0.1 \text{ \AA}$ shifts in atomic layer positions. The same is true for the occupancy of the hypothetical graphene layer placed 2.4 \AA above the SiC substrate ([Figure 3.7\(b\)](#)). Here, the mid-zones change in intensity by orders of magnitude as the graphene coverage is adjusted from 0.0 to 1.0 ML . These examples highlight the extreme sensitivity of the measurement to sub- \AA and sub-ML changes in structure, and will prove a powerful tool for the characterization of EG/SiC.

It should be noted, however, that the assumptions that make [Eq. 3.21](#) valid with this experimental design, namely that the CCD detector is capturing the entire diffracted signal and that we integrate the signal over some negligible range in q_z , and therefore have $R(q_z) \propto F_{\text{Tot}}(q_z)$, fail at very low values of $\theta/2\theta$. This is depicted in [Figure 3.8](#). The issue arises because at very small outgoing angles, the Ewald sphere intersects the truncation rod in an extended range in q_z , which effectually invalidates the assumption that we are measuring $F_{\text{Tot}}(q_z)$ at a discrete q_z . This issue is compounded by the fact that the CCD is unable to capture the entire diffracted signal in this regime, thereby causing the signal itself to extend beyond the limits of the active area of the

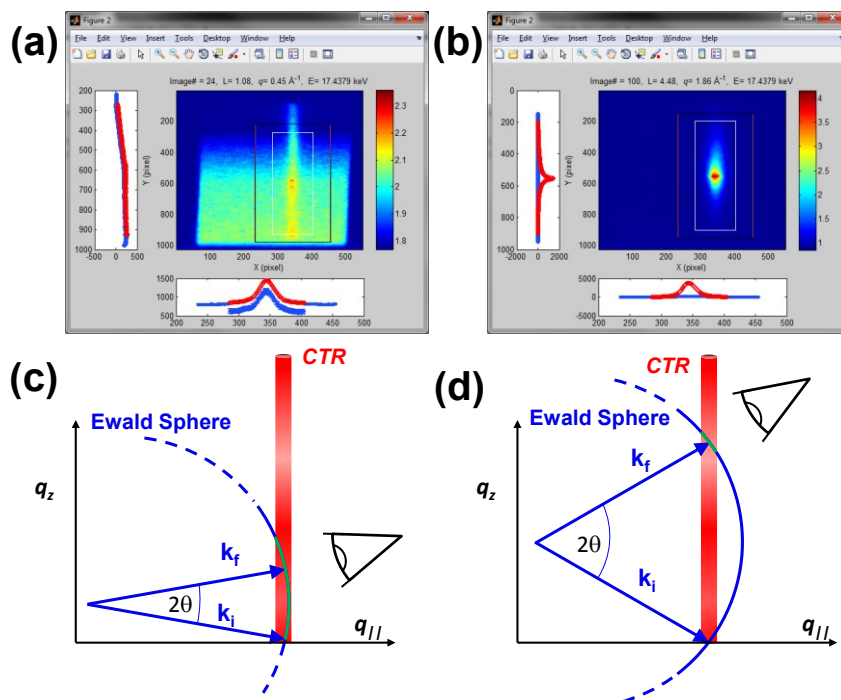


Figure 3.8: Examples of CCD images at various specular scattering conditions, q_z , and representations of the matching Ewald sphere intersection with the CTR. (a) and (c) depict measurements made at low $\theta/2\theta$, the intersection with the Ewald sphere extends over a large range in q_z , complicating data interpretation and resulting in the scattering of intensity beyond the CCD field of view. (b) and (d) show measurements at higher q_z , where the intersection of the Ewald sphere with the rod has a smaller range in q_z and is completely captured by the camera.

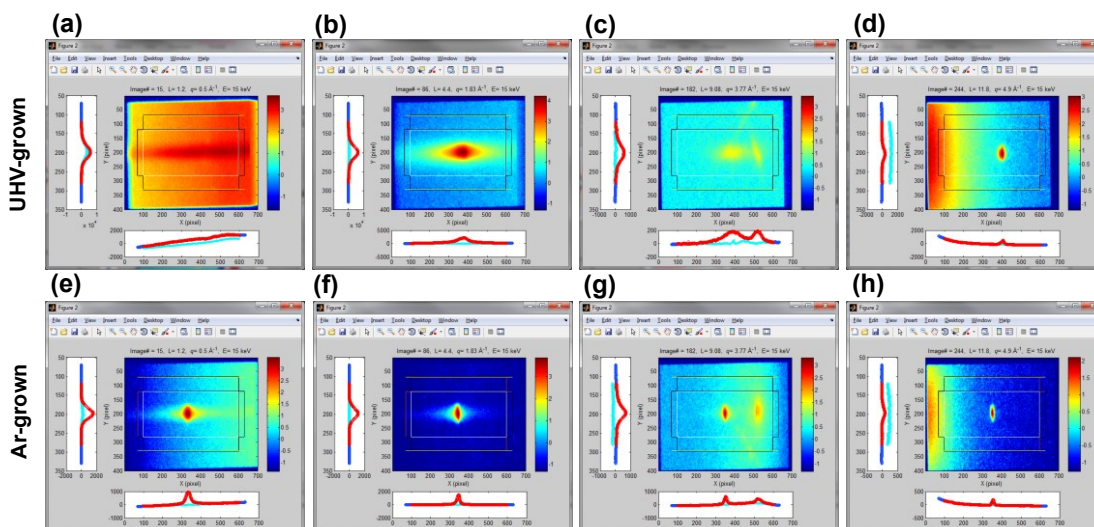


Figure 3.9: Examples of scattering signals at various scattering conditions for UHV-(a-d) and Ar-grown (e-h) EG/SiC(0001) samples. In general, the sharpening of the peaks due to the larger EG surface domains of the Ar-grown samples simplifies data extraction. (a) and (e) Scattering signal at low- q_z ($q_z = 0.5 \text{ \AA}^{-1}$), highlighting the improved signal from samples with improved surface morphology. (b) and (f) show signals from near the nominal graphite (0002) peak position. (c) and (g) Signals near integer values of L often exhibit scattering from quasiforbidden Bragg reflections, complicating data extraction, especially when the signal from the specular rod is diffuse. (d)-(h) Near the single-crystal Bragg conditions the background is dominated by thermal diffuse scattering from the substrate.

CCD, as seen in [Figure 3.8\(a\)](#). This effect is increased in the case of rough samples with small surface domains or high step-height density, which cause the transverse broadening of the rod in q_{\parallel} , thereby increasing the range in q_z in which the Ewald sphere intersects the rod. This effect is demonstrated in [Figure 3.8](#). The image shown [Figure 3.8\(a\)](#) is very near the typical low-angle limit we find for UHV-grown graphene samples ($q_z \sim 0.5 \text{ \AA}^{-1}$) where the intensity spills off the detector, prohibiting full signal integration from a single image. In the image in [Figure 3.8\(b\)](#), the measurement is higher up the rod ($q_z \sim 4.4 \text{ \AA}^{-1}$, near the nominal graphite (0002) diffraction peak), and the intersection angle of the Ewald sphere through the rod is sufficient for full capture by the detector. If the low- q_z data is to be obtained, it is necessary to perform full rocking-scan measurements using the conventional fixed-position detector method as depicted in [Figure 3.6\(b\)](#) [164, 165]. We should note, briefly, that the much improved sample morphology of Ar-grown EG/SiC supplied by D. Kurt Gaskill's group at the Naval Research Laboratory allows for much-improved data acquisition and analysis. These samples have much larger surface domain sizes ($\sim \mu\text{m}$) in comparison to UHV-grown samples ($\sim 100 \text{ nm}$) and therefore produce sharper CTR signals, in general [84, 88]. This yields better signal-to-background ratio, reduced count time, allows for improved access to midzone signal, and facilitates measurement to both higher and lower q_z . A brief comparison of scattering signals from a UHV- and an Ar-grown sample at four values of q_z is shown in [Figure 3.9](#).

Typically, the measured XRR data is compared to the theoretical calculations to test the validity of some modeled electron density profile. The model structure parameters, such as atomic layer position, width, density (see [Eq. 20](#)), and roughness ([Eq. 21](#) and [Eq. 22](#)) can all be tuned until agreement is reached between data and theory, and is traditionally done by using a

least-squares minimization routine. In addition, models are often constrained by using supplementary information from LEED, STM, XSW, or theoretical calculations. While this approach is powerful, it suffers from severe limitations, especially for complex systems where it is necessary to use a large number of fit parameters. In particular, it is difficult to ensure that the solution is correct because 1.) there may exist many statistically equivalent solutions 2.) the final result often depends the starting model, parameter choices, and fitting procedures, all of which are subjective values chosen by the researcher, and 3.) it is impractical to explore the entire parameter space due to computational practicalities. To address this shortcoming, some have employed various mathematical techniques that should allow for the structure to be derived directly from data, such as Fienup-based phase retrieval algorithms [167, 169, 170] or coherent Bragg rod analysis (COBRA) [171]. In this thesis, XSW-XPS measurements are used to constrain XRR model-based fitting ([Chapter 4](#)), and, in earlier experiments, Feinup-based algorithms are used to guide model parameter selection ([Section 6.1.2.4](#)).

3.2.2: XRR Experimental: APS

XRR experiments presented in this work were performed at beamlines 5-ID-C, 33-BM-C, and 6-ID-B at the Advanced Photon Source (APS) at Argonne National Lab. The APS is a 3rd-generation synchrotron light source which produces horizontally-polarized X-rays by accelerating 7 GeV electrons through either a bending magnet (BM) or an insertion device (ID). The typical experimental setup is shown in [Figure 3.10](#). X-rays are produced when the storage ring electron bunches are oscillated when passing through (in this example) an undulator insertion device (undulator A) to produce extremely bright X-ray beams. We tune the undulator gap to tune its 1st or 3rd harmonic to acquire the desired incident beam energy for the experiment.

This $\sim 1\%$ band-pass beam is then further monochromated by a L-N₂ cooled double-crystal Si(111) monochromator, which is used to select the desired energy of the incident X-ray beam with $\sim 10^{-4} E_\gamma$ bandwidth. X-rays are then further conditioned with an X-ray mirror, which allows for harmonic rejection and focusing of the beam.

Once the beam has been conditioned using the optics, it enters the experimental hutch, where additional components are used to monitor, collimate, filter, shutter, and detect the X-rays. Upstream of the sample are two ion chambers that are used to monitor the incident beam intensity both before and after the attenuating filter (which typically uses materials such as Al, Ti, Mo, and Ag). The filters are used to attenuate the incident beam intensity, when necessary (e.g., near Bragg reflections). An electronic fast shutter is used to block the beam from the sample when data is not being collected, and a collimating slit is located close to the sample to

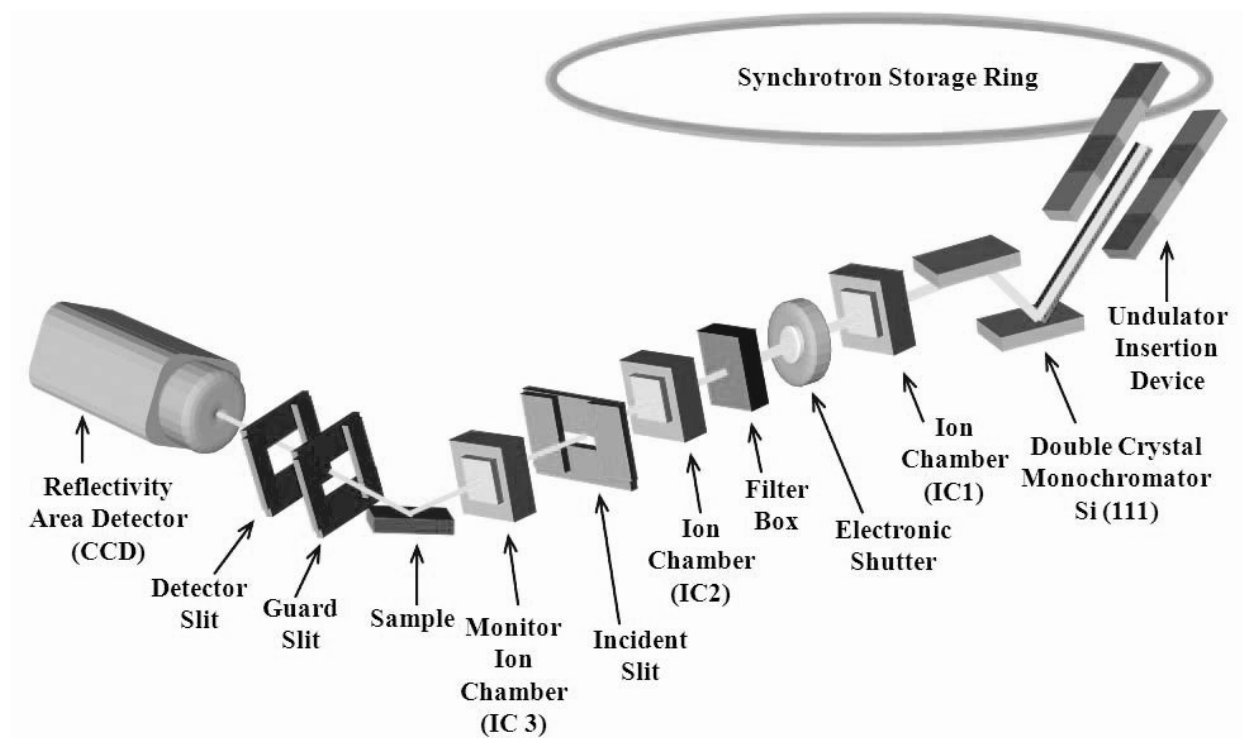


Figure 3.10: The typical setup for XRR experiments using a CCD detector at the APS. From Ref. [172].

define the beam dimensions. The fast shutter and filters are used to reduce X-ray induced damage to the sample by limiting the radiation dose. [Figure 3.10](#) also shows a third ion chamber (IC3), which is placed close to the sample to measure the incident beam flux on the sample. (For resonant scattering experiments IC3 needs to be highly accurate.)

The beam then impinges upon the sample mounted on a diffractometer. In the experiments described in this work the sample was mounted either in a kapton-windowed cell with flowing He or a Be-dome environmental cell under rough vacuum. The scattered beam subsequently passes through a guard slit on the detector 2θ arm, which reduces X-ray background signal extraneous to the sample itself, which may include scattering from the sample chamber window, incident beam slits, air scatter, or spurious fluorescence signal from various sources illuminated by the incident or scattered X-rays. Finally, the exposed active area of the CCD is defined by the detector slit placed immediately in front of the camera. In addition to the guard slits we often utilize a flight-path equipped with a pinhole that extends very near to the sample position and helps to reduce background signal (not shown). This was especially useful when using a Be-dome environment cell, which produces strong powder lines due to diffraction from the crystallites in the dome. All beamline components were controlled with SPEC and EPICS instrument control software. All XRR measurements were made in the σ -polarization scattering geometry using incident X-ray energies between 15-18 keV, and the scattered X-rays were collected with a Princeton Instruments PI-SCX CCD area detector. A detailed discussion of the use of the CCD detector for XRR measurements is discussed in by Fenter *et al.* in the Ref. [164].

Samples were aligned using the conventional half-beam alignment technique, but by utilizing the CCD detector effectively as an ion chamber. This was done by defining a region of interest (ROI) around the attenuated straight-through beam spot and integrating the signal region to measure signal intensity. The straight-through beam was highly attenuated in order to avoid damaging the sensitive CCD chip. Once the half-beam alignment was completed the pixel position of the center of the beam spot was recorded and both incident angle and detector angle were set to 0. Then, we move to the SiC(000 12) diffraction peak to perform crystallographic alignment, also using the CCD detector. To do this, one should follow the following alignment procedure:

1. Find the maximal intensity of the peak by tuning the incident beam angle θ and sample tilt, χ , as well as tuning the 2θ angle until the peak position on the detector is aligned precisely with the straight-through beam position.
2. Set the value assigned to the incident beam angle, θ to be half of the 2θ angle by setting the motor positions in SPEC. Prior to alignment, θ will typically be slightly off from $2\theta/2$ due to a slight tilting of the sample during mounting. When setting motors, be sure not to set the positions of any pseudomotors or SPEC may lose its orientation. On the 5-ID-C kappa diffractometers this means the experimenter should redefine the k th motor as opposed to the th pseudomotor.
3. At this geometry, execute the SPEC command *or0* to define this as the primary reflection for the experiment. Tune the SPEC-defined lattice parameters (command *setlat*) so that SPEC recognizes this position as the SiC(000 12) condition, i.e., where $\frac{c_{SiC} q_z}{2\pi} = L = 12$.
4. After crystallographic alignment one should test the intensity and profile of the scattered beam at various points along the $000L$ rod in order to deduce necessary slit settings, count times, scan resolution, and filter requirements. A SPEC macro for the L -scan is then designed based on these values.

A typical macro is shown in [Figure 3.11\(a\)](#) for the low- q_z region on an Ar-grown EG/SiC sample, which utilizes EPICS commands to control the beam attenuation. A second example near the intensity minimum at $L = 10$, taken at 5-ID-C, is shown in [Figure 3.11\(b\)](#). For experiments on SiC it is important to avoid regions near the integer values of L because the presence of allowed or quasiforbidden Bragg reflections [173, 174] can cause detector saturation. In addition, the L -scan macros are typically capable of automated measurement to within $\pm 0.1 L$ of the single-crystal Bragg conditions before there is risk of detector saturation, although care must be taken to account for alignment drift during *in situ* temperature-dependent experiments. The Bragg peak data are measured manually after the completion of each L -scan.

<p>(a)</p> <pre>def OOL ' com "Gaskill Epitaxial Graphene E51" epics_put("33bmc:pf4a:fPosA", 0) epics_put("33bmc:pf4a:fPosB", 4) br 0 0 0.04; waitmove; ct 1; br 0 0 0.08; waitmove; ct 1; br 0 0 0.12; waitmove; ct 1; epics_put("33bmc:pf4a:fPosA", 5) epics_put("33bmc:pf4a:fPosB", 2) br 0 0 0.16; waitmove; ct 1; epics_put("33bmc:pf4a:fPosA", 0) epics_put("33bmc:pf4a:fPosB", 2) br 0 0 0.20; waitmove; ct 1; epics_put("33bmc:pf4a:fPosA", 0) epics_put("33bmc:pf4a:fPosB", 1) br 0 0 0.24; waitmove; ct 1; epics_put("33bmc:pf4a:fPosA", 10) epics_put("33bmc:pf4a:fPosB", 0) br 0 0 0.28; waitmove; ct 1; epics_put("33bmc:pf4a:fPosA", 5) epics_put("33bmc:pf4a:fPosB", 0) br 0 0 0.32; waitmove; ct 1; br 0 0 0.36; waitmove; ct 1; br 0 0 0.40; waitmove; ct 1; epics_put("33bmc:pf4a:fPosA", 0) epics_put("33bmc:pf4a:fPosB", 0) br 0 0 0.44; waitmove; ct 1;</pre>	<p>(b)</p> <pre>br 0 0 9.92; waitmove; ct 30; br 0 0 10.08; waitmove; ct 30; br 0 0 10.12; waitmove; ct 60; br 0 0 10.16; waitmove; ct 60; br 0 0 10.20; waitmove; ct 60; br 0 0 10.24; waitmove; ct 60; br 0 0 10.28; waitmove; ct 60; br 0 0 10.32; waitmove; ct 60; br 0 0 10.36; waitmove; ct 60; br 0 0 10.40; waitmove; ct 60; br 0 0 10.44; waitmove; ct 60; br 0 0 10.48; waitmove; ct 60; br 0 0 10.52; waitmove; ct 60; br 0 0 10.56; waitmove; ct 60; br 0 0 10.60; waitmove; ct 120; br 0 0 10.64; waitmove; ct 120; br 0 0 10.68; waitmove; ct 120; br 0 0 10.72; waitmove; ct 120; br 0 0 10.76; waitmove; ct 120; br 0 0 10.80; waitmove; ct 120; br 0 0 10.84; waitmove; ct 120; br 0 0 10.88; waitmove; ct 120; br 0 0 10.92; waitmove; ct 60; br 0 0 11.08; waitmove; ct 60; br 0 0 11.12; waitmove; ct 120; br 0 0 11.16; waitmove; ct 120; br 0 0 11.20; waitmove; ct 60; br 0 0 11.24; waitmove; ct 60;</pre>
--	--

Figure 3.11: Typical XRR SPEC scan macros at various beamlines. (a) Low- q_z macro that utilizes EPICS commands for changing filters at 33-BM-C. (b) Macro commands near the $L = 10.7$ intensity minimum, coded for use at 5-ID-C. Note the avoidance of the $L = 10$ and $L = 11$ quasiforbidden Bragg regions.

3.3: X-ray Standing Wave

3.3.1: Dynamical Diffraction Theory

X-ray standing wave (XSW) is the second of the two primary characterization techniques used in this work. In this work, XSW is used to afford conventional photoelectron spectroscopy with a high degree of structural sensitivity, thereby resolving the spatial distribution of various elemental and chemical species at the EG/SiC(0001) interface with Å-scale precision. While XSW can, in principle, be employed with fluorescence, Auger, or photoelectron spectroscopy, herein we utilize XSW with XPS, which is the best option when seeking information about the chemical environment of the emitter atom. XSW-XPS has been utilized by numerous groups to

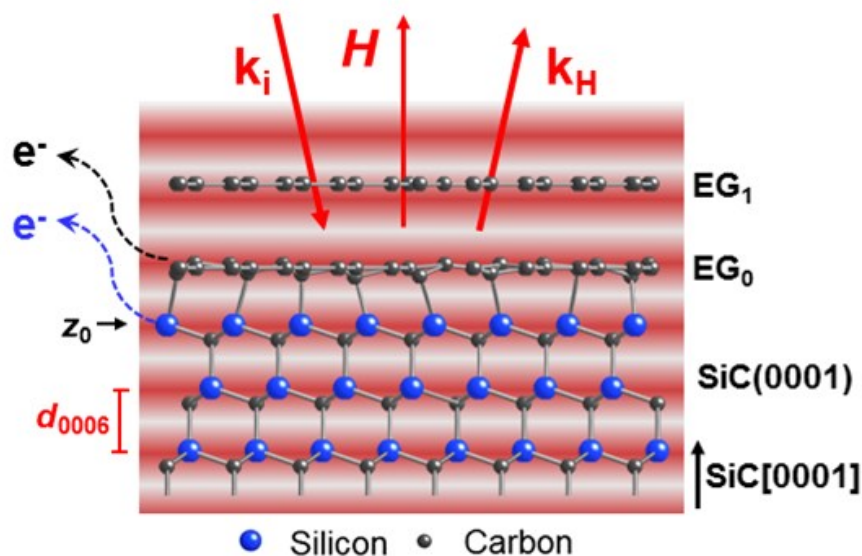


Figure 3.12: A schematic of the X-ray standing wave generated by the SiC(0006) Bragg reflection. Incident and reflected planewaves (with wave vectors k_0 and k_H , respectively) interfere to produce a standing wavefield (antinodes shaded red) with a period equivalent to the d_{0006} . The local intensity of this field can enhance or suppress emission of photoelectrons (e^-) from distinct chemical species, represented here by black and blue dashed arrows for C and Si, respectively.

evaluate the structure reconstructed surfaces, adsorbed monolayers on both semiconductor and metal surfaces, and buried interfaces and thin films (see Ref. [175] and references therein). The XSW study of valence electrons is particularly interesting because it enables the study site-specific valence states and is a direct, site-specific probe of electronic structure [176]. Although XSW measurements have been performed on a considerable variety of single-crystal substrates [175], the work presented in this thesis is, to our knowledge, the first XSW studies on SiC. Further information is available in XSW reviews by Zegenhagen [155], Woodruff [175], and Bedzyk [177, 178]. The principles in this section follow the descriptions given by Woodruff [175, 179] for E_γ -dependent XSW, as opposed to the measurements typically performed by our group, which are done with angular θ -scans.

The XSW phenomenon occurs when interference of two superimposed X-ray planewaves produces a sinusoidal standing wavefield. In the case of single-crystal Bragg diffraction, the incoming and outgoing X-ray beams interfere to produce a wavefield that extends both above and below the single-crystal surface ([Figure 3.12](#)). The total electric field (\mathbf{E}_T) resulting from the superposition of the incident \mathbf{E}_0 and reflected \mathbf{E}_H planewaves (see [Section 3.1.1](#)) is expressed as

$$\begin{aligned}\mathbf{E}_T(\mathbf{r}, t) &= (\hat{\mathbf{e}}_0 E_0 e^{-i \mathbf{k}_0 \cdot \mathbf{r}} + \hat{\mathbf{e}}_H E_H e^{-i \mathbf{k}_H \cdot \mathbf{r}}) e^{i \omega t} \\ &= e^{i \omega t} (\hat{\mathbf{e}}_0 E_0 e^{-i \mathbf{k}_0 \cdot \mathbf{r}} + \hat{\mathbf{e}}_H \frac{E_H}{E_0} e^{-i (\mathbf{k}_H \cdot \mathbf{r})}) \\ &= e^{i \omega t} E_0 e^{-i \mathbf{k}_0 \cdot \mathbf{r}} (\hat{\mathbf{e}}_0 + \hat{\mathbf{e}}_H \frac{E_H}{E_0} e^{-i (\mathbf{H} \cdot \mathbf{r})})\end{aligned}\tag{3.23}$$

for the $\mathbf{H} = \mathbf{k}_H - \mathbf{k}_0$ Bragg condition. The energy-dependent phase $\varphi(E_\gamma)$, between the two electric fields is defined as

$$\frac{E_H}{E_0} = \left| \frac{E_H}{E_0} \right| e^{i \varphi(E_\gamma)}.\tag{3.24}$$

Therefore, by substitution we find that the total electric field can be defined as

$$\mathbf{E}_T(\mathbf{r}, t) = e^{i\omega t} E_0 e^{-i \mathbf{k}_0 \cdot \mathbf{r}} (\hat{\boldsymbol{\epsilon}}_0 + \hat{\boldsymbol{\epsilon}}_H \left| \frac{E_H}{E_0} \right| e^{i(\varphi(E_\gamma) - \mathbf{H} \cdot \mathbf{r})}). \quad (3.25)$$

At position \mathbf{r} , for a symmetric reflection geometry, the standing wavefield intensity as a function of position and incident beam energy is the square of the complex field amplitudes:

$$\begin{aligned} I(\mathbf{r}, E) &= \frac{\mathbf{E}_T(\mathbf{r}, t) * \mathbf{E}_T^*(\mathbf{r}, t)}{|\mathcal{E}_0|^2} = \frac{|\mathbf{E}_T(\mathbf{r}, t)|^2}{|\mathcal{E}_0|^2} \\ &= \frac{|\mathcal{E}_0 e^{-i \mathbf{k}_0 \cdot \mathbf{r}} (\hat{\boldsymbol{\epsilon}}_0 + \hat{\boldsymbol{\epsilon}}_H \left| \frac{\mathcal{E}_H}{\mathcal{E}_0} \right| e^{i(\varphi(E_\gamma) - \mathbf{H} \cdot \mathbf{r})})|^2}{|\mathcal{E}_0|^2} \\ &= 1 + \left| \frac{\mathcal{E}_H}{\mathcal{E}_0} \right|^2 + p \left| \frac{\mathcal{E}_H}{\mathcal{E}_0} \right| [e^{i(\varphi(E_\gamma) - \mathbf{H} \cdot \mathbf{r})} + e^{-i(\varphi(E_\gamma) - \mathbf{H} \cdot \mathbf{r})}] \end{aligned} \quad (3.26)$$

Where $p = 1$ for σ -polarization and $p = \cos(2\theta_B)$ for π -polarization. Because the Bragg reflectivity is the intensity ratio of the of the two planewaves,

$$R(E_\gamma) = \frac{I_H}{I_0} = \left| \frac{\mathcal{E}_H}{\mathcal{E}_0} \right|^2, \quad (3.27)$$

the normalized intensity of the total electric field becomes

$$I(\mathbf{r}, E_\gamma) = 1 + R_B(E_\gamma) + 2p \sqrt{R_B(E_\gamma)} \cos(\varphi(E_\gamma) - \mathbf{H} \cdot \mathbf{r}) \quad (3.28)$$

The plot of the Bragg reflectivity is often called the Darwin curve or rocking curve. The period of the XSW is equal to the d -spacing of diffraction plane, $d_H = \frac{2\pi}{|\mathbf{H}|}$. Note that we have neglected

the extinction effects in this description because the extinction length, Λ_{ext} , is orders of magnitude larger than mean free path for the photoelectrons ($\sim\mu\text{m}$ vs. $\sim\text{nm}$).

Both the reflectivity and the phase between the incident and diffracted beams are well-described by dynamical diffraction theory [180]. From Batterman, the E -field amplitude ratio is defined in terms of the monochromator asymmetry factor b , polarization factor p , and normalized angular/energy parameter, η , as

$$\frac{\varepsilon_H}{\varepsilon_0} = -\sqrt{|b|} \frac{|p|}{p} \sqrt{\frac{F_H}{F_H}} (\eta \pm \sqrt{\eta^2 - 1}). \quad (3.29)$$

Here, the asymmetry factor b is

$$b = \frac{\gamma_0}{\gamma_H}, \quad (3.30)$$

where γ_0 and γ_H are the directions cosine of the incident and diffracted beams with respect to the incident surface and $b = -1$ for our case of a symmetric Bragg reflection (for more, see Ref. [180]). The normalized angular/energy parameter is

$$\eta = \frac{-2\left(\frac{\Delta E}{E_\gamma}\right) \text{Sin}^2(\theta_B) b + \Gamma F_0(1-b)}{|b|^{\frac{1}{2}} |p| \sqrt{F_H F_H}}, \quad (3.31)$$

where and $\Gamma = r_e \lambda^2 / \pi V_{u.c.}$ is a scaling factor and $\Delta E = E_\gamma - E_B$ is the offset of the Darwin curve from the geometrical Bragg energy (see [Eq. 3.13](#)) due to refraction. The \mathbf{H}^{th} Fourier component (or structure factor) of the electron density, comprised of N atoms at fractional unit cell positions \mathbf{r}_n , is defined in [Eq. 3.7](#) using the Laue condition ($\mathbf{q} = \mathbf{H}$). Here we expand that definition to account for the energy-dependent dispersion corrections and Debye-Waller temperature factor (e^{-M}),

$$F_H = \sum_{n=1}^N (f^0(H) + f''(E_\gamma) + if''(E_\gamma))_n e^{i\mathbf{H}\cdot\mathbf{r}_n} e^{-M}. \quad (3.32)$$

Note that the overbar notation indicates the $\bar{\mathbf{H}} = -\mathbf{H}$ reciprocal lattice vector and $\mathbf{H} = 0$ denotes the forward scattering condition. Due to the contributions of the dispersion corrections and depending on the choice of origin, F_H is a complex quantity and is comprised of real and imaginary components F'_H and F''_H ,

$$F_H = F'_H + iF''_H \quad (3.33)$$

Note that throughout this work the real and imaginary components of any complex parameter, X , will follow the notation from Batterman and Cole [180], which defines $\text{Re}(X) = X'$ and $\text{Im}(X) = X''$.

With the contributions to the E -field amplitude ratio ([Eq. 3.27](#)), and therefore reflectivity ([Eq. 3.25](#)) now defined, it is clear that the reflectivity is a function of η , which, in turn, is a function of ΔE (see [Eq. 3.29](#) and [Eq. 3.31](#)). This allows us to define important values such as the Darwin width in energy, ω_E , and the energy offset from the geometric Bragg energy, $\Delta E_{\eta'=0}$. Because refraction of X-rays inside the crystal causes the $\eta = 0$ position to shift from the center of the Darwin curve, we describe both ω_E and $\Delta E_{\eta'=0}$ as a function of the normalized parameter η' . The $\eta' = 1$ and $\eta' = -1$ points correspond respectively to the α -branch and β -branch of the dispersion surfaces surrounding the Bragg band-gap for the strong reflection condition that gives rise to the Darwin curve. The α -branch is on the low- E_γ side of the Darwin curve and the standing wavefield is out-of-phase with the strong scattering planes, and the β -branch is on the high- E_γ side and the standing wavefield is in-phase with the strong scattering planes. These

strong scattering planes are also referred to as the diffraction planes [181] and are at a position defined by the $\max(\text{Re}[\rho_H(\mathbf{r})])$. The Darwin width is defined as the difference between the $\Delta E_{\eta'=+1}$ and $\Delta E_{\eta'=-1}$ values,

$$\omega_E = \Delta E_{\eta'=-1} - \Delta E_{\eta'=1} = \frac{\Gamma E_\gamma |p| \sqrt{F'_H F'_H + F_0''^2 - F''_H F''_H}}{\sqrt{|b|} \sin^2(\theta_B)}, \quad (3.34)$$

and the energy offset is

$$\Delta E_{\eta'=0} = \frac{\Gamma F_0 E_\gamma}{2 \sin^2(\theta_B)} \frac{1 + |b|}{2|b|}. \quad (3.35)$$

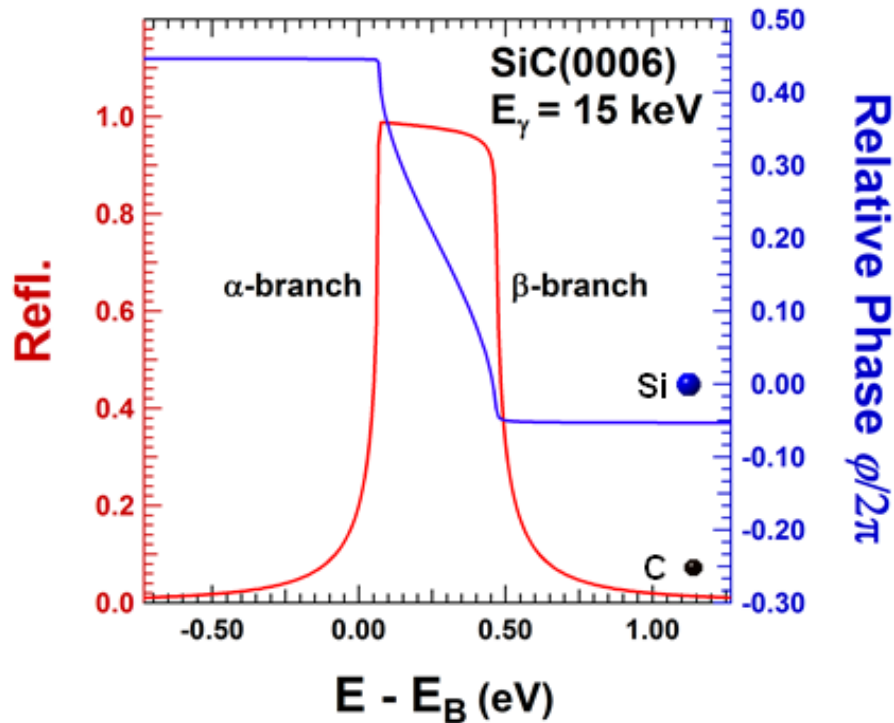


Figure 3.13: Calculated reflectivity and XSW phase for the SiC(0006) reflection at $E_\gamma = 15$ keV. The red line represents the reflected intensity as a function of energy offset from the geometrical Bragg condition, and the blue line represents the relative XSW phase. The antinodes of the XSW shift inwards by π radians as the SiC crystal is scanned through the strong Bragg condition. The phases of the geometrical structure factors for the Si (blue) and C atoms (black) are positioned with respect to the phase scale. Therefore the blue line also represents the XSW antinode position relative to the shown vertical positions of the Si and C atomic layers of the bilayer.

Using the dynamical diffraction equations described above, one can show that the relative phase, φ , of the standing wave field shifts by $-\pi$ radians as the incident beam energy is scanned from the low- E_γ to high- E_γ sides of the rocking curve, as shown for the example of the SiC(0006) reflection at 15.00 keV in [Figure 3.13](#). From [Eq. 3.24](#), this causes a regular shift in the position of the XSW antinodes by $\frac{1}{2}d_H$. The XSW phase approaches the F_H phase (β_H) asymptotically at the high- E_γ side and $\beta_H + \pi$ at the low- E_γ angle side [181], and therefore XSW is an absolute measurement of atomic positions. This relative phase as a function of E_γ , which can be described *ab initio* using the equations above and the crystal structure factor information, is also the source of the sub-Å spatial resolution afforded by the XSW technique. However, in order to use XSW to gather the elemental- and chemical-state specific information desired, it is necessary to understand the interaction of the standing wavefield with the atomic distributions of interest. In this case we focus on the influence of the XSW on measurable spectroscopic signal, specifically, its effect on the photoemission process.

3.3.2: X-ray Standing Wave with Photoemission

With the description of the intensity of the XSW described in the previous section, we proceed to discuss the interaction of the XSW atomic distributions via the photoelectric effect, described classically in [Section 3.1.2](#). In order to relate the XSW E -field intensity at position \mathbf{r} to the probability of a photoemission event, we must use the quantum mechanical description of the X-ray field and the photoelectron. This approach is outlined by Als-Nielsen and McMorrow [182], and the treatment with respect to XSW follows that described by Zegenhagen [155].

The photoemission process is an excitation of an electron from initial bound state $|i\rangle$ to final ejected state $|f\rangle$, where, if the final state is at the vacuum level, the photoelectron will possess the kinetic energy of the incident beam minus the $|i\rangle$ binding energy, $E_{kin} = E_\gamma - E_{BE}$. The transition probability is proportional to the transition matrix element \mathbf{M}_{fi} , which, by employing first-order perturbation theory can be described in terms of the initial and final state wavefunctions ψ_i and ψ_f ,

$$\mathbf{M}_{fi} \propto \int d^3\mathbf{r}_e \psi_f^* \mathbf{A} \cdot \mathbf{p} \psi_i, \quad (3.36)$$

and the interaction Hamiltonian consists of the momentum operator

$$\mathbf{p} = -i\hbar\nabla \quad (3.37)$$

where ∇ is the spatial gradient operator. The vector potential of the total XSW interference field, \mathbf{A} , which was derived in [Eq. 3.25](#), is

$$\mathbf{A} = e^{i\omega t} \mathcal{E}_0 e^{-i\mathbf{k}_0 \cdot \mathbf{R}} (\hat{\boldsymbol{\epsilon}}_0 + \hat{\boldsymbol{\epsilon}}_H \left| \frac{\mathcal{E}_H}{\mathcal{E}_0} \right| e^{i(\varphi(E_\gamma) - \mathbf{H} \cdot \mathbf{R})}). \quad (3.38)$$

Here, the position vector \mathbf{R} defines the position of the absorbing electron relative (\mathbf{r}_e) to the atomic position \mathbf{r} ,

$$\mathbf{R} = \mathbf{r}_e + \mathbf{r}. \quad (3.39)$$

Therefore, [Eq. 3.38](#) can be re-formed as

$$\mathbf{A} = e^{i\omega t} \mathcal{E}_0 e^{-i\mathbf{k}_0 \cdot \mathbf{r}} e^{-i\mathbf{k}_0 \cdot \mathbf{r}_e} (\hat{\boldsymbol{\epsilon}}_0 + \hat{\boldsymbol{\epsilon}}_H \left| \frac{\mathcal{E}_H}{\mathcal{E}_0} \right| e^{i\varphi(E_\gamma)} e^{-i\mathbf{H} \cdot \mathbf{r}} e^{-i\mathbf{H} \cdot \mathbf{r}_e}). \quad (3.40)$$

The exponential functions containing \mathbf{r}_e are of the form of Taylor series expansion,

$$e^x = \sum_{n=0}^{\infty} \frac{x^n}{n!} = 1 + x + \frac{x^2}{2!} \dots \quad (3.41)$$

which yields

$$\begin{aligned} e^{-i \mathbf{k}_0 \cdot \mathbf{r}_e} &= 1 - i(\mathbf{k}_0 \cdot \mathbf{r}_e) + \frac{1}{2} (\mathbf{k}_0 \cdot \mathbf{r}_e)^2 - \dots \\ e^{-i \mathbf{H} \cdot \mathbf{r}_e} &= 1 - i(\mathbf{H} \cdot \mathbf{r}_e) + \frac{1}{2} (\mathbf{H} \cdot \mathbf{r}_e)^2 - \dots \end{aligned} \quad (3.42)$$

This treatment is equivalent to the multipole expansion where the first term gives the dipole (E1) and the second term gives the electric quadrupole (E2) transitions [155, 183]. In the dipole approximation (zeroth-order approximation) all the terms to the left of the first order term are considered negligible, which is physically interpreted as the assumption that the spatial variation of the electromagnetic field over the initial-state wavefunction is insignificant. In the case of long X-ray wavelengths, deep core-level photoemission, and for electron shells with radial symmetry, this assumption is excellent and both exponential terms in [Eq. 3.42](#) are approximately equal to one. We note, however, that contributions from the non-dipole terms are dependent on the experimental geometry [183, 184]. Most importantly for this work, it was possible minimize non-dipole contributions to the photoelectric yield by orienting the photoelectron detector axis perpendicular to the polarization vector for the incoming X-ray beam [183, 184].

The dipole approximation leads to the reduction of the XSW vector potential to

$$\mathbf{A} = e^{i\omega t} E_0 e^{-i \mathbf{k}_0 \cdot \mathbf{r}} \left(\hat{\boldsymbol{\epsilon}}_0 + \hat{\boldsymbol{\epsilon}}_H \left| \frac{E_H}{E_0} \right| e^{i \varphi(E_\gamma)} e^{-i \mathbf{H} \cdot \mathbf{r}} \right), \quad (3.43)$$

and is independent of \mathbf{r}_e . We can therefore rewrite the matrix element from [Eq. 3.36](#) as

$$\mathbf{M}_{fi} \propto \mathbf{A} \int d^3 \mathbf{r}_e \psi_f^* \mathbf{p} \psi_i. \quad (3.44)$$

The absorption or dipole cross-section σ_D , which is proportional to modulus squared of the matrix element \mathbf{M}_{fi} , and is therefore also proportional to the intensity of interference field defined in [Eq. 3.40](#) and [Eq. 3.28](#):

$$\begin{aligned} \sigma_D &\propto |\mathbf{M}_{fi}|^2 \propto |\mathbf{A}|^2 \propto I(\mathbf{r}, E) \\ \sigma_D &\propto 1 + R(E_\gamma) + 2p\sqrt{R(E_\gamma)}\cos(\varphi(E_\gamma) - \mathbf{H} \cdot \mathbf{r}). \end{aligned} \quad (3.45)$$

Since the \mathbf{r}_e has dropped from the analysis due to the dipole approximation it is possible to neglect any effects due to the electron distribution about the atom and one can assume that the photoelectron origin is equivalent to the atomic center. Further discussion on possible multipole contributions to XSW yield and a general yield equation for are available in Refs. [175], [183], and [184].

3.3.3: XSW Interpretation

The result of the previous section demonstrates that the absorption cross section of an atom at some position \mathbf{r} with respect to the selected lattice origin is proportional to the intensity of the standing wavefield at that position. For a single atom described by a δ -function distribution, this would lead to the simple expression in which the XSW normalized yield a single atom is

$$Y_{atom}^H(E_\gamma) = 1 + R_B(E_\gamma) + 2p\sqrt{R_B(E_\gamma)}\cos(\varphi(E_\gamma) - \mathbf{H} \cdot \mathbf{r}). \quad (3.46)$$

However, because the XSW field extends far above and below the crystal surface, encompassing many (N) atoms, the actual situation is much more complicated. Any photoemission signal

attributed to an XPS-selected chemical or elemental species (s) is then an ensemble average over the positions of the N atoms located at positions \mathbf{r}_j ,

$$Y_s^H(E_\gamma) = 1 + R_B(E_\gamma) + 2p\sqrt{R_B(E_\gamma)}\frac{1}{N}\sum_{j=1}^N \cos(\varphi(E_\gamma) - \mathbf{H} \cdot \mathbf{r}_j). \quad (3.47)$$

By definition, the coherent position and fraction are the phase and amplitude, respectively, of the \mathbf{H}^{th} Fourier component (or H^{th} geometrical structure factor) of the normalized distribution for the elemental or chemical species (s) which is being monitored in the yield spectra. If the distribution width is much narrower than $d_H/2$, the *coherent position*, or P_s^H , will be a measure of the mean position and the *coherent fraction*, or f_s^H , will be a measure the degree of spread in the distribution, with ($f_s^H = 1$) being the maximum value and corresponding to a zero width δ -function distribution. These factors are also referred to as the amplitude and phase of the \mathbf{H}^{th} Fourier component. With the amplitude and phase of the \mathbf{H}^{th} Fourier component it is possible to reformulate [Eq. 3.47](#) as

$$Y_s^H(E_\gamma) = 1 + R_B(E_\gamma) + 2p\sqrt{R_B(E_\gamma)}f_s^H \cos(\varphi(E_\gamma) - 2\pi P_s^H). \quad (3.48)$$

To further complicate the interpretation, the XSW has a period of d_H , which means that, in principle, the measurement for a single Fourier component is insensitive to difference between a fully coherent layer ($f_s^H = 1$) of atoms located at some $d_H P_s^H$ or some integer multiple, $m d_H P_s^H$. This is called the modulo- d ambiguity. This effect can greatly complicate interpretation when considering film or nanoparticle structures with physical extents beyond that of a single d_H -spacing.

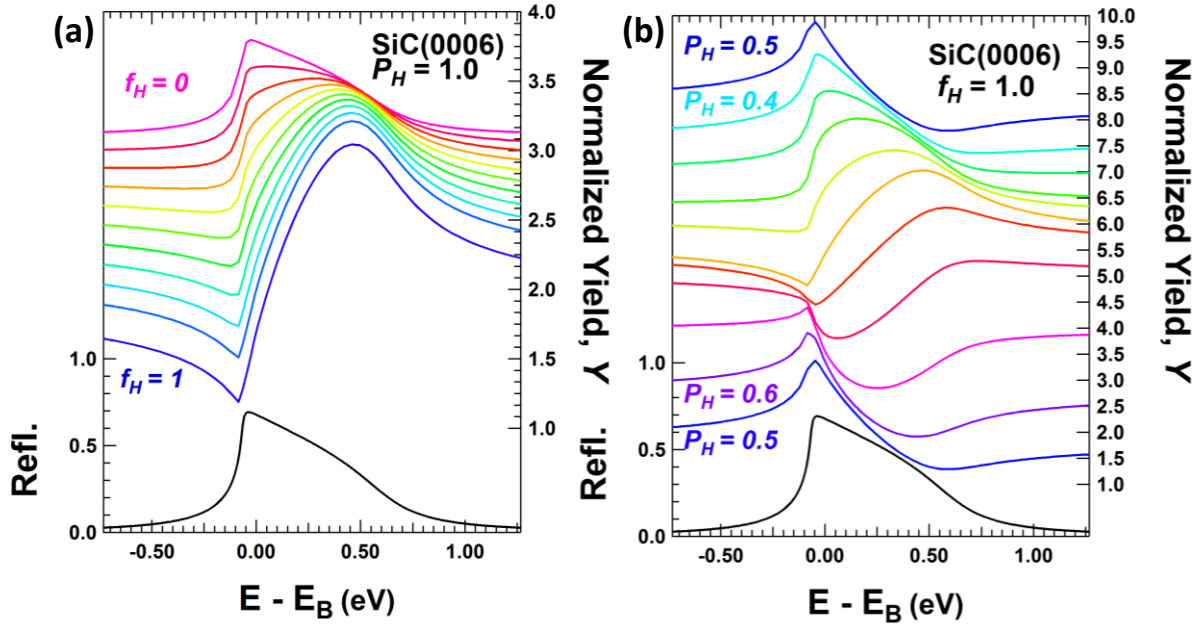


Figure 3.14: Calculated reflectivity and XSW yield curves for a series of (a) coherent fractions and (b) coherent positions at the SiC(0006) reflection simulated using 2.463 keV incident X-ray energy. Here, the origin has chosen to coincide with nominal bulk position of the Si atoms within the SiC unit cell. (b) For a set of coherent positions corresponding to the XSW antinodes positioned over the Si lattice position ($P^H = 1$), it is shown that as the coherent fraction increases from $f^H = 0$ to 1, the yield curves transition from a $1 + R(E_\gamma)$ shape (pink), where the modulation is insensitive to P^H , to a shape that is highly influenced by it. (b) For a high coherent fraction (perfectly coherent, $f^H = 1$), the shape of the yield curve is drastically affected by the coherent position of the hypothetical species.

[Figure 3.14\(a\)](#) demonstrates the effect of the value of the coherent fraction on the observed XSW yield modulation. From [Eq. 3.48](#) it is clear that a completely incoherent distribution of atoms ($f_s^H = 0$) would provide little meaningful structural information about the system. This scenario would completely eliminate any contributions from the third term in [Eq. 3.48](#), and the measured normalized yield would therefore be equal to $Y_s^H(E_\gamma) = 1 + R_B(E_\gamma)$. As f_s^H increases, however, the contribution from the third term in [Eq. 3.48](#) increases, and the characteristic XSW modulations become more distinct. Higher coherent fractions will lead to simpler and more straight-forward data analysis. Indeed, if the coherent fraction is unity, and all atoms are highly coherent with the substrate, there is little room for interpretation; there either exists a single layer of fully coherent atomic species or many layers of atomic species completely

in phase with each other, as in a bulk crystal. With high enough f_s^H values, scanning through an H Bragg condition will produce characteristic XSW modulations as a function of E_γ . This phenomenon is demonstrated in [Figure 3.14\(b\)](#).

It is important to note that one could have a totally correlated distribution relative to the diffraction plane periodicity and still measure $f_s^H = 0$. The simplest example for this condition is two equally occupied positions along the H -direction that are separated by $d_H/2$. To distinguish this from a completely uncorrelated distribution one only needs to analyze the higher-order harmonic XSW yield for the same elemental species [185].

There are many possible routes in the analysis of XSW data. Model-independent analysis can be performed to produce a direct space atomic density map projected onto the primitive bulk unit cell. The measurement of multiple H Fourier components can allow for a model-based global minimization of XSW parameters, also allowing for the construction of a 3D atomic density map. However, in this work we used simple model-based interpretation informed by supplemental techniques to construct atomic density profiles of chemically-distinct atomic distributions along the SiC[0001] direction. To do this we performed basic analysis of XPS core-shifted components from EG/SiC(0001) and created a model to describe their distribution. Then, we utilized high-resolution XRR ([Section 3.2](#)), which provides longer range information about the electron density profile in the z direction, in order to refine and confirm our XSW-derived models. This was necessary because we were interested in resolving the EG/SiC(0001) interfacial structure, but due to experimental limitations concerning spectral resolution, we were only able to extract information for a single $H = 0006$ Fourier component. We were, however, able to access numerous distinct chemical species. We also note that we did not attempt to

analyze any off-normal reflections because of the known long-range commensurability $(6\sqrt{3}\times 6\sqrt{3})R30^\circ$ of the interfacial layer. Because of our limitation to a single Fourier component, it was necessary to model the distributions of atoms through interpretation of the f_s and P_s (here we drop the H index here, because we only measure one H) and compare and refine the results with XRR and other characterization techniques ([Chapter 4](#)).

In this work we will find that the distributions of different chemical or atomic species can be often well-described using a single distribution of atoms, or atoms within the bulk crystal that are positioned in phase. In this case we model the distribution as a normalized Gaussian function with width σ_s . The Fourier transform of a Gaussian is a Gaussian, and the coherent fraction for this model is subsequently

$$f_s = e^{-2\pi^2 \frac{\sigma_s^2}{d_H^2}}. \quad (3.49)$$

Incorporated into this definition is the broadening of the distribution due to the Debye-Waller thermal vibrational amplitude. In some cases, however, it is clear that there are many phase contributions to the $H=0006$ Fourier component and therefore we must use a geometric model to interpret the results. Such is the case when we attempt to interpret the relative contributions to the XSW yield from multiple layers of graphene. Here, we describe each distinct atomic layer, indexed n , in terms of their occupancy c_n , Gaussian width, σ_n , and positional height, z_n . With this model we construct the so-called geometric structure factor to account for the relative contributions of N layers to the observed f_s and P_s values,

$$S_s = \frac{1}{\sum_{n=1}^N c_n} \sum_{n=1}^N c_n e^{i2\pi \frac{z_n}{d_H}} e^{-2\pi^2 \frac{\sigma_n^2}{d_H^2}}, \quad (3.50)$$

which can be used to calculate the effective coherent fraction,

$$f_s = |S_s^H| \quad (3.51)$$

and coherent position,

$$P_s = \frac{1}{2\pi} \text{Arg}(S_s^H). \quad (3.52)$$

It is important to note the consistency between the values used for the modeling of the geometric structure factor in [Eq. 3.50](#) and [Eq. 3.20](#). Both models account for atomic coverages, positions, and distribution widths that are easily transferrable to the other model. The complimentary nature of these two techniques is the critical to the results presented in [Chapter 4](#).

3.3.4: XSW Experimental: ESRF ID32

All XSW experiments were performed in the UHV surface analysis chamber at beamline ID32 at the European Synchrotron Radiation Facility (ESRF) in Grenoble, France. The ID32 beamline was designed specifically to perform XSW-XPS experiments near the back-reflection condition, and provides the high flux, UHV environment, X-ray energy resolution, and software framework necessary to measure C and Si core-level (or valence) photoemission signals from the EG/SiC system. In addition, the stability and control of the X-ray energies near 2.5 keV is absolutely critical to the success of the XSW-XPS experiment. This degree of control was not available at preliminary experiments performed at X24-A at NSLS-I, where thermal/mechanical drift in the monochromator was too high to allow for reproducible energy scans across the SiC(0006) reflection.

The ESRF is a 3rd-generation synchrotron which produces horizontally-polarized X-rays from electrons circulating in the storage ring with an energy of 6 GeV. A schematic of the key components of the ID32 beamline is shown in [Figures 3.15\(a\)-\(b\)](#) (for additional beamline information, see Ref. [186] or the [ID32 legacy website](#)). Electrons pass through a series of three undulators to provide X-rays of energies between ~ 2 -28 keV. The X-rays then pass through front-end slits before striking the liquid nitrogen-cooled Si(111) double-crystal high-heat-load monochromator. The X-rays continue through secondary collimating slits and are subsequently focused using a series of two-dimensional parabolic Be compound refractive lenses (CRLs). The X-rays can then be further conditioned by a series of optional dispersive (+/-, +/-) Si post-mono channel cuts. These additional channel cuts were not used in this work because it was found that the $\Delta E/E = 1.3 \times 10^{-4}$ resolution provided by the high-heat-load Si(111) mono was sufficient

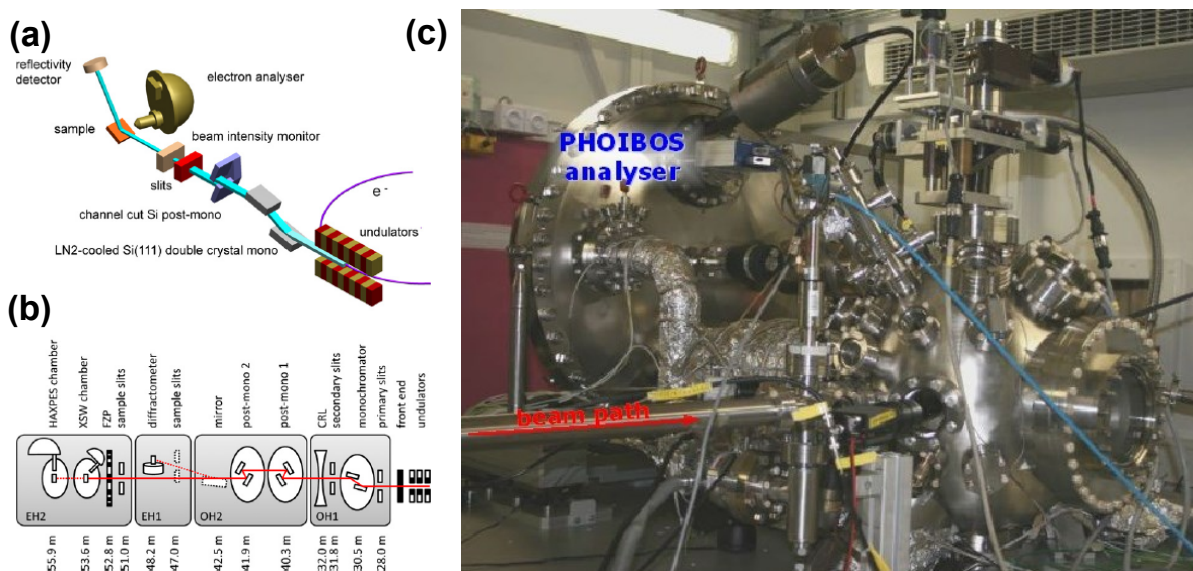


Figure 3.15: Beamline schematic and XSW/HAXPES chamber for ID32. (a)-(b) A schematic diagram of the beamline setup as well as the locations of the beamline components. Note that all experiments were performed in a π -scattering geometry, not the σ -scattering geometry depicted in (a). (c) A photograph of the experimental chamber, indicating the direction of the incident beam and the position of the PHOIBOS photoelectron analyser, as used in this work.

at ~ 2.5 keV ($\Delta E \sim 0.35$ eV) for the core-level spectra of interest. After the postmonochromators, the incident beam size is selected using a final set of collimating slits and passed through a beam-monitor Be foil before entering the experimental UHV chamber (base pressure $\sim 10^{-10}$ Torr) and striking the sample. The beamsize at the sample was $\sim 0.4 \times 0.1$ mm² or $\sim 0.4 \times 0.3$ mm² (h \times v). The intensity of the reflected beam is monitored using a Ni current collecting plate.

The experimental chamber ([Figure 3.15\(c\)](#)) is equipped with a Specs-PHOIBOS 225 HV hemispherical electron analyzer, capable of measuring photoelectrons with energies up to 15 keV. Experiments were performed with 30-40 eV pass energy, $\pm 7^\circ$ angular acceptance, and 3 mm entrance and exit slits, giving an analyzer resolution of ~ 0.35 eV. The overall energy resolution of the experiment, when accounting for the contribution of the incident beam bandwidth, is 0.5-0.6 eV. The acceptance axis of the electron detector lies in the horizontal plane with its normal position pointing perpendicular to the incident beam (and therefore in the polarization direction of the incident beam). It can also be rotated in the horizontal plane toward the incident beam by 45° . In this work we mounted the detector axis to be aligned with the incident beam polarization vector in order to minimize the effects of multipole contributions to the photoemission yield [183, 184]. The sample surface normal is maintained in the horizontal plane for these measurements. The vertically aligned sample rotation axis was used to adjust the Bragg angle to be near the back reflection condition. This geometry is highly surface-sensitive due to the small electron emission angle relative to the sample surface. To collect a less surface-sensitive photoelectron spectrum the sample can be rotated to decrease the angle between the surface normal and detector axis.

C 1s and Si 1s spectra were acquired at 32 points across the Darwin curve. Typical count times per spectrum were 30-60s, yielding a full XSW data save set every ~1 hr. Data was acquired using the SpecsLab control program, and was then converted to Vamas blocks using a MATLAB routine supplied by the ESRF group (*stitch.m*). Individual save sets were then loaded into XPS analysis program CasaXPS and fit with the program's built-in fitting functions. For each data set the model component peaks were held fixed in BE and in width for each step along the rocking curve. A Monte Carlo simulation routine, supplied by CasaXPS, was used to estimate the error associated with the integrated area of each spectral component at each energy step. Finally, both yield and reflectivity data was normalized to the beam monitor and exported into a three-column, tab-delimited ASCII file for loading into the SWAM analysis routine. All XSW data was analyzed using SWAMv4.1, described in [Appendix A](#).

3.4: Supplementary Techniques

This dissertation incorporates a large quantity of data from supplementary characterization methods, some of which was performed by collaborators. For information specific to STM measurements, we refer you to the work performed by the Hersam group members, particularly Dr. Qing Hua Wang [36, 124, 187], Dr. Arpana Deshpande and Chun-hong Sham [37, 188]. Information regarding Atomic Force Microscopy (AFM) can be found in the work by Dr. Justice Alaboson [188-190]. Other supporting measurements were performed by our group. These include LEED, grazing-incidence small/wide angle scattering (GIWAXS/GISAXS), low-angle XRR, and XRF.

3.4.1: LEED

LEED is an electron diffraction technique used for the analysis of ordered surface structures and is in many ways analogous to CTR ([Section 3.2.1](#)). Specifically, both measurements are surface-sensitive techniques that probe the truncation rod intensity along the L direction in reciprocal space, and provide information about the structure of surfaces and interfaces. LEED does hold some advantages over CTR, including the large interaction cross section of electrons vs. photons ($\sim 1 \text{ \AA}^2$ vs. $\sim 10^{-6} \text{ \AA}^2$) [191], the high flux production of electron beam sources, and reduced inelastic mean free paths/increased surface sensitivity ($\sim \text{\AA}$ vs. $\sim \mu\text{m}$). However, because electrons interact strongly with matter and multiple scattering is common, LEED cannot be quantitatively analyzed with the kinematical approximation and requires dynamical theory for thorough analysis. Here, we limit our analysis to a qualitative evaluation of the LEED patterns. In this work, LEED patterns are presented in tandem with XRR, XSW, and STM as a figure of merit to prove the cleanliness of the surface, confirm in-plane coherence lengths on the order of nms, and for verification of expected surface phases. All LEED measurements were performed on either in the ID32 preparation chamber or with the Bedzyk group surface analysis UHV setup.

3.4.2: Low-angle X-ray Reflectivity

In the grazing incidence specular reflectivity geometry, the correlation length-scale probed by the X-rays, $d \sim 2\pi/q_z$, is on the order of $\sim 10 \text{ \AA}$, and becomes essentially insensitive to ordering on the \AA -scale. In this regime, the reflection and refraction of X-rays is treated by Fresnel theory, similar to that used for classical optics [149]. However, due to the high frequency of X-rays, there are important differences in the refraction of X-rays from the commonly observed

refractive phenomena associated with visible light. Namely, in the X-ray frequency regime there is a small negative deviation from unity in the refractive index,

$$n = 1 - \delta - i\beta \quad (3.53)$$

where $\delta = \frac{1}{2\pi} N_e r_e \lambda^2 = \frac{1}{2} \Gamma F'_0$ and $\beta = \frac{1}{4\pi} \mu_0 \lambda = \frac{1}{2} \Gamma F''_0$. Here, N_e is the effective electron density and $\mu_0 = \frac{2\pi}{\lambda} \Gamma F''_0$ is the linear absorption coefficient (see [Section 3.3.2](#) for definitions of Γ , F'_0 , and F''_0).

In a low-angle XRR experiment, an X-ray impinges with incident angle θ and is scattered in a specular geometry. As the X-ray passes through a stratified media there are a very large number of possible reflection/transmission scenarios. Depending on the magnitude of the momentum transfer vector, q_z , the outgoing planewaves can constructively and destructively interfere due to the phases shifts (i.e., change in path length) caused by the refraction and reflection of the X-rays within the media ([Figure 3.16\(a\)](#)). The data can then be fit using Abeles matrix method [193] (which gives identical results to Parratt's recursion method [194]) to calculate the reflectivity of the stratified system as a function of q_z ([Figure 3.16\(b\)](#)). We employ

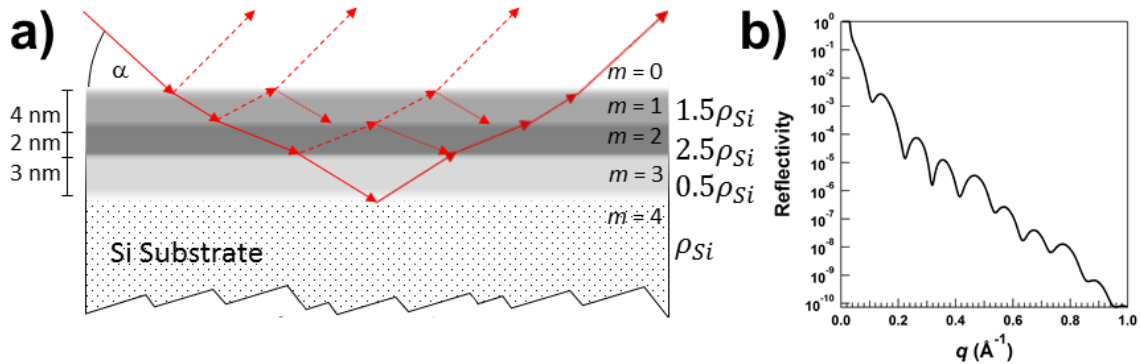


Figure 3.16: Principles of low-angle XRR (a) Examples of possible reflection and transmission paths of a wave at m , $m+1$ interfaces within a simulated stratified thin-film media placed atop a Si substrate. (b) Simulated reflectivity for the artificial structure in (a), calculated by *Motofit* [192].

the *Motofit* software package for Igor Pro [192], which facilitates the fitting of XRR data and the extraction of an electron density profile $\rho(z)$ along the surface normal direction. The XRR method is a powerful tool in the analysis of nanometer-scale electron density profiles. However, as is typical in most X-ray scattering techniques, low-angle XRR suffers from the phase problem, and therefore model-based fitting is commonly used for analysis.

Low-angle X-ray reflectivity data presented in this work were acquired at either 5-ID-C or 33-BM-C using a Cyberstar NaI scintillation detector and by rocking the sample through the specular rod. The low-angle XRR data was extracted following the method described by Rauscher *et al.* for conformally rough surfaces. This was necessary due the high levels of diffuse scattering near the specular rod in the form of Yoneda wings [195], which was typically observed for UHV-grown EG/SiC. Low-angle XRR results are included in [Chapter 6](#).

3.4.3: Grazing Incidence Small/Wide Angle X-ray Scattering

The core X-ray techniques used in this work, single-crystal XSW and CTR, are powerful tools in structural determination at the ångstrom scale. However, in this work we also investigate the in-plane ordering of patterned ZnO nanostructures grown on EG/SiC(0001) surface. To this end, we employ GISAXS and GIWAXS to access both long- and short-range in-plane ordering of these structures, as well as the orientational relationship between their domains.

Preliminary GISAXS experiments were performed in-house on a Rigaku S-Max 3000 machine equipped with a Micromax-002 fixed Cu anode source ($E_\gamma = 8.04$ keV) and micro-focusing K-B multilayer optics. Scattered X-rays were detected using a Bruker Hi-Star multiwire detector. The beam size at the sample position was $200 \mu\text{m}^2$, and the incident flux was $\sim 1.5 \times 10^6$ photons/s. More advanced measurements were performed at fixed-energy beamline 8-ID-E at the APS with the assistance of beamline scientist Dr. Joseph Strzalka. A schematic of the beamline setup is shown in [Figure 3.17](#) and a full beamline description is available in Ref. [196]. In this setup, monochromated X-rays (7.35 keV) were reduced to a spot $300 \times 300 \mu\text{m}^2$ in size with a tapered pinhole with a flux on the sample of $\sim 10^{10}$ p/s. Samples were mounted in rough vacuum

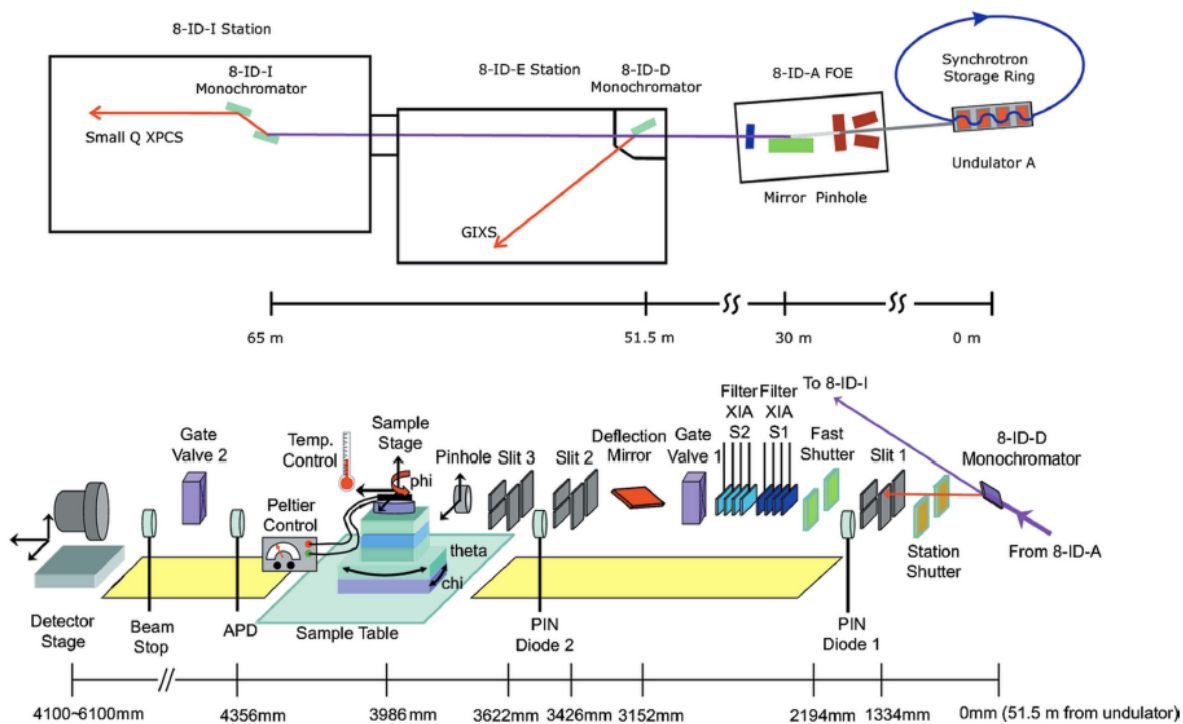


Figure 3.17: Schematic of the GIWAXS/GISAXS setup at APS 8-ID-E. In addition to the components shown in the diagram, we mounted the sample within a rough vacuum chamber and utilized a GIWAXS detector (not shown) mounted translation stage (allowing translation perpendicular to the beam incident beam direction) positioned 167 mm from the sample. From Ref. [196].

on a ϕ rotation stage, and scattered X-rays were detected using either a Pilatus 1M (SAXS) or 100 K (WAXS). In both experiments the sample was tilted such that the X-ray beam was incident on the sample surface (sample normal in the vertical plane) at an angle of $\alpha \sim 0.20^\circ$, which is $\sim 85\%$ of the critical angle α_c for the SiC/vacuum interface at this energy. Scattering from the low- q_z regions of the SiC $\{10\bar{1}L\}$ family of rods (at $q_y \sim 23.6 \text{ nm}^{-1}$) was acquired with the WAXS detector, while scattering from the ZnO nanostructures (at $q_y = \sim 0.96 \text{ nm}^{-1}$) was acquired using the SAXS detector. The signal intensities were monitored as the sample was rotated about its azimuthal angle in ϕ steps of 0.1° , 1° , or 5° . The results from this study are presented in [Chapter 7](#).

3.4.4: X-ray Fluorescence

While XPS, discussed in [Section 3.1.2](#), is a powerful chemical and elemental analysis tool, it is sometimes advantageous to use a secondary emission process for elemental analysis. XRF has some specific advantages in that it can be performed in open air using non-synchrotron X-ray sources such as rotating anodes. Additionally, the characteristic X-rays (of energy E_γ') of interest generally have energies above 5 keV, and will pass relatively unattenuated through μms of material. Therefore, as opposed to XPS, it is simple to access atomic distributions deeper than ~ 1 nm. Fundamentally, the allowed inter-shell transitions (see [Figure 3.18](#)) are dictated by quantum selection rules and the probability that a specific transition will occur is governed by Fermi's Golden rule [197]. The relative probabilities of these transitions between energy levels define the relative intensities of the observed fluorescence lines and are can be calculated using the Hartree-Fock approach. Here, energy dependent K - and L -shell XRF cross sections $\sigma(E_\gamma)$ are calculated

following the method of Puri *et al.* [198] using the program XRF_XSECT [199]. This well-understood phenomenon allows for the quantitative comparison of XRF yields of various samples.

The absolute coverage of an adsorbed surface species can be determined by comparing the X-ray fluorescence yield of a sample of interest to that of a calibrated standard. Spectra are acquired in identical experimental conditions for both unknown elemental species (indexed s) and a calibrated standard (indexed std). If the standard and the species of interest in the sample are different atoms, the data has to be corrected for the differing X-ray fluorescence cross sections, detector efficiency ($\eta(E_\gamma')$), and transmission factor as the X-rays pass from sample to detector ($T(E_\gamma')$). The absolute coverage is then,

$$\theta_s = \frac{Y_s}{Y_{std}} \frac{\sigma_{std}(E_\gamma)}{\sigma_s(E_\gamma)} \frac{\eta(E'_{std})}{\eta(E'_s)} \frac{T(E'_{std})}{T(E'_s)} \theta_{std}. \quad (3.54)$$

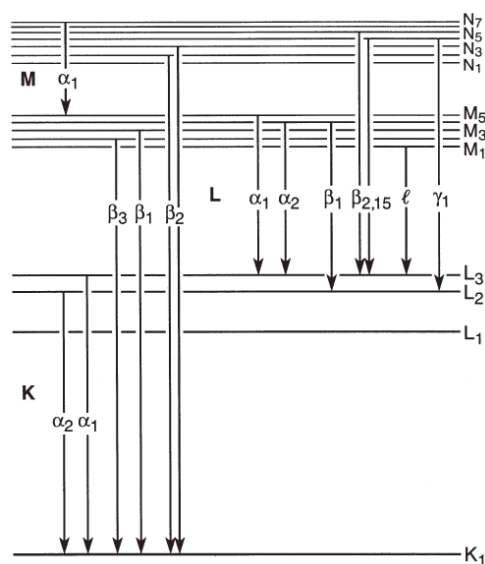


Figure 3.18: Examples of allowed inter-shell transitions and Siegbahn nomenclature for the X-ray emission lines. From Ref. [200].

XRF was performed on a two-circle diffractometer equipped with a Mo rotating anode target at the J.B. Cohen X-ray Diffraction Facility. X-rays were conditioned using a parabolic multilayer mirror and collimated with incident beam slits to produce Mo $K\alpha$ ($E = 17.45$ keV) X-rays with a 3.0×0.1 mm² beamsize at the sample surface. The Mo $K\alpha$ incident beam was used to excite the characteristic fluorescent X-rays from the samples, which were subsequently acquired using a 50 mm² Vortex EX Si drift-diode (SDD) detector positioned at a 90° take-off angle. The signals were then fit with Gaussian lineshapes using MATLAB routine *SUGOM.m* (see Appendix A in Ref. [201]), and the extracted integrated intensities, which are proportional to the atomic surface coverage, were compared to those of a standard of known coverage. The absolute coverage was found according to [Eq. 3.54](#). All sample and standards were measured under identical scattering geometries, with an incident beam angle of 5°. In this work, XRF coverage measurements were used to assess the self-terminating growth of ZnO molecular chains on self-assembled monolayers. The results are presented in [Chapter 7](#).

Chapter 4

XSW-XPS and XRR of Pristine EG/SiC(0001)

EPITAXIAL GRAPHENE grown on SiC(0001) is envisioned as a crucial element in future carbon-based electronics. However, important details remain unresolved concerning the structure and role of the interfacial layer positioned between the top Si layer of the SiC substrate and the graphene overlayers. To address the issues of the chemical composition and structure of this layer, we employ X-ray standing wave-excited photoelectron spectroscopy in conjunction with high-resolution X-ray reflectivity to produce a chemically-sensitive atomic profile of the graphene/SiC(0001) structure along the surface normal direction with sub-Å resolution. This analysis supports the model in which the interface layer solely consists of two chemically and structurally distinct C species forming a single graphene-like atomic layer. Every fourth C atom in this interface layer is covalently bonded to a Si-surface atom of the SiC substrate. The remaining carbons are in a graphene-like bonding configuration. The application of this highly-

precise, chemically-sensitive methodology helps to resolve inconsistencies between various proposed interfacial models.

4.1: Introduction

Graphene, which is an atom-thick sheet of sp^2 -bonded carbon atoms arranged in a hexagonal lattice, is of broad interest due to its unique physical properties [2, 3, 18, 48] and significant potential in numerous applications [8, 18, 98]. These properties make graphene particularly interesting as a principle component in nanoelectronic devices. However, the realization of this potential depends on the ability to produce clean, uniform, large-scale graphene sheets in a manner that is technologically compatible with industrial fabrication schemes. One promising synthesis method is to produce epitaxial graphene via the sublimation of Si from a silicon carbide (SiC) single crystal surface. This technique yields few-layer epitaxial graphene (EG) when the annealing is performed on the Si-terminated polar surface of the silicon carbide (SiC(0001)), and has been utilized to produce high-quality films at the wafer-scale [88, 202]. The resultant EG/SiC(0001) epitaxial structure exhibits the technologically-relevant properties characteristic of graphene, such as the Dirac cone band structure [10, 25, 95] and large room-temperature Hall mobilities [18, 88]. The observation of these unique properties has inspired research focused on finding a viable route for the implementation of EG/SiC(0001)-based electronic components.

The transformative potential for EG/SiC(0001) in electronics has motivated an intensive effort to understand the structure and composition of EG/SiC(0001). In the earliest studies it was discovered that EG/SiC(0001) always possesses a complex interfacial layer, which exhibits a $(6\sqrt{3}\times 6\sqrt{3})R30^\circ$ (or $6R3$) reconstruction with respect to the SiC substrate [17], and is varyingly

called the interfacial, $6R3$, EG_0 , or buffer layer. We will refer to it as the interfacial layer or EG_0 layer. This layer is known to have significant influence on the growth, morphology and electronic behavior of the overlaying graphene itself [10, 29, 73, 95, 103, 109]. It has been contentiously debated as the primary source of symmetry breaking and band gap opening in the overlaying graphene sheets [25, 26, 28] and is shown to be a primary source for carrier doping and scattering in the graphene layers [99, 101]. Recent work on H-intercalated graphene transistors highlights the importance of this layer to the resultant electronic properties of the overlaying graphene, and have shown that the decoupling of the EG_0 layer from the substrate greatly improves graphene properties critical to transistor performance [31]. In addition to these fundamental questions, a precise understanding of this structure is also central to the prospects of interfacial engineering [30, 33, 35], and molecular or atomic functionalization of EG/SiC(0001) [124, 126].

In light of the importance of this interfacial structure to the ultimate electronic behavior of the overlaying graphene, it is clear that a precise understanding of the interfacial structure is integral to the development of EG/SiC(0001) for nanoelectronics. For this reason a myriad of characterization techniques have focused specifically on the question of the interface [17, 21-24, 29, 107, 108, 112, 114, 203, 204]. These experiments, combined with numerous computational studies [32, 103, 110], have generated a multitude of interfacial models (see [Section 2.3.3](#)). The foremost of these models suggest both weak [17, 106, 205] and strong [24, 103, 109, 110] substrate-interlayer coupling, C-rich [23, 24, 103] or Si-rich interfacial structures [21, 22], and models with significant surface populations of Si dangling bonds [109-111]. Despite this disagreement in interpretation, it is becoming the general consensus is that the interfacial layer

consists of a corrugated, topologically graphene-like array of C atoms, but is not graphene-like electronically, i.e., the electrons do not exhibit the classical linear energy-momentum dispersion relationship near the Fermi edge at the Brillouin zone K-points [24].

In this Chapter we aim to clarify this issue by employing a suite of X-ray characterization techniques, including depth-sensitive X-ray photoelectron spectroscopy (XPS), X-ray standing wave-enhanced XPS (XSW-XPS), and X-ray reflectivity (XRR), which, when evaluated together, become a powerful tool ideally suited to elucidating the details of the EG/SiC(0001) interface. Our analysis ultimately yields a chemical-resolved EG/SiC(0001) interfacial map with sub-Å resolution along the substrate normal direction.

4.2: XSW on EG/SiC

The most novel approach employed in this work is the utilization of XSW-XPS, discussed fully in [Chapter 3](#), and reviewed elsewhere [155, 175, 178]. XSW affords conventional photoelectron spectroscopy with high spatial resolution due to the influence of the intensity of the X-ray standing wavefield (produced at a single-crystal $H = hki$ Bragg condition) on the occurrence of a photoemission event. A depiction of this phenomenon for the example of the SiC(0006) Bragg condition (d -spacing $d = d_{0006} = 2.52 \text{ \AA}$) is shown in [Figure 4.1](#). Here, the interference between incident (wavevector \mathbf{k}_θ) and reflected (wavevector \mathbf{k}_H) X-ray planewaves produces an X-ray standing wavefield with period equivalent to d . The XSW phase (φ) can be adjusted relative to the atomic planes by scanning the incident beam energy (E_γ) through a \sim eV-wide Bragg condition, which will in turn modulate the X-ray photoemission yields of atoms located within the crystal or at the sample surface. Depending on the spatial distribution of the atoms with respect to the substrate, this process will produce distinct modulations in the photoemission

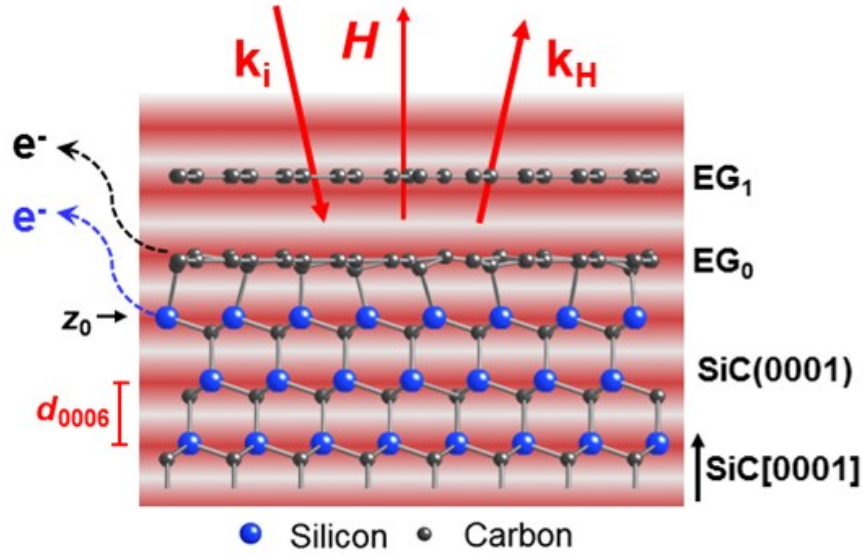


Figure 4.1: A schematic of the X-ray standing wave generated by the SiC(0006) Bragg reflection. Incident and reflected planewaves (with wave vectors k_i and k_H , respectively) interfere to produce a standing wavefield (antinodes shaded red) with a period equivalent to the d_{0006} . The local intensity of this field can enhance or suppress emission of photoelectrons (e^-) from distinct chemical species, represented here by black and blue dashed arrows for C and Si, respectively.

yield. In the dipole approximation for the photoelectric effect (see [Section 3.3.2](#)), the normalized E_γ -dependent photoelectron yield is:

$$Y(E_\gamma) = 1 + R(E_\gamma) + 2p\sqrt{R(E_\gamma)}f\cos[\phi(E_\gamma) - 2\pi P], \quad (4.1)$$

By fitting this equation to the photoelectron yield data from a particular chemical species, s , one can extract the parameters f_s and P_s (herein referred to as coherent fraction and coherent position) which are the measured amplitude and phase of the $H = 0006$ Fourier component of the atomic density profile, $N_s(z)$. Here z is the coordinate height with respect to an origin (z_0), which we choose to coincide with the bulk-like Si surface atom position shown in [Figure 4.1](#). In this work we will assume a normalized Gaussian distribution for each atomic layer

$s(z) = \frac{1}{\sigma\sqrt{2\pi}}\text{Exp}\left(-\frac{(z-z_s)^2}{2\sigma_s^2}\right)$, which models the (0006) Fourier component as:

$$F_s = f_s \text{Exp}(2\pi i P_s) = e^{\left(\frac{-2\pi^2 \sigma_s^2}{d^2}\right)} e^{(2\pi i \frac{z_s}{d})}. \quad (4.2)$$

The measured amplitude, f_s , of the Fourier component determines the Gaussian distribution width σ_s , and the measured phase $P_s = z_s/d \text{ modulo } -1$ determines its mean-height, z_s , relative to the defined origin. Note that the height is projected to lie within a single SiC(0006) d -spacing. Due to this modulo- d ambiguity, we complete the analysis by using high-resolution XRR, a measurement that is sensitive to electron density distributions over a much larger spatial extent,

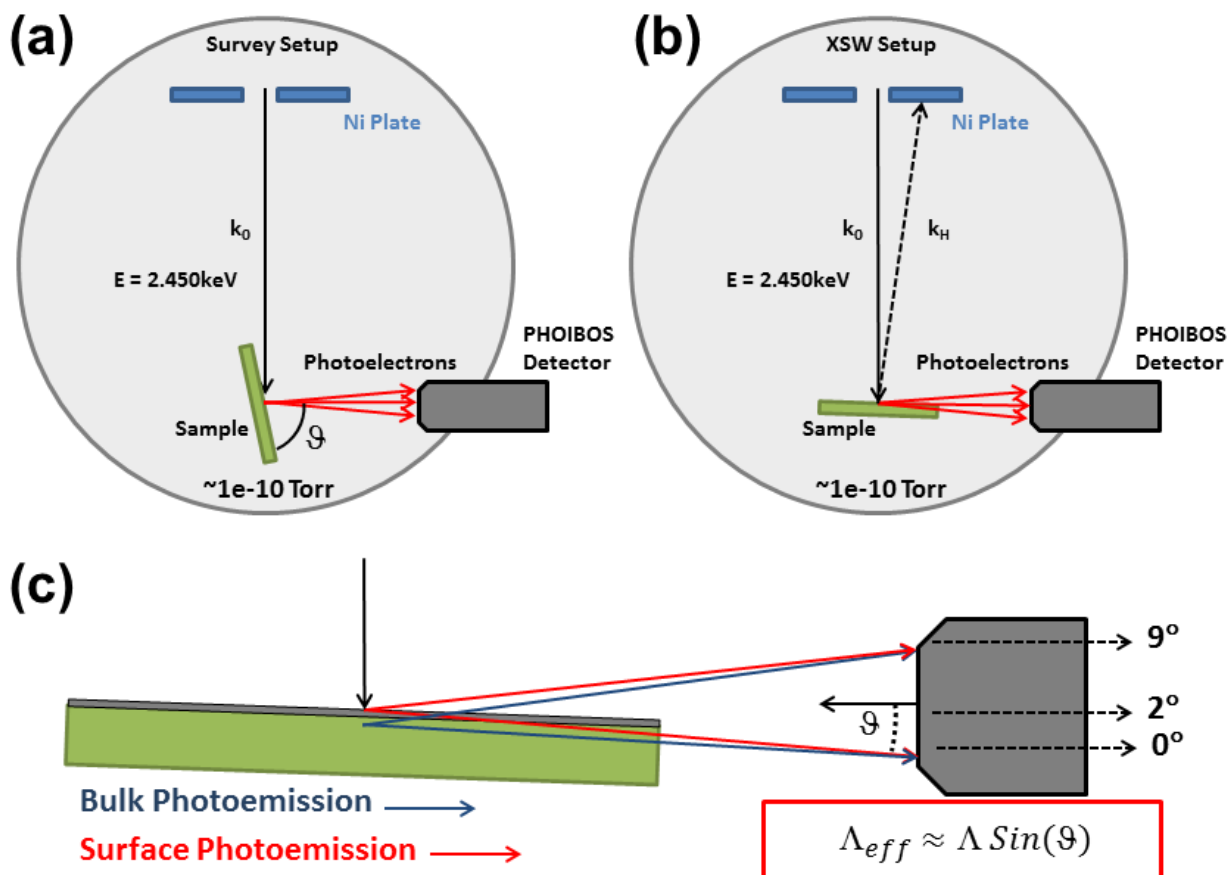


Figure 4.2: Top view of the experimental geometry for both (a) conventional XPS ($\vartheta \sim 78^\circ$) used for survey scans and coverage calculations and (b) highly surface-sensitive grazing-emission XPS and XSW measurements ($\vartheta \sim 2^\circ$). (c) Tuning the emission angle to ($\vartheta \sim 2^\circ$) geometry improves surface sensitivity by effectively increasing the solid pathlength through which photoelectrons originating deep within the crystal (blue line) must travel, as compared to those nearer to the surface (red line). The Λ_{eff} is approximated by applying the geometrical scale factor $\text{Sin}(\vartheta)$.

but without elemental/chemical sensitivity of XSW-XPS. XRR is described in detail in [Chapter 3](#) and elsewhere [167, 206], has been previously employed for this system in Refs. [21] and [207]. Ensuring consistency between these two highly sensitive structural measurements, each of which affords sub-Å spatial resolution, ultimately provides compelling evidence for the validity of our final structural model.

4.3: Sample Preparation

EG/SiC(0001) samples with ~ 1.3 and ~ 0.5 monolayer (ML) graphene coverage were prepared by high-temperature thermal decomposition of a Si-terminated 6H-SiC substrate in ultra-high vacuum (UHV). The ~ 1.3 ML sample was grown from a nitrogen-doped 6H-SiC(0001) substrate graphitized by sequential flashing at 1000°C for 5 minutes, 1100°C for 5 minutes, 1200°C for 2 minutes, 1250°C for 2 minutes and 1300°C for 1 minute. The ~ 0.5 ML sample was annealed at 1000°C for 5 minutes, 1100°C for 5 minutes, and 1200°C for 1 minute. The ~ 1.7 ML Ar-grown samples were grown on semi-insulating, nominally on-axis 6H-SiC(0001). To remove polishing damage, these crystals were etched in H_2 at 1520°C for 50 minutes prior to annealing at 1650°C in Ar atmosphere (99.9999%, 100 mbar) for 120 minutes. Samples were then cooled under Ar flow to 800°C and removed from the growth chamber.

4.4: Experimental

XSW-XPS measurements were performed in UHV (base pressure 1×10^{-10} Torr) at the ID32 endstation [208] of the European Synchrotron Radiation Facility (ESRF). The experimental setup is illustrated in [Figure 4.2](#). The incident X-ray energy was set to satisfy the SiC(0006) Bragg condition near back-reflection geometry (Bragg angle, $\theta_B \sim 88^\circ$ and $E_\gamma \sim 2.450$ keV) using a

Si(111) double crystal monochromator. The photon flux at the sample surface was 10^{12} ph/s within a $0.4 \times 0.1 \text{ mm}^2$ spot size. Photoelectrons were collected with a SPECS-PHOIBOS 225 electron analyzer positioned with analyzer axis mounted parallel to the X-ray polarization direction in order to minimize the influence of non-dipole contributions to the photoelectron yield [183, 209]. Prior to measurement, the sample was annealed in UHV at $\sim 600 \text{ C}^\circ$ in order to remove adventitious contaminants. Surface cleanliness and interface reconstruction was confirmed by the observation of the $(6\sqrt{3} \times 6\sqrt{3})R30^\circ$ low-energy electron diffraction (LEED) pattern (Figure 4.3). The total energy resolution of the photoelectron spectra was $\sim 0.60 \text{ eV}$, as determined by the incident beam bandwidth (0.34 eV) and the electron analyzer resolution. To vary the depth-sensitivity, the photoemission angle (ϑ) was set at either to $\sim 78^\circ$ or $\sim 2^\circ$, as shown in diagrams in Figure 4.2. Survey spectra taken with $\vartheta = 78^\circ$ are shown in Figure 4.4. The $\sim 2^\circ$ emission geometry was used for the identification of surface species and used during XSW experiments.

The XRR data was acquired at 5-ID-C at the Advanced Photon Source (APS) using $E_\gamma = 17.0 \text{ keV}$ X-rays collimated to a $2.0 \times 0.1 \text{ mm}^2$ spot size with a flux of $\sim 5 \times 10^{11}$ ph/s. The reflected intensity at the specular condition was measured using a Roper PI-SCX (CCD) area detector [164, 207]. The integrated intensity and uncertainties of the XRR signal were extracted following the methods described in Ref. [164]. Data fitting was limited to the region $\sim 0.5 < q_z < 6.0 \text{ \AA}^{-1}$. q_z is the out-of-plane component of the momentum transfer vector, $q_z = 4\pi \text{ Sin} (2\theta/2)/\lambda$, where 2θ is the scattering angle, and λ is the X-ray wavelength. For convenience, data is reported as a function of 6H-SiC reciprocal lattice units, $L = \frac{c_{\text{SiC}} q_z}{2\pi}$. Below $q_z \sim 0.5 \text{ \AA}^{-1}$, the finite surface domain size of UHV-grown samples resulted in significant lateral broadening of the specular

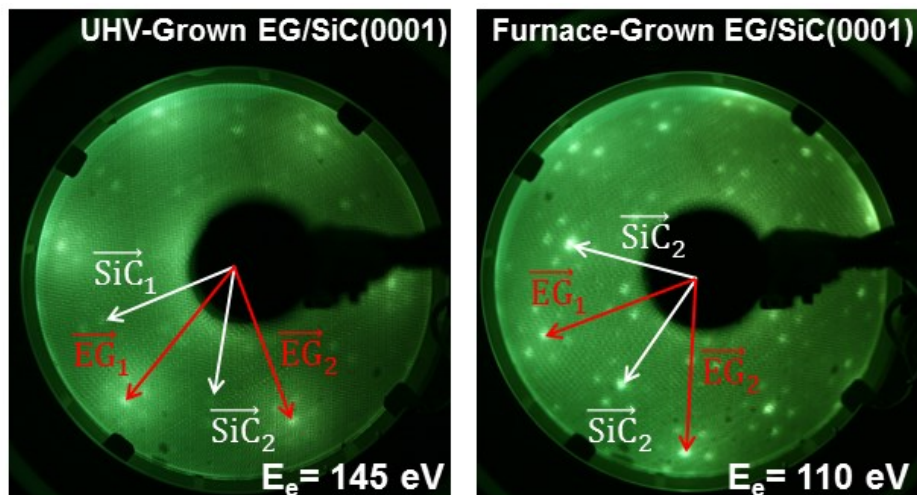


Figure 4.3: LEED patterns for both UHV-grown (left) and Ar-grown (right). Each image shows the typical EG/SiC(0001) pattern with bright 1×1 graphene (red arrow) and 1×1 SiC (white arrow) spots. The spots arranged in a hexagon about the graphene spots are due to the $(6\sqrt{3} \times 6\sqrt{3})R30^\circ$ reconstructed buffer layer. The sharper pattern and better signal-to-background ratio for the Ar-grown samples are due to the larger surface domains formed during Ar-growth.

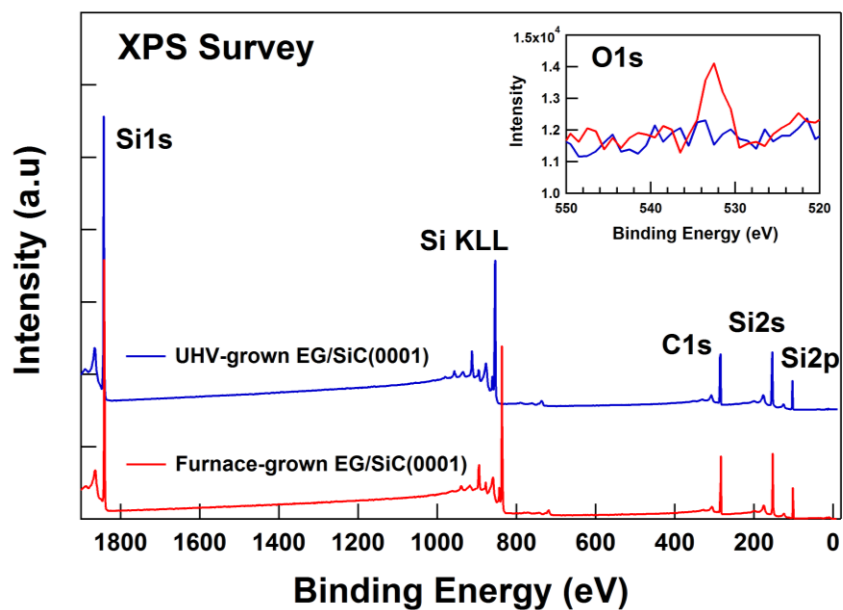


Figure 4.4: Survey spectra for Ar-grown (red) and UHV-grown (blue) EG/SiC(0001). Spectra were acquired using incident beam energies of 2.450 and 2.465 keV, respectively. The inset shows a small O signal present in the Ar-grown sample associated with a small amount of silicon oxide surface contamination.

rod, which inhibited accurate integration of the XRR signal. Further specifics on this measurement are available in [Sections 3.1](#) and [Section 6.1.2.3](#).

4.5: XPS Analysis

In [Figure 4.5](#) we present the depth-sensitive core-level spectra used to identify near-surface C and Si chemical species. For the measurement using an emission angle of $\vartheta = 78^\circ$, the Si 1s and C 1s spectra are dominated by bulk SiC components with binding energies (BE) of 1841.6 ± 0.1 eV and 283.8 ± 0.1 eV, respectively. Qualitatively, it is clear that the C 1s spectrum consists of multiple core-shifted components, the study of which has been the focus of previous work [24, 107, 108]. On the other hand, the Si 1s appears to consist of a single component, although it has been suggested that additional core-shifted components are present [30, 107]. By tuning the geometry to the more highly surface-sensitive configuration at $\vartheta = 2^\circ$, in which the photoelectron sampling depth (Λ) is effectively reduced by approximately an order of magnitude due to geometrical effects (see [Figure 4.2\(c\)](#)), it is possible to bias the spectra towards components originating from surface species. A comparison of the C 1s spectra in [Figures 4.5\(a\) and 4.5\(c\)](#) reveals heavy attenuation of the C_{Bulk} signal with respect to the spectral components at higher BE (relative integrated area $\times 1/30$). In contrast, no obvious surface species can be identified in the $\vartheta = 2^\circ$ Si 1s spectrum. There does, however, arise a slight broadening of the Si 1s peak (for spectral overlay, see [Figure 4.6](#)) which may be due to the presence of distinct, core-shifted surface species, or, alternatively, caused by the preferential detection of photoelectrons emitted from strained, but chemically bulk-like Si species at the EG/SiC(0001) interface.

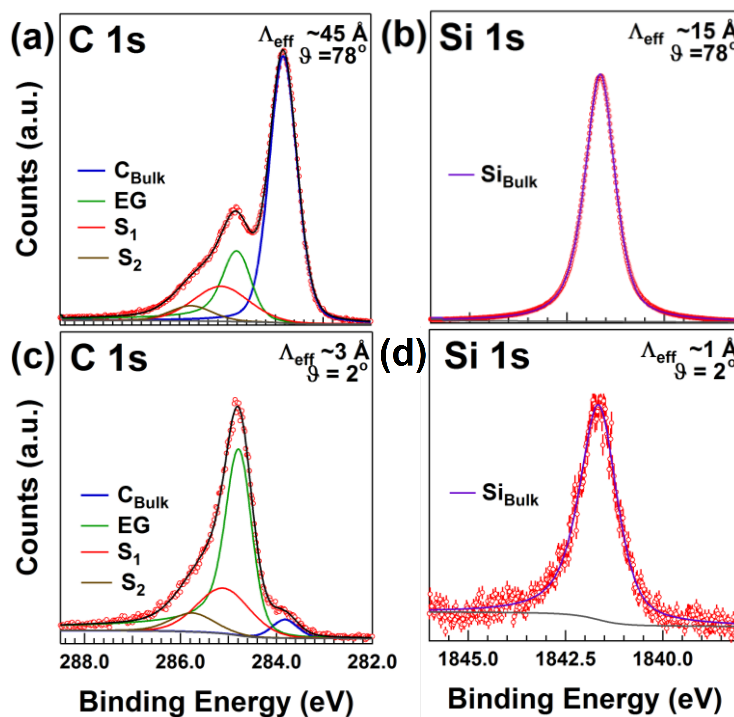


Figure 4.5: X-ray photoelectron spectra of the C 1s and Si 1s core-levels for ~ 1.3 ML EG/SiC(0001). The spectral components for bulk Si, bulk C, EG, S_1 , and S_2 are shown in purple, blue, green, red, and brown, respectively, and the envelope of all fitted components is in black. (a-b): Data collected with an emission angle of 78° . (c-d): Data collected with a highly surface-sensitive grazing-emission angle of 2° , showing fitted components used in the XSW analysis.

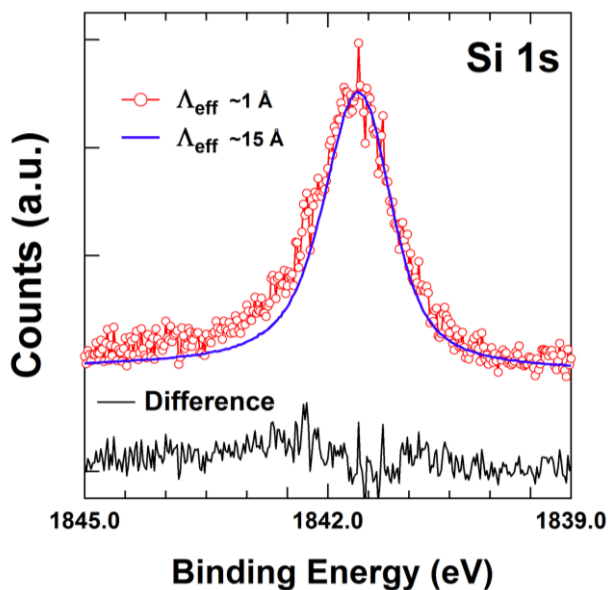


Figure 4.6: Overlay of Si 1s spectra taken at different emission angles $\vartheta = 78^\circ$ (blue) and $\vartheta = 2^\circ$ (red). The peak lineshape and position do not shift upon tuning the emission angle from $\vartheta = 78^\circ$ to $\vartheta = 2^\circ$, but the peak broadens by $\sim 20\%$, indicating increased spectral contribution from strained surface Si species. The difference map is shown in black.

While qualitative analysis of XPS is useful in identifying surface species, the accurate resolution of the spectra into distinct core-shifted constituents is critical for accurate XSW analysis. Failure to accurately model the data will result in flawed analysis and may lead to unphysical solutions or inconsistencies between XSW and XRR. It is for this reason that we deviate from the conventional peak-fitting model proposed by Emtsev *et al.* [24]. Although we also identify three distinct C 1s surface species, labeled in [Figures 4.5\(a\) and 4.5\(c\)](#) as EG, S₁, and S₂ (as is standard), we instead find these components shifted by +0.95, +1.35, and +1.95 eV with respect to the C_{Bulk} peak, and, most notably, the intensity ratio of the S₁ and S₂ peaks is essentially reversed ([Figures 4.5\(a\) and 4.5\(c\)](#)) when compared the model of Emtsev *et al.* All peak-fitting parameters are provided in [Table 4.1](#). Our model is similar to that suggested earlier by Johansson *et al.* [107].

It should be noted that using the peak-fitting model similar to that presented in [Figure 4.5](#) and accounting for a small concentration of EG surface coverage (~15%), we are able to accurately fit the spectra for the nominally zero-layer graphene (6R3-only) sample from Ref. [24] (see [Appendix B](#)). In reality, the presence of inclusions of ML EG on step edges is the rule rather than the exception for nominally zero-layer graphene, and has been observed even on the highest-quality samples grown using state-of-the-art techniques [29, 112, 202]. It is therefore likely that the spectra in Ref. [24] should, in fact, be fit accounting for contributions from EG layers. Regardless, we are not limited to a single model our analysis and provide a full parallel analysis using the model proposed by Emtsev *et al.* in the [Appendix B](#), where we find that the XSW and XRR result for that peak-fitting model is incompatible with the physical interpretation associated with that model.

Table 4.1: Fitting parameters for C 1s and Si 1s spectra from EG/SiC(0001) samples. SGL denotes a summation Gaussian-Lorentzian, a -SGL denotes an asymmetric SGL, with asymmetry factors a and b . DS represents a Doniach-Sunjjic curve with asymmetry factor ϵ .

0.5 ML UHV-grown EG/SiC(0001)						
	Si 1s		C 1s			
Component	Si_{Bulk}	SiO_x	C_{Bulk}	EG	S₁	S₂
Lineshape	a -SGL	SGL	SGL	DS	SGL	SGL
ϵ or a/b	0.25,0.09	-	-	0.105	-	-
η	0.55	0.25	0.20	-	0.10	0.20
E_B	1841.70	1844.40	283.80	284.80	285.15	285.75
FWHM	1.25	2.05	0.85	0.70	1.15	1.00
1.2 ML UHV-grown EG/SiC(0001)						
	Si 1s		C 1s			
Component	Si_{Bulk}	SiO_x	C_{Bulk}	EG	S₁	S₂
Lineshape	a -SGL	SGL	SGL	DS	SGL	SGL
ϵ or a/b	0.25,0.09	-	-	0.105	-	-
η	0.55	-	0.20	-	0.10	0.20
E_B (eV)	1841.65	-	283.80	284.75	285.10	285.75
FWHM (eV)	1.12	-	0.90	0.70	1.1	1.0
1.7 ML Ar-grown EG/SiC(0001)						
	Si 1s		C 1s			
Component	Si_{Bulk}	SiO_x	C_{Bulk}	EG	S₁	S₂
Lineshape	a -SGL	SGL	SGL	DS	SGL	SGL
ϵ or a/b	0.25,0.09	-	-	0.105	-	-
η	0.55	0	0.20	-	0.10	0.20
E_B (eV)	1841.65	1844.10	283.90	284.80	285.10	285.75
FWHM (eV)	1.1	1.95	0.85	0.64	1.0	0.9

The Si 1s spectrum has been suggested to be comprised of a bulk Si peak and two additional core-shifted Si components positioned at both high-BE and low-BE sides of the peak, associated with either “surface” and “defect” Si species [30, 107]. We note, however, that even a moderate population of surface-specific species would presumably dominate the spectra in a similar fashion to that observed for the C 1s spectra, while the observed increase in the relative intensity on the wings of the Si_{Bulk} peak are marginal (relative integrated area $\times 3$ as compared to Si_{Bulk}). We therefore adopt a model in which the bulk Si peak is slightly asymmetrically

broadened due to the diversity in Si-C bond lengths and bond angles as a result of interfacial strain. Upon tuning the geometry to reduce the Λ_{eff} ([Figure 4.5\(d\)](#)), the contributions of the Si_{Bulk} from deeper within the crystal are reduced, resulting in the observed ($\sim 20\%$) broadening of the peak. We therefore fit all Si 1s spectra using a single asymmetric Lorentzian ([Figures 4.5\(b\) and \(d\)](#)), and allow the fitted width to increase upon tuning the emission angle to $\vartheta = 2^\circ$. Again, we are not limited in the number of models we can examine, and therefore we provide a parallel analysis for the model proposed by Riedl *et al.* in [Appendix B](#) but find no compelling evidence for the existence of unique core-shifted Si 1s species.

4.6: XSW Analysis

Using the peak-fitting models described above and shown in [Figures 4.5\(a\) and 4.5\(c\)](#), we extract the E_γ -dependent photoemission XSW yields, shown in [Figure 4.7](#). Each of the 5 components exhibits a distinct XSW modulation and an associated high coherent fraction, demonstrating that each component possesses coherent registry with the substrate lattice along the SiC[0001] direction. Best-fits of the yield equation ([Eq. 4.1](#)) to the data are shown overlaid for each chemical species in [Figure 4.7](#). Best-fit f_s and P_s values, along with their 1σ confidence levels and χ^2 values, are reported for each component in [Table 4.2](#).

The extreme surface sensitivity of the experimental geometry means that XSW analysis of the “bulk” species is highly biased towards the top few SiC bilayers, which makes the measurement particularly sensitive to potential relaxations or disorder within those layers. The Si_{Bulk} signal, shown in [Figure 4.7](#), exhibits a coherent fraction of 0.8 ± 0.1 , which is far enough from unity to suggest that some fraction of Si near-surface atoms deviate from bulk Si positions.

The coherent position of $P_{\text{Si}_{\text{Bulk}}} = 0.98 \pm 0.02$ indicates that the Si_{Bulk} atomic distribution is centered about the nominal bulk Si position, within error. We can therefore use [Eq. 4.2](#) to solve for the distribution width of Si atoms in the topmost SiC bilayers to be $0.27 \pm 0.07 \text{ \AA}$, which is partly comprised of a $\sim 0.1 \text{ \AA}$ thermal vibrational amplitude. The XSW results for the C_{Bulk} signal give $f_{\text{C}_{\text{Bulk}}} = 1.0 \pm 0.1$ and indicate essentially perfect coherency. As observed for Si_{Bulk} result, the C_{Bulk} XSW result reveals that the C_{Bulk} distribution is centered about the nominal SiC single crystal values, within error. However, the small deviations of XSW best-fit results for the bulk species from the nominal Si and C single crystal values (-0.05 and $+0.05 \text{ \AA}$ for Si and C, respectively), may indicate some slight displacement. For comparison, simulations of the XSW modulation expected for perfect bulk Si and C species in SiC are also shown in [Figure 4.7](#), where $f_s \sim 1$ is based on a 0.1 \AA thermal vibrational amplitude.

The results for the S_1 and S_2 components are the primary focus of this work because of their conventional association with C located within the interfacial layer [24, 107, 108]. XSW data and fits for these two components are shown in [Figure 4.7](#). The coherent fractions and coherent positions for these two species are $P_{\text{S}_1} = 0.95 \pm 0.05$, $P_{\text{S}_2} = 0.82 \pm 0.04$, $f_{\text{S}_1} = 0.4 \pm 0.2$ and $f_{\text{S}_2} = 0.9 \pm 0.2$. If we assume single coherent layers of atoms associated with these two signals, the P_{S_1} and P_{S_2} values can be converted into absolute positions relative to the bulk-like terminal Si layer by the relationship $d \times P_s = z_s$. This interpretation positions the S_1 component at $z_{\text{S}_1} = 2.39 \pm 0.13 \text{ \AA}$ and the S_2 component at $z_{\text{S}_2} = 2.06 \pm 0.10 \text{ \AA}$. The very large coherent fraction observed for the S_2 component indicates a narrow distribution of those atoms about z_{S_2} , while f_{S_1} is significantly smaller, suggesting a broader distribution of the S_1 atoms.

Table 4.2: XSW results for Si 1s and C 1s components. The result for EG contain contributions from multiple EG layers and therefore make use of XRR for complete analysis. The origin for the P_s scale is at the ideal Si bulk-like position within SiC.

Component, s	χ^2	P_s	z_s (Å)	f_s	σ_s (Å)
Si _{Bulk}	3.01	0.98±0.02	2.47±0.05	0.8±0.1	0.27 ^{+0.06} _{-0.1}
C _{Bulk}	1.14	0.77±0.02	1.94±0.05	1.0±0.1	0.05 ^{+0.12} _{-0.0}
S ₁	4.11	0.95±0.05	2.39±0.13	0.4±0.2	0.5 ^{+0.2} _{-0.1}
S ₂	2.24	0.82±0.04	2.07±0.10	0.9±0.2	0.18 ^{+0.15} _{-0.13}
EG	2.94	0.42±0.02	$z_{EG1} = 5.82$	0.48±0.05	$\sigma_{EG1} = 0.21$
			$z_{EG2} = 9.16$		$\sigma_{EG2} = 0.11$
			$z_{EG3} = 12.57$		$\sigma_{EG3} = 0.05$

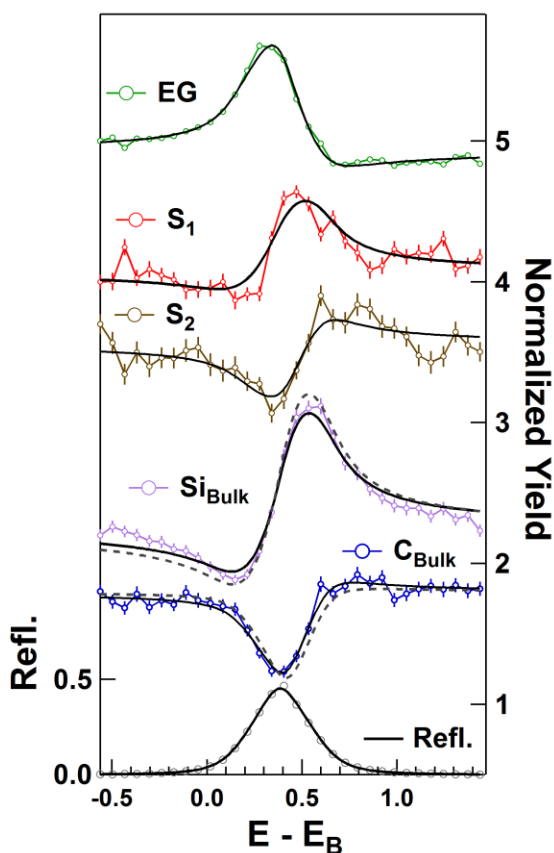


Figure 4.7: XSW modulations of fitted XPS components from [Figure 4.5](#). Measured reflectivity from the SiC(0006) Bragg peak (grey circles) and best-fit (black line) are plotted on the left axis as a function of energy offset from the geometrical Bragg condition, E_B . The normalized yields from each component are represented by colored circles that are coded to the components in [Figures 4.5](#) and best fits are in black lines on the right axis. Simulated C_{Bulk} and Si_{Bulk} curves from a perfect bulk SiC single crystal are shown in dashed black. Normalized yields are offset for clarity.

The final C 1s component arises from C atoms located in the EG overlayers. It is important to note here that growth of graphene on SiC(0001) is never observed to be limited to an isotropic monolayer, and regions covered by higher-order EG layers are located preferentially on SiC steps [88, 210]. Therefore, unlike the S₁ and S₂ components, the f_{EG} and P_{EG} values are determined by the superposition of contributions from $n > 1$ layers, making it challenging to perform direct XSW analysis using only a single measured Fourier component. However, by utilizing the long-range structural information afforded by XRR we are able to explore models with varying EG layer coverage. By ensuring consistency between XSW results for all components and the longer-range XRR results, we offer an elegant and comprehensive model for the EG/SiC(0001) interfacial structure.

To validate the XSW result and formulate a chemically-resolved interfacial map we use the XSW best-fit (within 1σ confidence levels) solutions to constrain the analysis of XRR data. XRR data is typically analyzed by comparing measured reflectivity values to calculated values from a model consisting of k atomic layers, each determined by layer occupancy (c_k), layer position (z_k), and layer distribution width (σ_k), as described in [Section 3.2.1](#) and Refs. [167, 206]. We note that our earlier work (presented in [Chapter 6](#)) finds that the interfacial XRR data can be well-fit using a simple broad interfacial EG₀ layer of graphene-like density, in contrast to previous work by Hass *et al.*, which presents a more complex interpretation [21]. However, in this work we are able to constrain the XRR fitting model with the XSW results (see [Table 4.2](#)), which helps eliminate ambiguities that commonly arise during model-based XRR analysis. From XSW we find that the bulk Si and C are in essentially bulk-like positions, although the slight deviation of f_{SiBulk} from unity and the phase shifts in P_{CBulk} and P_{SiBulk} advocate for the allowed

broadening and displacement of the distributions of atoms in the top-most SiC bilayers. Also, our interpretation of the XSW data for the S_1 and S_2 species is that these two components have single, well-defined distributions within the interfacial layer, and we therefore model this region accordingly. We allow for 3 EG_k graphene layers ($k = 1, 2, 3$) during fitting, as has been commonly observed with scanning-tunneling microscopy of these samples.

4.7: XRR Results

The XSW-constrained best-fit XRR result is shown in [Figure 4.8\(a\)](#). The result yields χ^2 and R -factors of 7.19 and 0.079 respectively. When fitted over the same q_z range ($1.0 < q_z < 6.0$) as the data in Ref. [207] (and [Chapter 6](#)) both χ^2 and R -factor values are found to be superior than those of our previous work for EG/SiC(0001) grown under similar conditions ($\chi^2 = 4.86$ vs. 6.53, R -factor = 0.06 vs. 0.11), indicating the improved quality of this interfacial model. The total EG coverage found in this analysis is $\Theta_{\text{XRR}} \sim 1.35$ ML, a value close to the approximate coverage derived from XPS ($\Theta_{\text{XPS}} \sim 1.3$ ML). The fit finds the EG_1 , EG_2 , and EG_3 layers positioned at 5.82, 9.17, and 12.57 Å above the terminal Si layer with coverages of 0.86, 0.45, and 0.03 ML, respectively. The S_1 and S_2 layer positions converge to $z_{S_1} = 2.45$ Å and $z_{S_2} = 2.13$ Å, respectively, well within the 1σ confidence levels derived from the XSW results ([Table 4.2](#)). The $2\pi/q_{\text{max}}$ resolution-broadened electron density profile (N_e) derived from the XRR fit is

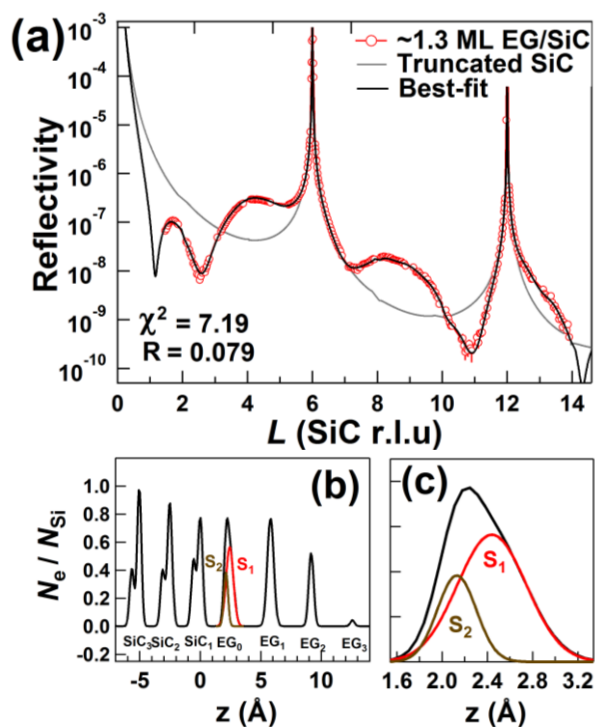


Figure 4.8: XRR results for ~ 1.3 ML UHV-grown EG/SiC(0001). (a) X-ray reflectivity data for ~ 1.3 ML EG/SiC(0001) (red circles), best-fit result (black line), and a simulated ideally-terminated bulk-SiC crystal (grey line). Sharp peaks at $L = 6.0$ and 12.0 are bulk diffraction peaks from the single-crystal SiC substrate. Broad peaks at $L \sim 4.4, 8.8,$ and 13.2 are due to scattering from layers displaced by graphitic-like d -spacing. (b) The XRR-derived electron density profile for the solution in (a). The electron density is normalized to that of an ideally occupied Si layer in SiC. (c) An inset of the interfacial regions reveals that the summation of the electron density from the two interfacial species forms a broad, Gaussian-shaped interfacial layer.

shown in [Figure 4.8\(b\)](#), where q_{\max} is the range over which the scattering data is acquired. The magnified interfacial region shown in [Figure 4.8\(c\)](#) conveys why the single-Gaussian models of the interface employed in Ref. [207] yield good fitting results. It should be noted here that the top-most bulk Si layers are found to be slightly depleted, which is presumably a result of the Si sublimation that occurs during the graphene growth process and may be attributed to near-surface Si vacancies [211]. The top-most Si layer is found to be only 85% occupied, which, in turn, limits the maximum number of sp^3 -rehybridized interfacial C atoms to $\sim 25\%$ of the atoms within the layer. Finally, the C atoms in the topmost 3 SiC bilayers are found to relax slightly

outwards by, on average, 0.09 Å, consistent with the XSW result, which finds an average relaxation of 0.05 ± 0.05 Å.

From this result it is possible to use the XRR-derived complex geometrical structure factor for the three EG layers (see [Section 3.3.3](#)),

$$S_{EG} = \frac{1}{\sum_{n=1}^N c_k} \sum_{k=1}^N c_k e^{i2\pi \frac{z_k}{d_H}} e^{-2\pi^2 \frac{\sigma_k^2}{d_H^2}}. \quad (4.3)$$

to back-calculate the expected f_{EG} and P_{EG} from using the S_{EG} amplitude $f_{EG} = |S_{EG}|$ and phase $P_{EG} = \text{Arg}(S_{EG})/2\pi$. These back-calculated values ($P_{EG} = 0.49$ and $f_{EG} = 0.41$) agree almost precisely with the XSW-derived values for EG listed in [Table 4.2](#) and provide strong support for our methodology. The combined XSW and XRR results ultimately allow for the construction of a complete, chemically-resolved interfacial map of the EG/SiC(0001) interfacial structure.

4.8: Discussion

The XSW- and XRR-consistent atomic-density profile from the combined analysis is shown in [Figure 4.9](#), and an enlargement of the interfacial region is shown in [Figure 4.9\(b\)](#). The minimum width for the atomic layers is set to 0.1 Å thermal vibrational. The main conclusion to be drawn from this map is that the interfacial region consists of a broad, C-only layer with graphene-like atomic density. Within this layer there exist two vertical distributions of distinct, but overlapping, C species, which are displaced from each other by 0.3-0.4 Å. The S₂ species, which is associated with the highest BE signal in the C 1s spectrum ([Figures 4.5\(c\)](#)) and accounts for ~25% of the interfacial C, is located 2.1 ± 0.1 Å above the terminal Si layer. This displacement is only 0.2 Å larger than the nominal Si-C bond distance of 1.9 Å, supporting the suggestion that

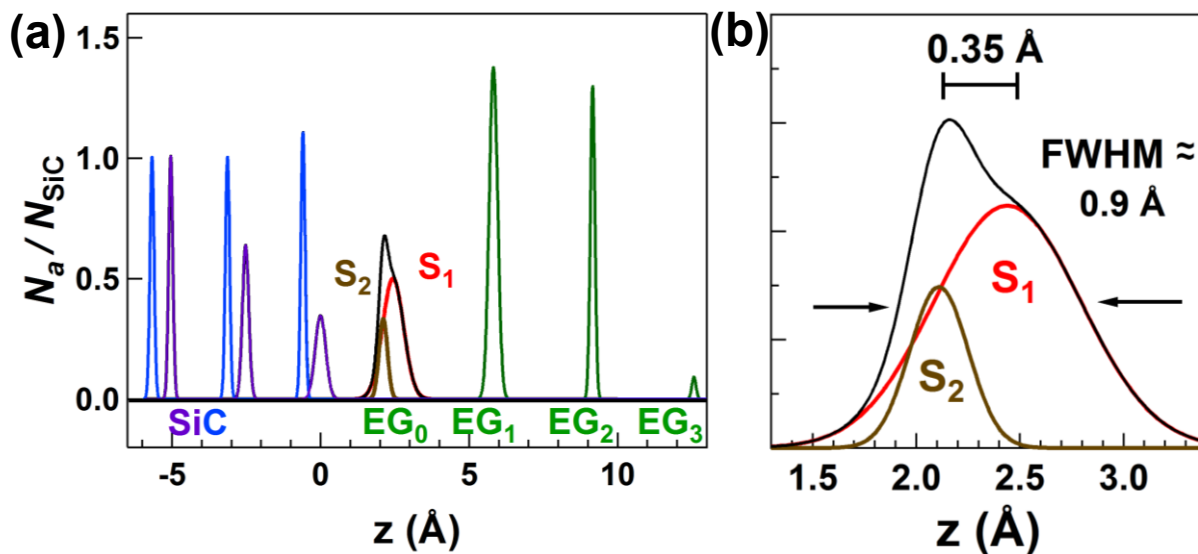


Figure 4.9: The 1D chemically-sensitive interface map derived from combined analysis of both XSW-XPS and XRR. (a) The long-range electron density profile. (b) An enlargement of the interfacial region highlights the two surface components, S_1 and S_2 , which are separated by ~ 0.35 Å and form a ~ 0.9 Å wide low-areal density interface layer. Minimum peak widths are 0.1 Å.

there exists C-Si sp^3 -hybridization between the interfacial layer and the SiC. The narrow distribution of the S_2 species ($\sigma_{S_2} = \sim 0.18$ Å), and its close agreement with that of the top-most Si layer ($\sigma_{S_2} = \sim 0.27$ Å), suggests strong coherency between the two layers, supporting the assertion that the two layers are indeed covalently bound. In addition, the ratio of the occupancies of the topmost Si layer and the S_2 is $\sim 1:1$, implying that practically every Si atom within the topmost SiC bilayer is covalently bound to an interfacial C. This substantiates the claim that there exist essentially no unsaturated Si dangling bonds at the interface [24].

These results also indicate that the S_1 species, which accounts for the other 75% of the interfacial C, is positioned at 2.45 ± 0.10 Å above the topmost Si layer, but possess a significantly larger distribution width ($\sigma_{S_1} = \sim 0.5$ Å) as compared to the S_2 species. Due to this broadening the peak of the atomic density profile is reduced at the interface, which is consistent with the observation of a highly corrugated interfacial layer found in both scanning probe and

computational studies [8, 32, 103, 108]. This structure would also explain the effectively reduced atomic density cross-section often observed with cross-sectional tunneling electron microscopy [27, 212].

Our analysis yields no evidence for the complex interfaces suggested by some groups. Of these models we give special attention to those proposed by Rutter *et al.* [22] and Hass *et al.* [21], which each suggest the presence of large populations of interfacial adatoms. These models prove inconsistent with our data. First, we see no convincing evidence of non-bulk Si species, particularly from Si tetramers or other Si adatoms, which would exhibit large, negatively core-shifted Si 1s components with respect to the bulk SiC due to the presence of Si-Si bonds. Second, it is important to note that ambiguities associated with the model-based fitting of XRR data may lead to numerous solutions, and therefore quantitative analysis of complex interfaces such as EG/SiC(0001) requires great care. Our XRR analysis benefits from the constraints provided by structurally-sensitive XSW-XPS measurement and finds that the XRR data can be well-fit with a C only interfacial layer with graphene-like density. In essence, apart from a discrepancy in the identification of core-level signals, our work supports the model suggested by Emtsev *et al.* [24] and Varchon *et al.* [32], in which there exists a single corrugated graphene-like interfacial layer. This layer possesses two distinct C species, one of which is covalently bound to the substrate in a Si-C-C₃ bonding configuration, while the other is in a graphene-like C-C₃ bonding configuration, albeit with considerable *sp*³ character. With respect to the discrepancy in XPS, we note the following: 1) The C 1s XPS data can be well-fit with numerous peak-fitting models, 2) Emtsev *et al.* did not account for the likely presence of sub-ML EG coverage in their peak-fitting model, and 3) there are a large number of proposed influences on

the precise binding energies of the interfacial species (e.g., bond charge-transfer, spontaneous substrate polarization [99], interfacial defect states [23], charge-transfer doping from the substrate [24] or contaminants, band bending [30], and sp^2 - vs. sp^3 -hybridization) and therefore the accurate identification of chemical species using only core- and valence-level shifts is tenuous. Regardless, the binding energies that we find for the S_1 ($= BE_{EG} + \sim 0.4$) and S_2 ($= BE_{EG} + \sim 1.0$) are more in accordance with what might be expected from graphene-like and sp^3 -hybridized species, respectively, and are entirely consistent across multiple high-resolution measurements.

4.9: Supplemental Samples

Before concluding this Chapter, we would like discuss results for supplementary samples possessing varying coverages and grown using different processes. High-resolution C 1s and Si 1s spectra taken with emission angle $\vartheta = 2^\circ$ are shown in [Figure 4.10](#) for both ~ 0.5 UHV-grown ([Figures 4.10\(a\) and \(b\)](#)) and ~ 1.7 ML Ar-growth EG/SiC(0001) ([Figures 4.10\(c\) and \(d\)](#)). Both these samples exhibit C 1s spectra typical of EG/SiC(0001), but in both Si 1s spectra there exists a strong high-BE shifted component consistent with a SiO_x chemical species [213]. This signal is only discernible when tuned to the $\vartheta = 2^\circ$ geometry, indicating that it is associated with a surface oxide. Due to the relatively low spectral resolution of this experiment, we do not attempt to identify any sub-oxide signal within the Si 1s spectrum, as those observed previously [213]. We do note, however, that in the case of the 1.7 ML sample, which has less oxide signal, the core-level shift is 0.3 eV less than that of the ~ 0.5 ML sample, suggesting increased contribution

from some lower-BE sub-oxide species. The oxygen concentration can be estimated by comparing the integrated intensity O 1s signal to that of the EG C 1s signal. The density of C in EG form is estimated from the unit cell definition to be 38.20 C/nm^2 , and therefore, by correcting for the relative C and O photoionization cross-sections at $\sim 2.5 \text{ keV}$, we find an areal concentration of $\sim 2 \text{ O/nm}^2$ for the 1.7 ML furnace-grown sample, and $\sim 6 \text{ O/nm}^2$ for the 0.5 ML UHV-grown sample. These oxides may be a result of the presence of trace O_2 in the system during growth, or, in the case of the UHV-grown sample, exposure to air of the more reactive sub-ML sample, which has possesses large regions of exposed EG_0 .

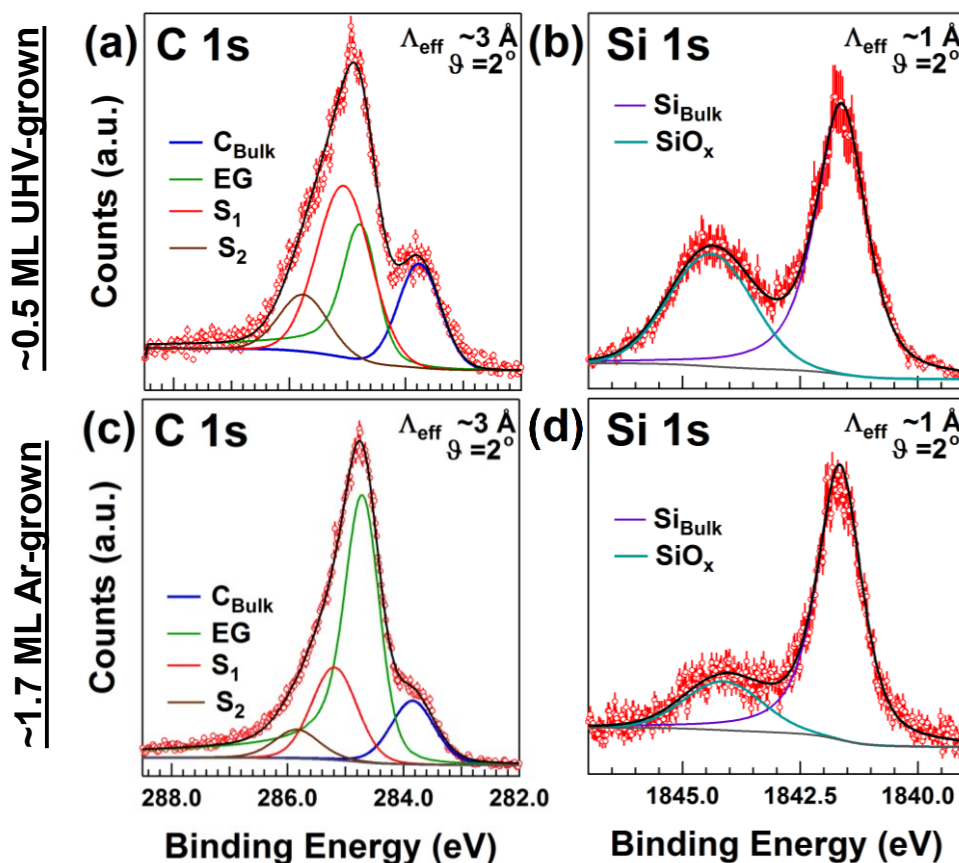


Figure 4.10: C 1s and Si 1s spectra from $\sim 0.5 \text{ ML}$ UHV-grown (a-b) and $\sim 1.7 \text{ ML}$ Ar-grown (c-d) EG/SiC(0001). (a) and (c): The C 1s spectra for both samples closely resemble that observed for the UHV-grown sample in [Figure 4.5](#), differing mostly due to graphene coverage. (b) and (d): Both Si 1s spectra however, show a high-BE core-shifted component (light blue) identified as originating from a SiO_x surface oxide species.

Table 4.3: XSW results for ~0.5 UHV-grown and ~1.7 ML Ar-grown graphene.

UHV-grown ~0.5 ML EG/SiC(0001)					
Component, s	χ^2	P_s	z_s (Å)	f_s	σ_s (Å)
Si _{Bulk}	2.12	0.99±0.01	2.49±0.03	0.90±0.03	0.18 ^{+0.03} _{-0.03}
SiO _x	2.03	N/A	N/A	0.1±0.1	N/A
C _{Bulk}	6.22	0.74±0.02	1.87±0.05	0.95±0.08	0.1 ^{+0.07} _{-0.1}
S ₁	1.36	0.9±0.1	2.3±0.2	0.3±0.2	0.6 ^{+0.2} _{-0.2}
S ₂	1.21	0.8±0.05	2.0±0.1	0.9±0.2	0.18 ^{+0.15} _{-0.13}
EG	1.45	0.27±0.04	N/A	0.70±0.3	N/A
Ar-grown ~1.7 ML EG/SiC(0001)					
Component, s	χ^2	P_s	z_s (Å)	f_s	σ_s (Å)
Si _{Bulk}	0.33	1.00±0.01	2.52±0.03	0.94±0.08	0.1 ^{+0.07} _{-0.1}
SiO _x	1.09	N/A	N/A	0.0 ^{+0.2} _{-0.0}	N/A
C _{Bulk}	3.37	0.74±0.02	1.87±0.05	0.86±0.07	0.22 ^{+0.06} _{-0.06}
S ₁	3.11	1.00±0.05	2.52±0.13	0.3±0.1	0.6 ^{+0.1} _{-0.05}
S ₂	0.86	0.84±0.03	2.12±0.07	1.00±0.14	0.1 ^{+0.07} _{-0.1}
EG	1.21	0.34±0.04	N/A	0.52±0.09	N/A

XSW results for supplementary samples are shown in [Figure 4.11](#), and the results are summarized in [Table 4.3](#). The most notable observation is that the Si_{Bulk}, C_{Bulk}, S₁ and S₂ values are essentially identical between all three samples, within error. Considering that these samples were made under with various growth techniques, in different labs, and with varying EG and oxide coverage, this result a testament to the ubiquitousness of the interfacial layer. The SiO_x component is randomly distributed, indicating that there exists a thick or broadly distributed region of silicon oxide near to the SiC surface. The ~0.5 ML UHV-grown C 1s XSW EG result is interesting as it is close to the value expected for perfect monolayer graphene (at $z_{EG_1} \sim 5.8$ Å), as single monolayer would give a coherent position of $P_{EG_1} = 0.30$). This, along with the relatively high coherent fraction ($f_{EG_1} = 0.7 \pm 0.3$), indicates

that most of the EG signal originates from monolayer graphene. Contribution from EG₂ (at $z_{EG_1} \sim 9.15$ Å) would, in principle, shift the phase positive and reduce the coherent fraction. It should be noted that this sub-monolayer sample suffered from significantly poorer statistics when compared to the others, which is reflected in the generally larger degree of scatter in the data and

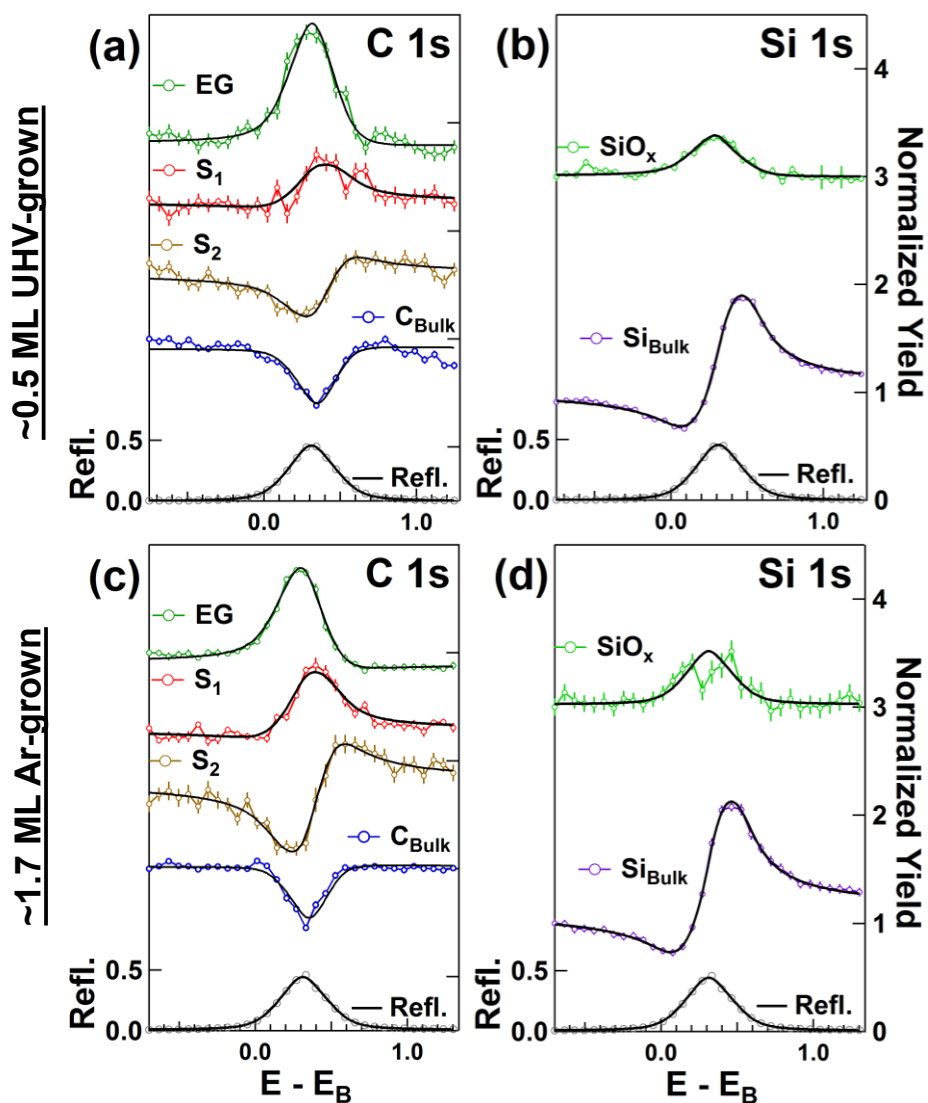


Figure 4.11: XSW results for ~0.5 ML UHV-grown and ~1.7 ML Ar-grown EG/SiC(0001). (a-b) are C 1s and Si 1s XSW yields for ~0.5 ML UHV-grown EG/SiC(0001), respectively. (c-d) are XSW yields for C 1s and S 1s ~1.7 ML Ar-grown EG/SiC(0001), respectively. Data colors are coded to match the XPS components identified in [Figure 4.10](#).

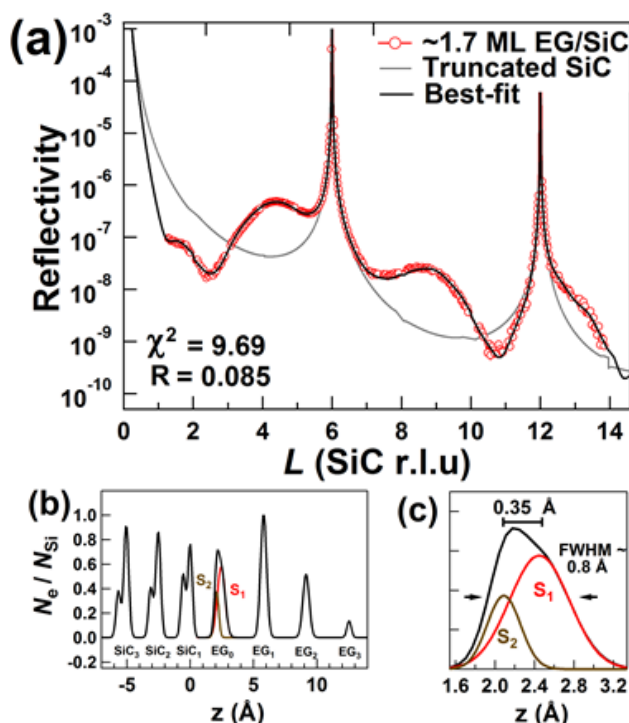


Figure 4.12: XRR analysis for the ~ 1.7 ML Ar-grown EG/SiC(0001). (a) XRR data is in red, best fits in black, and simulated bulk-truncated SiC in grey. Results are similar to those found for the UHV-grown EG/SiC, apart from a higher degree of graphene coverage. (b) The resolution-broadened chemically sensitive atomic density profile and (c) zoom-in of the interfacial region.

ultimately larger uncertainty values.

The ~ 1.7 ML Ar-grown sample serves as an excellent check for the XSW-XPS + XRR analysis discussed earlier. Qualitatively, the XSW values for S₁ and S₂ agree extremely well with those in the shown in [Sections 4.4](#) (within 1σ in both cases), indicating that the two interfacial layers have essentially identical structure. The XSW result for the EG layer is different due to the varying amount of EG coverage on the samples. The XRR data and XSW-constrained best-fit is shown in [Figure 4.12](#). The resultant structure is found to be similar to the of the ~ 1.3 ML UHV-grown sample, with $z_{EG_1} \sim 5.80$ Å, $z_{EG_2} \sim 9.15$ Å, and $z_{EG_2} \sim 12.55$ Å, giving a χ^2 value of 9.69 and R -factor of 0.085 for fits over the same q_z -range. The slightly poorer fit values may be a result of the SiO_x component, which is not accounted for in this XRR model. Relative layer coverages

were $c_{\text{EG}_1} \sim 1.00$ ML, $c_{\text{EG}_2} \sim 0.55$ ML, and $c_{\text{EG}_3} \sim 0.10$ ML, yielding a total coverage of ~ 1.7 ML. The back-calculation of the XSW values gives of $f_{\text{EG}} = 0.38$ and $P_{\text{EG}} = 0.44$, near the 1σ of the uncertainty limits reported in [Table 4.3](#). In all, we find that the analysis for the UHV 1.3 ML sample is consistent with the results for both the Ar-grown ~ 1.7 ML and UHV-grown ~ 0.5 ML samples. The generalization of our analysis to multiple samples with varying coverages produced by different groups bolsters the assertion that the interfacial structure is consistent independent of growth-mode, morphology, and EG coverage.

4.10: Conclusions

In summary, we have employed XSW-XPS with XRR to create a structural profile of the EG/SiC(0001) interface with unprecedented resolution and chemical sensitivity. This interfacial layer, the understanding of which is critical for the advancement of graphene-based electronics, is confirmed to consist of C only, and to possess two distinct chemical species located at 2.1 ± 0.1 and 2.40 ± 0.1 Å above the topmost layer Si of the SiC substrate. Our results support the strongly-interacting interfacial layer model while ruling out any significant presence of Si species at the interface or within the interface layer. As progress continues towards engineered EG/SiC nanostructures, both XSW and XRR will prove to be powerful tools for the precise structural determination of intercalated, doped or functionalized EG/SiC.

Chapter 5

Characterization of Hydrogen Intercalated EG/SiC(0001)

IN THE PREVIOUS Chapter, I presented the study of the interfacial structure of EG/SiC(0001) using a suite of structurally- and chemically-sensitive X-ray characterization techniques. However, understanding the pristine, unmodified, EG/SiC(0001) structure is only the first step as we learn to control and engineer the graphene surface and interface. To this end, it has been recently shown that modification of the physical and electronic structure of epitaxial graphene on SiC(0001) can be accomplished by the intercalation of various chemical species to the EG/SiC(0001) interface. Specifically, the intercalation of hydrogen to the EG/SiC(0001) interface has been suggested to induce the decoupling of the interfacial layer from the substrate and subsequently pacify the dangling Si bonds, leaving a so-called quasi-freestanding graphene sheet. In this Chapter we use X-ray scattering and photoemission spectroscopy to probe the

effects of hydrogen intercalation into the interface. We support this result with a qualitative discussion of XSW-XPS results.

5.1: Introduction

As discussed in [Chapter 2](#), the unique properties of graphene hold great potential for use in nanoelectronics, and one of the most promising routes to producing high-quality graphene is through the growth of epitaxial graphene (EG) on SiC. However, the growth of EG/SiC(0001) is always accompanied by the ubiquitous $(6\sqrt{3}\times 6\sqrt{3})R30^\circ$ interfacial layer. The presence of this interfacial layer is thought to be responsible for both the *n*-type doping of the pristine graphene overlayers and is correlated to the relatively modest electron mobility of EG/SiC(0001) ($\sim 1000 \text{ cm}^2\text{V}^{-1}\text{s}^{-1}$) [19, 24, 99, 102]. Recently, however, there has been progress in the modification of this interface in order to tune the properties of the overlying graphene sheet [33, 78, 116]. In particular, the intercalation of various atomic species, including H, Li, O, Na, F, Si, Ge and Au [34, 35, 118-122], has been demonstrated using a variety of intercalation methods (see Ref. [33] and references therein). Each of these intercalants demonstrates distinctive effects on the overlying electronic properties of the overlying graphene. For example, Au and Ge intercalants can imbue both *n*- and *p*-type doping, depending, presumably, on their concentration at the interface [34, 35]. It is clear from these studies that the interfacial structure post-intercalation is critical to the ultimate electronic behavior of the graphene itself.

Various characterization methods have been employed to investigate the nature of these intercalated structures. These include scanning-tunneling microscopy (STM) and atomic-force microscopy (AFM), low-energy electron diffraction and microscopy (LEED and LEEM), and core-level and angle-resolved photoelectron spectroscopy (CLPES and ARPES) [33]. However,

none of these techniques is well-suited to accessing the buried interfacial structure with atomic-scale resolution, and therefore the current interfacial models of intercalated EG/SiC(0001) structures are unrefined. Herein we investigate the atomic scale structure of the archetypal system, H-intercalated Si-terminated SiC (EG/H/SiC(0001)), using synchrotron-based high-resolution X-ray reflectivity (XRR) and X-ray photoelectron spectroscopy (XPS). This Chapter also includes supporting discussion of qualitative X-ray standing wave-enhanced XPS (XSW-XPS).

5.2: Experimental

Two semi-insulating, $8 \times 8 \text{ mm}^2$, nominally on-axis ($0^\circ \pm 0.5^\circ$) 6H-SiC(0001) substrates, originating from the same SiC wafer, were graphitized using a Aixtron/Epigress VP508 Hot-Wall CVD reactor. Samples were first etched in H_2 at $\sim 1500^\circ \text{C}$ in order to remove polishing

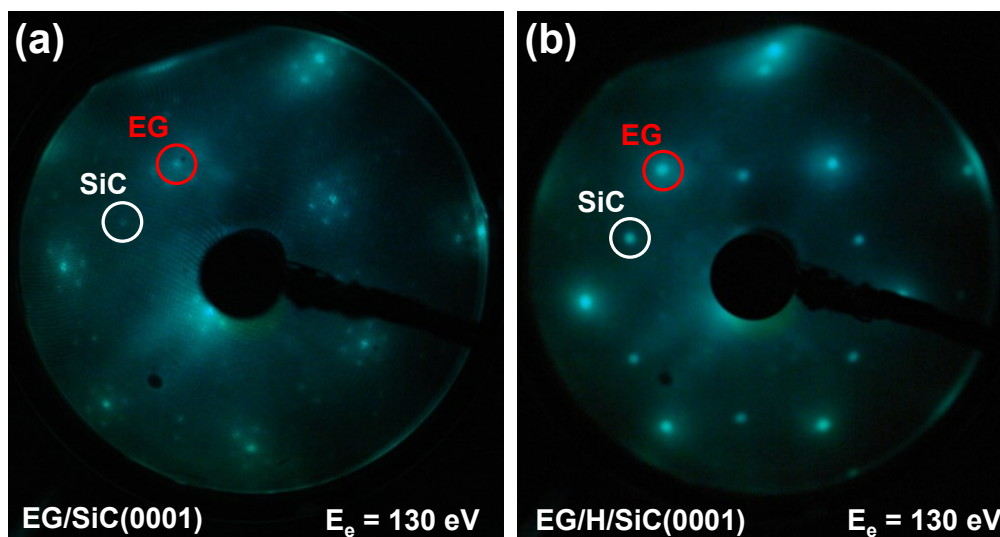


Figure 5.1: LEED patterns for pristine EG/SiC and H-intercalated EG/SiC at 130 eV. The EG and SiC LEED spots are indicated in red and white, respectively. (a) Before intercalation, the typical $(6\sqrt{3} \times 6\sqrt{3})R30^\circ$ superstructure spots are evident. (b) After intercalation the $(6\sqrt{3} \times 6\sqrt{3})R30^\circ$ spots are strongly suppressed and the EG spots increase in relative intensity.

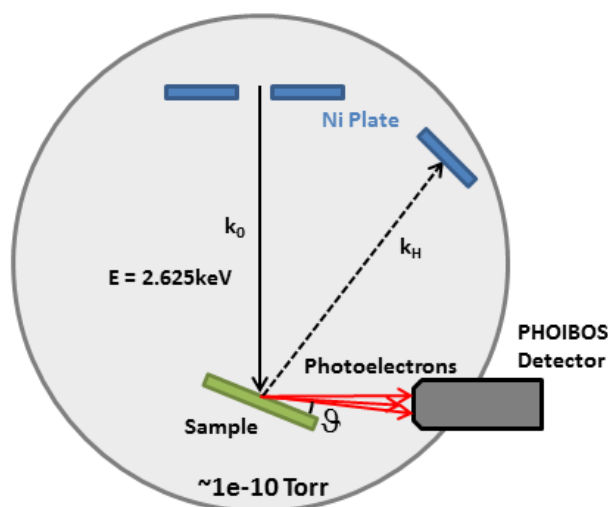


Figure 5.2: Top view of experimental geometry at ID32 at the ESRF. For survey scans the incident beam energy was tuned slightly away from the Bragg condition, but the experimental geometry was identical for both XPS and XPS-XSW measurements.

damage and then graphitized at $\sim 1650^\circ$ C in 100 mbar Ar atmosphere. Because the samples originated from the same wafer and were graphitized in identical conditions, the samples possess nominally identical graphene coverage and morphology. Following graphitization, the reactor was vented to air and one of the two sister samples was removed, while the second was annealed at 900° C in Pd-purified H_2 gas at atmospheric pressure. Samples were then loaded into UHV and degassed for 1 hr at 500° C for LEED measurements. The LEED patterns ([Figure 5.1](#)) show the suppression of $(6\sqrt{3} \times 6\sqrt{3})R30^\circ$ spots for the H-intercalated sample, in congruence with that observed in Ref. [30].

Samples were transferred in ambient for specular XRR measurements at beamline 6-ID-B at the Advanced Photon Source. Samples were mounted in a kapton He flow cell and measurements were performed using X-rays monochromated to an energy of $E_\gamma = 15.0$ keV, following the methods described in [Section 3.2](#). Both the specularly reflected signal and background were measured simultaneously using a CCD detector, as described in Ref. [164].

These Ar-grown samples possess superior surface morphology in comparison to the UHV-grown samples (see [Section 3.2.1](#)), and it was possible to collect and analyze data from $L \sim 1-16$ ($q_z \sim 0.4-6.6 \text{ \AA}^{-1}$) using data acquired only with the CCD.

XPS and XSW-XPS measurements were performed at ID32 at the European Synchrotron Radiation Facility (ESRF) [186]. There, samples were loaded into UHV and mildly degassed at 380° C . XSW-XPS measurements were performed at an X-ray energy of 2.625 keV for SiC(0006) in a π -scattering configuration with Bragg angle $\theta_B \sim 69^\circ$ and a photoemission angle of $\vartheta \sim 20^\circ$ with respect to the detector axis, as depicted in [Figure 5.2](#). Survey scans and higher resolution core-level spectra were acquired in the same geometry, but the incident beam energy was offset from the Bragg energy (E_B) by a few 10s of eV in order to avoid producing an X-ray standing wave, which would influence the relative intensities of the XPS yields. The X-rays were monochromated using a high-heat-load Si(111) monochromator (resolution $\Delta E/E = 1.4 \times 10^{-4}$) and collimated to a 0.4×0.3 (h \times v) mm² spot size at the sample surface (for more information see [Section 3.3.4](#)). The diffracted intensity was measured in the π -scattering geometry with a Ni current-collecting plate. C 1s and Si 1s photoelectrons were monitored using a PHOIBOS 225 analyzer mounted with detector axis perpendicular to the incoming X-ray polarization vector in order to minimize multipole contributions to the XSW yield [183].

5.3: X-ray Photoelectron Spectroscopy

Survey XPS spectra from both pristine and H-intercalated EG/SiC are shown in [Figure 5.3](#). Both samples exhibit the signals expected from an EG/SiC system, although both samples contain significant contaminant species. The pristine EG/SiC possess a large O 1s signal and a weak F 1s

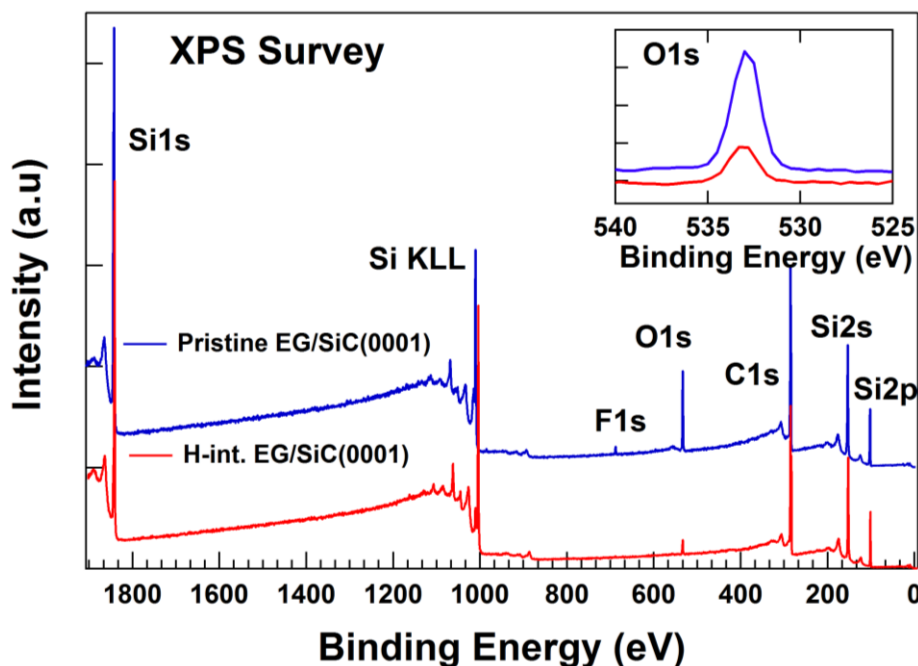


Figure 5.3: Survey spectra for both pristine and H-intercalated EG/SiC(0001). Typically Si and C lines are observable, but both pristine EG and H-intercalated EG contain contaminant O, and pristine EG contains contaminant F.

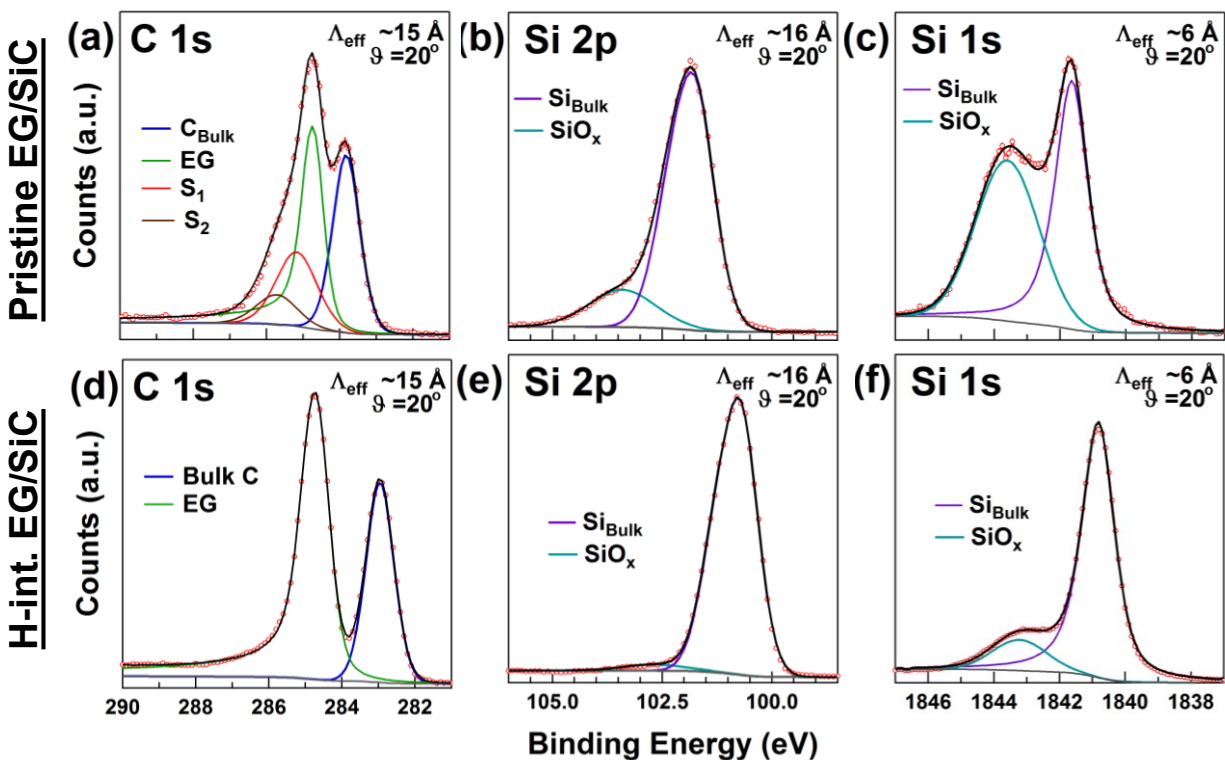


Figure 5.4: XPS spectra from pristine (a-c) and H-intercalated (d-f) EG/SiC. (a) The C 1s spectrum exhibits bulk C (blue), EG (green), and surface species S_1 (red) and S_2 (brown). (b-c) Si 2p and Si 1s spectra for EG/SiC show strong SiO_x signals associated with a surface oxide. (d) Upon intercalation, the S_1 and S_2 species are converted into EG, and the intensity at high-BE diminishes. (e-f) The EG/H/SiC Si 2p and 1s spectra are similar to (b) and (c), except for shifts due to band bending and lower oxide coverage.

signal. The F is presumably a contaminant from the polishing process that was not completely removed. The O 1s peak has a binding energy (BE) of 533 eV, which agrees well with what is expected for SiO₂ (533-534 eV). The EG/H/SiC spectrum, on the other hand, possesses much less oxygen and no discernible fluorine signal.

The nature of these signals is further elucidated with higher resolution C 1s, Si 1s, and Si 2p spectra, shown in [Figure 5.4](#). The pristine EG/SiC C 1s spectrum ([Figure 5.4\(a\)](#)) shows the characteristic EG/SiC line profile, exhibiting peaks corresponding to C_{Bulk}, EG, and the two core-shifted interfacial species, S₁, and S₂. Upon intercalation ([Figure 5.4\(c\)](#)), the high-BE signals associated with the S₁ and S₂ species are eliminated, and the EG peak increases in relative intensity as compared to the bulk C signal. The ratio of the integrated areas of the surface species (S₁ + S₂ + EG) to that of the bulk C peak is ~3:1 in both cases, signifying identical coverage of carbon surface species before and after the intercalation process. For the pristine EG/SiC, the total graphene coverage can be estimated by comparing the integrated area of the two surface components, S₁ and S₂, to that of the EG peak, and reveal a total EG coverage of ~1.8 ML.

Both pristine and intercalated EG/SiC Si 2p spectra ([Figures 5.4\(b\) and \(e\)](#)) contain a high-BE core-shifted component in addition to the Si_{Bulk} signal (plotted fits are summations of components of the Si 2p spin orbit doublet). This high-BE signal is typically associated with a SiO₂ oxide species on SiC, and is often observed to be accompanied by a Si in a suboxide C₃-Si-O binding configuration [213, 214]. The magnitude of the shift from the bulk Si 1s component is slightly different for the pristine and intercalated samples, being +2.0 eV for EG/SiC and +1.7 eV for EG/H/SiC, but the most drastic difference is the intensity of the peak. Because the measurements for all spectra were taken in identical geometries ([Figure 5.2](#)), this indicates that

EG/SiC possesses a greater amount of Si oxide species within the XPS probing depth. This is supported by the relative strengths of the O 1s signal as seen in the survey spectra ([Figure 5.3](#)). Additionally, through investigation of the photoelectrons originating from the Si 1s core-level, which have a smaller kinetic energy and therefore shorter inelastic mean free path (estimated using the TPP-2M equation [215, 216]), it is obvious that the SiO_x signal increases relative to the Si_{Bulk} as the probing depth decreases for both pristine and intercalated EG/SiC. This supports the assessment that the SiO_x is positioned near or at the surface of the SiC crystal.

Upon intercalation, the formation of H-Si bonds causes a respective band-bending to occur [30, 99], which shifts the measured binding energies of the bulk and oxide Si and C components in the spectra by ~1 eV. The shift in the EG components upon H-intercalation has recently been attributed to spontaneous polarization from the substrate, which is dependent on the polytype of SiC [99]. While we do not observe a measurable shift in the position of the EG peak, our graphene is thicker and our XPS resolution poorer than in the study by Riedl *et al.* [30], and therefore there exist uncertainties in the fitted BE for the pristine EG/SiC sample. We cannot, therefore, rule out the existence of a shift of a few tenths of an eV after intercalation. The difference in the absolute positions of the oxide Si peaks with respect to their bulk components between the EG/SiC and EG/H/SiC samples ($BE_{\text{BulkSi}}+2.0$ eV and $BE_{\text{BulkSi}}+1.7$ eV, respectively, for Si 1s) may be caused by the difference in near-surface space charge density between the two samples due to the differences in Fermi level pinning at the interface [99].

5.4: X-ray Reflectivity

XRR data and best-fits are shown in [Figure 5.5\(a\)](#). The pristine EG/SiC sample exhibits XRR curves that are qualitatively similar to those observed in [Section 4.7](#). The H-intercalated EG/SiC,

however, shows orders of magnitude differences in scattered intensity at various points along the rod. Most notable of these are at $L \sim 5.5$ and $L \sim 12.5$, where the EG/H/SiC data show deep minima where destructive interference occurs, suggesting the existence of a highly modified interfacial structure.

To extract the electron density profiles corresponding to these curves, it is necessary to construct a model and fit the data to the reflectivity equation derived in [Section 3.2.1](#) (Eqs. 3.19-3.21). In the case of the pristine EG/SiC, we base our model on the results from [Chapter 4](#), allowing for a 2-component interfacial layer but allowing for 5 EG layers due to increased EG thickness. However, this model yielded very poor fits in the high- and low- q_z regions, yielding χ^2 values of greater than 80. It is therefore necessary to reconsider our model. The difference

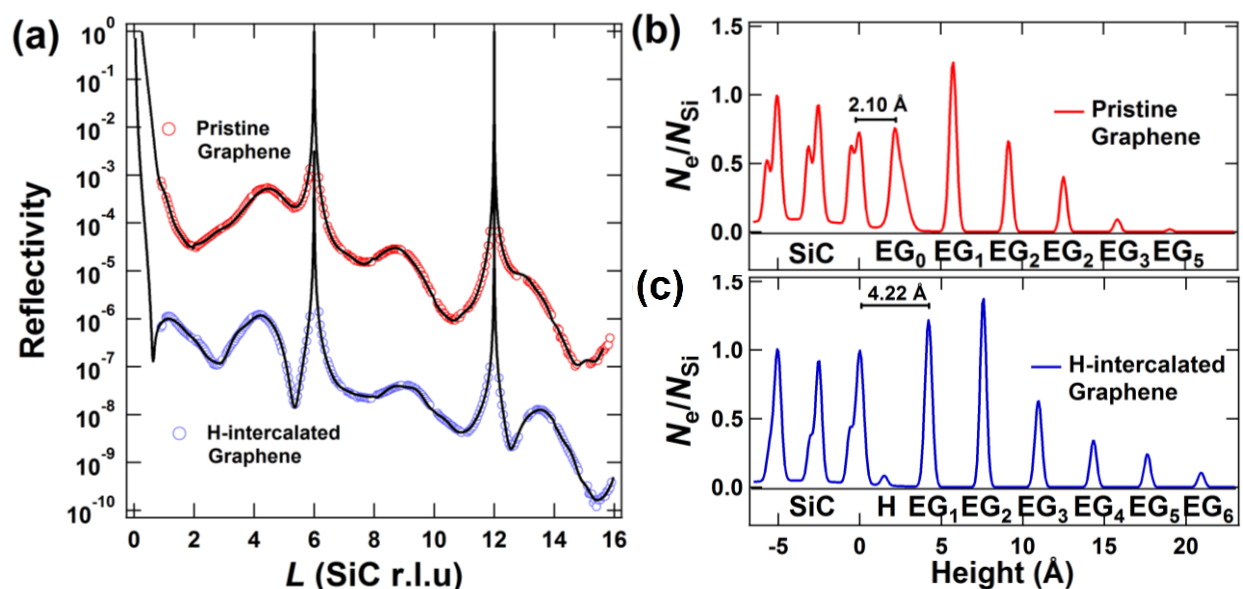


Figure 5.5: XRR data and best fits, together with their corresponding electron-density profiles, for pristine and H-intercalated EG/SiC. (a) Pristine EG/SiC (red) and H-intercalated EG/SiC (blue), data is plotted with best-fit curves corresponding to values of $\chi^2 = 5.27$ and $\chi^2 = 8.35$, respectively. Qualitatively, the two curves show sharp contrast, especially in the regions near $L \sim 5.5$ and 12.5 , indicating a distinct change in the interfacial structure after intercalation. (b) The electron density profile for pristine EG/SiC corresponding to the fit in (a). A broad interfacial layer consisting of two displaced C distributions is located at 2.10 Å above the terminal Si. (c) The H-intercalated EG/SiC electron density shows that the interfacial layer in (b) has been converted to a layer with graphene-like density positioned 4.22 Å above the SiC surface. Layer coverage and EG d -spacing are conserved.

between these samples and those measured in [Chapter 4](#) is the dominance of the Si oxide in the Si 1s spectrum. While this oxide signal was also present during the analysis of the Ar-grown samples in [Section 4.9](#), the species was found to possess no order with respect to the substrate. Therefore, to model the presence of a disordered oxide species within the substrate, a broad distribution of electron density was added to the topmost SiC bilayers of the SiC unit cell. After this density was added the fits improved greatly, reducing the best-fit χ^2 value to 5.27 for pristine EG/SiC, which is over an order of magnitude improvement over the oxide-free model. The electron density profile in [Figure 5.5\(b\)](#) is extracted from best-fit EG/SiC data in [Figure 5.5\(a\)](#). The interface layer was found to be qualitatively identical to that found in [Section 4.7](#), and the total EG coverage was found to be ~ 1.85 ML, in excellent agreement with the XPS estimation of 1.8 ML. The coverage ratios of the overlayers were $\text{EG}_1:\text{EG}_2:\text{EG}_3:\text{EG}_4:\text{EG}_5 = 1:0.48:0.29:0.06:0.01$ ML.

The H-intercalated EG/SiC followed the same model as the pristine EG/SiC, but a ML of H was added at the nominal Si-H bond-distance of 1.5 Å. It should be noted that this layer was not necessary in order to achieve good fits due to its low electron density, but its inclusion did improve the best-fit χ^2 value by ~ 1 . The best fit is shown in [Figure 5.5\(a\)](#), and the associated electron density profile is shown in [Figure 5.5\(c\)](#). The total coverage for the EG/H/SiC was found to be 3.0 ML, approximately 1 ML more graphene than that found for EG/SiC, indicating that the interfacial layer is indeed converted into a EG layer. The best-fit solution also finds that the newly-formed EG_1 is displaced from the terminal Si in the SiC by 4.22 Å, or similarly, from the nominal H monolayer, by 2.72 Å. χ^2 map of the absolute position of the newly-formed EG_1 layer above the top-most Si ([Figure 5.6](#)) yielded 1σ , 2σ , and 3σ confidence levels for this result

of $2.72^{+0.04}_{-0.06}$, $2.72^{+0.05}_{-0.07}$, and $2.72^{+0.06}_{-0.08}$ Å. These values compare well to results DFT results reported in Ref. [217], which found a displacement of 2.59 Å displacement of the EG film from the H layer. In addition, the average d -spacing between the graphene sheets for the H-intercalated EG was 3.34 Å, agreeing nearly precisely with the result from pristine EG/SiC (3.33 Å), and indicating that the intercalation process has essentially no effect on the structure of the EG film itself, apart from decoupling and displacement.

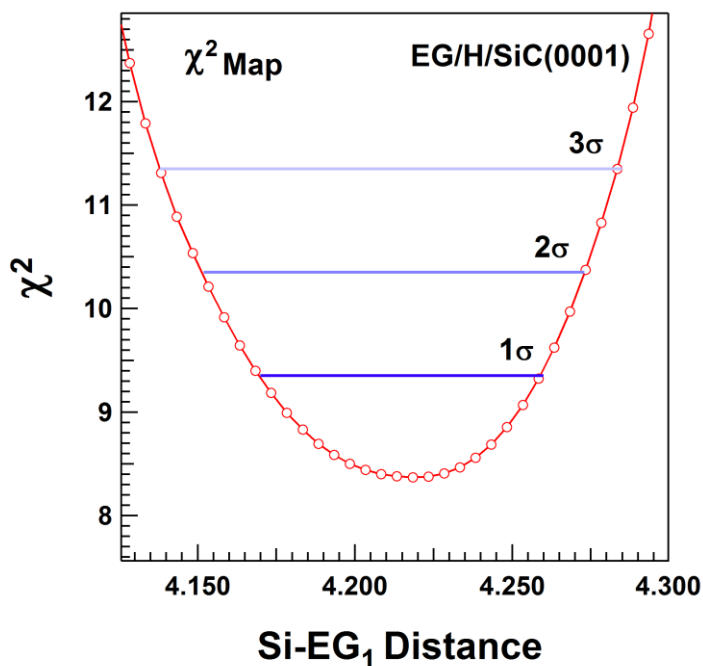


Figure 5.6: Best-fit χ^2 values as a function of Si-EG₁ distance for H-intercalated EG/SiC. χ^2 values are shown in red and 1 σ , 2 σ , and 3 σ confidence levels are shown in progressively fainter shades of blue. With our fitting model, we report the displacement of the EG film to be $2.72^{+0.06}_{-0.08}$ Å with 99.7% confidence (3 σ).

5.5: X-ray Standing Wave

To further investigate the structural changes that take place upon intercalation, a qualitative discussion of XSW data is presented. We note that due to experimental limitations at ID32, it was necessary to perform experiments in a π -scattering geometry with a Bragg angle $\theta_B \sim 69^\circ$

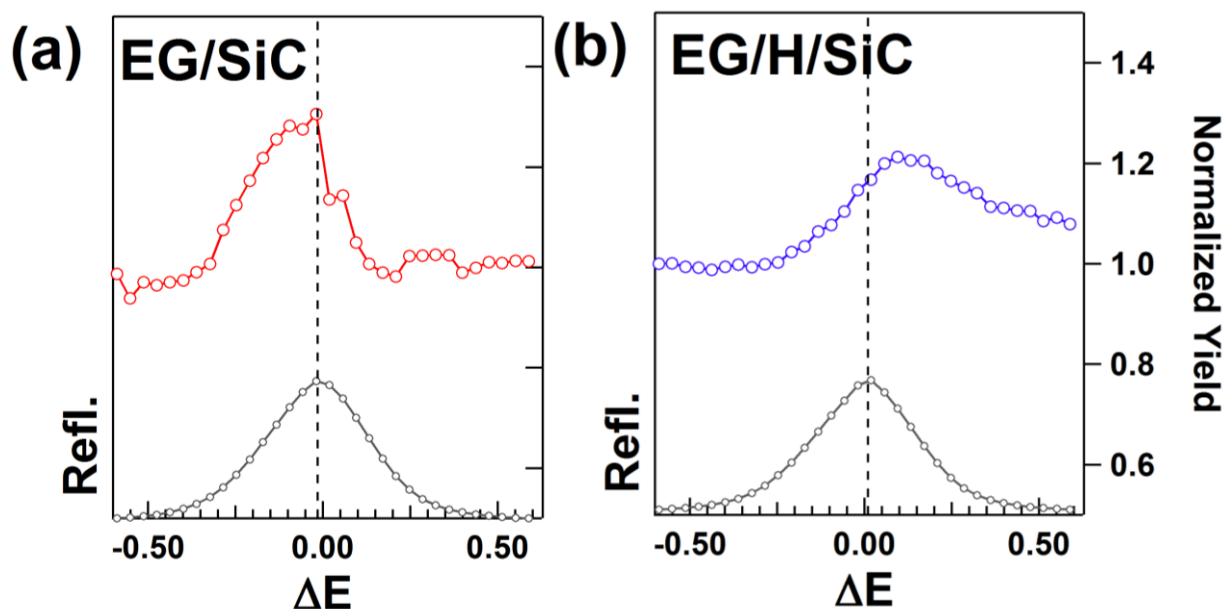


Figure 5.7: XPS-selected XSW yield curves for EG for both (a) pristine and (b) H-intercalated EG/SiC. Reflectivity curves are shown in grey for both samples. EG yield curves for pristine EG/SiC (red) and the H-intercalated EG/SiC (blue) display distinctive XSW modulations that indicate a $\sim\pi$ phase shift in the average position of the EG layers between the two samples.

([Figure 5.2](#)). In the π -scattering geometry the XSW yield becomes sensitive to polarization effects, the angular distribution of the photoelectron yield excited by the coherently coupled incoming and outgoing X-ray planewaves [218] and non-dipole contributions [183, 184]. These factors complicate experimental analysis, and, at this time, the SWAM analysis software ([Appendix A](#)) is not capable of accurate analysis.

Regardless, some qualitative information can be obtained simply by comparing the EG C 1s yield from the pristine and intercalated EG/SiC, as shown in [Figure 5.7](#). At first glance, the difference between the EG coherent positions for the two samples is clear. For the EG/SiC sample the yield maximum appears on the low- E_γ side of the rocking curve, while the EG/H/SiC yield maximum appears on the high- E_γ side. This is verified by XSW by using XRR best-fit

results to construct the geometric structure factor and calculating the coherent position for each sample. The geometrical structure factor for the EG species is defined from [Eq. 3.50](#),

$$S_{EG} = \frac{1}{\sum_{n=1}^N c_n} \sum_{n=1}^N c_n e^{i2\pi \frac{z_n}{d_H}} e^{-2\pi^2 \frac{\sigma_n^2}{d_H^2}}. \quad (5.1)$$

where c_n is the occupancy of the n^{th} EG layer, z_n is the layer position, σ_n is the Gaussian distribution width, and d_H is the d -spacing for the H reflection. These values can all be extracted from XRR data and used to calculate the coherent position,

$$P_s^H = \text{Arg}(S_s^H)/2\pi. \quad (5.2)$$

Using this method, the EG/SiC yield a coherent position of $P_{Pris.} \sim 0.28$, similar to that observed in [Section 4.7](#). Calculations for the EG/H/SiC coherent position give $P_{Hint} \sim 0.83$, placing the two species nearly precisely out-of-phase, as observed in the XSW yield curves. This, at the very least, qualitatively supports the XRR model-fitting results. Additional analysis with more advanced tools will be necessary for a full interpretation of the XSW data.

5.6: Discussion/Conclusions

In this Chapter we used XRR, guided by XPS, to extract the electron density profiles for two EG/SiC samples with identical EG coverage, but one of which was exposed to an H-intercalation procedure. We find, in agreement with previous reports [30], that the interfacial layer is decoupled from the SiC substrate, and with our measurement we are able to precisely characterize the structural consequence of the decoupling. Namely, after intercalation, the epitaxial graphene coverage is conserved and the EG d -spacing remains unchanged. We report the displacement of the freshly-formed EG layer above the SiC surface to $4.22_{-0.08}^{+0.06}$ Å, with

99.7% confidence. Similarly, the displacement above a H monolayer (fixed above the SiC at 1.5 Å) is $2.72_{-0.08}^{+0.06}$ Å, in close agreement with calculations [217]. However, the influence of a large concentration of near-surface Si oxide species, identified by XPS, raises some uncertainty in the analysis. For future work, it will be necessary eliminate the oxide contamination in samples in order to facilitate a more straight-forward data interpretation. Regardless, this Chapter presents an clear picture of the structural consequences of H-intercalation to the EG/SiC(0001) interface. Considering the influence that these new interfacial structures have on the overlaying graphene sheet, it will be critical to understand the fundamental structural consequences of intercalation if we hope to efficiently engineer the EG/SiC interface. Similar studies on analogous systems should prove powerful in the ultimate understanding of these interesting structures.

Chapter 6

Self-assembled Organic Monolayer Functionalization of EG/SiC(0001)

THIS CHAPTER describes the use of X-ray techniques to structurally characterize EG/SiC(0001) functionalized with perylene-3,4,9,10-tetracarboxylic dianhydride (PTCDA). These organic molecules can be used as seeding layers for the subsequent growth of films and nanostructures with atomic layer deposition (ALD). The results presented in this Chapter provide insight into the nature of the interaction between the organic molecules and the graphene substrate, as well as conveys information about the structural consequences of ALD thin film growth. The work in this Chapter has been published in two separate, but related, publications as J.D. Emery *et al.*, *Surface Science*, **605**, 1685-1693 (2011), and J.M.P. Alaboson *et al.*, *ACS Nano*, **5** (6), 5223-5232 (2011).

6.1: PTCDA Monolayers on Epitaxial Graphene

6.1.1: Introduction

The chemical functionalization of graphene has recently emerged as an important area in graphene research because the integration of graphene in devices and applications requires interfacing graphene with other materials while controlling its band gap and doping [219, 220]. Numerous covalent and non-covalent functionalization schemes have been demonstrated on graphene surfaces [61, 219-222]. Recently, interest in self-assembled organic monolayers of PTCDA on graphene has been explored in order to introduce reactive seeding-sites for improved ALD of dielectric films [36, 144, 190, 223-226]. PTCDA monolayers exhibit highly ordered growth on a variety of substrates including various metals and reactive surfaces [227-232], and have been extensively studied with a number of techniques including scanning tunneling microscopy (STM) [36, 228, 230, 233], X-ray diffraction (XRD) [233-235], and X-ray standing waves (XSW) [236-239]. In particular, STM probes the lateral structure of PTCDA layers with molecular resolution, while X-ray techniques resolve the vertical structure and allow for characterization of the substrate under the molecular layers. Previous ultra-high vacuum (UHV) STM work has shown that PTCDA forms a well-ordered monolayer on epitaxial graphene (EG) on SiC(0001) that is very stable and electronically decoupled from the graphene [36].

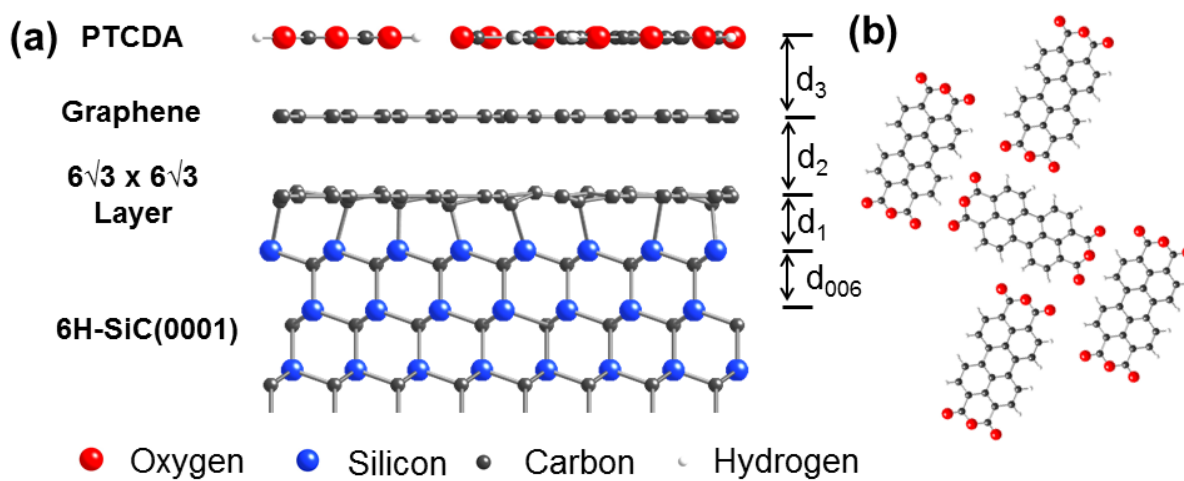


Figure 6.1: (a) An idealized depiction of a 1 ML PTCDA/1 ML EG/6H-SiC(0001) heterostructure with oxygen, silicon, carbon, and hydrogen atoms shown in red, blue, gray, and white, respectively. The crystallographic view corresponds to the $[10\bar{1}0]$ projection of 6H-SiC. The interfacial layer is represented by the graphene-like layer which interacts with the Si-terminated SiC substrate (see [Chapter 4](#)). Nominally, $d_{006} = 2.52$ Å, $d_1 = 2.30$ Å, $d_2 = 3.35$ Å, and $d_3 = 3.22$ Å. (b) A top-view schematic of the lateral organization of the PTCDA molecules in a herringbone arrangement.

In this Chapter, we employ a combination of UHV STM and high-resolution X-ray reflectivity (XRR) to characterize PTCDA monolayers on epitaxial graphene on SiC(0001). We derive an atomic-scale structural description of functionalized epitaxial graphene formed on 6H-SiC(0001) substrates through the growth of nominally 1 or 2 monolayer (ML) thick PTCDA thin films, a model of which is shown in [Figure 6.1](#). We use high-resolution XRR [167, 206] in conjunction with room-temperature UHV STM to obtain the vertical and lateral structure of PTCDA layers on epitaxial graphene. We use a combination of Fienup-based phase-retrieval [240, 241] and model-based least-squares analyses to derive structures describing the EG/SiC(---1) interface and the PTCDA overlayers. The XRR and STM data show that PTCDA possesses long-range molecular ordering within the surface plane, indicating π - π^* interactions between the PTCDA molecules and graphene surface. While previous XRR studies have been conducted on

the basic structure of epitaxial graphene and the interface between the SiC lattice and graphene overlayers [21, 242], here we use XRR to resolve the interfacial structure of the PTCDA layers on epitaxial graphene on the 6H-SiC(0001) surface. The flexibility of surface X-ray scattering allows it to be applied non-destructively in a variety of sample environments to investigate structures of buried interfaces and/or exposed surfaces.

6.1.2: Experimental

6.1.2.1: Sample Preparation

Growth of epitaxial graphene and PTCDA monolayers were performed in a home-built UHV system with base pressures of 5×10^{-11} Torr and separate chambers for sample preparation and STM imaging. The sample preparation procedures are similar to those reported previously [36, 243], and in [Section 4.3](#). The samples were prepared using nitrogen-doped (*n*-type) 6H-SiC(0001) wafers (Cree, Inc.). The wafers were diced into 9×6 mm² samples and cleaned by ultrasonication in acetone and isopropanol. After introduction into the UHV chamber, the samples were outgassed at 600°C for 8-12 h. The samples were then cleaned by annealing at 1100°C to remove the native oxide, and then graphitized by repeated heating to 1350°C to produce a mixture of single-layer and bilayer graphene, as verified by STM imaging as shown in [Figure 6.2\(a\)](#). The PTCDA powder (97% purity, Sigma Aldrich) was loaded into an alumina-coated W crucible and thoroughly outgassed in UHV before use. The PTCDA was thermally evaporated onto the room temperature epitaxial graphene substrate, with the coverage level calibrated by subsequent STM imaging. Typical deposition rates were 0.05 ML/s. PTCDA coverage on the graphene samples was controlled by the duration of exposure to the evaporated

PTCDA flux. Three samples were studied: a bare graphene sample and two PTCDA-functionalized samples with nominal coverages of 1 and 2 ML of PTCDA ([Figure 6.2\(d\)](#)). Despite results indicating less than full ML coverages, for simplicity these three samples are referred to in the text as the “0 ML PTCDA”, “1 ML PTCDA”, and “2 ML PTCDA” samples.

6.1.2.2: Scanning Tunneling Microscopy

Scanning tunneling microscopy characterization of the bare and PTCDA-functionalized graphene samples was performed in the same home-built UHV system that was used for sample preparation [244]. The system is equipped with a scanning tunneling microscope in a separate UHV chamber so that the samples could be imaged immediately after preparation without breaking vacuum. STM imaging was conducted at room temperature in constant current mode using electrochemically etched W probes. The imaging bias voltage was applied to the sample with respect to the STM tip that was grounded through a current preamplifier. Additionally, the robustness of the graphene structure was verified to be unaltered by PTCDA deposition by heating the substrate to desorb the PTCDA and re-imaging the graphene. A more thorough description of room-temperature STM and Scanning Tunneling Spectroscopy (STS) of this system is provided by Wang *et al.* in Refs. [36] and [124].

6.1.2.3: X-ray Reflectivity

Specular XRR was measured at beamline 33-BM-C of the X-ray Operation and Research Division, at the Advanced Photon Source (APS) of Argonne National Laboratory. The incident beam size was 0.1 mm (vertical) by 2.0 mm (horizontal). The beam was vertically focused by Pd-coated mirrors and conditioned by a double-crystal Si(111) monochromator with horizontal sagittal focusing to produce $E_\gamma = 17.00$ keV X-rays with an incident flux of $\sim 10^{10}$ photons/sec.

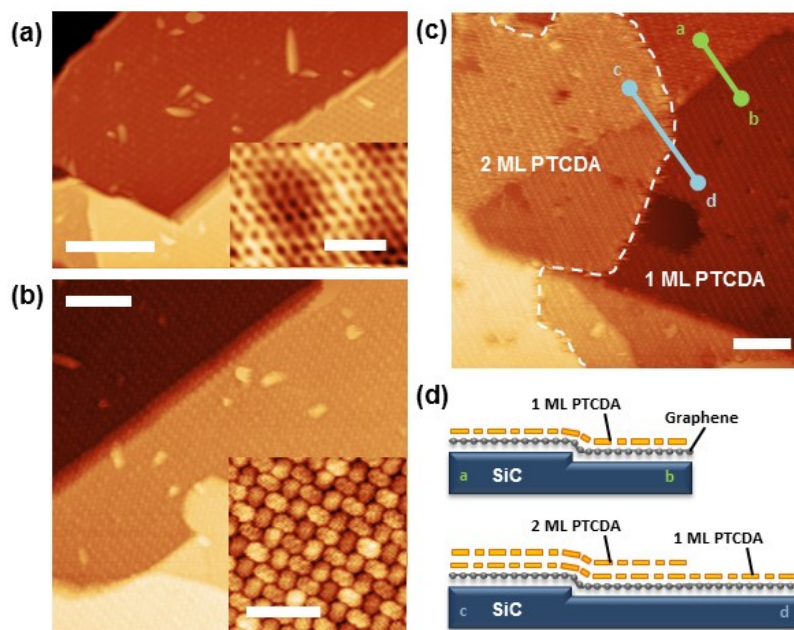


Figure 6.2: UHV STM images of the sample surfaces. (a) Clean epitaxial graphene (Sample bias -2.1 V, tunneling current 50 pA, scale bar 20 nm). Inset: Atomically resolved image showing the honeycomb lattice of graphene (-0.4 V, 50 pA, 1 nm). (b) Single monolayer coverage of PTCDA on epitaxial graphene (-1.9 V, 22 pA, 10 nm). Inset: Molecularly resolved image showing that the PTCDA monolayer has a herringbone arrangement (-2.0 V, 70 pA, 4 nm). (c) At ~ 1.5 ML PTCDA coverage, the sample concurrently possesses regions with 1 ML and 2 ML PTCDA (-1.9 V, 22 pA, 10 nm). The region to the left of the white dashed line has two layers of PTCDA, while the region to the right has one layer. (d) Schematic depth profiles of the two lines, a-b and c-d, indicated in (c). The SiC step edge in both profiles is the same, but is covered by one layer of PTCDA in line a-b and two layers in line c-d.

All samples were contained within a small beryllium dome vacuum chamber mounted directly onto the diffractometer and maintained at $\sim 10^{-3}$ Torr. Reflectivity data, which is shown in [Figure 6.3](#), is presented as a function of q_z , but is also plotted as a function of the 6H-SiC reciprocal lattice unit (SiC *r.l.u.*), $L = \frac{q_z c_{SiC}}{2\pi}$. Here, $c_{SiC} = 15.120$ Å is the *c*-axis lattice constant for the 6H-SiC hexagonal unit cell [174]. The data points in [Figure 6.3\(a\)](#) near the sharp quasiforbidden SiC(000*L*) Bragg peaks [174] $L = n$ (except $L = 6n$), where n is an integer, were removed for simplification of the reflectivity analysis.

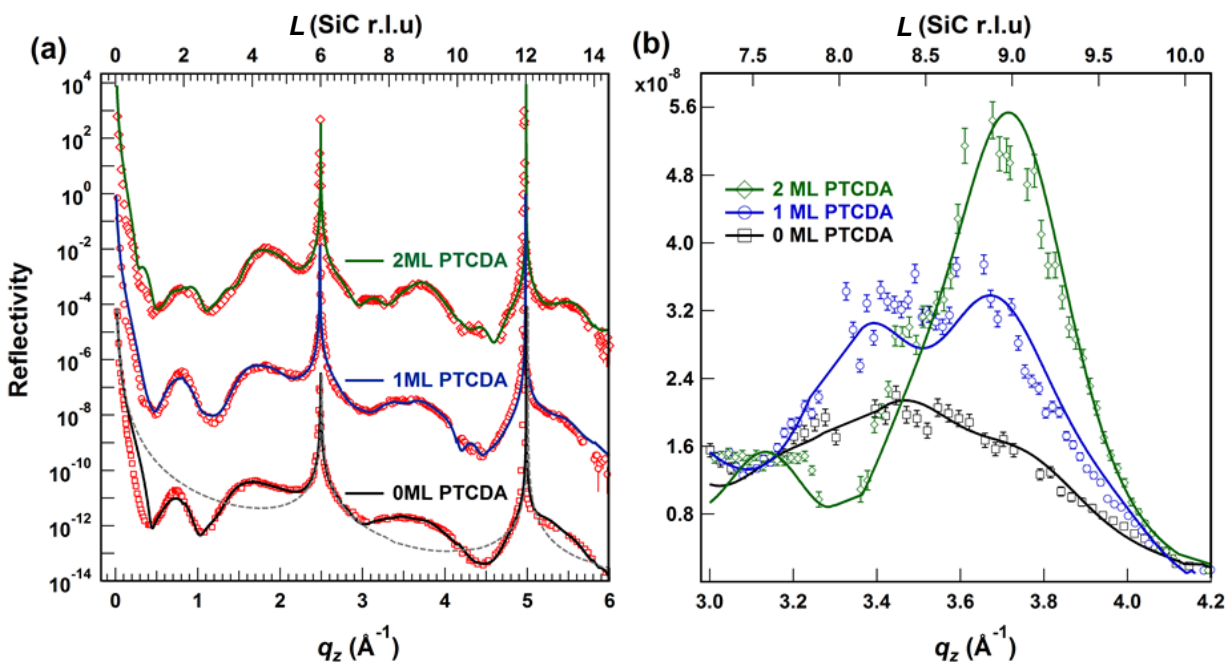


Figure 6.3: X-ray reflectivity (XRR) data for 0 ML, 1 ML, and 2 ML PTCDA coverage. (a) XRR data and fits from 0 ML PTCDA (red squares and black line), 1 ML PTCDA (red circles and blue line) and 2 ML PTCDA (red diamonds and green line). For clarity, the reflectivity signals are vertically scaled by 10^{-4} , 1, and 10^4 , for the 0, 1 and 2 ML PTCDA samples, respectively. The calculated reflectivity for an ideally terminated 6H-SiC(0001) surface is shown for comparison as a gray dashed line atop the 0 ML data (scaled by 10^{-4}). (b) The same XRR data and fits as shown in (a) but on a linear intensity scale and over a limited q_z -range that includes the 2nd-order diffraction peak for the PTCDA/graphene thin film. Here, the data are have marker symbols matching those in (a), but are colored to correspond to the matching fits.

The X-ray scattered intensity pattern in the vicinity of the specular condition was collected either by a 2D area detector or by using “rocking curves” with a point detector (see [Section 3.2](#) for further details). The majority of data ($q_z = 1.0 - 6.0 \text{ \AA}^{-1}$) were acquired using a charge-coupled device (CCD) 2D detector. This is the preferred approach because the CCD samples the rocking curve at each value in q_z with using the entire area of the detector, increasing the speed of data collection by 30 to 40 times when compared to the conventional rocking-curve method [164]. However, low-angle reflectivity data ($q_z = 0 - 1.25 \text{ \AA}^{-1}$) were acquired with a scintillation detector by performing a “rocking-curve” measurement because the lateral broadening of the specular rod due to the finite surface domain size made it difficult to fully

integrate the reflectivity signal when the low- q_z scattering signal extended beyond the CCD field of view (see [Section 3.2](#)). Broader sweeps through reciprocal space were possible with the scintillation point detector setup. CCD and point-detector data were matched to a shared range $q_z = 1.00 - 1.25 \text{ \AA}^{-1}$ and combined to produce a single reflectivity curve.

The XRR signal were extracted from the CCD images following the procedure outlined in Ref. [164]. Specular and diffuse scattered intensity in the low- q_z range were extracted following the method described by Rauscher *et al.* for conformally rough surfaces [245]. Uncertainties for all data points are determined from counting statistics [164]. Both bare and functionalized graphene surfaces were re-measured after X-ray exposure to ensure that no damage occurred as a result of X-ray radiation over the time scales necessary for data acquisition.

As described in [Section 3.2](#), specular X-ray reflectivity is defined as the ratio of the intensity of the scattered to incident X-ray intensity when the reflected angle is equal to the incident angle,

$$R(q_z) = \left(\frac{4\pi r_e}{q_z A_{u.c.}} \right)^2 |F_{u.c.} F_{CTR} + F_{Int} + F_{OL}|^2. \quad (6.1)$$

The structure factors themselves have been separated into those derived from the bulk unit cell ($F_{u.c.}$), the crystal truncation rod (CTR) form factor ($F_{CTR} = (1 - e^{iq_z c})^{-1}$), the interfacial structure (F_{Int}), and the overlayer (F_{OL}) contributions [206]. Here, the F_{Int} term includes near-surface SiC bilayers which have relaxed due to graphene formation, and the F_{OL} term includes contributions from the reconstructed interfacial layer, the graphene, and the PTCDA. The

structure factor for each layer is expressed as the sum over all atomic sites within a layer, as derived in [Section 3.2.1](#),

$$F(q_z) = \sum_m c_m f_m^a(q_z) e^{iq_z z_m} e^{-\frac{1}{2}(q_z u_m)^2}. \quad (6.2)$$

From these parameters, the electron density profile along the SiC[0001] direction is constructed. All features in the electron density profiles have been broadened by the experimental resolution of the data $\pi/q_{max} = 0.52 \text{ \AA}$ [246].

6.1.2.4: Fienup-based Analysis

It is well-known that the X-ray surface scattering is a powerful method to resolve surface structures. However, it is often limited by the loss of phase information that occurs during the measurement of scattered X-rays. In the study of thin films and interfaces, the phase problem makes it challenging to directly and unambiguously relate measured specular reflectivity to an electron density profile. Recently, the use of error-correction algorithms have been expanded from applications in optics [241, 247] to 1D imaging of interfacial structures. In this case, the application of the Fienup algorithm to X-ray imaging, described in depth elsewhere [240], generates an electron density profile when supplied with only the known SiC crystal and a generic few-layer graphene film structure factors. This algorithm imposes consistency between the measured diffracted intensity and the unmeasured phases by iteratively correcting the phase of the interfacial structure factor with respect to the “known” graphene film and the substrate reference structures (F_{Ref}).

A schematic of the Fienup algorithm as is shown in [Figure 6.4](#). The algorithm functions by iteratively performing Fourier and inverse Fourier transforms on a provisional interfacial

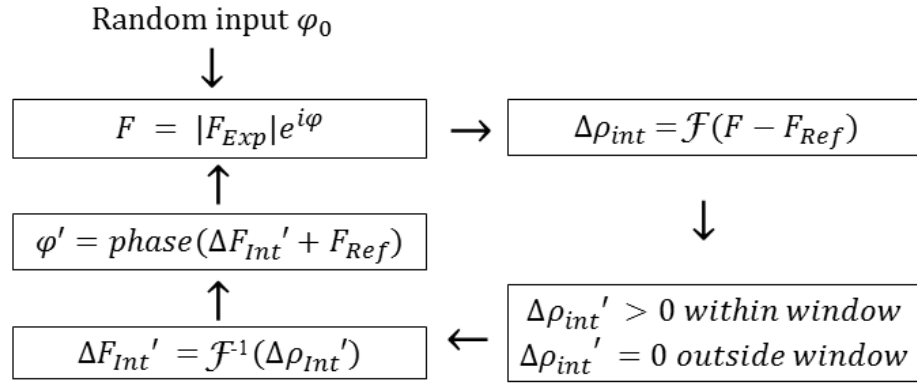


Figure 6.4: Schematic of the iterative Fienup algorithm. F_{Exp} , ΔF_{Int} , and F_{Ref} are the experimental, interfacial, and reference structure factors, respectively, $\Delta\rho_{Int}$ is the interfacial electron density, and φ is the phase. The algorithm iterates between real and reciprocal space until a stable solution for the phase is reached. Adapted from Ref. [248].

structure factor, $\Delta F_{Int}' = F_{Tot} - F_{Ref}$, and provisional interfacial electron density, $\Delta\rho_{Int}' = \rho_{Tot} - \rho_{Ref}$, respectively. This analysis requires a known reference structure (here taken to be the SiC substrate and the graphene film), as well as a real-space support constraint which defines the interfacial region. Initially, a random phase, φ_0 , F_{Ref} (with known φ), and the magnitude of the total experimental structure factor $|F_{Exp}|$ is transformed to obtain the initial interfacial density, $\Delta\rho_{Int}$. Then the real-space constraints are then applied, which force $\Delta\rho_{Int}$ to be positive within the constraint window, and zero outside, giving $\Delta\rho_{Int}'$. An inverse Fourier transform of $\Delta\rho_{Int}'$ gives $\Delta F_{Int}'$, for which the total phase for that iteration φ' is calculated. The new phase φ' is then used in the next iteration, and the algorithm is iterated until a stable solution is found.

Fienup-based analysis was performed solely on the bare graphene sample. In this case, an 8.5 Å wide real-space window corresponding to the interfacial region of interest was defined. This range covers the top 3 SiC bilayers and extends to the 1st EG layer. No structural assumptions were made in the region between the top-most Si layer and the 1st EG layer. The EG film was assumed to consist of 3 layers of decreasing occupancy, and with interlayer distances set to the nominal graphite d -spacing, $d_G \sim 3.35\text{Å}$, as obtained from preliminary model-based fits

of the data. Note that the absolute positions of the graphene layers above the terminal Si layer are unknown, so in order to ensure that the assumed height of the graphene overlayer does not dictate the interface structure, a sequence of Fienup routines were run, each with the graphene film layer located at varying heights above the sample. To encompass a range that may yield reasonable structures, analyses were performed at 0.25 Å interval steps over a range of $z = 1$ to 8 Å, where z is the height of the first graphene layer above the terminal Si layer.

In this work, the Fienup algorithm is used only to derive an initial structure as a foundation for later model-based analysis. While this analysis is employed with the intention to help eliminate subjectivities that may arise during the modeling of the interface, ultimately a full model-based fitting approach is necessary to achieve the most accurate results.

6.1.2.5: Model-based Analysis

Guided by the results of Fienup-based analysis, least-squares fitting was performed by allowing structural parameters to vary while fitting models to the data. Free parameters for the analysis include bilayer displacement of the top three ($j = 1, 2, 3$) SiC bilayers, ($\Delta z_{BL,j}$), Si and C occupancy of the top three bilayers ($c_{Si,j}$ and $c_{C,j}$), as well as occupancy, positions, and root-mean-squared (*rms*) distribution widths for the ($k = 1$ to 6) overlayers ($c_{OL,k}$, $z_{OL,k}$, $u_{OL,k}$). Subscript values for each layer increase from the bulk towards the top the film layer (see [Figure 6.5](#)). For simplicity, we report all fractional occupancies in the SiC crystal with respect to the fully occupied Si ($1.707 \text{ e}^-/\text{\AA}^2$) or C ($0.733 \text{ e}^-/\text{\AA}^2$) single-crystal values (i.e., $c_{Si,1} = \rho_{Si,1}/1.707 \text{ e}^-/\text{\AA}^2$), and all overlayer fractional occupancies are reported with respect to a fully occupied

graphene layer ($\rho_G = 2.2930 \text{ e}^-/\text{\AA}^2$). The PTCDA areal density is derived from analysis of the STM images of the 1 ML PTCDA surface unit cell that has 2 molecules and an area of 317.18 \AA^2 (Figure 6.2(c)). This corresponds to $\rho_{PTCDA} = 1.26 \text{ e}^-/\text{\AA}^2$ ($=24 Z_C + 6 Z_O + 8 Z_H$)/ 158.59 \AA^2 , where Z_C , Z_O , and Z_H are the atomic numbers of carbon, oxygen, and hydrogen, respectively), giving $\rho_{PTCDA}/\rho_G = 0.55$. Here, it is also important to note that in the limit where the diffuse scattering around the surface signal is fully integrated, the inherent substrate surface roughness, which is attributed to the presence of SiC surface steps, does not affect the measured CTR intensity [249]. The use of the area detector enables us to obtain and integrate the diffuse scattering

intensity from the specular rod. Consequently, the apparent β roughness obtained during least-squares analysis (defined using the Robinson roughness formalism [206]) converged to zero.

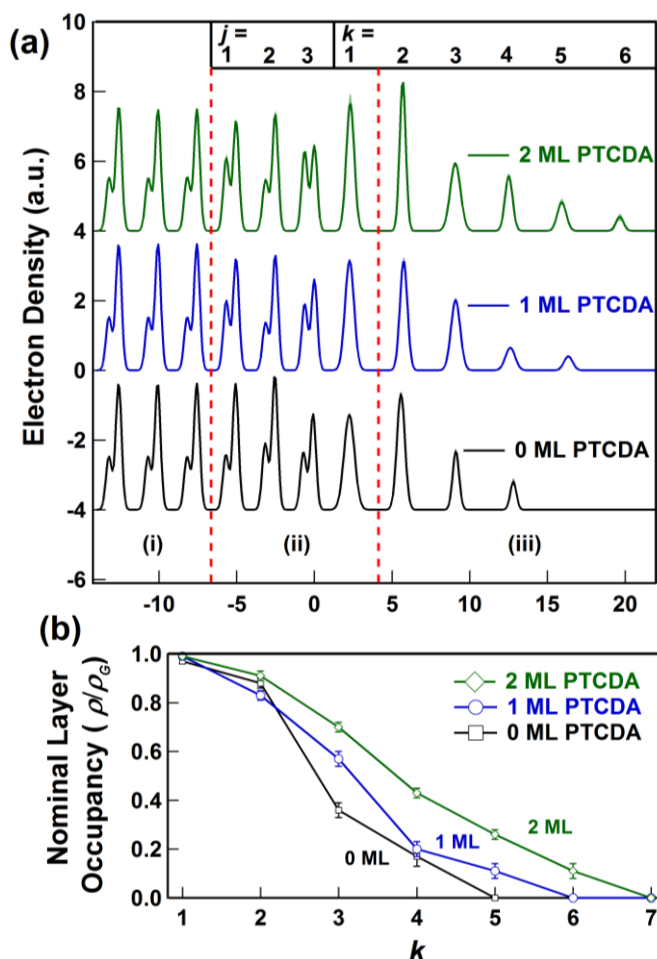


Figure 6.5: Results from XRR fitting results shown in Figure 6.3. (a) Extracted electron density profiles (offset vertically by -4, 0, and +4 respectively). Layers are identified by their subscripts, j and k . Region (i) is the bulk SiC structure that was fixed during fitting procedures. Region (ii) is the defined interface region, consisting of 3 SiC bilayers and the interfacial reconstructed layer ($k = 1$). Region (iii) includes both the graphene and PTCDA overlayers. The general increase in electron density in the overlayers is observable in layers $k = 2-6$ as PTCDA layers are added to the bare graphene. (b) The fit-determined occupation of each overlayer relative to the electron density in an ideal sheet of graphene. General increases in each partially occupied layer, as well as additional growth in layers $k = 5$ and 6 are observable with 1 ML and 2 ML PTCDA deposition.

Bare graphene (0 ML PTCDA), 1 ML PTCDA, and 2 ML PTCDA data were allowed 21, 24, and 27 free fitting parameters, respectively. Analysis was limited to 3 graphene layers for the non-functionalized sample, with a single new atomic layer added for each layer of PTCDA. In the XRR analysis, we do not explicitly distinguish between the graphene and PTCDA layers. Since we find from STM (see [Section 6.1.3.1](#) below) that the PTCDA covers graphene steps smoothly, this approximation is reasonable considering that the nominal interlayer spacings for graphene layers ($d_G \sim 3.35 \text{ \AA}$), and for the planar PTCDA(102) layers ($d_{PTCDA} = 3.22 \text{ \AA}$) [234], are well-matched. This close match means that additional PTCDA molecules will populate graphene planes if no graphene is present, e.g., in the case of incomplete bilayer coverage. Additionally, because our vertical real-space resolution cannot discern individual features at distances less than $\pi/q_{max} = 0.52 \text{ \AA}$, we are not able to resolve PTCDA and graphene molecules within the same layer only separated by 0.1-0.2 \AA . However, we expect that the differences between graphene and PTCDA may be sensed through the precise locations and *rms* widths of the PTCDA layers. Bottom-up consistency was imposed so that results from the bare EG/SiC data were used to constrain the parameters of the more complex PTCDA-functionalized systems.

6.1.3: Results

6.1.3.1: STM

The epitaxial graphene surfaces after UHV graphitization and PTCDA monolayer deposition are seen in the room temperature UHV STM images of [Figure 6.2](#). The clean epitaxial graphene surface is shown in [Figure 6.2\(a\)](#), and has a mixture of single-layer and bilayer regions. Underlying atomic steps in the SiC substrate are visible in the topography of [Figure 6.2\(a\)](#) as

the graphene sheet conformally covers the substrate. The inset of [Figure 6.2\(a\)](#) shows an atomically resolved STM image of the graphene honeycomb lattice. PTCDA forms a well-ordered monolayer with a herringbone arrangement after deposition onto epitaxial graphene by thermal evaporation, as shown in [Figure 6.2\(b\)](#). The PTCDA monolayer continuously covers the underlying SiC atomic steps wherever the graphene sheet also continuously covers the SiC steps, as was shown previously in Ref. [36]. The PTCDA monolayer is conformal, and the existing topography of the substrate is clearly visible. As the PTCDA coverage increases, a full monolayer is formed before a second layer begins. At ~ 1.5 ML PTCDA in [Figure 6.2\(c\)](#), a region of 1 ML PTCDA is observed on the right half of the image and a region of 2 ML PTCDA is observed on the left half, with the boundary indicated by the dashed line. The second layer also has a herringbone arrangement with the same unit cell and is aligned with the first layer, in agreement with previous reports [250]. We also observe that both the first and second PTCDA layers continuously cover the underlying SiC steps in [Figure 6.2\(c\)](#). The depth profiles along two lines in [Figure 6.2\(c\)](#) are shown schematically in [Figure 6.2\(d\)](#), and illustrate that the underlying SiC step is unchanged while the PTCDA coverage increases from one layer to two layers on the left half of [Figure 6.2\(c\)](#).

6.1.3.2: High-Resolution XRR

Specular reflectivity data for a bare epitaxial graphene film grown on the 6H-SiC(0001) surface are shown in [Figure 6.3\(a\)](#). The allowed bulk SiC (0006) and (000 12) peaks can be seen at $q_z = 2.49 \text{ \AA}^{-1}$ and 4.99 \AA^{-1} . As a point of reference, graphite (0002), (0004) and (0006) reflections are nominally expected at $q_z = 1.87, 3.74,$ and 5.71 \AA^{-1} . A broad thin-film modulation in the reflectivity is observed between $q_z = 0.40 \text{ \AA}^{-1}$ and 1.05 \AA^{-1} with an oscillation period Δq_z of 0.65

\AA^{-1} . This low- q_z oscillation corresponds to the relatively longer length-scale features of the electron density profile, specifically the electron-density contrast between substrate and film, indicating an approximate thin film thickness of 1 nm. As the reflectivity of the entire oscillation remains below the normalized reflectivity calculated for a truncated SiC surface ([Figure 6.3\(a\)](#)), this feature indicates that the integrated average electron density of the graphene film itself is less than that of the SiC substrate.

The data for 1 ML and 2 ML PTCDA show a systematic trend of shifted peak positions, increased reflectivity, and reduced peak width near $q_z = 1.87 \text{\AA}^{-1}$, 3.74\AA^{-1} , and 5.71\AA^{-1} . These features are clearer when a sub-range of these data are shown on a linear reflectivity scale near the second-order EG/PTCDA peak in [Figure 6.3\(b\)](#). Qualitatively, these features indicate that as PTCDA layers are added to the bare graphene surface, the film is thickening and the average d -spacing is reducing slightly. In the first approximation, the integrated intensity is proportional to the total occupation of the layers, while the peak width is inversely proportional to the film thickness [147, 251]. The data from the 2 ML PTCDA also exhibits additional thickness fringes that begin to appear on the shoulders of the graphene peaks, indicating the coherent growth of the PTCDA film ([Figure 6.3\(a\)](#)). The quality of fit for the low- q_z is generally poorer than the high- q_z , likely due to the influence of SiC surface roughness in the low- q_z region, which contributes diffuse scattering intensity near the specular rod in the form of Yoneda wings [252] and therefore complicates accurate signal integration.

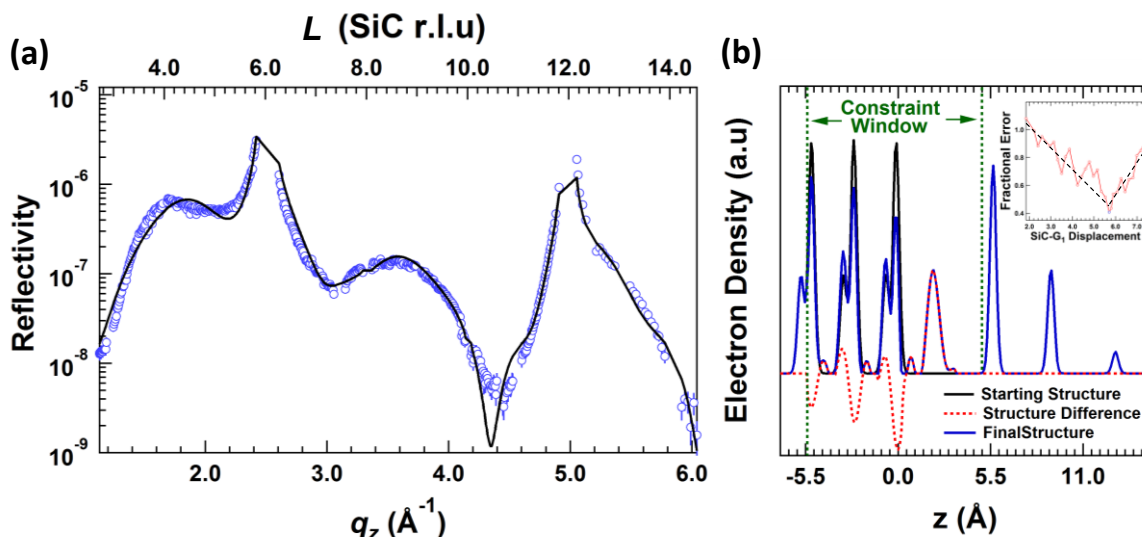


Figure 6.6: Results of Fienup-based analysis for bare EG/SiC. (a) Comparison between Fienup-derived reflectivity and data at the minimal R -factor value. (b) Results indicate that additional electron density is required at ~ 2.3 \AA in order to best match XRR measurements for bare graphene. The starting structure, including only reference structure of the SiC and a generic graphene overlayer are shown in solid black. The red dotted line indicates the change in electron density, and the blue line shows the final structure. The inset in (b) shows the minimum R -factors for various SiC-EG₁ displacements with the minimum R -factor at ~ 5.70 \AA .

The results from Fienup-based analysis are presented in [Figure 6.6](#). The best fractional error (R -factor) of 0.403 was achieved when the graphene reference overlayer was 5.70 \AA above the SiC surface (inset of [Figure 6.6](#)). All calculations that yielded fractional errors of less than 1.0 resulted in a structure with a single large electron density maximum located at 2.3 \AA above the Si-terminated SiC, as shown in [Figure 6.6\(b\)](#). It is also important to address a number of features arose during Fienup analysis. Calculations consistently revealed relaxed near-surface SiC bilayers with decreased atomic layer occupation in the Si planes and slightly increased in the C planes. Due to the regularity of this feature in our analysis, we chose to base further analysis on this interface structure. Additionally, weak peaks appear at ~ 0.9 \AA above the SiC bilayers, which are qualitatively similar to the Si and C interlayer adatom features proposed by Hass *et al.* in Ref. [21]. When included in model-based analysis, however, these features were found to be

superfluous during least-squares minimization and were therefore excluded in the final evaluation.

The best least-squares fits are shown overlaid on the data in [Figure 6.3\(a\)](#). The parameters for each fit are shown in [Table 6.1](#). The fits show very good agreement with data in high q_z -regions, indicating that the final models accurately resolve the atomic distribution of the graphene and PTCDA layers. The χ^2 and R -factors (see footnote²) were lowest with the bare graphene system and increased with system complexity. Regions of high reflectivity in which dynamical diffraction effects are dominant (e.g. $q_z < 0.20 \text{ \AA}^{-1}$, and near SiC Bragg peaks) were omitted from fits and are not reflected in the goodness-of-fit factors. When allowed to vary independently, the individual Si and C layer positions within a SiC bilayer were found to have a high degree of covariance. This issue was remedied by fixing the bilayer separation to the bulk-like value. We will note, however, that in later studies this was relaxed because of higher-resolution XSW-XPS results suggesting distinct relaxations for Si and C (see [Chapter 4](#))

Consistent with previous studies, the resulting model includes changes to the near-surface SiC layers as well as the formation of a few film layers associated with the formation of a laterally continuous graphene. As seen in [Table 6.1](#), the displacements of each SiC bilayer ($\Delta z_{BL,j}$) were found to be negligible within the limits of the error. It can also be seen that for SiC bilayers closer to the surface the Si occupancy fractions ($c_{Si,j}$) decrease and the C occupancy fractions ($c_{C,j}$) increase. The extracted electron-density profiles representing the best-fit parameters are shown in [Figure 6.3\(b\)](#). Due to the acquisition and integration of most of the

² The figures of merit are $\chi^2 = \frac{1}{N-N_p} \sum_k \left(\frac{I_{exp,k} - I_{calc,k}}{\delta y_k} \right)^2$ and $R\text{-factor} = \frac{1}{N} \sum_k \left| \frac{I_{exp,k} - I_{calc,k}}{I_{exp,k}} \right|$, where $I_{exp,k}$, and $I_{calc,k}$ are the measured and calculated intensities at the k^{th} data point, and δy_k is the uncertainty. N and N_p are the number of data points and fit parameters, respectively.

diffuse scatter during the experiment, the model electron densities are found to have with a Robinson roughness factor defined by $\beta = 0$ [168]. The electron density profiles in [Figure 6.5\(a\)](#) are therefore represented with sharp interfaces devoid of surface roughness effects. Additionally, it is important to note that the electron density profiles show peaks that are combinations ([Eq. 6.2](#)) of the occupancies, positions, and widths of the overlayers. For this reason the peak heights are not directly proportional to coverages. Therefore, for clarity, [Figure 6.5\(b\)](#) compares the total derived coverages for each layer k for the respective 0 ML, 1 ML, and 2 ML samples.

The electron density profile for the optimized structure of the bare graphene (0 ML) sample is shown in [Figure 6.5\(a\)](#), with the best-fit determined parameters listed in [Table 6.1](#). The

Table 6.1: Least-squares fitting results for XRR data. Standard deviations in the last significant figure are shown in parentheses after the reported values. Indices j and k correspond to bottom-to-top SiC bilayers and nominal graphene layers, respectively. The bilayer vertical offset, Si occupancies, and C occupancies of the SiC bilayers are $\Delta z_{BL,j}$, $c_{Si,j}$, and $c_{C,j}$, respectively. The vertical position, occupancy, and *rms* distribution widths of the graphene layers are $\Delta z_{OL,k}$, $c_{OL,k}$, and $u_{OL,k}$. Atomic planes corresponding to indices j and k , as well as the electron density profile corresponding to each fitting result, are shown in [Figure 6.5\(a\)](#), and relative nominal graphene coverages are shown in [Figure 6.5\(b\)](#).

	χ^2	<i>R-factor</i>	j	$\Delta z_{BL,j}(\text{\AA})$	$c_{Si,j}$	$c_{C,j}$	k	$z_{OL,k}(\text{\AA})$	$c_{OL,k}$	$u_{OL,k}(\text{\AA})$
0 ML PTCDA	6.53	0.11	1	0.01(1)	0.99(1)	1.05(3)	1	2.25(1)	0.97(1)	0.27(1)
			2	0.00(1)	1.03(3)	1.24(3)	2	5.58(2)	0.88(2)	0.17(1)
			3	0.00(1)	0.75(1)	1.06(3)	3	9.13(2)	0.36(3)	0.09(3)
			4				4	12.80(3)	0.17(4)	0.07(6)
1 ML PTCDA	7.78	0.23	1	0.01(1)	0.90(2)	1.26(6)	1	2.29(1)	0.99(1)	0.21(1)
			2	-0.01(1)	0.95(2)	0.90(5)	2	5.77(2)	0.83(2)	0.15(1)
			3	-0.00(1)	0.75(1)	1.42(4)	3	9.09(2)	0.57(3)	0.20(3)
			4				4	12.61(3)	0.20(3)	0.25(5)
			5				5	16.32(5)	0.11(3)	0.21(9)
2 ML PTCDA	11.75	0.31	1	0.00(1)	0.89(2)	1.24(6)	1	2.27(1)	0.99(1)	0.16(2)
			2	0.01(1)	0.93(2)	1.01(5)	2	5.69(2)	0.91(2)	0.09(3)
			3	0.01(1)	0.67(2)	1.48(7)	3	9.07(3)	0.70(2)	0.28(3)
			4				4	12.51(2)	0.43(2)	0.17(3)
			5				5	15.94(4)	0.26(2)	0.21(5)
			6				6	19.66(6)	0.11(3)	0.2(1)

first non-SiC layer ($k = 1$), which is identified as the $(6\sqrt{3}\times 6\sqrt{3})R30^\circ$ reconstructed layer, is positioned at a height of $2.25(1)$ Å above the topmost SiC bilayer, and has a nearly graphitic electron density. The three subsequent graphene layers are indexed as $k = 2, 3, 4$ and are spaced at $\Delta z_{OL} = 3.33(3), 3.55(4),$ and $3.67(4)$ Å, respectively. The first spacing matches well to the bulk graphite inter-planar spacing, but the subsequent graphene layers show a slight outward relaxation.

The overall coverage (Θ) of graphene is found by adding the occupancy of the three graphene layers ($c_{OL,2-4}$). This resulting coverage of $\Theta_{EG} = 1.4(1)$ ML is reasonable considering the STM observations of domains of both 1 and 2 ML graphene. We note that the XRR model fit shows that each subsequent graphene layer has an increased *rms* width ($u_{OL,2}$), which is in qualitative agreement with previous X-ray, STM and theoretical results [101, 253-256], although the reported values of the widths in these references vary. An important feature of these fit results is their consistency with the Fienup-based direct-methods results, including the Si and C occupancies within the SiC bilayers and the structure of the $(6\sqrt{3}\times 6\sqrt{3})R30^\circ$ reconstructed interface.

For the optimized model of the 1 ML PTCDA system, one additional atomic overlayer ($k = 5$) has been added to the 0 ML model to account for the deposited PTCDA. Referring to [Figure 6.3\(a\)](#), since the positions of the broad peaks for the 1 ML PTCDA case nearly coincide with those in the 0 ML data and since STM shows smooth coverage of PTCDA over graphene steps, it is reasonable to assume that the PTCDA layers occupy “graphene” positions. Therefore, the electron density added by the PTCDA is represented in the model by increased “graphene” coverage to each layer and one additional topmost layer. When compared to the bare graphene

results, the graphene coverage in layers $k = 2$ to 5 for the 1 ML PTCDA sample rises to 1.7(1) ML, equivalent to an increase of 0.3(2) ML of “graphene”. Due to the difference in electron-density between graphene and PTCDA, this corresponds to 0.6(3) ML of PTCDA. The results show that PTCDA deposition grows coherently with the graphene interfacial layer over the macroscopic footprint of the X-ray beam. The results also show that layers that contain adsorbed PTCDA display increased distribution widths when compared to the bare graphene results.

The 2 ML PTCDA results maintain the trends exhibited by the 1 ML results. The addition of the $k = 6$ overlayer allows for the sufficient narrowing of the graphene peaks to provide a reasonable fit in [Figure 6.3\(a\)](#). The average d -spacing of the PTCDA/EG layers, Δz_{OL} , is now ~ 3.41 Å. Note that on average, the overall inter-planar spacing has decreased by 0.11 Å from 3.52 Å observed for the 0 ML PTCDA sample. This change in inter-planar spacing corresponds to a calculated shift in the thin-film reflection of $+0.13$ Å⁻¹ for an idealized 2 ML PTCDA/EG system. This result is similar to the actual observed shift of $+0.25$ Å⁻¹, which qualitatively shows that the average d -spacing reduces as more PTCDA is adsorbed. The additional occupancy of the nominal graphene layers is now 1.0(2) ML, which corresponds to 1.6(3) ML of adsorbed PTCDA. This trend verifies the observations from 1 ML PTCDA case. Again, distribution widths of the atomic layers containing PTCDA are wider than those containing mostly graphene.

6.1.4: Discussion

6.1.4.1: EG/SiC Interface Structure

Because XRR is sensitive only to the electron density of a structure (with little elemental sensitivity), it alone is unsuitable to for a full structural determination of the system. In [Chapter 4](#)

we presented a more directed approach to resolving the EG/SiC(0001) interfacial structure, which, to a large degree, originated from questions that arose during work on this project. It was found that approximating the interfacial layer using a broad graphene-like electron density distribution located ~ 2.3 Å above the SiC surface is a good approximation of the actual interfacial structure, and is sufficient for the analysis of the PTCDA/EG/SiC(0001).

It is useful, however, to present a direct comparison to the work of Hass *et al.* in Ref. [21], in which XRR studies on UHV-grown epitaxial graphene on 4H-SiC(0001) was performed. The model they propose consists of a dense carbon layer with additional C or Si adatoms supplying the additional electron density at the EG/SiC interface required to fit their data. Here, we note that our attempts to fit adatom models to the data yielded fits with only marginal changes in χ^2 , and were ultimately unnecessary for good fitting. Instead, as suggested from the Fienup-based analysis, our model contains a single, broad graphene-like interfacial component representing the buffer layer. It is important to note, however, that the samples from this present study differ from those of Ref. [21] in polytype, sample preparation, growth conditions, and measurement conditions, all of which may explain differences in the interfacial structure. However, as discussed in [Chapter 4](#), XSW-XPS analysis of EG/SiC(0001) structures grown in various laboratories and under various environments yield no spectroscopic evidence of the adatom structures suggested by Hass *et al.* [21] or Rutter *et al.* [22].

Our analysis indicates that the interfacial regions consists of a SiC surface with structural and stoichiometric modifications to the top 3 bilayers and only a single dense $(6\sqrt{3}\times 6\sqrt{3})R30^\circ$ reconstructed layer at the interface, which is supported by the work presented in [Chapter 4](#). The stoichiometric modification to the top three bilayers may be due to structural artifacts that arise

during growth. Work by Ohta *et al.*[94] and Hupalo *et al.*[257], propose a growth mechanism governed by carbon diffusion at SiC step edges. This triple bilayer step-flow growth mechanism may be common for 6H-SiC(0001) due to the dominance of half unit cell terraces [258, 259]. This growth mechanism may account for increased electron density as the SiC bilayers retreat, leaving a graphitic layer of carbon in the SiC planes, which would yield a higher areal electron density. While the exact source of these observations not clear, the increased carbon concentration at the interface is consistent with various spectroscopic studies [260, 261] and is constant throughout the 0 ML, 1 ML and 2 ML PTCDA-functionalized graphene samples.

6.1.4.2: STM-Observed Lateral Structure and XRR-Observed Vertical Structure

STM imaging of PTCDA on epitaxial graphene shows the lateral structure of the organic layers with molecular resolution. The PTCDA molecules assemble into well-ordered monolayers with domains spanning hundreds of nanometers. The second PTCDA monolayer assembles on top of the first, and maintains the same herringbone arrangement and alignment as the first layer. These layers seamlessly cover both monolayer and bilayer graphene without a break in the lateral ordering. By depositing increasing amounts of PTCDA on the epitaxial graphene surface, we observe the PTCDA coverage progresses from isolated islands to a full monolayer followed by a second layer deposited on the first full monolayer. However, due to the convolution of electronic and topographic contributions to the tunneling current, we are not able to make conclusive measurements of the vertical structure of the PTCDA multilayers in STM.

XRR measurements resolve the vertical atomic-scale distribution of PTCDA overlayers on the graphene surface and supplement observations from STM. The interlayer spacing is characteristic of the nature of the bonding and surface adsorption of PTCDA is nontrivially

dependent on the substrate [262]. For more reactive Cu(111) and Ag(111) surfaces, PTCDA is found to have bonding distances of 2.86 Å and 2.66 Å, respectively, indicating weak chemisorption [236, 237]. However, previous results on more inert substrates, such as Au(111), indicate physisorption [234, 239]. For the PTCDA/EG/SiC(0001) interaction, weak physisorption is expected due to the chemical inertness of graphene and the relatively large spatial extent of the π -orbitals for both the graphene and the aromatic carbon atoms in PTCDA.

Our results show that the PTCDA seamlessly coats monolayer and bilayer graphene and that the PTCDA effectively fills in partial graphene layers. Qualitatively, the increase in the intensity in the region of the graphene peaks indicates increased occupancy and thickness of the graphene layers. This observation can be seen from the 0 ML, 1 ML, and 2 ML PTCDA structures presented in [Figure 6.5](#). This evidence supports the view that the expected π - π^* stacking is occurring because the bonding distances of the PTCDA to the graphene is nearly identical to that of the graphene layers themselves. While the similarity in the bonding mechanism complicates the separation of the PTCDA and graphene structures, we can conclude that the spacing between the PTCDA and the graphene is $d = \sim 3.40$ Å. This value is very close to the sum of two van der Waals radii for aromatic molecules (here, approximated by perylene), $2r_{vdW} = 3.50$ Å. [239, 263].

In addition to the interlayer spacings, XRR fits find that, in general, the adsorption of the PTCDA molecules to the surface yields increased distribution widths of the upper layers from ~ 0.10 Å for the bare graphene to ~ 0.20 Å for both 1 ML and 2 ML PTCDA. There are a number of possible sources for this observation. First, as in the case of Ag(111) and Cu(111) substrates, the chemisorptive nature of the substrate-molecule interaction can cause a change in the

adsorption geometries because of distortions of the carboxylic oxygen atoms [236-238, 262]. However, in the case of weakly bonding systems with large intermolecular spacings, large vertical molecular distortions within a single PTCDA molecule are not expected [239]. On the other hand, it has been recently shown that energetically favorable modified growth modes caused by the interaction of intermolecular bonding between PTCDA molecules may cause tilting of individual layers [264]. This tilt parallel to the surface could explain the observed increase in PTCDA electron density peak widths as PTCDA is deposited on the surface. Lastly, it is possible that the PTCDA is still planar and parallel to the graphene plane, but a slight mismatch in d -spacing between the PTCDA and graphene could lead to an effective smearing of the distribution profile.

A close relationship exists between the substrate-molecule bonding distance and the electrical properties of the system. Physisorption, characterized by large bonding distances, is an indication of the weak electronic interactions between the graphene substrate and the adsorbed PTCDA. While the results of this work indicate that the large structural separation of the PTCDA from the graphene, it does not uniquely rule out a stronger substrate-film relationship. This measurement does, however, support previous work involving scanning tunneling spectroscopy (STS) show that the electronic properties of the PTCDA are largely decoupled from that of the substrate in both epitaxial graphene [36] and gold substrates [231, 265].

In all, the combined STM and XRR results verify that the PTCDA monolayers on EG/SiC are well-ordered both laterally and vertically, and are essentially electronically decoupled from the substrate with typical π - π^* stacking distances. This weak interaction should help to preserve the electronic properties of the underlying graphene, and makes PTCDA a suitable candidate for

graphene functionalization applications, such as the seeding of the growth of high- κ dielectrics in graphene-based transistors.

6.2: Seeding ALD of High- κ Dielectrics on EG/SiC with Self-Assembled Monolayers

6.2.1: Introduction

Building on the system presented in the last Section, we turn our attention to utilizing PTCDA monolayers as a seeding template for ALD growth of metal oxide dielectrics. A main challenge in the development of top-gated graphene-based field-effect transistors (FETs) is the growth of high dielectric constant (high- κ) materials to act as the gate insulator. For optimal performance, these dielectric films should be ultrathin, conformal, and pinhole-free with minimal disorder or traps at the dielectric-graphene interface. However, due to the chemical inertness and hydrophobicity of graphene, the direct growth or deposition of dielectric layers on bare graphene leads to non-uniform films [223, 266] with poor electrical performance.

Several surface treatment strategies have been pursued by researchers to improve the uniformity of gate dielectric growth on graphene by ALD, including the deposition and oxidation of metal films [139, 140, 267-270], functionalization of graphene via ozone [271, 272] or nitrogen dioxide [273], and the spin-coating of polymer films as seed layers [136, 274]. Although these methods possess clear advantages compared to ALD of dielectrics directly on pristine graphene, important issues remain unresolved [275]. For example, graphene surface pre-treatments that involve oxidized metal nucleation layers, ozone, or nitrogen dioxide generally lead to surface damage of the graphene and degradation of its electronic properties [140, 273]. Furthermore, polymer seeding layers decrease the overall capacitance of the gate dielectric layer

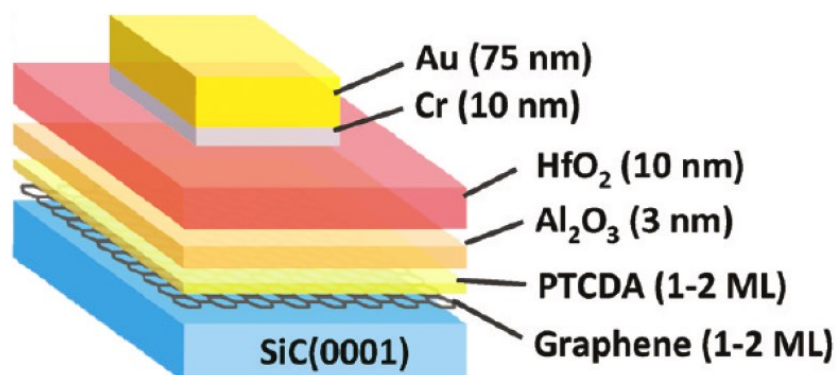


Figure 6.7: Schematic of the metal-oxide-graphene parallel-plate capacitor structure with a 10 nm HfO₂ and 3 nm Al₂O₃ dielectric stack on a PTCDA-functionalized EG/SiC(0001) surface.

due to increased gate thickness and a reduced effective k value [136, 274]. Additional solution-phase deposited organic seeding layers have also been explored, although the electrical properties of the resulting ALD alumina have not been reported [223]. Consequently, a clear need remains for a graphene chemical functionalization scheme that efficiently and uniformly seeds ALD growth while preserving the underlying graphene structure and achieving desirable dielectric properties such as low leakage current and high capacitance.

In this Section, we demonstrate the use of the PTCDA/EG/SiC(0001) system as an ALD seeding layer that overcomes the aforementioned issues. PTCDA/EG/SiC(0001) samples were prepared in the same manner as described in [Section 6.1.2.1](#), resulting in a highly uniform and ordered self-assembled monolayer as verified with UHV STM. Subsequent ALD yields homogeneous and conformal dielectric stacks of 3 nm Al₂O₃ and 10 nm HfO₂ (see [Figure 6.7](#)), which are used to fabricate metal-oxide-graphene capacitors with measured capacitance of ~ 700 nF/cm² and leakage current of $\sim 5 \times 10^{-9}$ A/cm² at 1 V gate bias, and are described in full in Ref. [190]. For the purpose of this Section, which is to structurally characterize the dielectric stacks on PTCDA/EG/SiC(0001), I distill the full text of the publication [190] to focus on the results of

low- and high-angle XRR. I do, however, include a series of comparative AFM results because they best show the effects of the PTCDA functionalization on the overlaying dielectric film morphology. Additional structural and chemical characterization, including conductive atomic force microscopy (c-AFM), ellipsometry, XPS, cross-sectional scanning electron microscopy (SEM), as well as electrical characterization, is included in the full text of Ref. [190]. Our efforts focused on using high-angle XRR as a sub-surface structural probe to verify the structural integrity of the underlying graphene following ALD dielectric growth. Low-angle XRR investigates the quality of the dielectric layers grown on the PTCDA/EG/SiC(0001). In all, this work reveals the effectiveness of sublimated PTCDA monolayers for the seeding of ALD on EG, thus facilitating the development of graphene-based nanoelectronic devices and circuits.

6.2.2: AFM-derived Film Morphology

After PTCDA deposition, described in [Section 6.1.2.1](#), ALD of Al_2O_3 and HfO_2 was then performed in a custom viscous flow ALD reactor [276] at a growth temperature of 100°C . [Figure 6.8](#) shows AFM images comparing the bare and PTCDA-functionalized EG/SiC(0001) surfaces prior to ALD deposition ([Figures 6.8\(a\) and \(d\)](#)), as well as after ALD deposition of 25 cycles of Al_2O_3 ([Figures 6.8\(b\) and \(e\)](#)) and 25 cycles of HfO_2 , respectively ([Figures 6.8\(c\) and \(f\)](#)). In [Figures 6.8\(b\) and \(c\)](#), the high- κ dielectric films on the bare EG surface are found to be patchy and discontinuous, which confirms previous reports of ALD on non-functionalized graphene and HOPG surfaces [223, 266, 270]. In contrast, [Figures 6.8\(e\) and \(f\)](#) show AFM images of two PTCDA/EG surfaces following the same ALD treatment as EG (i.e., 25 cycles of Al_2O_3 and 25 cycles of HfO_2 , respectively). With the PTCDA seeding layer, the resulting ALD dielectric films possess high uniformity and appear to conformally coat the underlying terraces of the EG

surface as evidenced by the presence of atomic steps in the post-ALD AFM images. Quantitatively, the measured *rms* roughness of both films on PTCDA/EG is less than 0.3 nm. This superlative uniformity, conformality, and smoothness of the dielectric films persists even following extended ALD treatments that yield films with thicknesses above 15 nm.

6.2.3: XRR-derived Film and Interface Structure

To further characterize these dielectric stacks and their interface with the PTCDA monolayer, low- and high-angle XRR was performed in a way similar to that described in [Section 6.1.2.3](#). At high incident angles XRR is largely insensitive to the amorphous dielectric overlayer and is instead sensitive to the atomic-scale ordering of periodic surface and interface structures. On the other hand, independent analysis concentrating on the low-angle region of the XRR curves (see

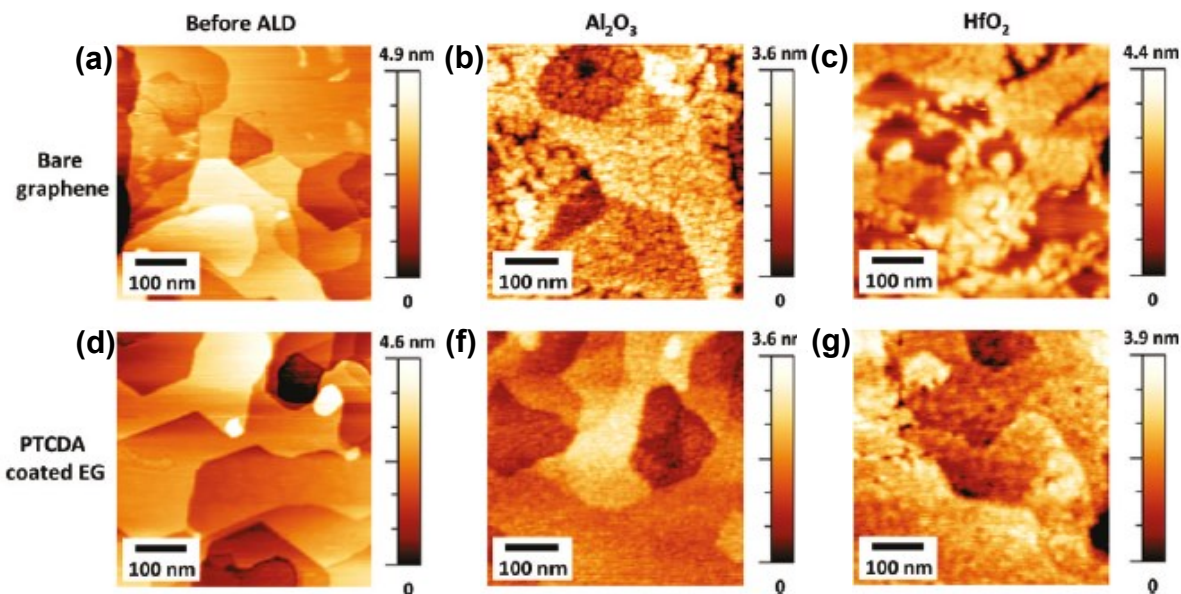


Figure 6.8: Representative AFM images of bare, functionalized and ALD-exposed EG/SiC(0001) (a-c) AFM images of a bare epitaxial graphene surface before (a), and after ALD of 25 cycles of Al_2O_3 (b) and 25 cycles (c) of HfO_2 . (d-f) AFM images of a PTCDA-functionalized epitaxial graphene surface immediately after PTCDA deposition (d), and following ALD of 25 cycles of Al_2O_3 (e) and 25 cycles of HfO_2 (f). All AFM images were taken in intermittent contact mode.

[Section 3.4.2](#)), which is sensitive to the thicker amorphous dielectric overlayers, was used to investigate the thickness, density, and roughness of the dielectric films.

[Figure 6.9](#) displays specular XRR curves of three samples: bare EG/SiC, PTCDA/EG/SiC, and $\text{HfO}_2(10\text{nm})/\text{Al}_2\text{O}_3(3\text{nm})/\text{PTCDA}/\text{EG}/\text{SiC}$. This data is qualitatively very similar to that shown in [Figure 6.3](#). As observed in the previous section, the allowed bulk SiC(0006) and (000 12) peaks can be seen at $q_z = 2.49$ and 4.99 \AA^{-1} . Again, due to the similar inter-planar spacings ($\sim 3.4 \text{ \AA}$) of both graphene-graphene layers and PTCDA-graphene layers, the diffracted signals from these layers appear near the same positions along the XRR curve, at $q_z = 1.70, 3.60,$ and 5.55 \AA^{-1} . These features are present in all three data sets. In addition to the high- q_z film signals, a broad thin-film oscillation can be observed in each data set with minima

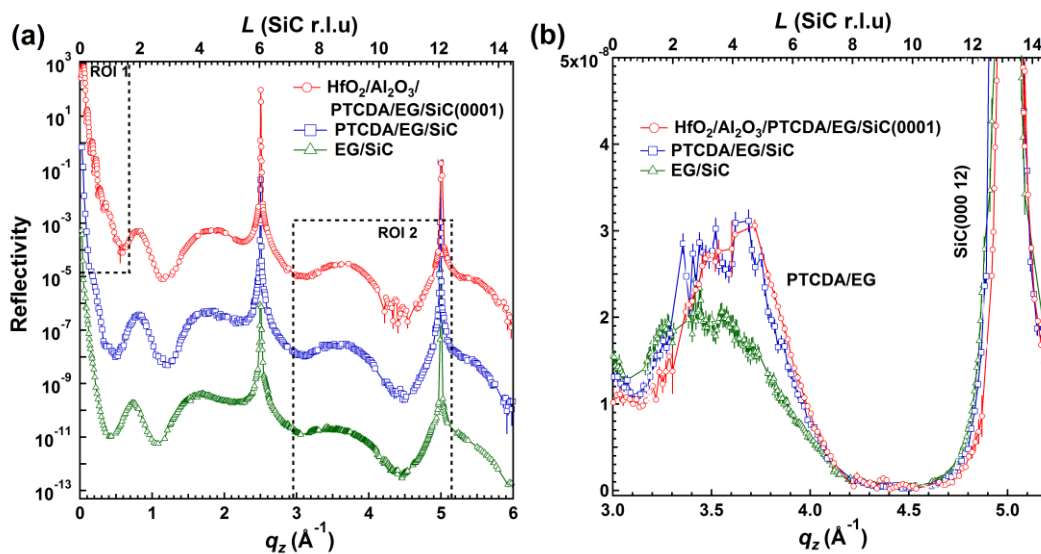


Figure 6.9: Comparison of XRR data for (a) EG/SiC(0001) (green), PTCDA/EG/SiC(0001) (blue), and $\text{HfO}_2/\text{Al}_2\text{O}_3/\text{PTCDA}/\text{EG}/\text{SiC}$ (red). Sharp features at $q_z = 2.49$ and 4.99 \AA^{-1} correspond to the SiC(0006) and (000 12) Bragg peaks, while the broad peaks at $q_z = 1.70, 3.60,$ and 5.55 \AA^{-1} correspond to graphene and PTCDA overlayers. (b) In the first range of interest (ROI 2), the PTCDA/EG/SiC data exhibit a greater reflected intensity at $q_z \sim 3.60 \text{ \AA}^{-1}$ compared to that of bare EG/SiC. This feature is a result of the additional PTCDA monolayer, and persists in the data after ALD deposition on the PTCDA-functionalized graphene surface ($\text{HfO}_2/\text{Al}_2\text{O}_3/\text{PTCDA}/\text{EG}/\text{SiC}$), indicating persistent interlayer structure following ALD. In (b) ROI 2 is presented on a linear scale for clarity.

near $q_z = 0.40$ and 1.05 \AA^{-1} . The positions of these minima imply an oscillation period Δq_z of 0.65 \AA^{-1} , a result of the PTCDA/EG interlayer structure of $\sim 1 \text{ nm}$ in thickness. For the purpose of this discussion, the contributions from the EG and PTCDA layers will be referred to as the “interlayer”.

Here, we note specifically that an increase in the reflected intensity near the interlayer peaks (at $q_z = 1.70, 3.60,$ and 5.55 \AA^{-1}) indicates the presence of a PTCDA overlayer. For clarity, in [Figure 6.9\(b\)](#), all three data sets have been presented on a linear scale in the first region of interest (ROI 2) near the second-order interlayer peak. It is clear that the reflectivity from the bare EG/SiC sample differs from the other two PTCDA-functionalized samples. Notably, the PTCDA/EG/SiC(0001) and the HfO₂/Al₂O₃/PTCDA/EG/SiC SiC(0001) data are nearly identical in this region, as well as along the rest of the XRR curve, excluding the very low- q_z region where Kiessig fringes due to the presence of the dielectric film are evident. The agreement between the XRR spectra for the two PTCDA-functionalized samples indicates that the PTCDA remains structural intact in terms of layer occupation and stacking position relative to the underlying graphene following ALD growth of the high- κ dielectric film.

In [Figure 6.10](#), we present the low- q_z XRR data, denoted by ROI 1 in [Figure 6.9\(a\)](#). Analysis of the low- q_z data to extract the electron density profile was performed as described in

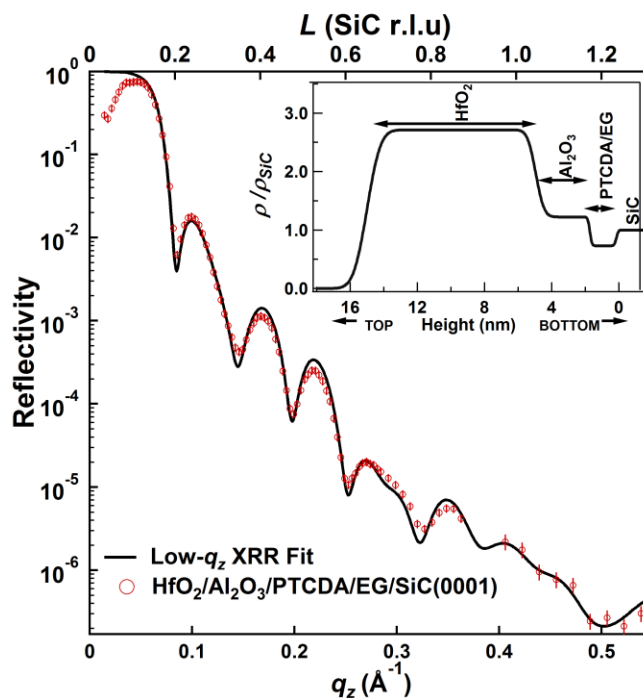


Figure 6.10: The low- q_z XRR for the first range of interest (ROI 1) from [Figure 6.9\(a\)](#). Kiessig fringes are observed, corresponding to a smooth, uniform dielectric film with sharp interfaces. The inset is the best least-squares fit result for the film overlayer strictly from the low- q data, with the electron density normalized to that of the bulk SiC substrate.

[Section 3.4.2](#). Least-squares fitting [192] of the reflectivity data in the range of $L = 0.2$ and 1.3 yielded a total dielectric film overlayer of thickness $t_{\text{tot}} = 13.2 \pm 0.4$ nm, with the HfO₂ thickness, $t_{\text{HfO}_2} = 10.0 \pm 0.2$ nm, and Al₂O₃ thickness, $t_{\text{Al}_2\text{O}_3} = 3.2 \pm 0.2$ nm. The best-fit χ^2 value corresponding to this fit was 3.98. The model provides for a low-density PTCDA/EG interface region, which the fit found to be 1.5 ± 0.2 nm thick. This thickness is consistent with the work in [Section 6.1](#) which finds that the PTCDA/EG layer combined with the underlying $(6\sqrt{3} \times 6\sqrt{3})R30^\circ$ SiC reconstructed layer is 1-2 nm thick (see [Figure 6.5\(a\)](#)). Extracted electron densities (normalized to the SiC substrate, ρ/ρ_{SiC}) are found to be $\rho_{\text{HfO}_2}/\rho_{\text{SiC}} = 2.57 \pm 0.04$ and $\rho_{\text{Al}_2\text{O}_3}/\rho_{\text{SiC}} = 1.18 \pm 0.04$, in agreement with expected values derived from bulk crystal structures, which are nominally 2.50 for $\rho_{\text{HfO}_2}/\rho_{\text{SiC}}$ and 1.18 for $\rho_{\text{Al}_2\text{O}_3}/\rho_{\text{SiC}}$. Additionally, the PTCDA/EG

interlayer electron density ($\rho_{\text{PTCDA/EG}}/\rho_{\text{SiC}} = 0.71\pm 0.03$) is close to the nominal value for a graphite crystal ($\rho_{\text{graphite}}/\rho_{\text{SiC}} = 0.65$), reflecting the similarity between the two structures. Extracted XRR *rms* roughnesses, which take into account both topography and density fluctuations, indicate exceptionally smooth surfaces and interfaces ($\sigma_{\text{HfO}_2,\text{Air}} = 0.63\pm 0.05$ nm, $\sigma_{\text{Al}_2\text{O}_3,\text{HfO}_2} = 0.39\pm 0.05$ nm, and $\sigma_{\text{PTCDA/EG,Al}_2\text{O}_3} = 0.20\pm 0.2$ nm). Overall, the low- q_z XRR analysis indicates that the HfO₂ and Al₂O₃ dielectric layers grown on PTCDA/EG are smooth, uniform, and highly ordered. Furthermore, the high-angle XRR confirms that the buried PTCDA/EG layer remains structurally intact following ALD deposition.

6.2.4: Discussion

It should be noted that after this work was completed, a follow-up resonance Raman spectroscopy study was performed on the same system to investigate the chemical integrity of the interface structure and determine the nature of the ALD growth mechanism [226]. James *et al.* found that after ALD deposition the PTCDA molecules remain molecularly intact. This indicates that the mechanism for nucleation of the ALD film growth is not caused by a direct chemical reaction between the precursor and PTCDA molecule. Instead, it is suggested that ALD growth is nucleated by adsorbed water molecules that have hydrogen bonded to the PTCDA layer. This study confirms our structural measurements, further verifying the integrity of the PTCDA/EG interfacial layer.

In summary, we have demonstrated the utility of vacuum sublimated organic monolayers of PTCDA as a seeding layer for ALD dielectric growth on EG/SiC(0001). The sub-surface sensitive XRR results show that the underlying PTCDA and graphene remain intact and possess a sharp interface with the ALD-grown dielectric films. Electrical measurements, presented in the

full text in Ref. [190] verify electrical integrity, and metal-oxide-graphene parallel-plate capacitors were fabricated and shown to possess desirable characteristics including high capacitance values of ~ 700 nF/cm² and low leakage currents of $\sim 5 \times 10^{-9}$ A/cm² at 1 V gate bias. This demonstration of high- κ dielectric performance shows the viability of organic self-assembled monolayers as seeding layers for ALD, thus providing a promising pathway the realization of high-performance graphene-based nanoelectronics.

Chapter 7

Templated Nanostructure Growth on EG/SiC(0001)

EXPANDING on the results presented in the previous section for the atomic layer deposition (ALD) of dielectric films on functionalized epitaxial graphene (EG) on SiC(0001), here we describe a functionalization scheme designed for the directed growth of nanostructures on the EG/SiC(0001) surface. It is found that 10,12-pentacosadiynoic acid (PCDA) self-assembles on graphene to form well-ordered monolayers and possesses functional moieties that preferentially react with ALD precursors used for zinc oxide and alumina. While the work in this Chapter was conceived by Justice Alaboson and Mark Hersam, the work includes a novel grazing-incident X-ray diffraction experiment that merits inclusion in this thesis. I therefore highlight and expand the X-ray scattering sections, but in order to maintain the

important narrative, I include the paper in full. I note, however, that some supplementary information is left out, but in those cases I refer to the full published work: J.M.P. Alaboson *et al.*, Nano Letters, doi:10.1021/nl4000932 (2013).

7.1: Introduction

As discussed in [Chapter 6](#), early attempts at materials integration with graphene have largely focused on the incorporation of ALD high- κ dielectrics for graphene-based field-effect transistor applications. Recent work has shown that many of the chemical modification schemes mentioned in [Section 6.2](#) can be controlled down to the nanometer-scale, although such work has been limited to localized serial nanopatterning with limited scalability to large areas [277-279].

In contrast, non-covalent self-assembled organic monolayers can achieve wafer-scale functionalization of graphene, with low-defect density domains that span hundreds of nanometers [36, 280, 281]. The resulting molecular-level structure of these self-assembled monolayers is guided by hydrogen bonding between molecular functional groups and non-covalent interactions with the underlying graphene layer. While reports exist of using such self-assembled systems for nanostructuring graphene [280, 282-285], these patterning strategies are often based on nanospheres or block copolymers, which are substantially larger than small organic molecules. Furthermore, functional groups incorporated in the constituent organic molecules of self-assembled systems have rarely been utilized to enable tailored reactivity or to direct subsequent chemistry on graphene.

Here, we demonstrate that self-assembled monolayers of PCDA on EG can be used to template the reaction and directed growth of ALD films with sub-10 nm lateral resolution. PCDA is deposited via sublimation in ultrahigh vacuum (UHV) and is shown to self-assemble

into well-ordered monolayer domains consisting of one-dimensional (1D) molecular nanostructures that coat the surface in a manner consistent with the symmetry of the underlying graphene lattice. Typical ALD chemistries for the growth of ZnO and Al₂O₃ are investigated on these PCDA/EG templates. The results show that ALD precursors preferentially react with the molecular functional groups of PCDA, and these reactions can be either self-terminating, with limited vertical growth, or non-terminating, where film growth is observed as a function of ALD cycle number. The retention of the 1D molecular-scale ordering on the PCDA template following ALD depends on the chemical details of the precursor-molecular functional group interactions, as well as the overall stability of the PCDA monolayer, the latter of which can be enhanced via ultraviolet-induced cross-linking. Furthermore, selected ALD chemistries also prove to stabilize the PCDA monolayer, which subsequently produce larger domain sizes upon annealing. Overall, the combination of PCDA and ALD provide multiple pathways for the formation of sub-10 nm oxide nanostructures on graphene.

7.2: Growth, AFM and STM of PCDA/EG/SiC(0001)

The EG samples were grown on *n*-type (nitrogen doped) 6H-SiC(0001) wafers (Cree, Inc.) by UHV graphitization [36, 190, 278]. Following *in situ* scanning tunneling microscopy (STM) confirmation of successful graphene growth, PCDA monolayers were formed on the graphene surface by sublimating PCDA ($\geq 97\%$, Sigma Aldrich) from alumina-coated W boats at room temperature in UHV. PCDA self-assembles into well-ordered monolayer domains consisting of 1D molecular arrays that coat the entire graphene surface, as shown in the STM image of [Figure 7.1\(a\)](#). The molecular structure and assembly of PCDA on graphene are presented schematically

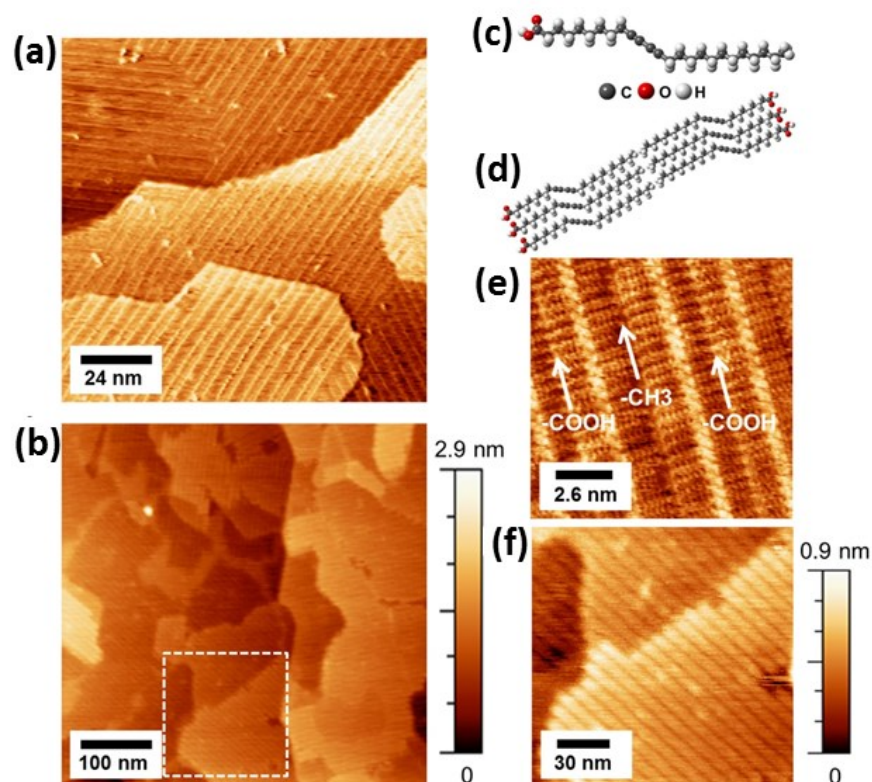


Figure 7.1: Self-assembled monolayer of 10,12-pentacosadiynoic acid (PCDA) on epitaxial graphene (EG). (a) UHV STM image of PCDA on epitaxial graphene (EG). PCDA self-assembles into monolayer domains consisting of 1D stripes on the graphene surface. (b) AFM image of a PCDA/EG surface in ambient conditions, showing the 1D molecular arrays. (c) Molecular structure of 10,12-pentacosadiynoic acid (PCDA). (d) Schematic of the molecular assembly of PCDA. (e) Molecularly resolved UHV STM image of PCDA/EG. The bright protrusions are the diacetylene groups, while the terminal ends of the molecule are indicated in the figure. (f) Zoomed-in AFM image of (a). The periodicity of the stripes in AFM corresponds to the length of two PCDA molecules.

in [Figures 7.1\(c\) and \(d\)](#), respectively. The molecular domains are also seen to seamlessly span the atomic steps of the underlying EG/SiC substrate. In the molecularly-resolved STM image ([Figure 7.1\(e\)](#)), the bright protrusions consist of the central diacetylene moieties of PCDA, while the terminal carboxylic and methyl ends are indicated with arrows [286]. The PCDA monolayer is primarily stabilized by hydrogen bonding between the carboxylate groups of adjacent molecules and π - π interactions between the diacetylene groups of neighboring molecules and the graphene surface. Hence, both the carboxylate and diacetylene moieties are responsible for self-

assembly and important to overall monolayer stability, while also serving as possible sites for ALD precursor interactions. Consequently, the result of ALD on PCDA/EG templates depends on the details of the ALD reaction.

Representative ambient atomic force microscopy (AFM) images of the UHV-deposited PCDA samples are shown in [Figures 7.1\(b\) and \(f\)](#), thus confirming that the well-ordered stripes on the graphene surface are preserved following removal from the UHV environment. The distance between adjacent stripes was measured to be 7.3 ± 0.3 nm, which is attributed to the two-molecule terminal group periodicity of the monolayer [286, 287], with some reports assigning the center of the protrusions to the terminal carboxylate groups of PCDA [287]. The orientations of the PCDA domains are effectively 6-fold symmetric, oriented $\sim 60^\circ$ and 120° with respect to each other [286]. A similar ordering is also observed on HOPG and MoS₂ substrates, which have basal planes with hexagonal symmetry similar to that of graphene [288, 289].

7.3: ZnO ALD on PCDA/EG

ALD was performed in a Savannah S100 ALD reactor (Cambridge Nanotech, Cambridge MA). For ALD of ZnO, the substrates were exposed to sequential doses of diethyl zinc (DEZ) and deionized water, with a purge step between each precursor dose. [Figure 7.2\(a\)](#) is an AFM topography image of the PCDA/EG sample after 15 cycles of ALD ZnO showing retention of the 6-fold ordering. X-ray photoelectron spectroscopy (XPS) was used to verify the presence of Zn on the sample surface following ALD. The acquired spectra were calibrated relative to the graphene C 1s peak at 285 eV. [Figure 7.2\(b\)](#) shows an XPS survey spectrum of the PCDA/EG sample after 15 cycles of ZnO ALD, with the Zn 2p peaks highlighted. The binding energy

position of ~ 1022.6 eV for the Zn $2p_{3/2}$ peak (inset) is attributed to the presence of Zn-O. Other peaks in the survey scan are attributed to Si, C, and O, as expected for ZnO on EG/SiC.

After verification of the presence of ZnO with XPS, the absolute coverage of Zn was determined using X-ray fluorescence (XRF) and comparing Zn fluorescence signal to that of a Pt standard (see [Section 3.4.4](#)). [Figure 7.2\(c\)](#) shows the XRF-derived Zn coverage as a function of ALD cycles for SiO_2/Si and PCDA/EG/SiC substrates. The Zn coverage on the PCDA/EG surface is constant through the range of 5-60 ALD deposition cycles. Exposure of a PCDA/EG substrate to 15 pulses of the DEZ precursor alone, which is still effectively one ALD half-cycle, yielded identical XRF saturation coverage, suggesting that the DEZ precursor reaction with PCDA is self-terminating and the second ALD half-cycle reaction with H_2O does not occur. By contrast, ALD growth on the SiO_2/Si surface progresses

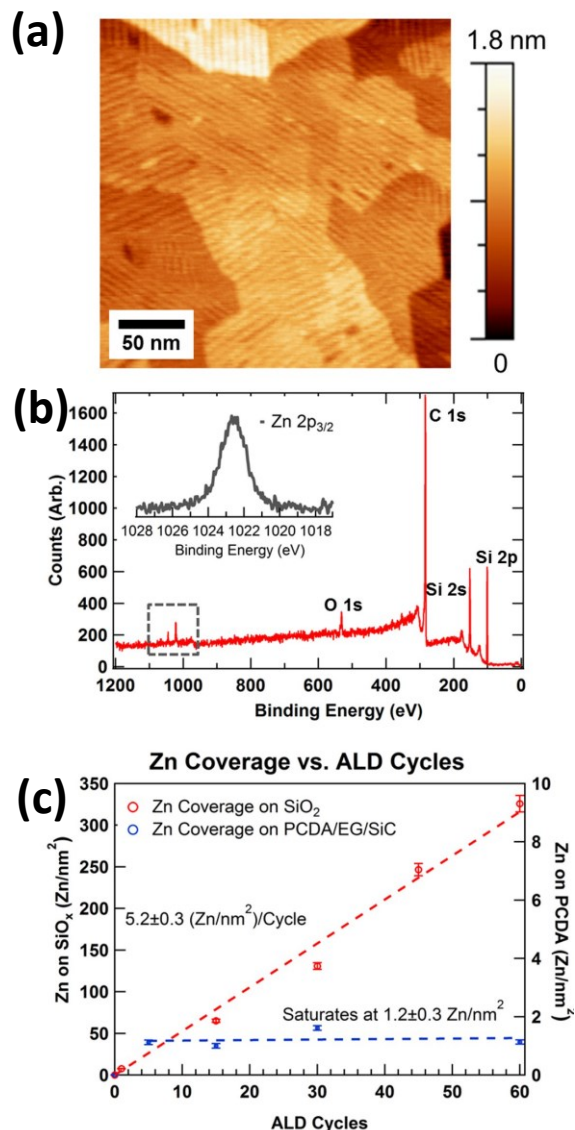


Figure 7.2: ALD of ZnO on PCDA/EG. (a) AFM image of PCDA/EG after 15 cycles of ALD ZnO using DEZ and H_2O as precursors. (b) A survey XPS spectrum of PCDA/EG after ZnO ALD showing the presence of Zn. (inset) The Zn $2p_{3/2}$ peak position is at ~ 1022.6 eV, indicating a Zn-O bond. The spectra were calibrated with respect to the C 1s peak at ~ 285 eV. (c) XRF Zn coverages as a function of ALD cycles for SiO_2/Si and PCDA/EG substrates. On SiO_2/Si , a linear increase in the coverage of Zn is observed, with a growth rate of 5.2 ± 0.3 (Zn/nm^2)/cycle. On the other hand, the Zn coverage terminates at 1.2 ± 0.3 Zn/nm^2 on the PCDA/EG substrate.

linearly, as is typical of non-terminating ALD processes [276, 290]. The growth rate on SiO₂/Si is calculated to be 5.2±0.3 (Zn/nm²)/cycle, while the Zn coverage on PCDA/EG terminates at 1.2±0.3 Zn/nm².

While limited in vertical growth, the modification of PCDA/EG with DEZ (ZnO-PCDA/EG) is sufficient to enhance its thermal stability. As described fully in Ref. [188], while the as-deposited PCDA completely desorbs at 110°C under a pressure of 0.2 Torr, the ZnO-PCDA/EG remain thermally stable under identical conditions, as verified by the persistence of the stripes after heating. Furthermore, DEZ-modified PCDA/EG promotes enhanced ordering as the maximum domain size increases by a factor of four compared to unmodified PCDA/EG following annealing. Similar crystallization into large domains has also been observed for molecules of phosphonic acids on HOPG [291].

7.4: GIWAXS/GISAXS

The self-terminating reaction of DEZ with PCDA and its improved thermal stability suggest that Zn is reacting uniformly with the PCDA/EG template. To gain further insight into the mechanism of ZnO ALD on PCDA/EG/SiC(0001), we performed grazing-incidence small/wide angle X-ray scattering (GISAXS/GIWAXS), which allows for the precise determination of the spatial distribution and orientation of the Zn chains with respect to the underlying lattice. The experimental geometry is shown in [Figure 7.3](#), and the experimental procedure is described in Section 3.4.3. Briefly, the incident beam angle was tune to $\sim 0.85 \times \alpha_c$, where α_c is the critical angle for SiC. The sample, which was mounted in rough vacuum to avoid beam damage, was rotated about its surface normal, and both GIWAXS and GISAXS data were collected at integral steps in ϕ with area detectors. The GISAXS and GIWAXS data are collected as a

function of q_y and q_z , which are the in-plane and the out-of-plane components of the scattering vector $\mathbf{q} = \mathbf{k}_f - \mathbf{k}_i$, where \mathbf{k}_i and \mathbf{k}_f are the incoming and outgoing X-ray wave vectors.

[Figure 7.3](#) shows a 2D GISAXS pattern for ZnO-PCDA/EG in which two first-order q_z -extended Bragg rods at $q_y = \pm 0.96 \text{ nm}^{-1}$ are observed (as indicated in the figure by white arrows). These peaks are not observed prior to ZnO ALD (see [Figure 7.4](#)). The difference in the observed intensities of these rods depends on the azimuthal orientation of the sample, which determines the intersection of the Ewald sphere with the rods at $h = \pm 1$ of the ZnO reciprocal lattice, also shown in [Figure 7.3](#). Lorentzian fits to the q_z -integrated intensity for these rods reveal a 1D periodicity of $d = 2\pi/|q_y| = 6.57 \pm 0.04 \text{ nm}$ between the ZnO chains and a correlation length $L \sim 2\pi/\delta q_y \sim 100 \text{ nm}$ (δq_y is the FWHM for the Bragg rods in the intensity profile). These values are

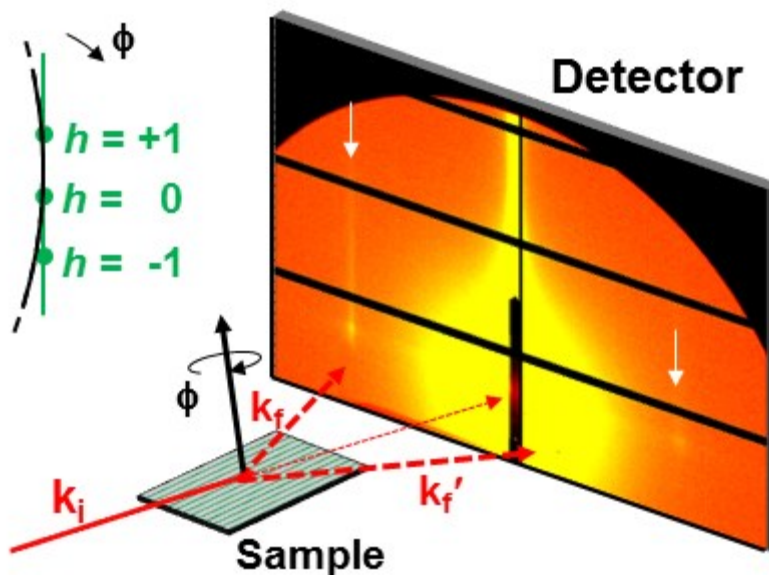


Figure 7.3: Schematic of the GISAXS measurements on ZnO-PCDA/EG showing a GISAXS pattern near a ZnO 1D crystal Bragg condition. The $h = \pm 1$ Bragg conditions for ZnO at $q_y = \pm 0.96 \text{ nm}^{-1}$ (indicated with white arrows) are satisfied at slightly different sample azimuthal angles, ϕ , as illustrated with the Ewald sphere construction. (For clarity, the reciprocal lattice is scaled by $5\times$ as compared to the Ewald sphere radius).

consistent with the AFM-derived domain size and two-molecule periodicity, which indicates a coherent coupling between the Zn and the PCDA positions that is commensurate with the two-molecule periodicity of PCDA. The above GISAXS results, together with the verification of the presence of Zn-O from XPS, indicate that the carboxylate groups are the host sites for Zn atoms on PCDA/EG.

The orientational relationship between the ZnO-PCDA and the underlying

EG lattice can be quantified by directly measuring the near in-plane scattered intensity for the ZnO first-order rods and the SiC $\{10\bar{1}L\}$ family of rods as a function of azimuthal angle, ϕ . The integrated intensities from sequentially-collected GISAXS ZnO and GIWAXS SiC signals are shown on the same ϕ -scale in [Figure 7.5\(a\)](#). An intensity map showing q_y -projected scattering patterns as a function of ϕ is shown in [Figure 7.5\(b\)](#). As discussed above, the diffraction peaks at $q_y = \pm 0.96 \text{ nm}^{-1}$ arise from the periodic distribution of Zn coupled with the PCDA carboxylate headgroups, which implies that the PCDA alkyl backbone will be oriented approximately normal [286] to the 1DZnO nanostructures. As seen in [Figures 7.5\(a\) and \(b\)](#), intensity doublets (maxima separated by 7°) are observed at 60° intervals in ϕ , confirming the effective 6-fold symmetry of ZnO-PCDA on EG/SiC, as is consistent with the AFM images in [Figure 7.2\(a\)](#). The

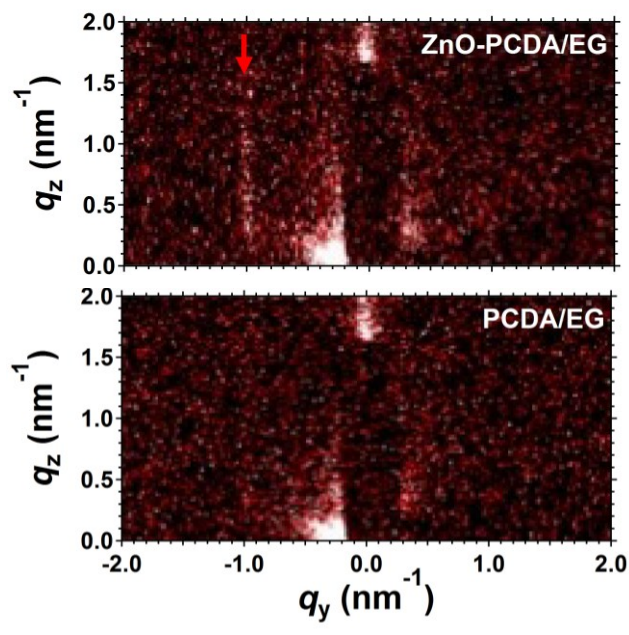


Figure 7.4: Scattered intensity for both DEZ-treated (top) and as-deposited PCDA/EG/SiC (bottom) substrates. The red arrow indicates the scattered intensity from the one-dimensional ZnO nanostructures, which is not observable for as-deposited PCDA/EG/SiC(0001).

7° separated doublet feature is consistent with observations of misoriented PCDA domains observed in STM in [Figure 7.6](#) [37, 292]. Hexagonal symmetry is also evident for the $\text{SiC}\{10\bar{1}L\}$ family of rods, for which the scattered intensity is maximized at an angular offset of $\Delta\phi = -18 \pm 0.5^\circ$ with respect to the ZnO rods.

The existence of these misoriented PCDA domains has been previously observed locally with STM studies of PCDA monolayers on EG/SiC(0001) [37, 292] and other hexagonal substrates. Our GIWAXS/GISAXS analysis, however, provides direct quantitative structural information of complex multilayered interfaces, ensemble-averaged over $\sim\text{mm}^2$ surface areas. The symmetric, bimodal distribution of the scattered intensity from the ZnO chains ([Figures 7.5\(a\) and \(b\)](#)) signifies the existence of two structurally equivalent domains which differ only by their $\pm 3.5^\circ$ orientation (of the chain direction) with respect to the SiC $\langle 10 \rangle$ directions (note, for in-plane crystallographic directions we provide only hk indices). A number of physical explanations could lead to this bimodal distribution of domains including the tilting of the alkyl chains themselves from the EG $\langle 10 \rangle$ lattice directions or a slight offset of adjacent molecules along the EG $\langle 10 \rangle$ direction [293]. Supporting evidence for the GISAXS/GIWAXS-measured ZnO-PCDA orientation on EG can be found from STM/AFM analysis of the step-edge orientation of SiC(0001). First, the diacetylene (the bright features observed in the STM image of [Figure 7.1\(a\)](#)) and the carboxylate functional group rows align along the step-edge orientation of the SiC(0001) substrate (see images in this paper and in Ref. [37]). Second, analysis of the step-edge orientation of the SiC

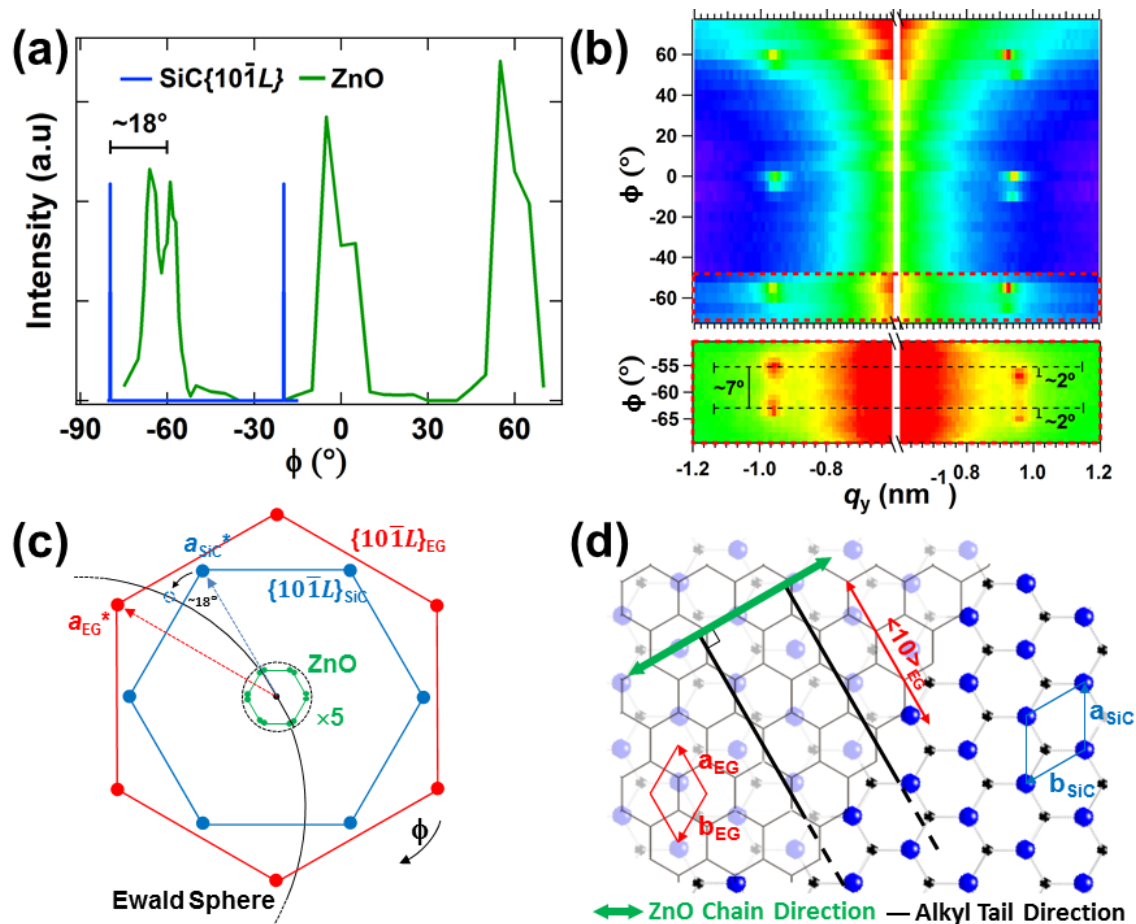


Figure 7.5: Grazing incidence small/wide angle X-ray scattering results. (a) The measured ϕ angular dependence of the near in-plane integrated intensities for the GISAXS ZnO rods (green line), and GIWAXS SiC{10 $\bar{1}$ L} rods (blue line). (b) q_z -projected scattered intensity map. The regular spikes in intensity in the low-resolution map (top) at $q_y = \pm 0.96 \text{ nm}^{-1}$ that repeat every 60° correspond to 1D ZnO nanostructures spaced 6.57 nm apart, and rotationally oriented by 120° . The high-resolution map shows two approximately equally populated ZnO domains rotated 7° with respect to each other. A reciprocal-space representation showing the relative positions of the ZnO (green), SiC (blue), and EG (red) rods projected on to the $L = 0$ hk plane in accordance with the measurements in (b). The region inside the dashed circle has been scaled by $5\times$ for clarity. A 1D ZnO reciprocal lattice from a single domain corresponds to two first order rods ($h = \pm 1$) separated by 180° in ϕ , which are found to lie along the a_{SiC}^* reciprocal lattice vector. These are observed in (a) and (b) to be split into two domains separated by 7° , which due to the three domain orientations produce a total of 12 rods. (d) A diagram of the real-space structure corresponding to the results in (a), (b) and (c), with EG and SiC in-plane unit cells in red and blue, respectively. The nominal ZnO chain direction is shown in green, and the alkyl chains lie along the EG $\langle 10 \rangle$ directions. The alkyl chains extend beyond the limits of the diagram.

shows that it is, in turn, aligned along the SiC<10> direction. In particular, [Figure 7.6](#) shows the step-edge orientation analysis of SiC. [Figures 7.6\(b\)-\(d\)](#) are fast Fourier transform (FFT) images from the indicated regions of [Figure 7.6\(a\)](#), all showing the same orientations of two sets of hexagonal dots with 30° rotation, which originate from the graphene lattice and PCDA moiré pattern orderings (as indicated in [Figure 7.6\(b\)](#)). While the step-edges are not perfectly aligned with each other, as can be seen by the step segments highlighted with green lines in [Figure 7.6\(a\)](#), they are both found to be offset only by a few degrees from the EG<1 $\bar{1}$ > (SiC<10>) directions, as seen in [Figure 7.6\(c\)](#). This observation implies that the carboxylate groups, which

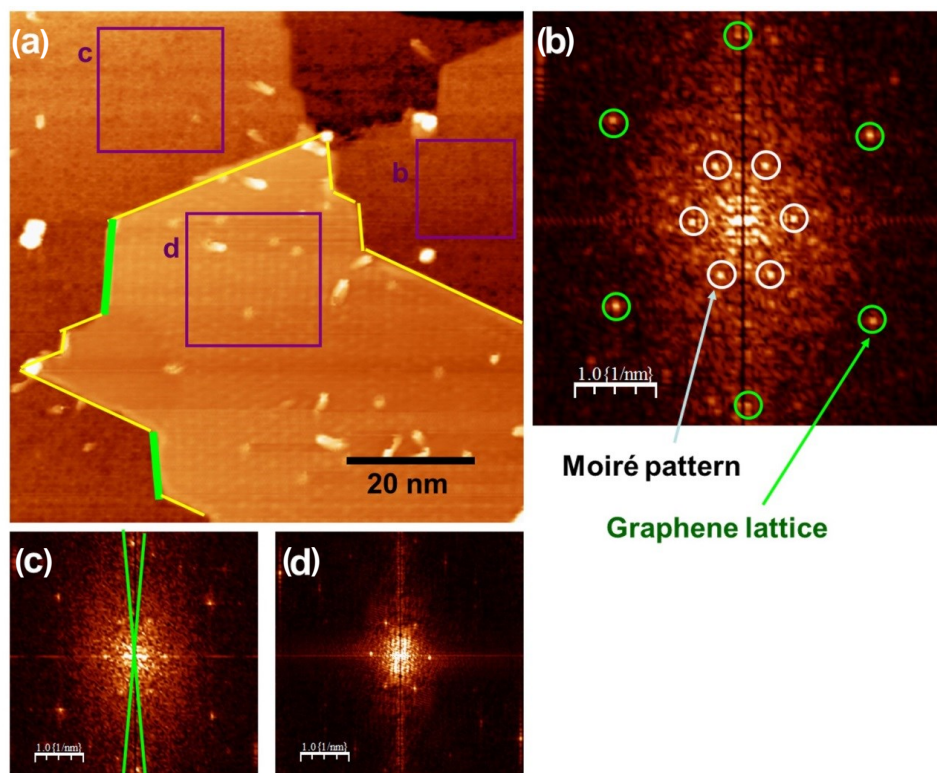


Figure 7.6: STM and the associated fast Fourier transforms for results for various regions on PCDA-functionalized EG/SiC(0001) (a) STM image on clean EG/SiC(0001) surface. (b-d) Fast Fourier Transform (FFT) images derived from the indicated regions in (a), revealing two sets of hexagonal dots. The two sets of dots originate from the graphene lattice and moiré pattern, respectively, as indicated in (b). Misoriented step segments are highlighted with green lines in (a) and are reproduced in (c) showing that the two sets of step edges are within a few degrees of the EG <1 $\bar{1}$ > (SiC <10>) directions.

are the host sites for the Zn atoms, are also aligned along the SiC<10> directions, and consequently, the alkyl tails of PCDA align along the EG<10> directions, in agreement with the X-ray scattering results. The PCDA alkyl tails, therefore, align along the <10> family of directions of the EG lattice. [Figure 7.5\(d\)](#) depicts the corresponding real-space representation of the orientational relationships between the EG/SiC(0001), the ZnO-PCDA nanostructure, and the PCDA alkyl backbone. Particularly, the alkyl tail orientation is consistent with that observed for as-deposited PCDA molecules on HOPG [37], and highlights the effectiveness of PCDA monolayers for templating 1D ALD ZnO nanostructures.

7.5: Raman Scattering

The coordination of Zn to the carboxylic ends of PCDA share features similar to the coordination of divalent metal ions to fatty acids in solution [294-304]. Specifically, divalent metal ions coordinate to the carboxylate groups, with a metal ion to molecule ratio generally believed to be 1:2 [296, 302, 303, 305]. Monolayers of these fatty acids coordinated to divalent ions have been deposited from solution or via Langmuir-Blodgett deposition onto a variety of surfaces [300] including HOPG [305]. Similar to that observed for ZnO-PCDA/EG/SiC, the presence of metal ions coordinated to the fatty acids stabilizes the molecules in solution, and enhances the long-range packing order and thermal stability in the resulting monolayer [300]. While the coordination of divalent metal ions to fatty acids in solution is largely believed to be ionic [294, 296, 297, 301-303], transition metals such as Zn may have multiple carboxylate binding modes, including covalent monodentate and bidentate modes [306].

In contrast to DEZ, the reaction of trimethyl aluminum (TMA) with PCDA is non-terminating and leads to the growth of Al₂O₃ films. ALD Al₂O₃ was performed on PCDA/EG

substrates by exposure to sequential doses of TMA and H₂O. [Figure 7.7\(b\)](#) is a plot of the Al 2p XPS peak absolute intensity as a function of ALD cycles. The intensity of the Al 2p XPS peak increases as a function of ALD cycles, which is attributed to the non-terminating reaction of TMA with PCDA and the subsequent growth of Al₂O₃. [Figure 7.7\(b\)](#) shows the integrated area of the Al 2p peak as function of ALD cycles for both PCDA/EG and SiO₂/Si surfaces, which reveal linear ALD growth on both surfaces. [Figure 7.7\(a\)](#) is an AFM image of a PCDA/EG surface after 5 cycles of ALD Al₂O₃. The resulting disordered lamellar structure is noticeably distinct from the striped morphology of as-deposited PCDA/EG ([Figure 7.1\(e\)](#)) and also distinct from the structure after ALD Al₂O₃ deposition on bare graphene (see [Section 6.2](#)), which shows discontinuous film growth [190, 223].

Raman spectroscopy was employed to determine the chemical activity of the PCDA monolayer following ALD oxide deposition as shown in [Figure 7.7\(d\)](#). The acetylene stretching frequency for PCDA is located between 2077 cm⁻¹ and 2101 cm⁻¹, depending on the degree of polymerization and side chain disorder [307-309]. Raman spectra for PCDA on EG show peaks due to the graphene phonons (D band at 1380 cm⁻¹, G band at 1604 cm⁻¹, and 2D band at 2742 cm⁻¹), the PCDA acetylene stretch centered at 2082 cm⁻¹, and a peak at 1458 cm⁻¹ attributed to a C=C stretch. First, the breadth and asymmetry of the acetylene stretch of as-deposited PCDA/EG indicate that there could be a coexistence of the “blue” and “red” polymer PCDA phases on the graphene surface, which are nominally attributed to an ordered and disordered polymer, respectively [307-309], which is also corroborated by the C=C stretch [307] present in the “blue phase”. The presence of these polymer phases indicates that some polymerization of PCDA is occurring under Raman laser irradiation.

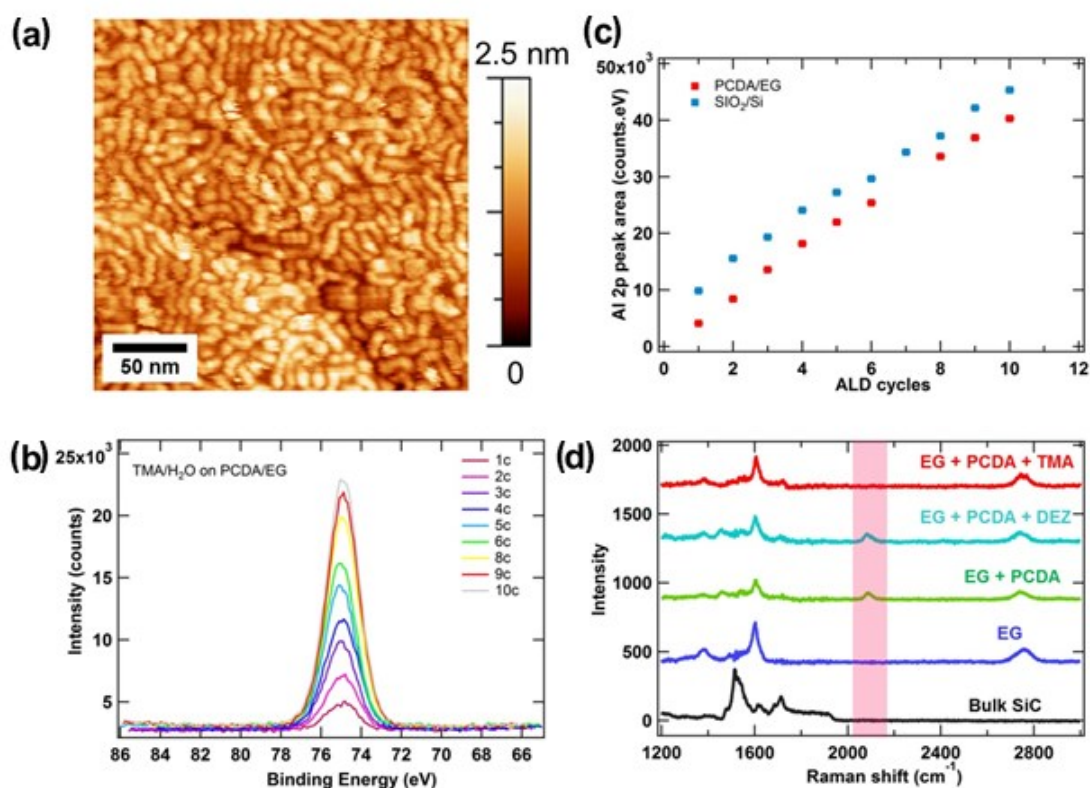


Figure 7.7: AFM and XPS results for TMA-exposed PCDA/EG/SiC(0001), and Raman spectra for all samples. (a) AFM image of a PCDA/EG surface after 5 ALD Al_2O_3 cycles showing a lamellar morphology. (b) XPS Al 2p peak for PCDA/EG as a function of ALD cycles. The Al 2p position at ~ 74.7 eV indicates the presence of Al_2O_3 . The increase in intensity as a function of ALD cycles is attributed to the growth of Al_2O_3 with repeated ALD cycles. The spectra were calibrated relative to the C 1s peak at 285 eV. (c) Integrated area of the Al 2p peak as a function of ALD cycles for both PCDA/EG and SiO_2/Si . Linear growth with cycle number is seen for both surfaces. (d) Raman spectra of EG, PCDA/EG, ZnO-PCDA/EG, and TMA/ H_2O modified PCDA/EG (the bulk SiC spectrum has been subtracted). The peak at 2082 cm^{-1} (highlighted by the pink region) is attributed to the diacetylene stretch of PCDA, which survives DEZ but not TMA ALD chemistry.

Following ALD of zinc oxide using DEZ and water, the acetylene peak remains and shifts to a slightly higher frequency (2087 cm^{-1}), and the C=C stretch remains at 1458 cm^{-1} . The persistence of these stretches with the same spectral intensity as in the neat PCDA film reveals that the DEZ does not interact with the acetylene carbons. In contrast, deposition of alumina via TMA and H_2O destroys the vibrations of both the acetylene and C=C stretch, thus pointing to the loss of these functional groups due to attack by the more aggressive TMA precursor. Furthermore, it is observed that an initially striped ZnO-PCDA/EG surface is

transformed to the disordered lamellar structure upon TMA and H₂O exposures, as seen discussed in the full text in Ref. [188].

While TMA is expected to react with the carboxylate group of PCDA according to previous work on non-hydrolytic ALD with carboxylic acids [310-312], Raman spectroscopy indicates that TMA additionally attacks the acetylene groups. This attack by TMA share similarities with carboalumination reactions, which can involve the reaction of aluminum alkyls with carbon-carbon double and triple bonds, and is a well-established synthetic protocol in organometallic chemistry and organic synthesis (e.g. Ziegler-Natta polymerization) [313-316].

7.6: UV Polymerization

Since the acetylene groups are a primary contributor to PCDA monolayer stability and are subject to attack by TMA, cross-linking the PCDA preceding ALD is likely to enhance the ordering stability during Al₂O₃ deposition. To test this hypothesis, cross-linking of PCDA was performed on EG via ultraviolet (UV) irradiation [286]. In particular, PCDA/EG substrates were exposed to UV irradiation from a UV pen lamp (254 nm, Spectroline, 11SC-1) in a N₂ glove box. The cross-linked diacetylene cores of PCDA molecules are shown in the molecularly resolved STM image of [Figure 7.8\(a\)](#). The mechanism of UV polymerization, the changes in the angle of the side chains, and the height of the polymerized PCDA chains on EG have been reported previously [286]. AFM images of a PCDA/EG surface after a 90 min UV irradiation is shown in [Figure 7.8\(b\)](#), revealing elevated stripes, ~2.5 Å high, that are attributed to the polymerized PCDA chains [286]. The spatial extent of cross-linking can be modulated by the UV irradiation time as discussed in Ref. [188]. [Figures 7.8\(c\) and \(d\)](#) are AFM images after 5 Al₂O₃ ALD cycles on a 90 min UV-irradiated PCDA/EG sample. The presence of aligned stripes and sharp

edges, in contrast to the lamellar structure observed on as-deposited PCDA ([Figure 7.7\(a\)](#)), indicate that cross-linking enhances ordering following Al_2O_3 ALD. This improved ordering can be attributed to the enhanced structural and thermal stability provided by cross-linking as demonstrated by desorption measurements presented in Ref. [188]. Lateral growth of Al_2O_3 on PCDA is observed with increasing number of ALD cycles, also presented in presented in Ref. [188]. In this case, the thicker Al_2O_3 films continue to possess sharp and aligned edges,

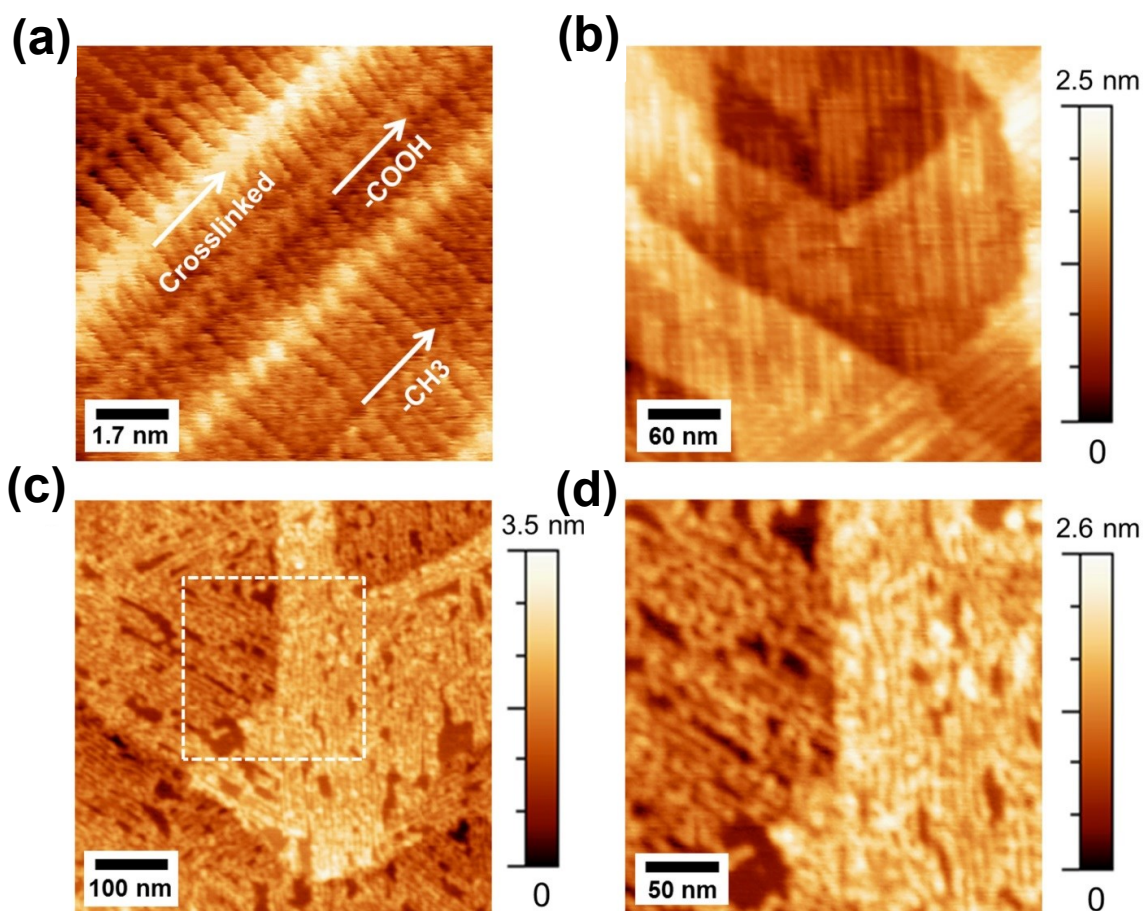


Figure 7.8: Atomic layer deposition on cross-linked PCDA/EG. (a) Molecularly resolved UHV STM image showing the cross-linked diacetylene cores of PCDA next to a molecular chain that has not yet undergone cross-linking. (b) AFM image in ambient of a UV irradiated PCDA/EG surface showing the presence of elevated stripes attributed to cross-linked PCDA. (c) AFM image after 5 ALD Al_2O_3 cycles on cross-linked PCDA/EG. (d) Zoomed-in image of (c) showing better aligned arrays compared to Al_2O_3 on as-deposited PCDA/EG [Figure 7.7\(a\)](#). The UV irradiation time was 90 min.

templated by the underlying monolayer, although the top-surface becomes non-uniform.

7.7: Summary

In summary, self-assembled organic monolayers of PCDA have been used as a template for directed ALD growth on EG/SiC(0001). UHV-sublimated PCDA self-assembles into well-ordered monolayer domains consisting of 1D molecular arrays that coat the surface in a manner consistent with the symmetry of the underlying graphene lattice. DEZ and TMA, typical ALD chemistries for the growth of ZnO and Al₂O₃, respectively, were investigated on these PCDA/EG templates. DEZ was found to react with PCDA/EG in a self-terminating manner, and the original striped morphology of PCDA was retained following exposure. Furthermore, DEZ treatment enhances the thermal stability of PCDA/EG, which subsequently promotes enhanced ordering as the maximum domain size increases by a factor of four compared to unmodified PCDA/EG following annealing. Spectroscopic and X-ray scattering experiments suggest that DEZ reacts with the carboxylate groups of PCDA, where Zn atoms coordinate between neighboring PCDA molecules. Furthermore, due to this templating effect, the ZnO chains are shown to align only along specific orientations with respect to the underlying graphene lattice, as precisely measured with GIWAXS/GISAXS. On the other hand, sequential exposures of PCDA to TMA/H₂O lead to the non-terminating ALD growth of Al₂O₃. In contrast to the as-deposited PCDA/EG surface, Al₂O₃ growth on PCDA/EG results in a disordered lamellar morphology, due in part to the absence of the stabilizing PCDA acetylene groups, which are attacked and removed during TMA exposure. Finally, cross-linking PCDA via UV irradiation enhances its stability, allowing for the ordered vertical growth of Al₂O₃, up to 5 TMA/H₂O ALD cycles, before lateral Al₂O₃ growth outside of the template becomes dominant. Overall, the combination of PCDA and

ALD provides multiple pathways to forming sub-10 nm oxide nanostructures on graphene, which can likely benefit ongoing efforts to realize graphene-based nanoelectronic, sensing, and energy technologies.

Chapter 8

Summary and Future Work

THIS THESIS has focused on the use of synchrotron-based X-ray characterization tools to investigate a selection of pristine, intercalated, and functionalized graphene structures. The techniques used in this work provide novel structural information about these EG/SiC(0001) systems with precision and elemental/chemical sensitivity inaccessible to many techniques commonly used in the study of graphene. In this Chapter, the main conclusions of this research will be reviewed and the implications highlighted. Finally, since this work represents only a few of the many EG/SiC systems that could benefit from similar studies, I will suggest potential directions for future research.

8.1: Summary

In [Chapter 4](#), a comprehensive XSW-XPS and XRR study of the EG/SiC(0001) interfacial structure is performed. Using the chemical sensitivity afforded by photoelectron spectroscopy and the sub-Å scale resolution provided by single-crystal XSW, we are able to uniquely identify the structural origins of the components of the EG/SiC(0001) C 1s and Si 1s photoelectron spectra. With respect to the interfacial EG₀ layer, we find that there exist two distinct chemical species that are positioned 2.1 ± 0.1 and 2.4 ± 0.1 Å above the terminal Si layer of the underlying SiC substrate. These two components, called S₂ and S₁, respectively, have inequivalent distribution widths and concentrations within the interfacial layer, with the S₂ species found to be highly coherent with the substrate. This high coherency indicates a narrow spatial distribution and strong interaction with the SiC substrate, likely in the form of covalent interaction. The second species, S₁, assumes a broader distribution of ~ 0.5 Å, indicating the presence of significant corrugation along the SiC[0001] direction and the adoption of considerable *sp*³ character. The superposition of these two components yields the broad interfacial structural commonly observed in STM and TEM studies. The combined XSW-XPS and XRR analysis allows for the construction of a highly precise atomic density profile along the SiC[0001] direction and provides a comprehensive and precise model of the EG/SiC interface. This result should help to clarify long-standing uncertainties concerning the nature of this highly-debated interfacial structure and provide a strong conceptual foundation upon which to continue studies of pristine, intercalated, and functionalized EG/SiC.

In [Chapter 5](#), an approach similar to that employed in [Chapter 4](#) was used to investigate the structural consequences of H-intercalation to the EG/SiC(0001) interface. Prior suggest that

the H-intercalation process was proposed physically decouples the EG₀ layer from the SiC substrate via the breaking of Si-C bonds at the interface and subsequent passivation of the Si-terminated SiC substrate. XRR data on two sister samples, identical in preparation apart from a 700° anneal in H₂ atmosphere, reveal a drastic change in structure due to the decoupling of the interfacial layer from the substrate. It is found that after the decoupling process, the EG₀ layer does indeed convert into a structurally EG-like layer, and is displaced from the SiC substrate. The graphene film subsequently sits atop a Si-H terminated surface, positioned at ~2.7 Å above the H layer, assuming a typical Si-H bonding distance of 1.5 Å. In addition, our results find that apart from this decoupling and displacement of the EG₀ layer, there is little change in the graphene film itself, i.e., the EG *d*-spacing remains essentially constant. This observation supports the assertion that the H-intercalation process only influences the interfacial structure and does not intercalate between the EG film layers, which would presumably affect the EG *d*-spacing.

In [Chapter 6](#), a series of functionalized graphene structures were characterized using a suite of X-ray characterization techniques. First, the results for the prototypical PTCDA/EG/SiC(0001) were studied using a combination of STM and XRR. It was found that the self-assembled PTCDA monolayers possessed a high degree of both vertical and lateral ordering. STM results found that the PTCDA molecules carpeted the EG surface in a herringbone packing arrangement, and XRR found that PTCDA layers lay essentially flat on the surface and exhibited a typical π -stacked relationship with the EG. The high degree of in-plane ordering indicate that there exist relatively strong molecule-molecule interactions, resulting in robust monolayer formation, while the large (~3.4 Å) PTCDA-EG/SiC(0001) distance suggest a

weak, electronically decoupled interaction EG/SiC(0001) substrate. This study laid the foundation for the for a follow up work to explore the use of the PTCDA monolayer as a ultrathin organic seeding layer for the subsequent ALD of high- κ dielectric thin film stacks of Al_2O_3 and HfO_2 . High-resolution XRR was used to probe the buried $\text{HfO}_2/\text{Al}_2\text{O}_3/\text{PTCDA}/\text{EG}/\text{SiC}(0001)$ interfaces and found that the PTCDA layer remained structurally intact after ALD. Low-angle confirmed the results of AFM that found that the dielectrics dielectric films were smooth, conformal, and uniform. Finally, electrical measurements of metal-oxide-graphene parallel-plate capacitors exhibited excellent electronic properties, suggesting an effective method for the integration of epitaxial graphene with other electronic materials.

In [Chapter 7](#), we presented the final installment of the functionalization theme, which was centered on the directed ALD of nanostructures using 1D molecular arrays of self-assembled PCDA molecules. These molecules preferentially align into domains which reflect the underlying symmetry of the graphene lattice. Upon exposure of these monolayers to the ALD precursor diethyl zinc, it was found that the carboxylate groups of the PCDA molecule preferentially react with the precursor, leading to the formation of large ordered domains of ZnO molecular chains. Using a combined GIWAXS/GISAXS study, we established the orientational relationship of these domains with respect to the underlying substrate, finding that the ZnO chains are aligned along the SiC<10> family of directions, presumably because this allows the alkyl tails of the PCDA molecules to lay along the preferred EG<10> direction. This work highlights the influence of the chemical structure of the molecular monolayer on both its

assembly and potential for functionalization, as well as the identifying routes for the formation of sub-10 nanometer nanostructures on graphene.

8.2: Future Work

One of the conclusions of this work is that a combined application XSW-XPS and XRR is perhaps one of the most powerful methods in the study of the complex, low-dimensional, EG/SiC interfacial structures. For these structures, this suite of techniques holds provides chemically-sensitive, vertical profiles not accessible with other, more conventional methods. However, the work presented in this thesis was limited to only a handful of structures and can conceivably be expanded to address a wide variety of similar systems. A well-established understanding of the measurement with respect to EG/SiC, as well as the development of the necessary analysis procedures should stimulate the extension of this approach to other systems. In the following sections I outline particular systems of interest or technical expansions of the work that may be appropriate future work.

8.2.1: EG on C-face and Non-Polar SiC

This thesis concentrated specifically on graphene grown on the Si-terminated face of SiC because, as opposed to the other polar (C-terminated) face of SiC, because graphene growth on SiC(0001) is fairly well-controlled to \sim ML coverage and the C and Si core-level photoelectron spectra were well-studied, if not well-understood. Graphene grown on SiC(000 $\bar{1}$), on the other hand, is distinct from that what is observed on the Si-face. Namely, EG grown on the C-face is more difficult to control and the graphene layers order into turbostatically stacked layers rotated by 0° and 30° with respect to the SiC substrate, although there is evidence of a large population

rotational stacking faults. In addition, the interfacial ordering between the graphene and the SiC(000 $\bar{1}$) is rather poorly-understood as compared to that of SiC(0001) [17, 19, 24, 109, 317].

Historically, interpretations of LEED data have indicated a C-rich interfacial phase persisting deep into the SiC bulk and possessing a large population of sp^3 -hybridized C atoms. The Conrad and Magaud groups have proposed a C-rich interfacial structure that possesses strong covalent interactions with the SiC(000 $\bar{1}$) surface based on high-resolution XRR and non-specular CTR, as well as DFT [318, 319]. Their XRR suggests that there exists a strongly-bonded graphene layer at ~ 1.65 Å above the terminal C layer which would act as a buffer layer, similar in some ways to what exists on Si-face SiC. Others, however, contend that, based on the lack of spectroscopic evidence of a distinct interfacial phase and observation of well-formed π -bands even at low graphitic coverage, that interaction with the graphene layer and the substrate must be weak [320]. In their 2008 PRB, Emtsev and coworkers note that this weakly-bonded configuration is consistent with the turbostatic relationship graphene layers arrayed on the C-face of SiC. To date, this issue remains largely unresolved due to the experimental challenges of deconvoluting the signals within the EG/SiC(000 $\bar{1}$) X-ray photoelectron spectrum, as well as well-known ambiguities that arise during the model-based analysis of CTR data (see [Section 3.2](#)).

A study similar to that presented in [Chapter 4](#) may prove the best route for the structural determination of the EG/SiC(000 $\bar{1}$) interface (and its prephases [321]). The success of such an experiment is contingent on the production of an EG/SiC(000 $\bar{1}$) sample with relatively low coverage in order to reduce the dominance of the EG peak in the C 1s spectrum. This has historically been challenge [17, 19, 72], although some recent advances in growth methods

indicate that well-formed $\sim 1\text{ML}$ EG/SiC(000 $\bar{1}$) is obtainable [19, 322, 323]. Distinct, separable components within the C 1s core-level spectrum would, of course, facilitate the study, but whether these distinct signals exist is still debated [320, 324]. There is, however, one recent measurement have identified both high- and low-BE interfacial components, shifted by ± 0.5 eV with respect to the EG peak [323], but the authors do not suggest a source for this signal beyond their its origin at the interface. An XSW-XPS experiment should, at the very least, clarify whether the sources of these signals are in distinct positions with respect to the SiC. A dual-pronged approach utilizing both XRR and XSW-XPS would provide complementary electron density profile and chemically-resolved atomic density information that may lead to the ultimate resolution of the elusive EG/SiC(000 $\bar{1}$) interfacial structure.

Apart from the polar faces of SiC, graphene is has been shown to grow on the non-polar a -plane (11 $\bar{2}$ 0) and m -plane (1 $\bar{1}$ 00) of SiC [81], as well as the semi-polar r -plane (10 $\bar{1}$ 4) [325], despite the lack of a hexagonal growth template on those surfaces. The non-hexagonal substrate symmetry may lead to distinct interfacial structures and electronic behavior, thereby offering new possibilities for epitaxial graphene growth unlike those observed on the polar faces. Initial reports suggest that growth of graphene one these surfaces lack a highly-interacting interfacial layer that exists for EG/SiC(0001) [325]. Application of the techniques presented in this work could provide valuable structural information about these new EG systems, perhaps helping to avoid the confusion that arose during the initial structural studies of EG/SiC(0001).

8.2.2: Intercalated EG/SiC(0001)

In the present work, the study of intercalated EG/SiC structures was limited to the archetypical H-intercalated EG/SiC(0001) system [30]. Recent progress has indicated, however, that the

successful intercalation of various atomic species into the EG/SiC(0001) interface is the rule rather than the exception, and intercalation (or at least EG₀ layer decoupling) has been claimed for H, Li, O, F, Na, Si, Ca, Ge, and Au (see Ref. [33] and references therein). Notably, however, there exists no detailed structural information for any of these intercalated structures. The techniques presented in this work are particularly suited to tackle this challenge. While, in principle, study of any of the structures arising from the intercalation of the atomic species identified in [Figure 8.1](#) is possible, I have identified Ge [35] and Au [34] as the most attractive of these options both scientifically and experimentally. The initial works on each of these species [33-35] report improved electronic properties of the graphene due to the decoupling of the interfacial layer from the substrate. In addition, it appears that the quantity of intercalants present at the interface can be adjusted to tune the degree of *n*- and *p*-doping of the overlaying graphene sheets. The ability to tune the properties of the graphene by engineering the interface opens interesting avenues for the control of graphene nanostructures. In terms of electronic behavior, Ge is interesting because two coexistent *n*- and *p*-doped phases can be formed [35], opening the possibility of the construction of lateral *p-n* graphene junctions via controlled intercalation. On the other hand, Au intercalation has shown asymmetric *n*- and *p*-type doping strength [34]. Calculations have shown that this may be due to the difference in the electronegativity and strain at 3/8 ML and 9/8 ML Au interfacial coverage [326].

From an experimental point of view, both Ge and Au have easily accessible and analyzable fluorescence lines at energies of $E_\gamma \sim 9.87$ keV for the Ge K α or $E_\gamma \sim 9.65$ keV for the Au L α , making them ideal candidates for XSW-XRF. Accordingly, Ge K and Au L₃ edges are conveniently located at 11.103 and 11.919 keV, respectively, opening the possibility for

1																		18																											
1A																8A																													
1	H Hydrogen 1.01																	2	He Helium 4.00																										
2	3 Li Lithium 6.94	4 Be Beryllium 9.01															5 B Boron 10.81	6 C Carbon 12.01	7 N Nitrogen 14.01	8 O Oxygen 16.00	9 F Fluorine 19.00	10 Ne Neon 20.18																							
3	11 Na Sodium 22.99	12 Mg Magnesium 24.31	3 Sc Scandium 44.96	4 Ti Titanium 47.87	5 V Vanadium 50.94	6 Cr Chromium 52.00	7 Mn Manganese 54.94	8 Fe Iron 55.85	9 Co Cobalt 58.93	10 Ni Nickel 58.69	11 Cu Copper 63.55	12 Zn Zinc 65.39	13 Al Aluminum 26.98	14 Si Silicon 28.09	15 P Phosphorus 30.97	16 S Sulfur 32.07	17 Cl Chlorine 35.45	18 Ar Argon 39.95																											
4	19 K Potassium 39.10	20 Ca Calcium 40.08	21 Sc Scandium 44.96	22 Ti Titanium 47.87	23 V Vanadium 50.94	24 Cr Chromium 52.00	25 Mn Manganese 54.94	26 Fe Iron 55.85	27 Co Cobalt 58.93	28 Ni Nickel 58.69	29 Cu Copper 63.55	30 Zn Zinc 65.39	31 Ga Gallium 69.72	32 Ge Germanium 72.61	33 As Arsenic 74.92	34 Se Selenium 78.96	35 Br Bromine 79.90	36 Kr Krypton 83.80																											
5	37 Rb Rubidium 85.47	38 Sr Strontium 87.62	39 Y Yttrium 88.91	40 Zr Zirconium 91.22	41 Nb Niobium 92.91	42 Mo Molybdenum 95.94	43 Tc Technetium (98)	44 Ru Ruthenium 101.07	45 Rh Rhodium 102.91	46 Pd Palladium 106.42	47 Ag Silver 107.87	48 Cd Cadmium 112.41	49 In Indium 114.82	50 Sn Tin 118.71	51 Sb Antimony 121.76	52 Te Tellurium 127.60	53 I Iodine 126.90	54 Xe Xenon 131.29																											
6	55 Cs Cesium 132.91	56 Ba Barium 137.33	57 La Lanthanum 138.91	72 Hf Hafnium 178.49	73 Ta Tantalum 180.95	74 W Tungsten 183.84	75 Re Rhenium 186.21	76 Os Osmium 190.23	77 Ir Iridium 192.22	78 Pt Platinum 195.08	79 Au Gold 196.97	80 Hg Mercury 200.59	81 Tl Thallium 204.38	82 Pb Lead 207.2	83 Bi Bismuth 208.98	84 Po Polonium (209)	85 At Astatine (210)	86 Rn Radon (222)																											
7	87 Fr Francium (223)	88 Ra Radium (226)	89 Ac Actinium (227)	104 Rf Rutherfordium (261)	105 Db Dubnium (262)	106 Sg Seaborgium (266)	107 Bh Bohrium (264)	108 Hs Hassium (269)	109 Mt Meitnerium (268)																																				
* If this number is in parentheses, then it refers to the atomic mass of the most stable isotope.																																													
<table border="1"> <tbody> <tr> <td>58 Ce Cerium 140.12</td> <td>59 Pr Praseodymium 140.91</td> <td>60 Nd Neodymium 144.24</td> <td>61 Pm Promethium (145)</td> <td>62 Sm Samarium 150.36</td> <td>63 Eu Europium 151.96</td> <td>64 Gd Gadolinium 157.25</td> <td>65 Tb Terbium 158.93</td> <td>66 Dy Dysprosium 162.50</td> <td>67 Ho Holmium 164.93</td> <td>68 Er Erbium 167.26</td> <td>69 Tm Thulium 168.93</td> <td>70 Yb Ytterbium 173.04</td> <td>71 Lu Lutetium 174.97</td> </tr> <tr> <td>90 Th Thorium 232.04</td> <td>91 Pa Protactinium 231.04</td> <td>92 U Uranium 238.03</td> <td>93 Np Neptunium (237)</td> <td>94 Pu Plutonium (244)</td> <td>95 Am Americium (243)</td> <td>96 Cm Curium (247)</td> <td>97 Bk Berkelium (247)</td> <td>98 Cf Californium (251)</td> <td>99 Es Einsteinium (252)</td> <td>100 Fm Fermium (257)</td> <td>101 Md Mendelevium (258)</td> <td>102 No Nobelium (259)</td> <td>103 Lr Lawrencium (262)</td> </tr> </tbody> </table>																		58 Ce Cerium 140.12	59 Pr Praseodymium 140.91	60 Nd Neodymium 144.24	61 Pm Promethium (145)	62 Sm Samarium 150.36	63 Eu Europium 151.96	64 Gd Gadolinium 157.25	65 Tb Terbium 158.93	66 Dy Dysprosium 162.50	67 Ho Holmium 164.93	68 Er Erbium 167.26	69 Tm Thulium 168.93	70 Yb Ytterbium 173.04	71 Lu Lutetium 174.97	90 Th Thorium 232.04	91 Pa Protactinium 231.04	92 U Uranium 238.03	93 Np Neptunium (237)	94 Pu Plutonium (244)	95 Am Americium (243)	96 Cm Curium (247)	97 Bk Berkelium (247)	98 Cf Californium (251)	99 Es Einsteinium (252)	100 Fm Fermium (257)	101 Md Mendelevium (258)	102 No Nobelium (259)	103 Lr Lawrencium (262)
58 Ce Cerium 140.12	59 Pr Praseodymium 140.91	60 Nd Neodymium 144.24	61 Pm Promethium (145)	62 Sm Samarium 150.36	63 Eu Europium 151.96	64 Gd Gadolinium 157.25	65 Tb Terbium 158.93	66 Dy Dysprosium 162.50	67 Ho Holmium 164.93	68 Er Erbium 167.26	69 Tm Thulium 168.93	70 Yb Ytterbium 173.04	71 Lu Lutetium 174.97																																
90 Th Thorium 232.04	91 Pa Protactinium 231.04	92 U Uranium 238.03	93 Np Neptunium (237)	94 Pu Plutonium (244)	95 Am Americium (243)	96 Cm Curium (247)	97 Bk Berkelium (247)	98 Cf Californium (251)	99 Es Einsteinium (252)	100 Fm Fermium (257)	101 Md Mendelevium (258)	102 No Nobelium (259)	103 Lr Lawrencium (262)																																

Figure 8.1: Elements which have shown evidence of decoupling the interfacial layer from the SiC(0001) substrate upon intercalation.

resonant-anomalous X-ray reflectivity (RAXR) studies, which would be useful if the interfacial region proves too thick for XSW-XRF analysis. Fabrication of these intercalated heterostructures are well-described in the literature and are formed by deposition of the species from a Knudsen cell onto a EG/SiC(0001) surface and subsequent anneal at ~ 1000 C [34, 35]. These growth parameters are accessible in the UHV setup at 5-ID-C, which would allow for *in situ* monitoring of the interfacial structure during deposition, intercalation and de-intercalation.

8.2.3: Other 2D Materials: MoS₂, BN, and Silicene

Since the discovery of graphene, the interest in 2D materials such as MoS₂, BN, and other 2D materials has burgeoned [1, 327, 328]. Isolated sheets MoS₂ are direct bandgap semiconductors with band gaps of 1.8 eV, and have been shown to possess high room-temperature mobilities

[329]. Similarly, BN monolayers are direct bandgap insulators, and have been incorporated with graphene to great effect, improving mobilities and carrier inhomogeneities by approximately an order of magnitude over graphene devices supported on SiO₂ [330]. Both MoS₂ and BN monolayers have been grown directly on graphene substrates layers using CVD [331, 332], and so the direct incorporation with EG/SiC is plausible. As it is evident that the integration of various 2D materials, including EG, MoS₂, and BN is a promising route for nanoscale device fabrication, the characterization techniques presented in this work may assist in the investigation of the atomic-scale interaction between the 2D materials.

Another interesting material that has been recently isolated discovered is the silicon analog of graphene, silicene. This material is of specific interest for FET applications because, in contrast to graphene, it is predicted that a band gap can be induced in silicene (and germanene) monolayers upon application of transverse electric field transverse across to the sheet [333, 334]. Silicene is reported to grow on various Ag surfaces [334, 335], and possesses a electronic structure reminiscent of graphene [336]. The interaction of the Ag surface and the Si is thought to be critically important in the formation of the silicene atomic and electronic structure [334, 337], and is therefore deserving of thorough structural investigation. To date, structural studies have been mostly limited to STM and ARPES. Back-reflection XSW-XPS studies of adsorbates on Ag surfaces are well-established (for example see Ref. [175] and references therein), suggesting a low entrance barrier for studies of silicene on Ag.

8.2.4: Site-specific XSW-HARPES on EG/SiC

Recent advancements in hard X-ray angle resolved photoemission spectroscopy (HARPES) has laid the groundwork for some potentially interesting experiments in which general HARPES

studies may be enhanced by standing waves. Conventional ARPES measurements (using ~ 100 eV incident beam energy) are capable of mapping the angular and energy distribution of photoelectrons originating from the valence band, ultimately producing a map of the electronic structure. The low energies typically used in these experiments lead to highly surface-sensitive ARPES spectra. However, researchers interested in the bulk electronic structure often find the extreme surface sensitivity a serious drawback and have made attempts to extend ARPES measurements into the “high-energy” regime, e.g., up to ~ 6 keV. This can increase the inelastic mean free path to ~ 10 nm, depending on the specifics of the system.

A perhaps unintended benefit of the efforts extend ARPES into the \sim keV regime is that it would allow access to single-crystal Bragg conditions that were previously inaccessible due to the long wavelength limit ($2d_{\text{hkl}} > \lambda$). For the example of 6H-SiC this limit is $\lambda = 5.04 \text{ \AA}$ or 2.46 keV, well within the proven operational ranges for HARPES measurements [338]. In principle, performing XSW-HARPES is physically no different from previous studies which have used XSW to modulate valence-level photoelectron intensities [176], except in that the photoelectron angular dependence is resolved. This technique could provide highly-sensitive structural information about the sources of the photoelectrons observed in the ARPES band maps. This has specific applications to the EG/SiC system, for which some features observed in conventional ARPES spectra are not well understood. A good example of this is from the work of Emtsev *et al.* in which two localized gap states are observed near the E_F in the spectrum from a SiC(0001) surface covered with nominally only the $6\sqrt{3}$ reconstructed phase (see [Figure 8.2](#)) [24]. The source of these features is unknown, and although Emtsev and coworkers suggest these states may arise from defects or dangling bonds at the interface. In addition, it is unknown if these

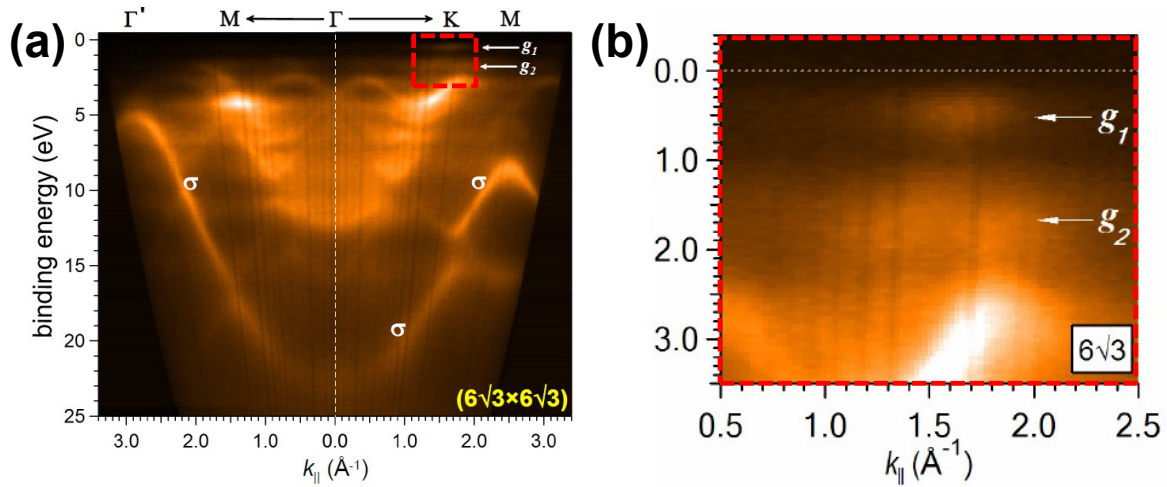


Figure 8.2: ARPES data for a nominal zero-layer graphene sample from Emtsev *et al.* (Ref. [24]). (a) The extended-range and (b) magnifications of the ARPES maps. Two localized surface states, g_1 and g_2 , are observed at 0.5 and 1.6 eV below the Fermi level, respectively. The origin of these states is unclear, but it is suggested that they may arise from interfacial defects [23, 24, 320] and may influence the behavior of the overlaying graphene.

states persist after full graphitization because the extreme surface sensitivity of the ARPES measurement highly biases the spectra towards photoelectrons emitted from the overlaying graphene sheets.

There are, of course, a myriad of challenges that could arise in an XSW-HARPES study. The high-energy nature of HARPES itself introduces new issues which are not critical to conventional ARPES measurements including k -space resolution, photoionization sensitivity (interaction cross-section), and recoil effects. A review of these considerations can be found in Ref. [338] and references therein. Regardless, the potential to acquire ARPES data with structure sensitivity is intriguing, and the information provided by such a study on EG/SiC may lead to the elucidation of sources of poorly-understood ARPES spectral features, leading to a more thorough understanding of the electronic structure of EG/SiC. The successful combination of XSW with HARPES would prove to be a powerful tool in the interpretation of ARPES spectra. This route

of research is made even more appealing considering the construction of the new HARPES beamline at Sector 29 at the Advanced Photon Source.

References:

- [1] K.S. Novoselov, D. Jiang, F. Schedin, T.J. Booth, V.V. Khotkevich, S.V. Morozov, A.K. Geim. "Two-dimensional atomic crystals," Proceedings of the National Academy of Sciences of the United States of America **102**(30), 10451-10453 (2005).
- [2] K.S. Novoselov, A.K. Geim, S.V. Morozov, D. Jiang, Y. Zhang, S.V. Dubonos, I.V. Grigorieva, A.A. Firsov. "Electric field effect in atomically thin carbon films," Science **306**(5696), 666-669 (2004).
- [3] A.K. Geim, K.S. Novoselov. "The rise of graphene," Nature Materials **6**(3), 183-191 (2007).
- [4] K.S. Novoselov, V.I. Fal'ko, L. Colombo, P.R. Gellert, M.G. Schwab, K. Kim. "A roadmap for graphene," Nature **490**(7419), 192-200 (2012).
- [5] A.H. Castro Neto, F. Guinea, N.M.R. Peres, K.S. Novoselov, A.K. Geim. "The electronic properties of graphene," Reviews of Modern Physics **81**(1), 109-162 (2009).
- [6] A.S. Mayorov, R.V. Gorbachev, S.V. Morozov, L. Britnell, R. Jalil, L.A. Ponomarenko, P. Blake, K.S. Novoselov, K. Watanabe, T. Taniguchi, *et al.* "Micrometer-scale ballistic transport in encapsulated graphene at room temperature," Nano Letters **11**(6), 2396-2399 (2011).
- [7] X. Du, I. Skachko, A. Barker, E.Y. Andrei. "Approaching ballistic transport in suspended graphene," Nature Nanotechnology **3**(8), 491-495 (2008).
- [8] C. Berger, Z.M. Song, X.B. Li, X.S. Wu, N. Brown, C. Naud, D. Mayou, T.B. Li, J. Hass, A.N. Marchenkov, *et al.* "Electronic confinement and coherence in patterned epitaxial graphene," Science **312**(5777), 1191-1196 (2006).
- [9] K.S. Novoselov, Z. Jiang, Y. Zhang, S.V. Morozov, H.L. Stormer, U. Zeitler, J.C. Maan, G.S. Boebinger, P. Kim, A.K. Geim. "Room-temperature quantum Hall effect in graphene," Science **315**(5817), 1379 (2007).

- [10] A. Bostwick, T. Ohta, T. Seyller, K. Horn, E. Rotenberg. "Quasiparticle dynamics in graphene," *Nature Physics* **3**(1), 36-40 (2007).
- [11] F. Schedin, A. Geim, S. Morozov, E. Hill, P. Blake, M. Katsnelson, K. Novoselov. "Detection of individual gas molecules adsorbed on graphene," *Nature Materials* **6**(9), 652-655 (2007).
- [12] Y.-M. Lin, P. Avouris. "Strong suppression of electrical noise in bilayer graphene nanodevices," *Nano Letters* **8**(8), 2119-2125 (2008).
- [13] Y. Hernandez, V. Nicolosi, M. Lotya, F.M. Blighe, Z. Sun, S. De, I. McGovern, B. Holland, M. Byrne, Y.K. Gun'Ko. "High-yield production of graphene by liquid-phase exfoliation of graphite," *Nature Nanotechnology* **3**(9), 563-568 (2008).
- [14] S. Stankovich, D.A. Dikin, R.D. Piner, K.A. Kohlhaas, A. Kleinhammes, Y. Jia, Y. Wu, S.T. Nguyen, R.S. Ruoff. "Synthesis of graphene-based nanosheets via chemical reduction of exfoliated graphite oxide," *Carbon* **45**(7), 1558-1565 (2007).
- [15] P.W. Sutter, J.-I. Flege, E.A. Sutter. "Epitaxial graphene on ruthenium," *Nature Materials* **7**(5), 406-411 (2008).
- [16] X. Li, W. Cai, J. An, S. Kim, J. Nah, D. Yang, R. Piner, A. Velamakanni, I. Jung, E. Tutuc, *et al.* "Large-area synthesis of high-quality and uniform graphene films on copper foils," *Science* **324**(5932), 1312-1314 (2009).
- [17] A.J. Van Bommel, J.E. Crombeen, A. Van Tooren. "LEED and Auger electron observations of the SiC(0001) surface," *Surface Science* **48**(2), 463-472 (1975).
- [18] C. Berger, Z. Song, T. Li, X. Li, A.Y. Ogbazghi, R. Feng, Z. Dai, A.N. Marchenkov, E.H. Conrad, P.N. First, *et al.* "Ultrathin epitaxial graphite: 2D electron gas properties and a route toward graphene-based nanoelectronics," *The Journal of Physical Chemistry B* **108**(52), 19912-19916 (2004).
- [19] W.A. de Heer, C. Berger, M. Ruan, M. Sprinkle, X.B. Li, Y.K. Hu, B.Q. Zhang, J. Hankinson, E. Conrad. "Large area and structured epitaxial graphene produced by confinement controlled sublimation of silicon carbide," *Proceedings of the National Academy of Sciences of the United States of America* **108**(41), 16900-16905 (2011).
- [20] L. Nyakiti, R. Myers-Ward, V. Wheeler, E. Imhoff, F. Bezares, H. Chun, J. Caldwell, A. Friedman, B. Matis, J. Baldwin. "Bilayer graphene grown on 4H-SiC(0001) step-free mesas," *Nano Letters* **12**(4), 1749-1756 (2012).
- [21] J. Hass, J.E. Millan-Otoya, P.N. First, E.H. Conrad. "Interface structure of epitaxial graphene grown on 4H-SiC(0001)," *Physical Review B* **78**(20), 205424 (2008).

- [22] G.M. Rutter, N.P. Guisinger, J.N. Crain, E.A.A. Jarvis, M.D. Stiles, T. Li, P.N. First, J.A. Stroscio. "Imaging the interface of epitaxial graphene with silicon carbide via scanning tunneling microscopy," *Physical Review B* **76**(23), 235416 (2007).
- [23] Y. Qi, S.H. Rhim, G.F. Sun, M. Weinert, L. Li. "Epitaxial graphene on SiC(0001): More than just honeycombs," *Physical Review Letters* **105**(8), 085502 (2010).
- [24] K.V. Emtsev, F. Speck, T. Seyller, L. Ley, J.D. Riley. "Interaction, growth, and ordering of epitaxial graphene on SiC{0001} surfaces: A comparative photoelectron spectroscopy study," *Physical Review B* **77**(15), (2008).
- [25] S.Y. Zhou, G.H. Gweon, A.V. Fedorov, P.N. First, W.A. De Heer, D.H. Lee, F. Guinea, A.H.C. Neto, A. Lanzara. "Substrate-induced bandgap opening in epitaxial graphene," *Nature Materials* **6**(11), 916-916 (2007).
- [26] E. Rotenberg, A. Bostwick, T. Ohta, J.L. McChesney, T. Seyller, K. Horn. "Origin of the energy bandgap in epitaxial graphene," *Nature Materials* **7**(4), 258-259 (2008).
- [27] X.J. Weng, J.A. Robinson, K. Trumbull, R. Cavalero, M.A. Fanton, D. Snyder. "Structure of few-layer epitaxial graphene on 6H-SiC(0001) at atomic resolution," *Applied Physics Letters* **97**(20), 201905 (2010).
- [28] S. Zhou, D. Siegel, A. Fedorov, F. El Gabaly, A. Schmid, A.C. Neto, D.-H. Lee, A. Lanzara. "Origin of the energy bandgap in epitaxial graphene," *Nature Materials* **7**(4), 259-260 (2008).
- [29] C. Riedl, U. Starke, J. Bernhardt, M. Franke, K. Heinz. "Structural properties of the graphene-SiC(0001) interface as a key for the preparation of homogeneous large-terrace graphene surfaces," *Physical Review B* **76**(24), 374009 (2007).
- [30] C. Riedl, C. Coletti, T. Iwasaki, A.A. Zakharov, U. Starke. "Quasi-free-standing epitaxial graphene on SiC obtained by hydrogen intercalation," *Physical Review Letters* **103**(24), 246804 (2009).
- [31] J.A. Robinson, M. Hollander, M. LaBella, K.A. Trumbull, R. Cavalero, D.W. Snyder. "Epitaxial graphene transistors: Enhancing performance via hydrogen intercalation," *Nano Letters* **11**(9), 3875-3880 (2011).
- [32] F. Varchon, P. Mallet, J.Y. Veuillen, L. Magaud. "Ripples in epitaxial graphene on the Si-terminated SiC(0001) surface," *Physical Review B* **77**(23), 235412 (2008).

- [33] U. Starke, S. Forti, K. Emtsev, C. Coletti. "Engineering the electronic structure of epitaxial graphene by transfer doping and atomic intercalation," *MRS Bulletin* **37**(12), 1177-1186 (2012).
- [34] I. Gierz, T. Suzuki, R.T. Weitz, D.S. Lee, B. Krauss, C. Riedl, U. Starke, H. Höchst, J.H. Smet, C.R. Ast, *et al.* "Electronic decoupling of an epitaxial graphene monolayer by gold intercalation," *Physical Review B* **81**(23), 235408 (2010).
- [35] K.V. Emtsev, A.A. Zakharov, C. Coletti, S. Forti, U. Starke. "Ambipolar doping in quasifree epitaxial graphene on SiC(0001) controlled by Ge intercalation," *Physical Review B* **84**(12), 125423 (2011).
- [36] Q.H. Wang, M.C. Hersam. "Room-temperature molecular-resolution characterization of self-assembled organic monolayers on epitaxial graphene," *Nature Chemistry* **1**(3), 206-211 (2009).
- [37] A. Deshpande, C.H. Sham, J.M.P. Alaboson, J.M. Mullin, G.C. Schatz, M.C. Hersam. "Self-assembly and photopolymerization of sub-2 nm one-dimensional organic nanostructures on graphene," *Journal of the American Chemical Society* **134**(40), 16759-16764 (2012).
- [38] H.W. Kroto, J.R. Heath, S.C. O'Brien, R.F. Curl, R.E. Smalley. "C₆₀: Buckminsterfullerene," *Nature* **318**(6042), 162-163 (1985).
- [39] S. Iijima. "Helical microtubules of graphitic carbon," *Nature* **354**(6348), 56-58 (1991).
- [40] P.R. Wallace. "The band theory of graphite," *Physical Review* **71**(9), 622-634 (1947).
- [41] H.P. Boehm, A. Clauss, G.O. Fischer, U. Hofmann. "Das Adsorptionsverhalten sehr dünner Kohlenstoff-Folien," *Zeitschrift für anorganische und allgemeine Chemie* **316**(3-4), 119-127 (1962).
- [42] G.W. Semenoff. "Condensed-matter simulation of a three-dimensional anomaly," *Physical Review Letters* **53**(26), 2449-2452 (1984).
- [43] Y. Zheng, T. Ando. "Hall conductivity of a two-dimensional graphite system," *Physical Review B* **65**(24), 245420 (2002).
- [44] F.D.M. Haldane. "Model for a quantum Hall effect without Landau levels: Condensed-matter realization of the "parity anomaly"," *Physical Review Letters* **61**(18), 2015-2018 (1988).

- [45] M.I. Katsnelson, K. Novoselov. "Graphene: New bridge between condensed matter physics and quantum electrodynamics," *Solid State Communications* **143**(1), 3-13 (2007).
- [46] N. Tombros, C. Jozsa, M. Popinciuc, H.T. Jonkman, B.J. Van Wees. "Electronic spin transport and spin precession in single graphene layers at room temperature," *Nature* **448**(7153), 571-574 (2007).
- [47] Y. Zhang, Y.W. Tan, H.L. Stormer, P. Kim. "Experimental observation of the quantum Hall effect and Berry's phase in graphene," *Nature* **438**(7065), 201-204 (2005).
- [48] K.S. Novoselov, A.K. Geim, S.V. Morozov, D. Jiang, M.I. Katsnelson, I.V. Grigorieva, S.V. Dubonos, A.A. Firsov. "Two-dimensional gas of massless Dirac fermions in graphene," *Nature* **438**(7065), 197-200 (2005).
- [49] R. Saito, G. Dresselhaus, M.S. Dresselhaus. *Physical properties of carbon nanotubes*: World Scientific; 1998.
- [50] J.H. Chen, C. Jang, S. Xiao, M. Ishigami, M.S. Fuhrer. "Intrinsic and extrinsic performance limits of graphene devices on SiO₂," *Nature Nanotechnology* **3**(4), 206-209 (2008).
- [51] S.V. Morozov, K.S. Novoselov, F. Schedin, D. Jiang, A.A. Firsov, A.K. Geim. "Two-dimensional electron and hole gases at the surface of graphite," *Physical Review B* **72**(20), 201401(R) (2005).
- [52] D.L. Rode. "Electron Transport in InSb, InAs, and InP," *Physical Review B* **3**(10), 3287-3299 (1971).
- [53] J. Moser, A. Barreiro, A. Bachtold. "Current-induced cleaning of graphene," *Applied Physics Letters* **91**(16), 163513 (2007).
- [54] L. Liao, J. Bai, R. Cheng, Y.-C. Lin, S. Jiang, Y. Qu, Y. Huang, X. Duan. "Sub-100 nm Channel Length Graphene Transistors," *Nano Letters* **10**(10), 3952-3956 (2010).
- [55] I. Meric, C.R. Dean, H. Shu-Jen, W. Lei, K.A. Jenkins, J. Hone, K.L. Shepard, editors. High-frequency performance of graphene field effect transistors with saturating IV-characteristics. *Electron Devices Meeting (IEDM), 2011 IEEE International*; 2011 5-7 Dec. 2011.
- [56] J. Cai, P. Ruffieux, R. Jaafar, M. Bieri, T. Braun, S. Blankenburg, M. Muoth, A.P. Seitsonen, M. Saleh, X. Feng. "Atomically precise bottom-up fabrication of graphene nanoribbons," *Nature* **466**(7305), 470-473 (2010).

- [57] M.Y. Han, B. Özyilmaz, Y. Zhang, P. Kim. "Energy band-gap engineering of graphene nanoribbons," *Physical Review Letters* **98**(20), 206805 (2007).
- [58] Z. Chen, Y.M. Lin, M.J. Rooks, P. Avouris. "Graphene nano-ribbon electronics," *Physica E: Low-dimensional Systems and Nanostructures* **40**(2), 228-232 (2007).
- [59] T. Ohta, A. Bostwick, T. Seyller, K. Horn, E. Rotenberg. "Controlling the electronic structure of bilayer graphene," *Science* **313**(5789), 951-954 (2006).
- [60] E.V. Castro, K.S. Novoselov, S.V. Morozov, N.M.R. Peres, J.M.B.L. dos Santos, J. Nilsson, F. Guinea, A.K. Geim, A.H.C. Neto. "Biased bilayer graphene: Semiconductor with a gap tunable by the electric field effect," *Physical Review Letters* **99**(21), 216802 (2007).
- [61] D.C. Elias, R.R. Nair, T.M.G. Mohiuddin, S.V. Morozov, P. Blake, M.P. Halsall, A.C. Ferrari, D.W. Boukhvalov, M.I. Katsnelson, A.K. Geim, *et al.* "Control of graphene's properties by reversible hydrogenation: Evidence for graphane," *Science* **323**(5914), 610-613 (2009).
- [62] J.T. Robinson, J.S. Burgess, C.E. Junkermeier, S.C. Badescu, T.L. Reinecke, F.K. Perkins, M.K. Zalalutdniov, J.W. Baldwin, J.C. Culbertson, P.E. Sheehan, *et al.* "Properties of fluorinated graphene films," *Nano Letters* **10**(8), 3001-3005 (2010).
- [63] F. Schwierz. "Graphene transistors," *Nature Nanotechnology* **5**(7), 487-496 (2010).
- [64] M.C. Lemme, T.J. Echtermeyer, M. Baus, H. Kurz. "A graphene field-effect device," *Electron Device Letters, IEEE* **28**(4), 282-284 (2007).
- [65] R.R. Nair, P. Blake, A.N. Grigorenko, K.S. Novoselov, T.J. Booth, T. Stauber, N.M.R. Peres, A.K. Geim. "Fine structure constant defines visual transparency of graphene," *Science* **320**(5881), 1308 (2008).
- [66] Y. Dan, Y. Lu, N.J. Kybert, Z. Luo, A.T.C. Johnson. "Intrinsic response of graphene vapor sensors," *Nano Letters* **9**(4), 1472-1475 (2009).
- [67] L. Liao, X. Duan. "Graphene for radio frequency electronics," *Materials Today* **15**(7), 328-338 (2012).
- [68] M.J. Allen, V.C. Tung, R.B. Kaner. "Honeycomb carbon: a review of graphene," *Chemical Reviews* **110**(1), 132 (2010).
- [69] C. Mattevi, H. Kim, M. Chhowalla. "A review of chemical vapour deposition of graphene on copper," *J Mater Chem* **21**(10), 3324-3334 (2010).

- [70] N. Bartelt, K. McCarty. "Graphene growth on metal surfaces," *Mrs Bulletin* **37**(12), 1158-1165 (2012).
- [71] S. Bae, H. Kim, Y. Lee, X. Xu, J.S. Park, Y. Zheng, J. Balakrishnan, T. Lei, H.R. Kim, Y.I. Song. "Roll-to-roll production of 30-inch graphene films for transparent electrodes," *Nature Nanotechnology* **5**(8), 574-578 (2010).
- [72] W.A. De Heer, C. Berger, X. Wu, P.N. First, E.H. Conrad, X. Li, T. Li, M. Sprinkle, J. Hass, M.L. Sadowski. "Epitaxial graphene," *Solid State Communications* **143**(1), 92-100 (2007).
- [73] W.A. de Heer, C. Berger, X.S. Wu, M. Sprinkle, Y. Hu, M. Ruan, J.A. Stroscio, P.N. First, R. Haddon, B. Piot, *et al.* "Epitaxial graphene electronic structure and transport," *Journal of Physics D-Applied Physics* **43**(37), (2010).
- [74] P.N. First, W.A. de Heer, T. Seyller, C. Berger, J.A. Stroscio, J.-S. Moon. "Epitaxial Graphenes on Silicon Carbide," *MRS Bulletin* **35**(04), 296-305 (2010).
- [75] M. Sprinkle, M. Ruan, Y. Hu, J. Hankinson, M. Rubio-Roy, B. Zhang, X. Wu, C. Berger, W. De Heer. "Scalable templated growth of graphene nanoribbons on SiC," *Nature Nanotechnology* **5**(10), 727-731 (2010).
- [76] M. Ruan, Y. Hu, Z. Guo, R. Dong, J. Palmer, J. Hankinson, C. Berger, W.A. de Heer. "Epitaxial graphene on silicon carbide: Introduction to structured graphene," *MRS Bulletin* **37**(12), 1138-1147 (2012).
- [77] S. Lee, M.F. Toney, W. Ko, J.C. Randel, H.J. Jung, K. Munakata, J. Lu, T.H. Geballe, M.R. Beasley, R. Sinclair, *et al.* "Laser-synthesized epitaxial graphene," *ACS Nano* **4**(12), 7524-7530 (2010).
- [78] A. Al-Temimy, C. Riedl, U. Starke. "Low temperature growth of epitaxial graphene on SiC induced by carbon evaporation," *Applied Physics Letters* **95**(23), 231907 (2009).
- [79] W. Strupinski, K. Grodecki, A. Wyszomolek, R. Stepniewski, T. Szkopek, P.E. Gaskell, A. Grüneis, D. Haberer, R. Bozek, J. Krupka, *et al.* "Graphene epitaxy by chemical vapor deposition on SiC," *Nano Letters* **11**(4), 1786-1791 (2011).
- [80] G. Pensl, R. Helbig. "Silicon carbide (SiC)- Recent results in physics and in technology," *Festkörperprobleme* **30**, 133-156 (1990).
- [81] B.K. Daas, S.U. Omar, S. Shetu, K.M. Daniels, S. Ma, T.S. Sudarshan, M.V.S. Chandrashekhara. "Comparison of epitaxial graphene growth on polar and nonpolar 6H-SiC faces: On the growth of multilayer films," *Crystal Growth & Design* **12**(7), 3379-3387 (2012).

- [82] A. Ouerghi, R. Belkhou, M. Marangolo, M. Silly, S. El Moussaoui, M. Eddrief, L. Largeau, M. Portail, F. Sirotti. "Structural coherency of epitaxial graphene on 3C-SiC (111) epilayers on Si (111)," *Applied Physics Letters* **97**, 161905 (2010).
- [83] A. Ouerghi, M. Marangolo, R. Belkhou, S. El Moussaoui, M. Silly, M. Eddrief, L. Largeau, M. Portail, B. Fain, F. Sirotti. "Epitaxial graphene on 3C-SiC (111) pseudosubstrate: Structural and electronic properties," *Physical Review B* **82**(12), 125445 (2010).
- [84] G.G. Jernigan, B.L. VanMil, J.L. Tedesco, J.G. Tischler, E.R. Glaser, A. Davidson, P.M. Campbell, D.K. Gaskill. "Comparison of epitaxial graphene on Si-face and C-face 4H-SiC formed by ultrahigh vacuum and RF furnace production," *Nano Letters* **9**(7), 2605-2609 (2009).
- [85] C. Riedl, C. Coletti, U. Starke. "Structural and electronic properties of epitaxial graphene on SiC(0001): A review of growth, characterization, transfer doping and hydrogen intercalation," *Journal of Physics D: Applied Physics* **43**(37), 374009 (2010).
- [86] J. Hass, W.A.d. Heer, E.H. Conrad. "The growth and morphology of epitaxial multilayer graphene," *Journal of Physics: Condensed Matter* **20**(32), 323202 (2008).
- [87] T. Seyller. *Epitaxial graphene on SiC (0001)*. In: Raza H., editor. in *Graphene Nanoelectronics*. Berling: Springer-Verlag Berlind Heidelberg; 2012). p. 135-159.
- [88] K.V. Emtsev, A. Bostwick, K. Horn, J. Jobst, G.L. Kellogg, L. Ley, J.L. McChesney, T. Ohta, S.A. Reshanov, J. Rohrl, *et al.* "Towards wafer-size graphene layers by atmospheric pressure graphitization of silicon carbide," *Nature Materials* **8**(3), 203-207 (2009).
- [89] C. Onneby, C. Pantano. "Silicon oxycarbide formation on SiC surfaces and at the SiC/SiO₂ interface," *Journal of Vacuum Science & Technology A: Vacuum, Surfaces, and Films* **15**(3), 1597-1602 (1997).
- [90] R. Kaplan. "Surface structure and composition of β - and 6H-SiC," *Surface Science* **215**(1-2), 111-134 (1989).
- [91] H. Hibino, H. Kageshima, F. Maeda, M. Nagase, Y. Kobayashi, H. Yamaguchi. "Microscopic thickness determination of thin graphite films formed on SiC from quantized oscillation in reflectivity of low-energy electrons," *Physical Review B* **77**(7), 075413 (2008).

- [92] T. Ohta, F. El Gabaly, A. Bostwick, J.L. McChesney, K.V. Emtsev, A.K. Schmid, T. Seyller, K. Horn, E. Rotenberg. "Morphology of graphene thin film growth on SiC (0001)," *New Journal of Physics* **10**(2), 023034 (2008).
- [93] C. Virojanadara, M. Syväjarvi, R. Yakimova, L.I. Johansson, A.A. Zakharov, T. Balasubramanian. "Homogeneous large-area graphene layer growth on 6H-SiC(0001)," *Physical Review B* **78**(24), 245403 (2008).
- [94] T. Ohta, N.C. Bartelt, S. Nie, K. Thürmer, G.L. Kellogg. "Role of carbon surface diffusion on the growth of epitaxial graphene on SiC," *Physical Review B* **81**(12), 121411 (2010).
- [95] T. Ohta, A. Bostwick, J.L. McChesney, T. Seyller, K. Horn, E. Rotenberg. "Interlayer interaction and electronic screening in multilayer graphene investigated with angle-resolved photoemission spectroscopy," *Physical Review Letters* **98**(20), 206802 (2007).
- [96] W.A. de Heer, C. Berger, X.S. Wu, P.N. First, E.H. Conrad, X.B. Li, T.B. Li, M. Sprinkle, J. Hass, M.L. Sadowski, *et al.* "Epitaxial graphene," *Solid State Communications* **143**(1-2), 92-100 (2007).
- [97] M. Orlita, C. Faugeras, P. Plochocka, P. Neugebauer, G. Martinez, D.K. Maude, A.-L. Barra, M. Sprinkle, C. Berger, W.A. De Heer. "Approaching the Dirac point in high-mobility multilayer epitaxial graphene," *Physical Review Letters* **101**(26), 267601 (2008).
- [98] A.K. Geim. "Graphene: Status and prospects," *Science* **324**(5934), 1530-1534 (2009).
- [99] J. Ristein, S. Mammadov, T. Seyller. "Origin of doping in quasi-free-standing graphene on silicon carbide," *Physical Review Letters* **108**(24), 246104 (2012).
- [100] S. Kopylov, A. Tzalenchuk, S. Kubatkin, V.I. Falco. "Charge transfer between epitaxial graphene and silicon carbide," *Applied Physics Letters* **97**(11), 112109 (2010).
- [101] G.M. Rutter, J.N. Crain, N.P. Guisinger, T. Li, P.N. First, J.A. Stroscio. "Scattering and interference in epitaxial graphene," *Science* **317**(5835), 219-222 (2007).
- [102] N. Ray, S. Shallcross, S. Hensel, O. Pankratov. "Buffer layer limited conductivity in epitaxial graphene on the Si face of SiC," *Physical Review B* **86**(12), 125426 (2012).
- [103] S. Kim, J. Ihm, H.J. Choi, Y.W. Son. "Origin of anomalous electronic structures of epitaxial graphene on silicon carbide," *Physical Review Letters* **100**(17), 176802 (2008).

- [104] I. Forbeaux, J.M. Themlin, J.M. Debever. "Heteroepitaxial graphite on 6H-SiC(0001): Interface formation through conduction-band electronic structure," *Physical Review B* **58**(24), 16396-16406 (1998).
- [105] L. Simon, J. Bischoff, L. Kubler. "X-ray photoelectron characterization of 6H-SiC (0001)," *Physical Review B* **60**(16), 11653 (1999).
- [106] V. vanElsbergen, T.U. Kampen, W. Monch. "Surface analysis of 6H-SiC," *Surface Science* **365**(2), 443-452 (1996).
- [107] L.I. Johansson, F. Owman, P. Martensson. "High-resolution core-level study of 6H-SiC(0001)," *Physical Review B* **53**(20), 13793-13802 (1996).
- [108] W. Chen, H. Xu, L. Liu, X.Y. Gao, D.C. Qi, G.W. Peng, S.C. Tan, Y.P. Feng, K.P. Loh, A.T.S. Wee. "Atomic structure of the 6H-SiC(0001) nanomesh," *Surface Science* **596**(1-3), 176-186 (2005).
- [109] F. Varchon, R. Feng, J. Hass, X. Li, B.N. Nguyen, C. Naud, P. Mallet, J.Y. Veuille, C. Berger, E.H. Conrad, *et al.* "Electronic structure of epitaxial graphene layers on SiC: Effect of the substrate," *Physical Review Letters* **99**(12), 125805 (2007).
- [110] A. Mattausch, O. Pankratov. "Ab initio study of graphene on SiC," *Physical Review Letters* **99**(7), 076802 (2007).
- [111] A. Mattausch, O. Pankratov. "Density functional study of graphene overlayers on SiC," *Physica Status Solidi B-Basic Solid State Physics* **245**(7), 1425-1435 (2008).
- [112] S. Goler, C. Coletti, V. Piazza, P. Pingue, F. Colangelo, V. Pellegrini, K.V. Emtsev, S. Forti, U. Starke, F. Beltram, *et al.* "Revealing the atomic structure of the buffer layer between SiC(0001) and epitaxial graphene," *Carbon*;10.1016/j.carbon.2012.08.050(0).
- [113] J.H. Park, W.C. Mitchel, H.E. Smith, L. Grazulis, K.G. Eyink. "Studies of interfacial layers between 4H-SiC(0001) and graphene," *Carbon* **48**(5), 1670-1673 (2010).
- [114] W. Norimatsu, M. Kusunoki. "Transitional structures of the interface between graphene and 6H-SiC(0001)," *Chemical Physics Letters* **468**(1-3), 52-56 (2009).
- [115] J. Park, W. Mitchel, L. Grazulis, K. Eyink, H. Smith, J. Hoelscher. "Role of extended defected SiC interface layer on the growth of epitaxial graphene on SiC," *Carbon* **49**(2), 631-635 (2011).
- [116] C. Virojanadara, A. Zakharov, R. Yakimova, L. Johansson. "Buffer layer free large area bi-layer graphene on SiC (0001)," *Surface Science* **604**(2), L4-L7 (2010).

- [117] F. Speck, J. Jobst, F. Fromm, M. Ostler, D. Waldmann, M. Hundhausen, H. Weber, T. Seyller. "The quasi-free-standing nature of graphene on H-saturated SiC (0001)," *Applied Physics Letters* **99**(12), 122106 (2011).
- [118] C. Virojanadara, S. Watcharinyanon, A. Zakharov, L.I. Johansson. "Epitaxial graphene on 6H-SiC and Li intercalation," *Physical Review B* **82**(20), 205402 (2010).
- [119] M.H. Oliveira, T. Schumann, F. Fromm, R. Koch, M. Ostler, M. Ramsteiner, T. Seyller, J.M.J. Lopes, H. Riechert. "Formation of high-quality quasi-free-standing bilayer graphene on SiC(0001) by oxygen intercalation upon annealing in air," *Carbon* **52**, 83-59 (2012).
- [120] A. Sandin, T. Jayasekera, J. Rowe, K.W. Kim, M.B. Nardelli, D.B. Dougherty. "Multiple coexisting intercalation structures of sodium in epitaxial graphene-SiC interfaces," *Physical Review B* **85**(12), 125410 (2012).
- [121] A.L. Walter, K.-J. Jeon, A. Bostwick, F. Speck, M. Ostler, T. Seyller, L. Moreschini, Y.S. Kim, Y.J. Chang, K. Horn. "Highly *p*-doped epitaxial graphene obtained by fluorine intercalation," *Applied Physics Letters* **98**(18), 184102 (2011).
- [122] F. Wang, K. Shepperd, J. Hicks, M.S. Nevius, H. Tinkey, A. Tejada, A. Taleb-Ibrahimi, F. Bertran, P. Le Fèvre, D.B. Torrance, *et al.* "Silicon intercalation into the graphene-SiC interface," *Physical Review B* **85**(16), 165449 (2012).
- [123] N.Y. Garces, V.D. Wheeler, D.K. Gaskill. "Graphene functionalization and seeding for dielectric deposition and device integration," *Journal of Vacuum Science & Technology B: Microelectronics and Nanometer Structures* **30**(3), 030801 (2012).
- [124] Q.H. Wang, M.C. Hersam. "Characterization and nanopatterning of organically functionalized graphene with ultrahigh vacuum scanning tunneling microscopy," *MRS Bulletin* **36**(7), 532-542 (2011).
- [125] J.T. Robinson, J.S. Burgess, C.E. Junkermeier, S.C. Badescu, T.L. Reinecke, F.K. Perkins, M.K. Zalalutdniov, J.W. Baldwin, J.C. Culbertson, P.E. Sheehan. Properties of fluorinated graphene films. DTIC Document, 2010.
- [126] J.E. Johns, M.C. Hersam. "Atomic covalent functionalization of graphene," *Accounts of Chemical Research* **46**(1), 77-86 (2012).
- [127] M.Z. Hossain, J.E. Johns, K.H. Bevan, H.J. Karmel, Y.T. Liang, S. Yoshimoto, K. Mukai, T. Koitaya, J. Yoshinobu, M. Kawai, *et al.* "Chemically homogeneous and thermally reversible oxidation of epitaxial graphene," *Nat Chem* **4**(4), 305-309 (2012).

- [128] N.P. Guisinger, G.M. Rutter, J.N. Crain, P.N. First, J.A. Stroscio. "Exposure of epitaxial graphene on SiC (0001) to atomic hydrogen," *Nano Letters* **9**(4), 1462-1466 (2009).
- [129] V. Wheeler, N. Garces, L. Nyakiti, R. Myers-Ward, G. Jernigan, J. Culbertson, C. Eddy Jr, D. Kurt Gaskill. "Fluorine functionalization of epitaxial graphene for uniform deposition of thin high- κ dielectrics," *Carbon* **50**(6), 2307-2314 (2012).
- [130] E. Bekyarova, M.E. Itkis, P. Ramesh, C. Berger, M. Sprinkle, W.A. de Heer, R.C. Haddon. "Chemical modification of epitaxial graphene: spontaneous grafting of aryl groups," *Journal of the American Chemical Society* **131**(4), 1336-1337 (2009).
- [131] J. Choi, K.-j. Kim, B. Kim, H. Lee, S. Kim. "Covalent functionalization of epitaxial graphene by azidotrimethylsilane," *The Journal of Physical Chemistry C* **113**(22), 9433-9435 (2009).
- [132] J. Choi, H. Lee, K.-j. Kim, B. Kim, S. Kim. "Chemical doping of epitaxial graphene by organic free radicals," *The Journal of Physical Chemistry Letters* **1**(2), 505-509 (2009).
- [133] C. Gómez-Navarro, J.C. Meyer, R.S. Sundaram, A. Chuvilin, S. Kurasch, M. Burghard, K. Kern, U. Kaiser. "Atomic structure of reduced graphene oxide," *Nano Letters* **10**(4), 1144-1148 (2010).
- [134] Q.H. Wang, M.Z. Hossain, M.A. Walsh, M.C. Hersam. "Molecular-scale tailoring of graphene surface chemistry via organic functionalization," *Graphene and Emerging Materials for Post-Cmos Applications* **35**(3), 201-203 (2011).
- [135] Q.H. Wang, M.C. Hersam. "Characterization and nanopatterning of organically functionalized graphene with ultrahigh vacuum scanning tunneling microscopy," *MRS Bulletin* **36**(07), 532-542 (2011).
- [136] D.B. Farmer, H.-Y. Chiu, Y.-M. Lin, K.A. Jenkins, F. Xia, P. Avouris. "Utilization of a buffered dielectric to achieve high field-effect carrier mobility in graphene transistors," *Nano Letters* **9**(12), 4474-4478 (2009).
- [137] Y.M. Lin, C. Dimitrakopoulos, K.A. Jenkins, D.B. Farmer, H.Y. Chiu, A. Grill, P. Avouris. "100-GHz Transistors from Wafer-Scale Epitaxial Graphene," *Science* **327**(5966), 662-662 (2010).
- [138] I. Gierz, C. Riedl, U. Starke, C.R. Ast, K. Kern. "Atomic hole doping of graphene," *Nano Letters* **8**(12), 4603-4607 (2008).
- [139] A. Pirkle, R.M. Wallace, L. Colombo. "In situ studies of Al₂O₃ and HfO₂ dielectrics on graphite," *Applied Physics Letters* **95**(13), (2009).

- [140] J.A. Robinson, M. LaBella III, K.A. Trumbull, X. Weng, R. Cavelero, T. Daniels, Z. Hughes, M. Hollander, M. Fanton, D. Snyder. "Epitaxial graphene materials integration: effects of dielectric overlayers on structural and electronic properties," *Acs Nano* **4**(5), 2667-2672 (2010).
- [141] X. Wang, X. Li, L. Zhang, Y. Yoon, P.K. Weber, H. Wang, J. Guo, H. Dai. "N-doping of graphene through electrothermal reactions with ammonia," *Science* **324**(5928), 768-771 (2009).
- [142] X. Dong, D. Fu, W. Fang, Y. Shi, P. Chen, L.-J. Li. "Doping single-layer graphene with aromatic molecules," *Small* **5**(12), 1422-1426 (2009).
- [143] X. Wang, S.M. Tabakman, H. Dai. "Atomic layer deposition of metal oxides on pristine and functionalized graphene," *Journal of the American Chemical Society* **130**(26), 8152-+ (2008).
- [144] P. Lauffer, K.V. Emtsev, R. Graupner, T. Seyller, L. Ley. "Molecular and electronic structure of PTCDA on bilayer graphene on SiC(0001) studied with scanning tunneling microscopy," *Physica Status Solidi B-Basic Solid State Physics* **245**(10), 2064-2067 (2008).
- [145] W. Chen, S. Chen, D.C. Qi, X.Y. Gao, A.T.S. Wee. "Surface transfer p-type doping of epitaxial graphene," *Journal of the American Chemical Society* **129**(34), 10418-10422 (2007).
- [146] C. Coletti, C. Riedl, D. Lee, B. Krauss, L. Patthey, K. Von Klitzing, J. Smet, U. Starke. "Charge neutrality and band-gap tuning of epitaxial graphene on SiC by molecular doping," *Physical Review B* **81**(23), 235401 (2010).
- [147] B.E. Warren. *X-ray diffraction*: Dover publications; 1990.
- [148] J.M. Cowley. *Diffraction physics*: North Holland; 1995.
- [149] J. Als-Nielsen, D. McMorrow. *Elements of modern X-ray physics*: Wiley; 2011.
- [150] R. Loudon. *The quantum theory of light*: Oxford University Press, USA; 2000.
- [151] F. Mandl, G. Shaw. *Quantum field theory*: Wiley; 2010.
- [152] C.M. Schlepütz. Systematic structure investigation of YBCO thin films with direct methods and surface X-ray diffraction. Switzerland: University of Zurich; 2009.
- [153] J.D. Jackson, R.F. Fox. "Classical electrodynamics," *American Journal of Physics* **67**, 841 (1999).

- [154] D.T. Cromer, J.B. Mann. "X-ray scattering factors computed from numerical Hartree-Fock wave functions," *Acta Crystallographica Section A* **24**(2), 321-324 (1968).
- [155] J. Zegenhagen. "Surface structure determination with X-ray standing waves," *Surface Science Reports* **18**(7-8), 202-271 (1993).
- [156] W. Mönch. *Semiconductor surfaces and interfaces*: Springer; 2001.
- [157] E.A. Kraut, R.W. Grant, J.R. Waldrop, S.P. Kowalczyk. "Precise determination of the valence-band edge in X-ray photoemission spectra: Application to measurement of semiconductor interface potentials," *Physical Review Letters* **44**(24), 1620-1623 (1980).
- [158] O. Ambacher, J. Smart, J. Shealy, N. Weimann, K. Chu, M. Murphy, W. Schaff, L. Eastman, R. Dimitrov, L. Wittmer. "Two-dimensional electron gases induced by spontaneous and piezoelectric polarization charges in N- and Ga-face AlGaIn/GaN heterostructures," *Journal of Applied Physics* **85**(6), 3222-3233 (1999).
- [159] M. Krause, J. Oliver. "Natural widths of atomic K and L levels, Ka X-ray lines and several KLL Auger lines," *Journal of Physical and Chemical Reference Data* **8**, 329-338 (1979).
- [160] S. Doniach, M. Sunjic. "Many-electron singularity in X-ray photoemission and X-ray line spectra from metals," *Journal of Physics C: Solid State Physics* **3**(2), 285 (1970).
- [161] C. Fadley. "Basic concepts of X-ray photoelectron spectroscopy," *Electron spectroscopy: theory, techniques and applications* **2**, 1-156 (1978).
- [162] T.L. Barr. *Modern ESCA: The principles and practice of X-ray photoelectron spectroscopy*: CRC; 1994.
- [163] D. Briggs, M.P. Seah. "Practical surface analysis by Auger and X-ray photoelectron spectroscopy," D Briggs, & M P Seah,(Editors), John Wiley & Sons, Chichester 1983, 533, (1983).
- [164] P. Fenter, J.G. Catalano, C. Park, Z. Zhang. "On the use of CCD area detectors for high-resolution specular X-ray reflectivity," *Journal of Synchrotron Radiation* **13**, 293-303 (2006).
- [165] H. Hong, Z. Wu, T.C. Chiang, P. Zschack, H. Chen. "Time-resolved reflection surface x-ray diffraction," *Review of Scientific Instruments* **73**(4), 1720-1723 (2002).
- [166] C.M. Schleputz, R. Herger, P.R. Willmott, B.D. Patterson, O. Bunk, C. Bronnimann, B. Henrich, G. Hulsen, E.F. Eikenberry. "Improved data acquisition in grazing-incidence X-

- ray scattering experiments using a pixel detector," *Acta Crystallographica Section A* **61**, 418-425 (2005).
- [167] P.A. Fenter. "X-ray reflectivity as a probe of mineral-fluid interfaces: A user guide," *Applications of Synchrotron Radiation in Low-Temperature Geochemistry and Environmental Sciences* **49**, 149-220 (2002).
- [168] I.K. Robinson. "Crystal truncation rods and surface roughness," *Physical Review B* **33**(6), 3830-3836 (1986).
- [169] J.R. Fienup. "Reconstruction of an object from the modulus of its Fourier transform," *Opt Lett* **3**(1), 27-29 (1978).
- [170] D.K. Saldin, R.J. Harder, V.L. Shneerson, W. Moritz. "Phase retrieval methods for surface x-ray diffraction," *Journal of Physics: Condensed Matter* **13**(47), 10689 (2001).
- [171] Y. Yacoby, R. Pindak, R. MacHarrie, L. Pfeiffer, L. Berman, R. Clarke. "Direct structure determination of systems with two-dimensional periodicity," *Journal of Physics: Condensed Matter* **12**(17), 3929 (2000).
- [172] V. Kohli. X-ray studies of ion adsorption at charged titania-electrolyte interfaces: Northwestern University; 2009.
- [173] A. Bauer, J. Kräußlich, L. Dressler, P. Kuschnerus, J. Wolf, K. Goetz, P. Käckell, J. Furthmüller, F. Bechstedt. "High-precision determination of atomic positions in crystals: The case of 6H-and 4H-SiC," *Physical Review B* **57**(5), 2647 (1998).
- [174] A. Bauer, P. Reischauer, J. Krausslich, N. Schell, W. Matz, K. Goetz. "Structure refinement of the silicon carbide polytypes 4H and 6H: unambiguous determination of the refinement parameters," *Acta Crystallographica Section A* **57**, 60-67 (2001).
- [175] D.P. Woodruff. "Surface structure determination using X-ray standing waves," *Reports on Progress in Physics* **68**(4), 743-798 (2005).
- [176] J. Woicik, E. Nelson, D. Heskett, J. Warner, L. Berman, B. Karlin, I. Vartanyants, M. Hasan, T. Kendelewicz, Z. Shen. "X-ray standing-wave investigations of valence electronic structure," *Physical Review B* **64**(12), 125115 (2001).
- [177] M.J. Bedzyk. "Scattering: X-ray standing wave techniques," *Encyclopedia of Condensed Matter Physics*, (2005).
- [178] M.J. Bedzyk, L. Cheng. "X-ray standing wave studies of minerals and mineral surfaces: Principles and applications," *Reviews in Mineralogy and Geochemistry* **49**(1), 221-266 (2002).

- [179] D. Woodruff, D. Seymour, C. McConville, C. Riley, M. Crapper, N. Prince, R.G. Jones. "A simple X-ray standing wave technique for surface structure determination-theory and an application," *Surface Science* **195**(1), 237-254 (1988).
- [180] B.W. Batterman, H. Cole. "Dynamical diffraction of X-rays by perfect crystals," *Reviews of Modern Physics* **36**(3), 681-717 (1964).
- [181] M.J. Bedzyk, G. Materlik. "Two-beam dynamical diffraction solution of the phase problem: A determination with x-ray standing-wave fields," *Physical Review B* **32**(10), 6456-6463 (1985).
- [182] J. Als-Nielsen, D. McMorrow. *Elements of modern X-ray physics*: Wiley; 2001.
- [183] I.A. Vartanyants, J. Zegenhagen. "Quadrupole contribution to the angular resolved photoemission from an X-ray interference field," *Physica Status Solidi B-Basic Research* **215**(1), 819-826 (1999).
- [184] F. Schreiber, K. Ritley, I. Vartanyants, H. Dosch, J. Zegenhagen, B. Cowie. "Non-dipolar contributions in XPS detection of X-ray standing waves," *Surface Science* **486**(3), L519-L523 (2001).
- [185] M. Bedzyk, G. Materlik. "Determination of the position and vibrational amplitude of an adsorbate by means of multiple-order x-ray standing-wave measurements," *Physical Review B* **31**(6), 4110 (1985).
- [186] J. Zegenhagen, B. Detlefs, T.L. Lee, S. Thiess, H. Isern, L. Petit, L. André, J. Roy, Y. Mi, I. Joumard. "X-ray standing waves and hard X-ray photoelectron spectroscopy at the insertion device beamline ID32," *Journal of Electron Spectroscopy and Related Phenomena* **178**, 258-267 (2010).
- [187] Q.H. Wang. *Investigating the assembly of hybrid organic and inorganic nanostructures on silicon and graphene with scanning tunneling microscopy*: Northwestern University; 2010.
- [188] J.M.P. Alaboson, C.-H. Sham, S. Kewalramani, J.D. Emery, J.E. Johns, A. Deshpande, T. Chien, M.J. Bedzyk, J.W. Elam, M.J. Pellin, *et al.* "Templating sub-10 nm atomic layer deposited oxide nanostructures on graphene via one-dimensional organic self-assembled monolayers," *Nano Letters*;10.1021/nl4000932, (2013).
- [189] J.M.P. Alaboson. *Nanopatterning and characterization of inorganic films grown by atomic layer deposition on silicon and graphene substrates*: Northwestern University; 2012.

- [190] J.M.P. Alaboson, Q.H. Wang, J.D. Emery, A.L. Lipson, M.J. Bedzyk, J.W. Elam, M.J. Pellin, M.C. Hersam. "Seeding atomic layer deposition of high-k dielectrics on epitaxial graphene with organic self-assembled monolayers," *ACS Nano* **5**(6), 5223-5232 (2011).
- [191] D.P. Woodruff, T.A. Delchar. *Modern techniques of surface science*: Cambridge University Press; 1994.
- [192] A. Nelson. "Co-refinement of multiple-contrast neutron/X-ray reflectivity data using MOTOFIT," *Journal of Applied Crystallography* **39**(2), 273-276 (2006).
- [193] O.S. Heavens. *Optical properties of thin solid films*: Dover Publications; 2011.
- [194] L.G. Parratt. "Surface studies of solids by total reflection of X-rays," *Physical Review* **95**(2), 359-369 (1954).
- [195] Y. Yoneda. "Anomalous surface reflection of X-rays," *Physical Review* **131**(5), 2010 (1963).
- [196] Z. Jiang, X. Li, J. Strzalka, M. Sprung, T. Sun, A.R. Sandy, S. Narayanan, D. Lee, J. Wang. "The dedicated high-resolution grazing-incidence X-ray scattering beamline 8-ID-E at the Advanced Photon Source," *Journal of Synchrotron Radiation* **19**(4), 0-0 (2012).
- [197] P.A.M. Dirac. "The quantum theory of the emission and absorption of radiation," *Proceedings of the Royal Society of London Series A* **114**(767), 243-265 (1927).
- [198] S. Puri, B. Chand, D. Mehta, M.L. Garg, N. Singh, P.N. Trehan. "K and L shell X-ray fluorescence cross sections," *Atomic Data and Nuclear Data Tables* **61**(2), 289-311 (1995).
- [199] J. Klug. *Synchrotron X-ray studies of epitaxial ferroelectric thin films and nanostructures*: Northwestern University; 2010.
- [200] A.C. Thompson, D. Vaughan. *X-ray data booklet*: Lawrence Berkeley National Laboratory, University of California Berkeley, CA; 2001.
- [201] J.A. Libera. *X-ray structural analysis of in-situ polynucleotide surface adsorption and metal-phosphonate multilayer film self-assembly*: Northwestern University; 2005.
- [202] S. Forti, K.V. Emtsev, C. Coletti, A.A. Zakharov, C. Riedl, U. Starke. "Large-area homogeneous quasifree standing epitaxial graphene on SiC(0001): Electronic and structural characterization," *Physical Review B* **84**(12), 125449 (2011).
- [203] U. Starke. "Atomic structure of hexagonal SiC surfaces," *physica status solidi (b)* **202**(1), 475-499 (1997).

- [204] U. Starke, C. Riedl. "Epitaxial graphene on SiC(0001) and SiC(0001)over-bar): from surface reconstructions to carbon electronics," *Journal of Physics-Condensed Matter* **21**(13), (2009).
- [205] J.E. Northrup, J. Neugebauer. "Theory of the adatom-induced reconstruction of the SiC(0001)root 3x root 3 surface," *Physical Review B* **52**(24), 17001-17004 (1995).
- [206] I.K. Robinson, D.J. Tweet. "Surface X-ray diffraction," *Reports on Progress in Physics* **55**(5), 599-651 (1992).
- [207] J.D. Emery, Q.H. Wang, M. Zarrouati, P. Fenter, M.C. Hersam, M.J. Bedzyk. "Structural analysis of PTCDA monolayers on epitaxial graphene with ultra-high vacuum scanning tunneling microscopy and high-resolution X-ray reflectivity," *Surface Science* **605**(17-18), 1685-1693 (2011).
- [208] J. Zegenhagen, B. Detlefs, T.L. Lee, S. Thiess, H. Isern, L. Petit, L. Andre, J. Roy, Y.Y. Mi, I. Joumard. "X-ray standing waves and hard X-ray photoelectron spectroscopy at the insertion device beamline ID32," *Journal of Electron Spectroscopy and Related Phenomena* **178**, 258-267 (2010).
- [209] J.J. Lee, C.J. Fisher, D.P. Woodruff, M.G. Roper, R.G. Jones, B.C.C. Cowie. "Non-dipole effects in photoelectron-monitored X-ray standing wave experiments: characterisation and calibration," *Surface Science* **494**(3), 166-182 (2001).
- [210] P. Sutter. "Epitaxial graphene: How silicon leaves the scene," *Nature Materials* **8**(3), 171-172 (2009).
- [211] X. Gao, S. Chen, T. Liu, W. Chen, A.T.S. Wee, T. Nomoto, S. Yagi, K. Soda, J. Yuhara. "Disorder beneath epitaxial graphene on SiC(0001): An x-ray absorption study," *Physical Review B* **78**(20), 201404 (2008).
- [212] J. Borysiuk, R. Bozek, W. Strupinski, A. Wyszomolek, K. Grodecki, R. Steapniewski, J.M. Baranowski. "Transmission electron microscopy and scanning tunneling microscopy investigations of graphene on 4H-SiC(0001)," *Journal of Applied Physics* **105**(2), (2009).
- [213] L.I. Johansson, C. Virojanadara, T. Eickhoff, W. Drube. "Properties of the SiO₂/SiC interface investigated by angle resolved studies of the Si 2p and Si 1s levels and the Si KLL Auger transitions," *Surface Science* **529**(3), 515-526 (2003).
- [214] J. Bernhardt, J. Schardt, U. Starke, K. Heinz. "Epitaxially ideal oxide-semiconductor interfaces: Silicate adlayers on hexagonal (0001) and (000 $\bar{1}$) SiC surfaces," *Applied Physics Letters* **74**(8), 1084-1086 (1999).

- [215] S. Tanuma, C. Powell, D. Penn. "Calculation of electron inelastic mean free paths (IMFPs) VII. Reliability of the TPP - 2M IMFP predictive equation," *Surface and Interface Analysis* **35**(3), 268-275 (2003).
- [216] R. Kosiba, J. Liday, G. Ecke, O. Ambacher, J. Breza. "Auger electron spectroscopy of silicon carbide," *Journal of electrical engineering* **55**(9-10), 269-272 (2004).
- [217] A. Markevich, R. Jones, S. Öberg, M. Rayson, J. Goss, P. Briddon. "First-principles study of hydrogen and fluorine intercalation into graphene-SiC(0001) interface," *Physical Review B* **86**(4), 045453 (2012).
- [218] L.E. Berman, M.J. Bedzyk. "Angular distribution of the photoelectron yield excited by two coherently coupled photon beams," *Physical Review Letters* **63**(11), 1172-1175 (1989).
- [219] K.P. Loh, Q. Bao, P.K. Ang, J. Yang. "The chemistry of graphene," *Journal of Materials Chemistry* **20**(12), 2277-2289 (2010).
- [220] C.N.R. Rao, A.K. Sood, K.S. Subrahmanyam, A. Govindaraj. "Graphene: The New Two-Dimensional Nanomaterial," *Angewandte Chemie-International Edition* **48**(42), 7752-7777 (2009).
- [221] E. Bekyarova, M.E. Itkis, P. Ramesh, R.C. Haddon. "Chemical approach to the realization of electronic devices in epitaxial graphene," *Physica Status Solidi-Rapid Research Letters* **3**(6), 184-186 (2009).
- [222] D.R. Dreyer, S. Park, C.W. Bielawski, R.S. Ruoff. "The chemistry of graphene oxide," *Chemical Society Reviews* **39**(1), 228-240 (2010).
- [223] X.R. Wang, S.M. Tabakman, H.J. Dai. "Atomic layer deposition of metal oxides on pristine and functionalized graphene," *Journal of the American Chemical Society* **130**(26), 8152-8153 (2008).
- [224] H. Huang, S. Chen, X. Gao, W. Chen, A.T.S. Wee. "Structural and electronic properties of PTCDA thin films on epitaxial graphene," *ACS Nano* **3**(11), 3431-3436 (2009).
- [225] V.K. Sangwan, D. Jariwala, S.A. Filippone, H.J. Karmel, J.E. Johns, J.M. Alaboson, T.J. Marks, L.J. Lauhon, M.C. Hersam. "Quantitatively enhanced reliability and uniformity of high- κ dielectrics on graphene enabled by self-assembled seeding layers," *Nano Letters* **13**(3), 1162-1167 (2013).
- [226] J.E. Johns, H.J. Karmel, J.M.P. Alaboson, M.C. Hersam. "Probing the structure and chemistry of perylenetetracarboxylic dianhydride on graphene before and after atomic

- layer deposition of alumina," *The Journal of Physical Chemistry Letters* **3**(15), 1974-1979 (2012).
- [227] M. Eremtchenko, J.A. Schaefer, F.S. Tautz. "Understanding and tuning the epitaxy of large aromatic adsorbates by molecular design," *Nature* **425**(6958), 602-605 (2003).
- [228] M. Rohlfing, R. Temirov, F.S. Tautz. "Adsorption structure and scanning tunneling data of a prototype organic-inorganic interface: PTCDA on Ag(111)," *Physical Review B* **76**(11), 115421 (2007).
- [229] A. Kraft, R. Temirov, S.K.M. Henze, S. Soubatch, M. Rohlfing, F.S. Tautz. "Lateral adsorption geometry and site-specific electronic structure of a large organic chemisorbate on a metal surface," *Physical Review B* **74**(4), 041402 (2006).
- [230] K. Glockler, C. Seidel, A. Soukopp, M. Sokolowski, E. Umbach, M. Bohringer, R. Berndt, W.D. Schneider. "Highly ordered structures and submolecular scanning tunnelling microscopy contrast of PTCDA and DM-PBDCI monolayers on Ag(111) and Ag(110)," *Surface Science* **405**(1), 1-20 (1998).
- [231] N. Nicoara, E. Roman, J.M. Gomez-Rodriguez, J.A. Martin-Gago, J. Mendez. "Scanning tunneling and photoemission spectroscopies at the PTCDA/Au(111) interface," *Organic Electronics* **7**(5), 287-294 (2006).
- [232] F.S. Tautz. "Structure and bonding of large aromatic molecules on noble metal surfaces: The example of PTCDA," *Progress in Surface Science* **82**(9-12), 479-520 (2007).
- [233] C. Ludwig, B. Gompf, W. Glatz, J. Petersen, W. Eisenmenger, M. Mobus, U. Zimmermann, N. Karl. "Video-Stm, LEED, and X-ray-diffraction investigations of PTCDA on graphite," *Zeitschrift Fur Physik B-Condensed Matter* **86**(3), 397-404 (1992).
- [234] P. Fenter, F. Schreiber, L. Zhou, P. Eisenberger, S.R. Forrester. "In situ studies of morphology, strain, and growth modes of a molecular organic thin film," *Physical Review B* **56**(6), 3046-3053 (1997).
- [235] B. Krause, A.C. Durr, K. Ritley, F. Schreiber, H. Dosch, D. Smilgies. "Structure and growth morphology of an archetypal system for organic epitaxy: PTCDA on Ag(111)," *Physical Review B* **66**(23), 235404 (2002).
- [236] A. Gerlach, S. Sellner, F. Schreiber, N. Koch, J. Zegenhagen. "Substrate-dependent bonding distances of PTCDA: A comparative x-ray standing-wave study on Cu(111) and Ag(111)," *Physical Review B* **75**(4), -045401 (2007).

- [237] A. Hauschild, K. Karki, B.C.C. Cowie, M. Rohlfing, F.S. Tautz, M. Sokolowski. "Molecular distortions and chemical bonding of a large π -conjugated molecule on a metal surface," *Physical Review Letters* **94**(3), 036106 (2005).
- [238] A. Hauschild, R. Temirov, S. Soubatch, O. Bauer, A. Scholl, B.C.C. Cowie, T.L. Lee, F.S. Tautz, M. Sokolowski. "Normal-incidence x-ray standing-wave determination of the adsorption geometry of PTCDA on Ag(111): Comparison of the ordered room-temperature and disordered low-temperature phases," *Physical Review B* **81**(12), 125432 (2010).
- [239] S.K.M. Henze, O. Bauer, T.L. Lee, M. Sokolowski, F.S. Tautz. "Vertical bonding distances of PTCDA on Au(111) and Ag(111): Relation to the bonding type," *Surface Science* **601**(6), 1566-1573 (2007).
- [240] P. Fenter, Z. Zhang. "Model-independent one-dimensional imaging of interfacial structures at < 1 Å resolution," *Physical Review B* **72**(8), 081408(R) (2005).
- [241] J.R. Fienup. "Reconstruction of an object from modulus of its Fourier-transform," *Optics Letters* **3**(1), 27-29 (1978).
- [242] J. Hass, R. Feng, J.E. Millan-Otoya, X. Li, M. Sprinkle, P.N. First, W.A. de Heer, E.H. Conrad, C. Berger. "Structural properties of the multilayer graphene/4H-SiC(000 $\bar{1}$) system as determined by surface x-ray diffraction," *Physical Review B* **75**(21), 214109 (2007).
- [243] J.A. Kellar, J.M.P. Alaboson, Q.H. Wang, M.C. Hersam. "Identifying and characterizing epitaxial graphene domains on partially graphitized SiC(0001) surfaces using scanning probe microscopy," *Applied Physics Letters* **96**(14), 143013 (2010).
- [244] E.T. Foley, N.L. Yoder, N.P. Guisinger, M.C. Hersam. "Cryogenic variable temperature ultrahigh vacuum scanning tunneling microscope for single molecule studies on silicon surfaces," *Review of Scientific Instruments* **75**(12), 5280-5287 (2004).
- [245] M. Rauscher, H. Reichert, S. Engemann, H. Dosch. "Local density profiles in thin films and multilayers from diffuse x-ray and neutron scattering," *Physical Review B* **72**(20), 205401 (2005).
- [246] P. Fenter, Z. Zhang, C. Park, N.C. Sturchio, X. Hu, S.R. Higgins. "Probing the reactivity of the dolomite-water interface using high resolution X-ray reflectivity," *Geochimica Et Cosmochimica Acta* **69**(10), A483-A483 (2005).
- [247] J. Miao, J. Kirz, D. Sayre. "The oversampling phasing method," *Acta Crystallographica Section D-Biological Crystallography* **56**, 1312-1315 (2000).

- [248] P. Fenter, Z. Zhang. "Model-independent one-dimensional imaging of interfacial structures at $<1\text{\AA}$ resolution," *Physical Review B* **72**(8), 081401(R) (2005).
- [249] R. Feidenhansl. "Surface-Structure Determination by X-Ray-Diffraction," *Surface Science Reports* **10**(3), 105-188 (1989).
- [250] H. Huang, S. Chen, X.Y. Gao, W. Chen, A.T.S. Wee. "Structural and electronic properties of PTCDA thin films on epitaxial graphene," *ACS Nano* **3**(11), 3431-3436 (2009).
- [251] J. Als-Nielsen, D. McMorrow. *Elements of Modern X-ray Physics*. West Sussex: John Wiley & Sons Ltd; 2000.
- [252] Y. Yoneda. "Anomalous Surface Reflection of X Rays," *Physical Review* **131**(5), 2010 (1963).
- [253] C. Riedl, U. Starke. "Structural and electronic properties of epitaxial graphene on SiC(0001)," *Silicon Carbide and Related Materials 2008* **615-617**, 219-222 1021 (2009).
- [254] C. Riedl, U. Starke, J. Bernhardt, M. Franke, K. Heinz. "Structural properties of the graphene-SiC(0001) interface as a key for the preparation of homogeneous large-terrace graphene surfaces," *Physical Review B* **76**(24), 245406 (2007).
- [255] F. Varchon, P. Mallet, J.Y. Veullen, L. Magaud. "Ripples in epitaxial graphene on the Si-terminated SiC(0001) surface," *Physical Review B* **77**(23), 235412 (2008).
- [256] J. Hass, F. Varchon, J.E. Millan-Otoya, M. Sprinkle, N. Sharma, W.A. De Heer, C. Berger, P.N. First, L. Magaud, E.H. Conrad. "Why multilayer graphene on 4H-SiC(000 $\bar{1}$) behaves like a single sheet of graphene," *Physical Review Letters* **100**(12), 125504 (2008).
- [257] M. Hupalo, E.H. Conrad, M.C. Tringides. "Growth mechanism for epitaxial graphene on vicinal 6H-SiC (0001) surfaces: A scanning tunneling microscopy study," *Physical Review B* **80**(4), 041401 (2009).
- [258] V. Borovikov, A. Zangwill. "Step bunching of vicinal 6H-SiC {0001} surfaces," *Physical Review B* **79**(24), 245413 (2009).
- [259] S. Nakamura, T. Kimoto, H. Matsunami, S. Tanaka, N. Teraguchi, A. Suzuki. "Formation of periodic steps with a unit-cell height on 6H-SiC (0001) surface by HCl etching," *Applied Physics Letters* **76**(23), 3412-3414 (2000).

- [260] L.I. Johansson, F. Owman, P. Mårtensson. "High-resolution core-level study of 6H-SiC(0001)," *Physical Review B* **53**(20), 13793 (1996).
- [261] T. Seyller, K.V. Emtsev, K. Gao, F. Speck, L. Ley, A. Tadich, L. Broekman, J.D. Riley, R.C.G. Leckey, O. Rader, *et al.* "Structural and electronic properties of graphite layers grown on SiC(0001)," *Surface Science* **600**(18), 3906-3911 (2006).
- [262] A. Gerlach, S. Sellner, S. Kowarik, F. Schreiber. "In-situ X-ray scattering studies of OFET interfaces," *Physica Status Solidi a-Applications and Materials Science* **205**(3), 461-474 (2008).
- [263] A. Bondi. "van der Waals Volumes and Radii," *J Phys Chem* **68**(3), 441-451 (1964).
- [264] X.Q. Tian, J.B. Xu, X.M. Wang. "Self-assembly of PTCDA ultrathin films on graphene: Structural phase transition and charge transfer saturation," *The Journal of Physical Chemistry C*, **114**(49), 20917-20924 (2010).
- [265] M. Toerker, T. Fritz, H. Proehl, F. Sellam, K. Leo. "Tunneling spectroscopy study of 3,4,9,10-perylenetetracarboxylic dianhydride on Au(100)," *Surface Science* **491**(1-2), 255-264 (2001).
- [266] Y. Xuan, Y.Q. Wu, T. Shen, M. Qi, M.A. Capano, J.A. Cooper, P.D. Ye. "Atomic-layer-deposited nanostructures for graphene-based nanoelectronics," *Applied Physics Letters* **92**(1), 013101 (2008).
- [267] T. Shen, J.J. Gu, M. Xu, Y.Q. Wu, M.L. Bolen, M.A. Capano, L.W. Engel, P.D. Ye. "Observation of quantum-Hall effect in gated epitaxial graphene grown on SiC (0001)," *Applied Physics Letters* **95**(17), (2009).
- [268] Q. Chen, H. Huang, W. Chen, A.T.S. Wee, Y.P. Feng, J.W. Chai, Z. Zhang, J.S. Pan, S.J. Wang. "In situ photoemission spectroscopy study on formation of HfO₂ dielectrics on epitaxial graphene on SiC substrate," *Applied Physics Letters* **96**(7), (2010).
- [269] A. Pirkle, Y.J. Chabal, L. Colombo, R.M. Wallace. *In-situ Studies of high-kappa dielectrics for graphene-based devices*. In: Obeng Y., DeGendt S., Srinivasan P., Misra D., Iwai H., Karim Z., Hess D. W., Grebel H., editors. in *Graphene and Emerging Materials for Post-CMOS Applications*2009). p. 215-224.
- [270] S. Kim, J. Nah, I. Jo, D. Shahrjerdi, L. Colombo, Z. Yao, E. Tutuc, S.K. Banerjee. "Realization of a high mobility dual-gated graphene field-effect transistor with Al₂O₃ dielectric," *Applied Physics Letters* **94**(6), 062107 (2009).

- [271] B. Lee, S.-Y. Park, H.-C. Kim, K. Cho, E.M. Vogel, M.J. Kim, R.M. Wallace, J. Kim. "Conformal Al₂O₃ dielectric layer deposited by atomic layer deposition for graphene-based nanoelectronics," *Applied Physics Letters* **92**(20), 203102 (2008).
- [272] B. Lee, G. Mordi, M.J. Kim, Y.J. Chabal, E.M. Vogel, R.M. Wallace, K.J. Cho, L. Colombo, J. Kim. "Characteristics of high- κ Al₂O₃ dielectric using ozone-based atomic layer deposition for dual-gated graphene devices," *Applied Physics Letters* **97**(4), 043107 (2010).
- [273] Y.-M. Lin, K.A. Jenkins, A. Valdes-Garcia, J.P. Small, D.B. Farmer, P. Avouris. "Operation of graphene transistors at gigahertz frequencies," *Nano Letters* **9**(1), 422-426 (2009).
- [274] Y.-M. Lin, C. Dimitrakopoulos, K.A. Jenkins, D.B. Farmer, H.-Y. Chiu, A. Grill, P. Avouris. "100-GHz transistors from wafer-scale epitaxial graphene," *Science* **327**(5966), 662 (2010).
- [275] L. Liao, X. Duan. "Graphene-dielectric integration for graphene transistors," *Materials Science & Engineering R-Reports* **70**(3-6), 354-370 (2010).
- [276] J.W. Elam, M.D. Groner, S.M. George. "Viscous flow reactor with quartz crystal microbalance for thin film growth by atomic layer deposition," *Review of Scientific Instruments* **73**(8), 2981-2987 (2002).
- [277] Q.H. Wang, M.C. Hersam. "Nanofabrication of Heteromolecular Organic Nanostructures on Epitaxial Graphene via Room Temperature Feedback-Controlled Lithography," *Nano Letters* **11**(2), 589-593 (2011).
- [278] J.M.P. Alaboson, Q.H. Wang, J.A. Kellar, J. Park, J.W. Elam, M.J. Pellin, M.C. Hersam. "Conductive atomic force microscope nanopatterning of epitaxial graphene on SiC(0001) in ambient conditions," *Advanced Materials* **23**(19), 2181-2184 (2011).
- [279] I.S. Byun, D. Yoon, J.S. Choi, I. Hwang, D.H. Lee, M.J. Lee, T. Kawai, Y.W. Son, Q. Jia, H. Cheong, *et al.* "Nanoscale lithography on monolayer graphene using hydrogenation and oxidation," *ACS Nano* **5**(8), 6417-6424 (2011).
- [280] M. Kim, N.S. Safron, E. Han, M.S. Arnold, P. Gopalan. "Fabrication and characterization of large-area, semiconducting nanoporated graphene materials," *Nano Letters* **10**(4), 1125-1131 (2010).
- [281] M.C. Prado, R. Nascimento, L.G. Moura, M.J.S. Matos, M.S.C. Mazzoni, L.G. Cancado, H. Chacham, B.R.A. Neves. "Two-dimensional molecular crystals of phosphonic acids on graphene," *ACS Nano* **5**(1), 394-398 (2011).

- [282] S.S. Kim, J.Y. Choi, K. Kim, B.H. Sohn. "Large area tunable arrays of graphene nanodots fabricated using diblock copolymer micelles," *Nanotechnology* **23**(12), 125301 (2012).
- [283] J.W. Bai, X. Zhong, S. Jiang, Y. Huang, X.F. Duan. "Graphene nanomesh," *Nature Nanotechnology* **5**(3), 190-194 (2010).
- [284] L. Liu, Y.L. Zhang, W.L. Wang, C.Z. Gu, X.D. Bai, E.G. Wang. "Nanosphere Lithography for the Fabrication of Ultranarrow Graphene Nanoribbons and On-Chip Bandgap Tuning of Graphene," *Advanced Materials* **23**(10), 1246-1251 (2011).
- [285] A. Sinitskii, J.M. Tour. "Patterning Graphene through the Self-Assembled Templates: Toward Periodic Two-Dimensional Graphene Nanostructures with Semiconductor Properties," *Journal of the American Chemical Society* **132**(42), 14730-14732 (2010).
- [286] A. Deshpande, C.H. Sham, J.M. Alaboson, J.M. Mullin, G.C. Schatz, M.C. Hersam. "Self-assembly and photopolymerization of sub-2 nm one-dimensional organic nanostructures on graphene," *Journal of the American Chemical Society* **134**(40), 16759-16764 (2012). Epub 2012/08/30.
- [287] Y. Okawa, D. Takajo, S. Tsukamoto, T. Hasegawa, M. Aono. "Atomic force microscopy and theoretical investigation of the lifted-up conformation of polydiacetylene on a graphite substrate," *Soft Matter* **4**(5), 1041-1047 (2008).
- [288] Y. Okawa, M. Aono. "Linear chain polymerization initiated by a scanning tunneling microscope tip at designated positions," *Journal of Chemical Physics* **115**(5), 2317-2322 (2001).
- [289] R. Giridharagopal, K.F. Kelly. "STM-Induced desorption of polydiacetylene nanowires and reordering via molecular cascades," *Journal of Physical Chemistry C* **111**(17), 6161-6166 (2007).
- [290] S.M. George, A.W. Ott, J.W. Klaus. "Surface chemistry for atomic layer growth," *Journal of Physical Chemistry* **100**(31), 13121-13131 (1996).
- [291] G.N. Fontes, B.R.A. Neves. "Effects of substrate polarity and chain length on conformational and thermal properties of phosphonic acid self-assembled bilayers," *Langmuir* **21**(24), 11113-11118 (2005).
- [292] R. Giridharagopal, K.F. Kelly. "Substrate-dependent properties of polydiacetylene nanowires on graphite and MoS₂," *ACS Nano* **2**(8), 1571-1580 (2008).

- [293] R. Hentschke, B.L. Schürmann, J.P. Rabe. "Molecular dynamics simulations of ordered alkane chains physisorbed on graphite," *The Journal of Chemical Physics* **96**(8), 6213-6221 (1992).
- [294] J.A. Spink, J.V. Sanders. "Soap Formation in Monomolecular Films on Aqueous Solutions," *Transactions of the Faraday Society* **51**(8), 1154-1165 (1955).
- [295] R.D. Neuman. "Calcium-Binding in Stearic Acid Monomolecular Films," *Journal of Colloid and Interface Science* **53**(2), 161-171 (1975).
- [296] D. June, E.I. Franses. "Interactions of Charged Langmuir Monolayers with Dissolved Ions," *Journal of Chemical Physics* **95**(11), 8486-8493 (1991).
- [297] B.P. Binks. "Insoluble Monolayers of Weakly Ionizing Low Molar Mass Materials and Their Deposition to Form Langmuir-Blodgett Multilayers," *Advances in Colloid and Interface Science* **34**, 343-432 (1991).
- [298] D.J.M. Linden, J.P.K. Peltonen, J.B. Rosenholm. "Adsorption of Some Multivalent Transition-Metal Ions to a Stearic-Acid Monolayer," *Langmuir* **10**(5), 1592-1595 (1994).
- [299] H.H. Li, G.Z. Mao, K.Y.S. Ng. "AFM study of templated growth of cadmium sulfide nanoparticles using pure and mixed arachidate films," *Thin Solid Films* **358**(1-2), 62-72 (2000).
- [300] D.K. Schwartz, J. Garnaes, R. Viswanathan, J.A.N. Zasadzinski. "Surface Order and Stability of Langmuir-Blodgett-Films," *Science* **257**(5069), 508-511 (1992).
- [301] J.M. Bloch, W.B. Yun. "Condensation of Monovalent and Divalent Metal-Ions on a Langmuir Monolayer," *Physical Review A* **41**(2), 844-862 (1990).
- [302] D.J. Elliot, D.N. Furlong, F. Grieser. "Fabrication of nano-sized particles of metallic copper and copper sulfide in Langmuir-Blodgett films," *Colloids and Surfaces a-Physicochemical and Engineering Aspects* **141**(1), 9-17 (1998).
- [303] N. Matsuura, D.J. Elliot, D.N. Furlong, F. Grieser. "In-situ measurement of lead(II) ion binding to an arachidic acid Langmuir monolayer using a quartz crystal microbalance," *Colloids and Surfaces a-Physicochemical and Engineering Aspects* **126**(2-3), 189-195 (1997).
- [304] S. Kundu, A. Datta, S. Hazra. "Manipulating headgroups in Langmuir-Blodgett films through subphase pH variation," *Chemical Physics Letters* **405**(4-6), 282-287 (2005).
- [305] G.Z. Mao, W.F. Dong, D.G. Kurth, H. Mohwald. "Synthesis of copper sulfide nanorod arrays on molecular templates," *Nano Letters* **4**(2), 249-252 (2004).

- [306] V. Zelenak, Z. Vargova, K. Gyoryova. "Correlation of infrared spectra of zinc(II) carboxylates with their structures," *Spectrochimica Acta Part a-Molecular and Biomolecular Spectroscopy* **66**(2), 262-272 (2007).
- [307] S.W. Joo, J.K. Lim, K. Cho. "Resonance Raman process and photo-induced phase transition via 632.8 nm irradiation for diacetylene monocarboxylic acid derivative self-assembled layers on Ag surfaces," *Journal of Photochemistry and Photobiology a-Chemistry* **194**(2-3), 356-361 (2008).
- [308] Y. Lifshitz, A. Upcher, O. Shusterman, B. Horovitz, A. Berman, Y. Golan. "Phase transition kinetics in Langmuir and spin-coated polydiacetylene films," *Physical Chemistry Chemical Physics* **12**(3), 713-722 (2010).
- [309] M. Cai, M.D. Mowery, J.E. Pemberton, C.E. Evans. "Dual-wavelength resonance Raman spectroscopy of polydiacetylene monolayers on Au surfaces," *Applied Spectroscopy* **54**(1), 31-38 (2000).
- [310] M. Li, M. Dai, Y.J. Chabal. "Atomic Layer Deposition of Aluminum Oxide on Carboxylic Acid-Terminated Self-Assembled Monolayers," *Langmuir* **25**(4), 1911-1914 (2009).
- [311] K.B. Klepper, O. Nilsen, H. Fjellvag. "Deposition of thin films of organic-inorganic hybrid materials based on aromatic carboxylic acids by atomic layer deposition," *Dalton Transactions* **39**(48), 11628-11635 (2010).
- [312] B. Yoon, D. Seghete, A.S. Cavanagh, S.M. George. "Molecular Layer Deposition of Hybrid Organic-Inorganic Alucone Polymer Films Using a Three-Step ABC Reaction Sequence," *Chemistry of Materials* **21**(22), 5365-5374 (2009).
- [313] A.G. Fallis, P. Forgione. "Metal mediated carbometallation of alkynes and alkenes containing adjacent heteroatoms," *Tetrahedron* **57**(28), 5899-5913 (2001).
- [314] P. Wipf, S. Lim. "Rapid Carboalumination of Alkynes in the Presence of Water," *Angewandte Chemie-International Edition in English* **32**(7), 1068-1071 (1993).
- [315] K.W. Egger, A.T. Cocks. "Reactions of Group-Iii Metal Alkyls in Gas-Phase .6. Addition of Ethylene to Trimethylaluminum," *Journal of the American Chemical Society* **94**(6), 1810-& (1972).
- [316] J.W. Bundens, J. Yudenfreund, M.M. Francl. "Transition states for the carboalumination of alkenes and alkynes," *Organometallics* **18**(19), 3913-3920 (1999).

- [317] J. Hass, R. Feng, J.E. Millan-Otoya, X. Li, M. Sprinkle, P.N. First, W.A. de Heer, E.H. Conrad, C. Berger. "Structural properties of the multilayer graphene/4H-SiC(000 $\bar{1}$) system as determined by surface x-ray diffraction," *Physical Review B* **75**(21), 214109 (2007).
- [318] J. Hass, F. Varchon, J.-E. Millan-Otoya, M. Sprinkle, N. Sharma, W.A. de Heer, C. Berger, P.N. First, L. Magaud, E.H. Conrad. "Why multilayer graphene on 4H-SiC (000 $\bar{1}$) behaves like a single sheet of graphene," *Physical Review Letters* **100**(12), 125504 (2008).
- [319] F. Varchon, R. Feng, J. Hass, X. Li, B.N. Nguyen, C. Naud, P. Mallet, J.Y. Veuille, C. Berger, E.H. Conrad, *et al.* "Electronic Structure of Epitaxial Graphene Layers on SiC: Effect of the Substrate," *Physical Review Letters* **99**(12), 126805 (2007).
- [320] K.V. Emtsev, T. Seyller, F. Speck, L. Ley, P. Stojanov, J.D. Riley, R.G.C. Leckey. "Initial stages of the graphite-SiC(0001) interface formation studied by photoelectron spectroscopy," *Silicon Carbide and Related Materials 2006* **556-557**, 525-528 (2007).
- [321] W.J. Choyke, H. Matsunami, G. Pensl. *Silicon carbide: Recent major advances*: Springer; 2003.
- [322] Z. Guo, R. Dong, P.S. Chakraborty, N. Lourenco, J. Palmer, Y. Hu, M. Ruan, J. Hankinson, J. Kunc, J.D. Cressler, *et al.* "Record maximum oscillation frequency in C-face epitaxial graphene transistors," *Nano Letters*;10.1021/nl303587r, (2013).
- [323] C. Mathieu, N. Barrett, J. Rault, Y.Y. Mi, B. Zhang, W.A. de Heer, C. Berger, E.H. Conrad, O. Renault. "Microscopic correlation between chemical and electronic states in epitaxial graphene on SiC(000 $\bar{1}$)," *Physical Review B* **83**(23), 235436 (2011).
- [324] L. Johansson, P.-A. Glans, N. Hellgren. "A core level and valence band photoemission study of 6H-SiC(0001)," *Surface Science* **405**(2), 288-297 (1998).
- [325] L.O. Nyakiti, V.D. Wheeler, R.L. Myers-Ward, N.Y. Garces, F.J. Bezares, C. Eddy Jr, J.D. Caldwell, D.K. Gaskill. Comparison of epitaxial graphene growth on non-polar and polar 6H-SiC. The Electrochemical Society PRiME 2012; Honolulu, HI 2012.
- [326] F.-C. Chuang, W.-H. Lin, Z.-Q. Huang, C.-H. Hsu, C.-C. Kuo, V. Ozolins, V. Yeh. "Electronic structures of an epitaxial graphene monolayer on SiC (0001) after gold intercalation: a first-principles study," *Nanotechnology* **22**(27), 275704 (2011).
- [327] R. Mas-Balleste, C. Gomez-Navarro, J. Gomez-Herrero, F. Zamora. "2D materials: to graphene and beyond," *Nanoscale* **3**(1), 20-30 (2011).

- [328] Q.H. Wang, K. Kalantar-Zadeh, A. Kis, J.N. Coleman, M.S. Strano. "Electronics and optoelectronics of two-dimensional transition metal dichalcogenides," *Nature Nanotechnology* **7**(11), 699-712 (2012).
- [329] S. Kim, A. Konar, W.-S. Hwang, J.H. Lee, J. Lee, J. Yang, C. Jung, H. Kim, J.-B. Yoo, J.-Y. Choi. "High-mobility and low-power thin-film transistors based on multilayer MoS₂ crystals," *Nature Communications* **3**, 1011 (2012).
- [330] C. Dean, A. Young, I. Meric, C. Lee, L. Wang, S. Sorgenfrei, K. Watanabe, T. Taniguchi, P. Kim, K. Shepard. "Boron nitride substrates for high-quality graphene electronics," *Nature Nanotechnology* **5**(10), 722-726 (2010).
- [331] Z. Liu, L. Song, S. Zhao, J. Huang, L. Ma, J. Zhang, J. Lou, P.M. Ajayan. "Direct growth of graphene/hexagonal boron nitride stacked layers," *Nano Letters* **11**(5), 2032-2037 (2011).
- [332] Y. Shi, W. Zhou, A.-Y. Lu, W. Fang, Y.-H. Lee, A.L. Hsu, S.M. Kim, K.K. Kim, H.Y. Yang, L.-J. Li. "Van der Waals epitaxy of MoS₂ layers using graphene as growth templates," *Nano Letters* **12**(6), 2784-2791 (2012).
- [333] Z. Ni, Q. Liu, K. Tang, J. Zheng, J. Zhou, R. Qin, Z. Gao, D. Yu, J. Lu. "Tunable bandgap in silicene and germanene," *Nano Letters* **12**(1), 113-118 (2011).
- [334] A. Kara, H. Enriquez, A.P. Seitsonen, L.C. Lew Yan Voon, S. Vizzini, B. Aufray, H. Oughaddou. "A review on silicene: New candidate for electronics," *Surface Science Reports* **67**(1), 1-18 (2012).
- [335] P. De Padova, C. Quaresima, C. Ottaviani, P.M. Sheverdyaeva, P. Moras, C. Carbone, D. Topwal, B. Olivieri, A. Kara, H. Oughaddou. "Evidence of graphene-like electronic signature in silicene nanoribbons," *Applied Physics Letters* **96**(26), 261905 (2010).
- [336] P. Vogt, P. De Padova, C. Quaresima, J. Avila, E. Frantzeskakis, M.C. Asensio, A. Resta, B. Ealet, G. Le Lay. "Silicene: Compelling experimental evidence for graphenelike two-dimensional silicon," *Physical Review Letters* **108**(15), 155501 (2012).
- [337] J. Gao, J. Zhao. "Initial geometries, interaction mechanism and high stability of silicene on Ag(111) surface," *Scientific Reports* **2**, (2012).
- [338] A. Gray, C. Papp, S. Ueda, B. Balke, Y. Yamashita, L. Plucinski, J. Minár, J. Braun, E. Ylvisaker, C. Schneider. "Probing bulk electronic structure with hard X-ray angle-resolved photoemission," *Nature Materials* **10**(10), 759-764 (2011).
- [339] D.T. Cromer, D. Liberman. "Relativistic calculation of anomalous scattering factors for X rays," *The Journal of Chemical Physics* **53**, 1891 (1970).

- [340] Z.G. Pinsker. *Dynamical scattering of X-rays in crystals*. Queisser H.-J., editor. Berlin, De: Springer-Verlag; 1978. 511 p.
- [341] B.W. Batterman. "Effect of dynamical diffraction in X-ray fluorescence scattering," *Physical Review a-General Physics* **133**(3A), A759-A764 (1964).
- [342] J.W. DuMond. "Theory of the use of more than two successive x-ray crystal reflections to obtain increased resolving power," *Physical Review* **52**(8), 872 (1937).

Appendix A: SWAM Analysis Routine

A.1: History

SWAM, or Standing Wave Analysis in MATLAB, is the latest iteration in a series of XSW analysis routines developed by the Bedzyk group. The original analysis program, DARE, was written by Jörg Zegenhagen and modified by Michael Bedzyk in 1986 to perform basic analysis of XSW data. Subsequently, in 1998, Likwan Cheng and Bedzyk extended DARE's capabilities to enable XSW analysis to any arbitrary crystalline structure with a defined unit cell. SWAN was written in Fortran and translated to C using MACF2C (Mac OS 9 or in the Classic environment). Subsequently, CodeWarrior, a now-discontinued program which uses the Mac Classic operating environment, was employed to handle the translated source code. SWAN was routinely updated by group members as late as 2005 (SWAN v2.1.3), when Anthony Escudro added functionality to help streamline SWAN analysis and improve rocking-curve fitting (see Escudro Thesis A.1.2). However, by 2009 the utilization of SWAN as the main XSW analysis tool for the group had become impractical because access to the program was limited to Mac operating systems which could run Classic (Classic compatibility with the Mac OS was dropped in 2005). This not only made access to SWAN limited for analysis, but also for editing, expansion, and annotation.

In 2009 Phillip Lin transcribed SWAN into a series of MATLAB subroutines and enabled a dialog-box-based interface which prompts the user for input. This became the first version of SWAM. While this program provided a much-improved interface over the command-

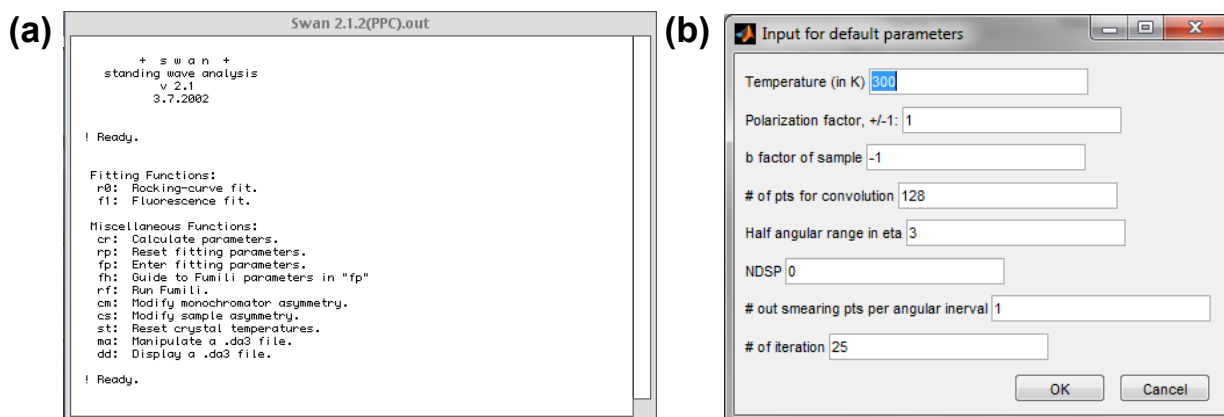


Figure A.1: Examples of user interfaces for (a) SWANv2.1.2 and (b) SWAMv2.4.

line routine used in both DARE and SWAN (see [Figure A.1](#)), the initial versions of SWAM were minimally annotated, insufficiently benchmarked, and largely undocumented. In addition, it takes only minimal advantage of useful MATLAB functionalities such as Graphical User Interfaces (GUIs) or built-in sub-functions. In essence, the early versions of SWAM were a set of routines written for Fortran but running in a MATLAB environment. Furthermore, since the SWAN-to-SWAM project was approached as a transcription rather than an upgrade, little consideration was given to the new routines and numerous errors (incorrect function definitions, neglect of measurement uncertainties values, improper nesting of loops, occasional generalization to centrosymmetric structures, etc.) were either propagated or compounded.

In 2011, Zhenxing Feng made a number of upgrades to SWAM (v2.0-v2.4). Before these versions, the dispersion corrections to the atomic form factor were acquired from a library containing a small number of tabulated f' and f'' values. The new and current versions of SWAM instead use the Cromer-Lieberman relation [339] to generalize the calculation of these corrections to any element at any incident X-ray energy. These versions also incorporated a new routine for the Gaussian broadening of rocking curves, as opposed to approximating the

broadening effects due to crystal mosaic by increasing the crystal asymmetry factor b , as was customary. Finally, Feng made the first attempts to add an option for analyzing XSW data taken with energy scans based on Escudro's Fortran routine, SWANE.

As of 2012, SWAM was a useful tool for analyzing XSW data acquired by monitoring XRF yields during angular scans (θ -scans) across the single-crystal Bragg reflections at Bragg angles (θ_B) less than 87° , and when the monochromator Darwin width is significantly less than the sample Darwin width, $\omega_M \ll \omega_S$. However, attempts to use this version to analyze data acquired from measurements of epitaxial graphene on SiC(0001), taken in 2011-2012 at ID32 at the ESRF, exposed a number of deficiencies and errors in the program. Upon further review it was clear that SWAM would require a major overhaul. The generalization of the program to various experimental conditions, correcting errors in calculation, and providing comprehensive documentation. While the basic structure of the routines are still directly related to their previous SWAN counterparts, most functions have been overhauled. The only totally new functionality is the addition of the χ^2 mapping routine, *chi2.m*, which is used to more precisely assess uncertainties in XSW results. The most current version of SWAM is v4.1.

Many improvements in performance and functionality have been included in the most recent SWAM version. The primary and accomplished goals of this project were:

1. Repair any errors in calculations and clean up bugs. Overhaul and annotate code with the goal of producing a concise, coherent and accessible set of routines.
2. Enable analysis of data taken in either angular (θ -) or energy (E -) scan modes.
3. Improve user interface and results output. Improve language and annotation so that input and output values can be well-understood by the user.
4. Provide thorough annotation within the code body itself so that the routines are accessible for alteration by future users. This includes identifying important equations and their sources.

5. Develop documentation with routine flowcharts, user guide, and symbolic equations for user reference.
6. Incorporation of detuned channel-cut options.
7. Develop a χ^2 -mapping routine in order to more accurately assess uncertainties in XSW results.

A.2: SWAM Guide

Initialization of SWAM is performed in one of two ways. Either a.) copy the directory in which SWAM is located into the Current Directory field within the MATLAB control panel. Then enter:

```
>>SWAM
```

into the command line (see [Figure A.2](#)). Alternatively, b.) Navigate to the SWAM directory on your computer. Double-click on *SWAM.m*, which will open the routine in the MATLAB editor. Press F5 to run. When prompted, make sure to change the directory to the SWAM folder because some components of the routine are contingent upon the main SWAM directory being the working directory. After initialization a modal listbox will appear which provides the user with four XSW simulation or analysis options ([Figure A.2](#)). Note that upon initialization, SWAM will search to see if the correct subdirectories are present within the current MATLAB path. If they are not, SWAM will add the directories to the user's path and save the path as a default SWAM path file, *pathdef.m*, which is located in the SWAM base directory. A glossary of terms used in the routines and a function directory are presented in Sections [A.4.1](#) and [A.4.2](#), respectively.

A.2.1: *cr.m*

The *cr.m* routine is the dynamical diffraction calculator. The functional flow chart is shown in [Figure A.3](#). This routine is used to calculate dynamical diffraction parameters for a selected single-crystal reflection ($H = hkl$) at a defined energy (E). These parameters include the unit cell volume ($V_{u.c.}$), hkl d-spacing (d_{hkl}), Debye-Waller factor (e^{-M}) structure factors ($F_0, F_H, F_{\bar{H}}$), susceptibilities ($\chi_0, \chi_H, \chi_{\bar{H}}$), geometrical Bragg angles (θ_B) and angular/energy offsets ($\Delta\theta, \Delta E$), Darwin width (ω_0, ω_E), index of refraction (n), critical angle (α_c), linear absorption coefficients (μ), and effective penetration depths (Λ). These parameters are all calculated based on user input and the contents of the crystal structure file, or *.ctl* file.

Upon selection of *cr.m* in the SWAM Function Selector, MATLAB displays an input dialog box (supported by MATLAB exchange subroutine *inputdlg.m*) that prompts the user for calculation and simulation input. This box is shown in [Figure A.4\(a\)](#). Default parameters are loaded into the fields based on the user's most recent analysis routine, which, for the example shown in [Figure A.4](#), is the calculation for the SiC(0006) crystal at 300 K at 2.4625 keV. The inputs are defined as followings:

- **Select X-ray Energy (keV):** Input the incident beam energy, in keV
- **Select Crystal File (.ctl file):** Input the crystal file name. Make sure that the crystal file is formatted correctly and located within the SWAM *.ctl* file directory. This value is case sensitive.
- **Select Crystal Reflection Plane (h,k,l):** Input the $H = h,k,l$ crystal plane for which the calculations will be performed. SWAM can tolerate comma- or space-delimited input.

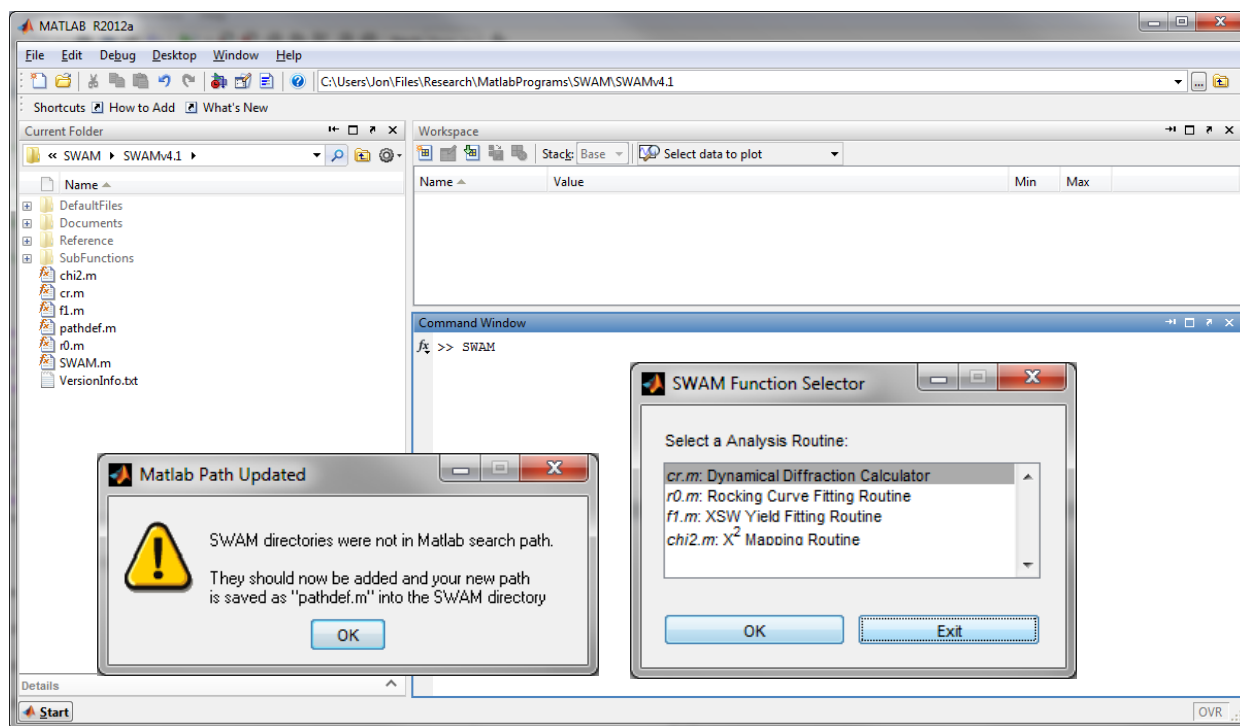


Figure A.2: SWAM initialization. The SWAM Function Selector provides the user with a choice of four analysis routines. SWAM will set the MATLAB path correctly if the user does not already have it set.

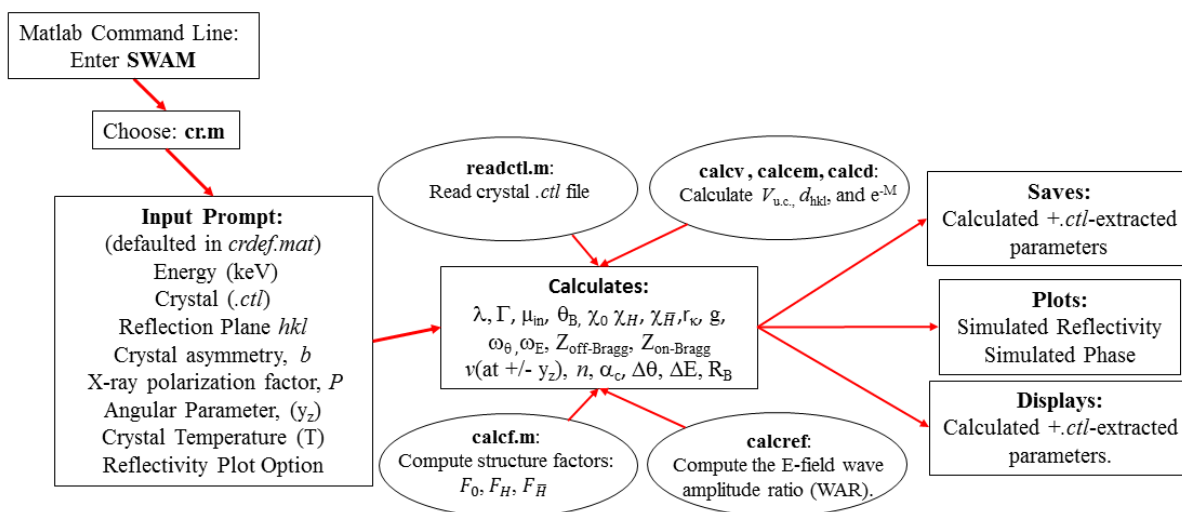


Figure A.3: Functional flowchart for *cr.m*.

- **Select Sample Asymmetry Parameter (b):** Input the degree of reflection asymmetry for the case of an asymmetric Bragg reflection or crystal offset. For a miscut sample, this parameter is defined in terms of sample miscut (ϕ) and the Bragg angle for the reflection, θ_B : $|b| = \frac{\sin(\theta_B - \phi)}{\sin(\theta_B + \phi)}$. For the Bragg case b is negative, and for the symmetric Bragg case $|b| = 1$. Further discussion on this parameter can be found in Batterman and Cole's Dynamical Diffraction review [180]. Traditionally, the effects of crystal mosaic on the broadening of rocking curves (RC) due to were approximated by increasing the magnitude of $|b|$.
- **Select Polarization Factor (P):** Input the X-ray polarization factor.
 - For the π -scattering geometry, the scattering vector is in the same plane as the incoming wavevector and the polarization vector. $P = \cos(2\theta_B)$.
 - For the σ -scattering geometry the scattering vector is perpendicular to the polarization vector and $P = 1$. This should be the default value for synchrotron experiments where the reflected and incident beam form a vertical plane.
- **Select Calculation Range ($\pm y_z$):** Input $\frac{1}{2}$ the y_z range over which the reflectivity calculations will be performed. The value y_z is consistent with the description used in Z.G. Pinsker's Dynamical Scattering of X-rays in Crystals[340] to be defined as:

$$y_z(\Delta\theta) = \frac{b\Delta\theta\sin(2\theta_B) + \frac{(1-b)}{2}\chi'_0}{|P|\sqrt{|b|}|Re(\sqrt{\chi_H\chi_{\bar{H}}})|} \quad (\text{A.1})$$

Or, as a function of ΔE ,

$$y_z(\Delta E) = \frac{-2b\frac{\Delta E}{E}\sin^2(\theta_B) + \frac{(1-b)}{2}\chi'_0}{|P|\sqrt{|b|}|Re(\sqrt{\chi_H\chi_{\bar{H}}})|} \quad (\text{A.2})$$

Typically, a value of at least ~ 2.5 is necessary in order to calculate the Bragg reflectivity across the entire Darwin range as well as include sufficient off-Bragg regions.

- **Select Crystal Temperature (K):** Input the crystal temperature in K. Note that the temperature is only used in the calculation of the Debye-Waller factor, and will not affect the calculation of the crystal d_{hkl} or $V_{u.c.}$.
- **Reflectivity Plot Option:** This option is the only new functionality in *cr.m* and was implemented in SWAMv4.0. The user can choose to either simulate the reflectivity curve as a function of θ or E , or to bypass the simulation all together.

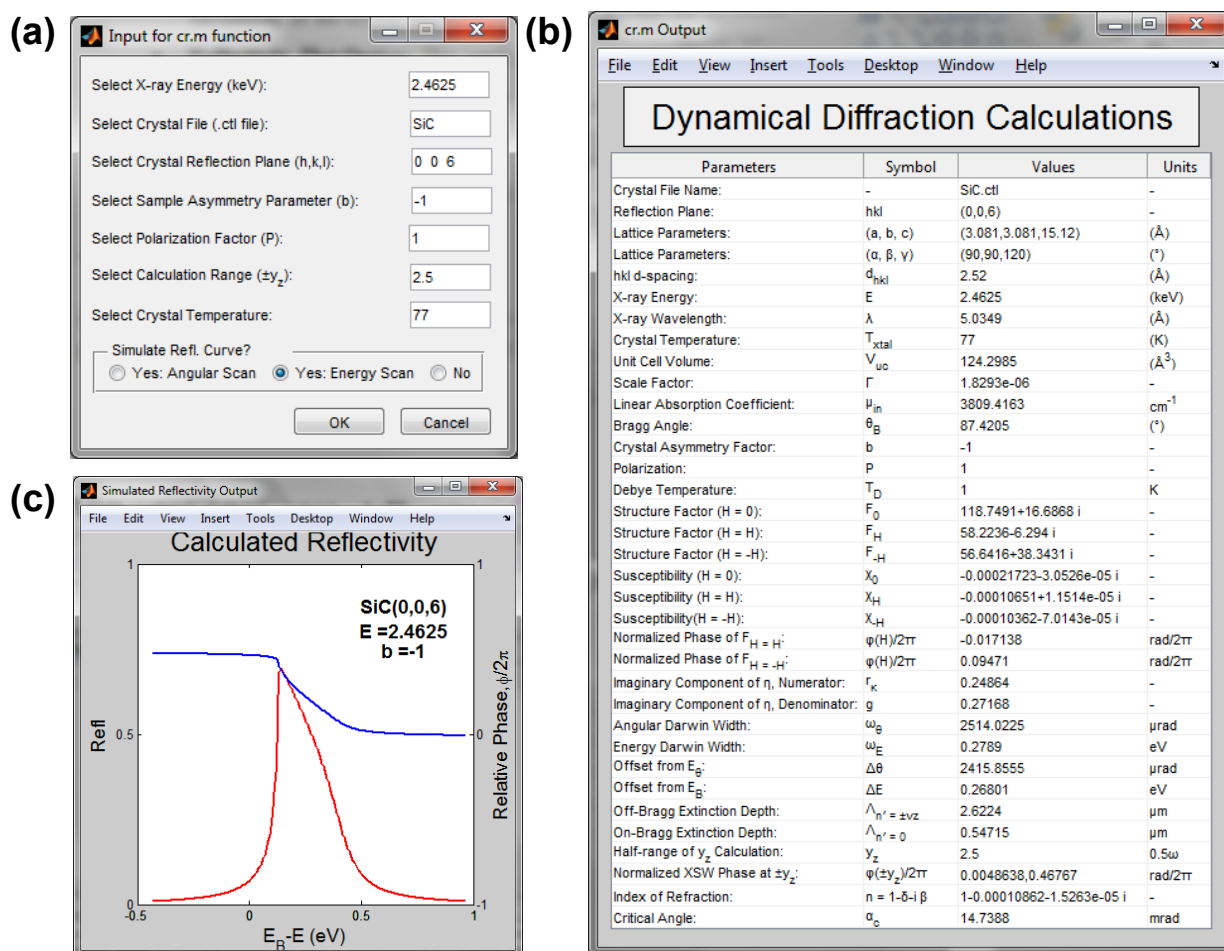


Figure A.4: Input and output panels for the *cr.m* routine.

Once the simulation parameters are input, the calculations will be performed. The calculation is completed in approximately 1 second using a 64-bit 2.67 GHz processor. The output from the routine is displayed in two MATLAB figures, shown in [Figures A.4\(b\) and \(c\)](#), contains a table in which all the parameters are defined plainly (first column) and symbolically (second column). The calculated values are displayed in the third column and the units are in the fourth. The output is rendered as a MATLAB table and, therefore, each cell can be selected and copied for transfer between programs. The second figure ([Figure A.4\(c\)](#)) displays the simulated (unconvoluted) reflectivity curve with accurate scaling and offsets. The figure also identifies the simulated

crystal reflection, the energy at which the calculation was performed, as well as parameters b and P .

Finally, the user is offered an option to save the output. If selected, the calculated parameters in [Figure A.4\(b\)](#) are written into a text file, which is subsequently appended with both the *.ctl* file used for the calculation as well as the simulated data. The user can save [Figure A.4\(c\)](#) as MATLAB figure file (*.mat* format) or other image format by using the *Save As...* option in the File menu.

A.2.2: *r0.m*

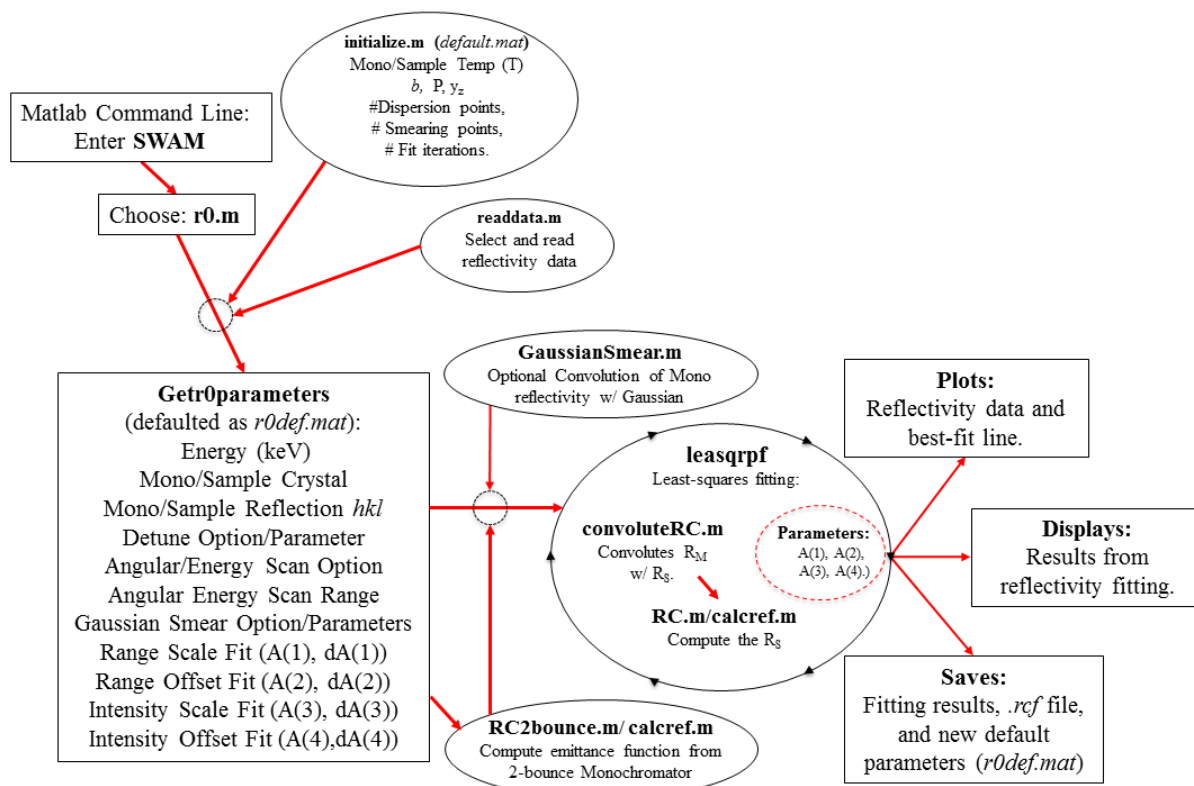
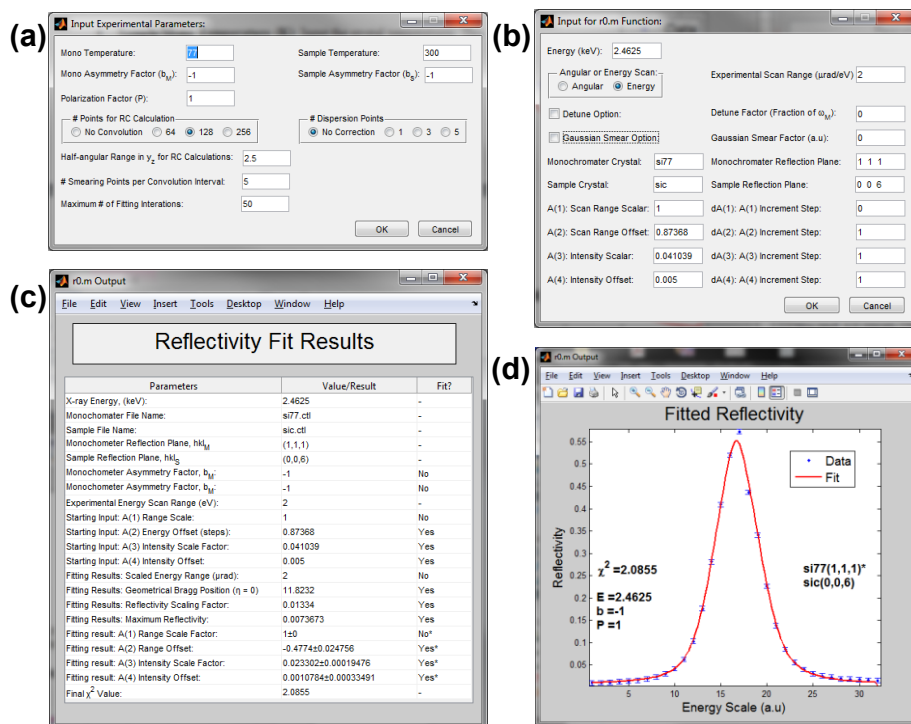
r0.m is the rocking curve fitting procedure. The functional flow chart is shown in [Figure A.5](#). This routine first accepts user input and calculates the ideal reflectivity of the monochromator (R_M) and sample crystal (R_S) (see [Section A.4.2](#)), then numerically convolutes the two to produce a theoretical rocking curve. The routine also includes an option for the Gaussian broadening of the rocking curve to account for sample mosaic. The resultant theoretical rocking curve is then fit to the experimentally measured rocking curve allowing for four free parameters, the experiment scan range scale factor and offset, and the reflected intensity scale factor and offset.

After fitting, *r0.m* allows the user to save two files. The first is the best-fit file, which contains the fitting results, *.ctl* file used for the reflectivity calculation, and the simulated reflectivity values. The second file is the reflectivity crystal file, or *rcf* file, which contains relevant parameters needed to calculate the rocking curve for the fitting of the XSW yield. The *rcf* file is subsequently called in both the yield-fitting (*fl.m*) and χ^2 -mapping (*chi2.m*) routines.

After selecting *r0.m* from the SWAM Function Selector, the user is prompted for a number of experimental parameters, as shown in [Figure A.6\(a\)](#). These include:

- **Sample/Mono Temperature (K):** Input the crystal temperatures. These values are used only for the calculation of the Debye-Waller factor and do not affect $V_{u.c.}$ or d_{hkl} .
- **Sample/Mono Asymmetry Factors (b):** Input the crystal asymmetry parameter.
- **Polarization Factor (P):** Input the X-ray polarization factor. This value is discussed in [Section 3.1.1](#) and Ref. [341]
- **# Points for RC Convolution:** Input the number of points that will be calculated for the monochromator rocking curve simulation. Note that this will only affect the number of points used to calculate R_M , not R_S , as the # Points used to calculate R_S is defined by the number of measured points acquired during the experiment. The No Convolution option will simply neglect the convolution with the monochromator and simulate a sample-only rocking curve. The other options (64, 128, 256) calculate R_M with the defined number of points. The selection will affect the precision and speed of the calculation.
- **# of Dispersion Points:** This option allows the user to choose the number of points used to account for the dispersion spread when the crystal just upstream of the sample has a d -spacing that does not match the sample d -spacing. This value is, in principle, defined by the source divergence. The effect of dispersion can be neglected when measurements are performed on an ID line, since the source divergence is smaller than ω_M . This value is defaulted to 0 because it is no longer typical to perform XSW experiments on bending magnet lines.
- **Half-angular Range in y_z for RC Calculations:** Input the range over which the RC calculations will be performed. See [Eq. A.1](#) and [Eq. A.2](#). Typical values are ~ 2.5 .
- **# Smear Points per Convolution Interval:** Input the number of points over which the smearing occurs at each convolution interval. Default values are ~ 5 .
- **Maximum # of Fit Iterations:** Input limits for fitting iterations. With reasonable starting values the number of iterations should not be more than 50.

When the experimental parameters are input, a navigation window (enabled by MATLAB Exchange routine *uigetfiles.m*) will prompt the user to select the reflectivity file. Currently, the file selection will filter file names to display only those files which contains the string “Refl”, and it is therefore recommended that the user name all reflectivity files accordingly. This can be bypassed, however, by clearing the *File Filter* field in the selection window. Upon file selection,

Figure A.5: Functional flowchart for *r0.m*.Figure A.6: Input (a)-(b) and output (c)-(d) panels and figures from the *r0.m* function.

the file-containing directory is saved as the current working directory for quick file access during subsequent fitting sessions. SWAM will then prompt the user for additional experimental input and initial fitting values, as shown in [Figure A.6\(b\)](#). Here, the user must input the following:

- **Energy (keV):** Input the incident X-ray energy.
- **Angular or Energy Scan:** Input the experimental mode in which the data was taken. SWAM can accommodate both modes due to two separate analysis trees that account for the differences in calculations.
- **Experimental Scan Range ($\mu\text{rad/eV}$):** Input the experimental range over which the data were acquired.
- **Detune Option/ Detune Factor (ω_M):** Decide whether to account for the monochromator detune. If activated, SWAM will perform calculations for R_M which account for two crystals detuned by some fraction of the Darwin width (ω_M). For example, a detune of 0.5 will calculate the monochromator emittance function as a product of two R_M for which the rocking curve centers ($\eta' = 0$) are offset by $0.5\omega_M$, as shown in [Figure A.7\(a\)](#). Not selecting the Detune Option will simply result in a calculation of R_M for a pair of non-detuned crystals.
- **Gaussian Smear Option/Gaussian Smear Factor (a.u.):** Decide whether to approximate the consequences of sample mosaicity by performing a convolution of R_M with a Gaussian. Note that due to the associative ($(f \otimes g) \otimes h = f \otimes (g \otimes h)$) and commutative properties ($f \otimes g = g \otimes f$) of the convolution function, it does not matter if the monochromator or sample rocking curve is broadened by the Gaussian, or the order in which the convolution is performed. Currently the Gaussian broadening factor is not directly tied to any physical value, and it is also not fit, which necessitates tedious guess-and-check methodology. These two issues should be remedied in future versions. An example of the consequence of the Gaussian smear is shown in [Figure A.7\(b\)](#).
- **Sample/Mono Crystal and Reflection Planes:** Choose *.ctl* files and reflections of interest. See [Section A.2.1](#).
- **Fit Parameters:** The values that can be fit during the routine are listed below. The user can input initial values and choose whether the parameter is fit ($dA \neq 0$) or not ($dA = 0$). Tuning the size of the increment step, dA , allows the user modify the manner in which the fitting routine explores the parameter space near the initial condition.
 - i. **A(1): Scan Range Scale:** This value scales the calculated scan range. Typically set to 1 and not fit.

- ii. **A(2): Scan Range Offset:** This value offsets the scan range. Typically allowed to fit.
- iii. **A(3): Intensity Scalar:** This value scales the intensity. This should be set to 1 if the reflectivity data was normalized by the straight-through incident beam.
- iv. **A(4): Intensity Offset:** This value offsets the simulated intensity. This can be used to account for constant background signal.

After the parameters are input, SWAM will attempt to fit the data, starting with the initial fitting parameters supplied by the user. The iteration number can be monitored in the MATLAB command window. When the fit is complete two windows are displayed. The results from the fit are shown in [Figure A.6\(c\)](#). Literal and symbolic parameters are shown in the first column, the final values and standard deviations are shown in the second, and the values in the third column identify which are the fitted values. Asterisked values in the third column denote the actual fit value. The second figure is a plot of the data vs. the fit, as shown in [Figure A.6\(d\)](#). Also displayed in the fit window are the best-fit χ^2 value and other relevant calculation parameters. The user is then provided with the options to save the fit results and parameters, output the *ref* file, and save the fit vs. data plot. Note that when saving the *ref* file it is recommended that the

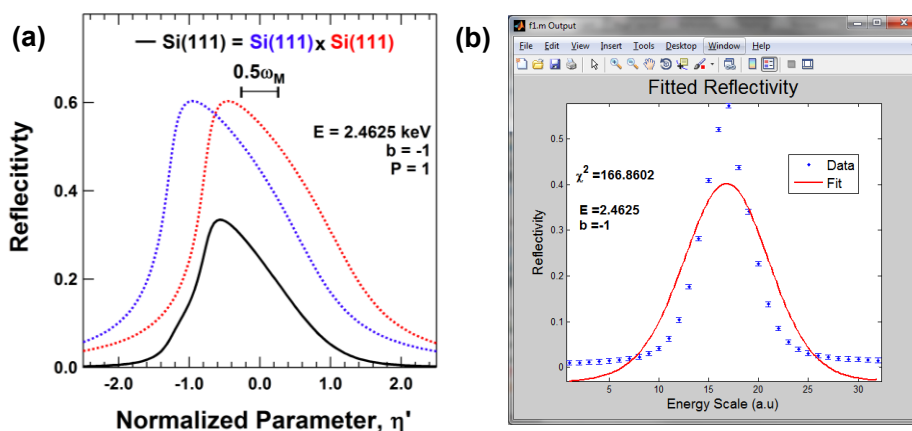


Figure A.7: Effects of (a) detuning and (b) Gaussian smearing of the monochromator. In (a), a $0.5 \omega_M$ detune thins and weakens the monochromator reflectivity curve. In (b), the convolution of the rocking curve with a Gaussian broadens the simulated rocking curve for SiC(0006). In this case, the simulated curve is much broader than the measured data and no Gaussian broadening was required to achieve a good fit.

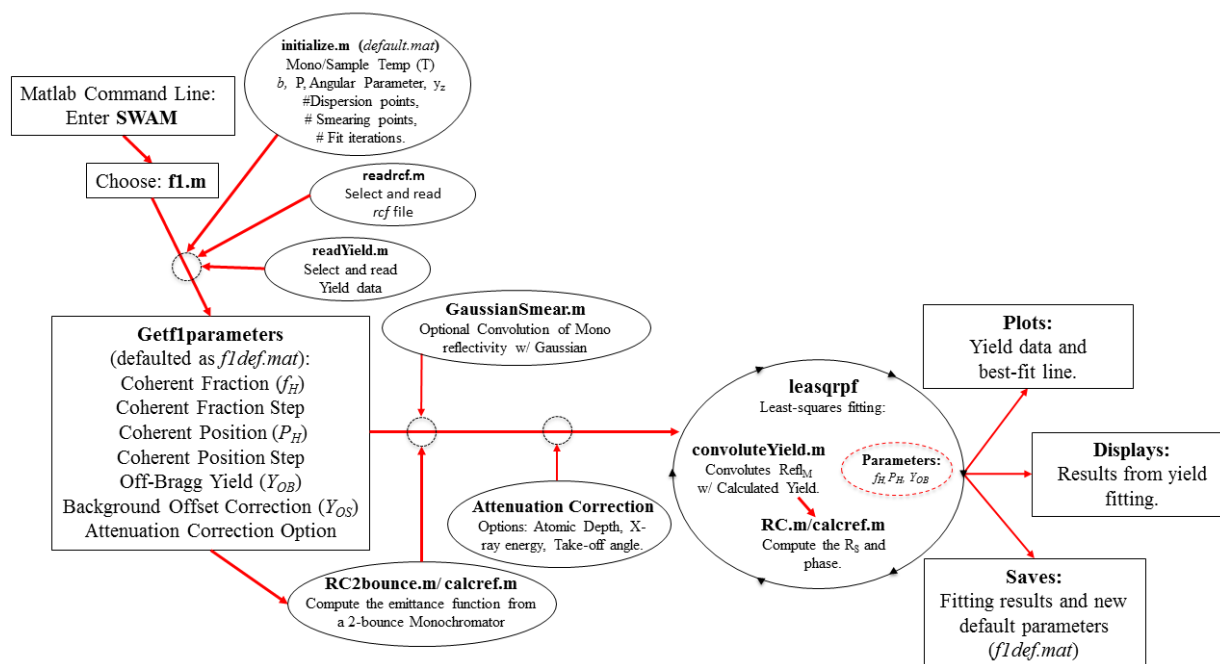


Figure A.8: Functional flowchart for the *fl.m* routine.

string “rcf” is present somewhere in the file name to facilitate file access for further χ^2 -mapping procedures. For convenience, SWAM then offers the user a refit option which, if selected, restarts the fitting routine at the data selection prompt.

A.2.3: *fl.m*

fl.m is the XSW yield analysis routine. The functional flow chart is shown in [Figure A.8](#). This routine takes the results from the rocking curve fitting procedure (the *rcf* file) and the yield data and fit it with the XSW yield equation: $Y(E_\gamma) = Y_{OB}[1 + R_B(E_\gamma) + 2p\sqrt{R_B(E_\gamma)}f_H\cos(\nu(E_\gamma) - 2\pi P_H)]$ as derived in [Section 3.3](#). The allowed free fit parameters are the coherent fraction, f_H , and the coherent position, P_H , as well as the off-Bragg yield (which is always fit), Y_{OB} , and the offset yield (Y_{OS}). The f_H and P_H values are of critical interest, as they are interpreted in order to extract structural information from the measurement.

Upon initialization of *fl.m* from the SWAM Function Selector, the same experimental parameters requested in *r0.m* (see [Section A.2.2](#) and [Figure A.6\(a\)](#)) are input again. Next, SWAM prompts the user for the *rcf* file and the yield data file. The yield file is recommended to contain “XSW_Input” within the title string so that the file filter can easily locate the yield files within the directory. SWAM then requests the information for yield fitting with the dialog box shown in [Figure A.9\(a\)](#):

- **Initial P_H/f_H values and interval steps:** P_H and f_H are two of the four values that can be fit in this routine. Due to the periodic nature of the yield function, the user should attempt to set initial values as close to their expected values as possible, or one might find themselves with solutions with $f_H < 0$ or $0 > P_H > 1$. Modifying the interval value associated with either P_H or f_H to be equal to 0 will fix that parameter. Selecting the size of the increment step, dA , will allow the user to tune how the fit explores the parameter space near the initial condition.
- **Use Attenuation (extinction) Correction?:** SWAM possesses an analysis tree which allows the user to accounts for the location from which the yield signal originates. The attenuation correction was not necessary for work presented in this thesis because the photoelectron signals originated from the very near-surface ($\ll 10$ nm from surface) region of the sample, and therefore the extinction effect had little influence on the data. However, one can chose either to apply integrated or selected path corrections for signals from measured species that reside deep within the bulk. For further discussion on this correction see L. Cheng and M.J. Bedzyk’s 2005 XSW review [178]. There are three options:
 - i. **Yes: Integrated:** This will account for a distribution of atomic species throughout a crystal volume. Input for this correction include the X-ray Energy (in keV) for the fluorescence X-rays emitted from the species of interest and the Take-off Angle ($^\circ$) between the sample surface and the fluorescence detector (in $^\circ$).
 - ii. **Yes: Selected Depth:** This option modifies the yield analysis by applying corrections for a distribution of atomic species at a specific depth. The depth and atomic step interval are tunable under Selected Depth Input. This option is disabled as of SWAMv4.1 as improvements are made on this analysis path.
 - iii. **No:** This option will neglect extinction effects.
- **Fit Yield with Offset?:** This option should always be set to 0 unless there is a contribution to the XRF yield which excited by the incident beam only.

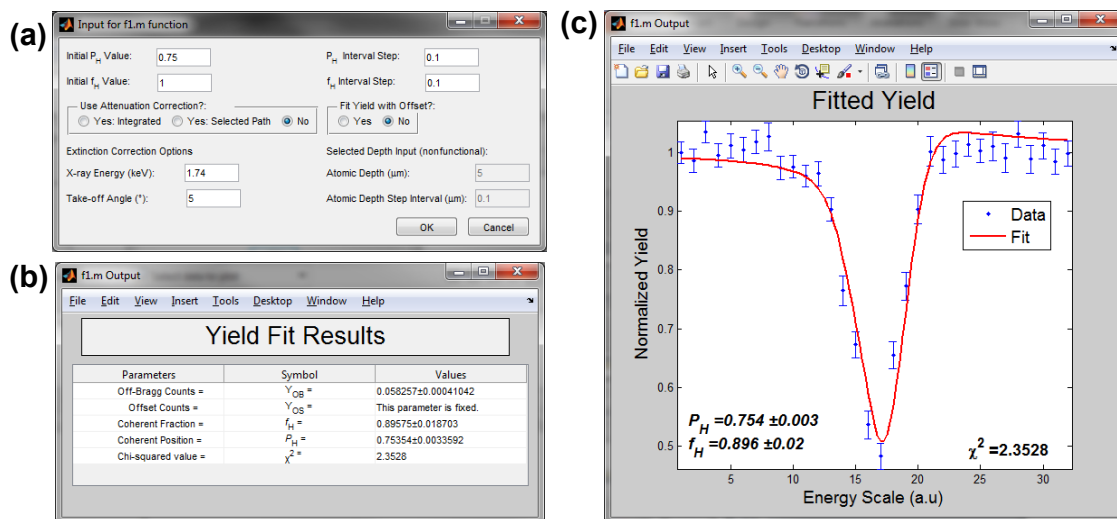


Figure A.9: An example of input and output panels for the *fl.m* function. (a) The input dialog box. (b) The output results. (c) The fitted yield curve.

After the parameters are selected, SWAM will attempt to fit the yield data. As in the *r0.m* routine, the iteration number can be monitored in the MATLAB command window. SWAM then displays two figures. The first ([Figure A.9\(b\)](#)) contains the yield fitting results, an example of which is shown for the bulk C signal monitored when scanning through the $H = 0006$ SiC Bragg condition at 2.4625 keV. [Figure A.9\(c\)](#) shows the plot of the best-fit result and the measured data. This figure includes the P_H and f_H results (reported with standard deviations) and the best-fit χ^2 value. The user is then provided with the option to save the best-fit results and the figure, if desired. When finished, SWAM then offers the option to fit another yield set.

A.2.4: *chi2.m*

chi2.m is the XSW error analysis routine. Traditionally, XSW values are reported along with their standard deviations, which will typically underestimate the uncertainty associated with the fit results. Because analysis in this thesis required precise knowledge of the uncertainties associated with the extracted P_H and f_H , a χ^2 -mapping routine was developed to explore the

confidence levels of the fit results. It is important to note, however, that the validity of the confidence levels are highly dependent on the accuracy of the error estimates for the data points. While the other routines *cr.m*, *r0.m*, and *fl.m* have each been overhauled, *chi2.m* the only entirely new functionality developed for this version of SWAM.

The best-fit solution found in the *fl.m* is found where the goodness-of-fit parameter,

$$\chi^2 = \sum_{k=1}^N \frac{(y_{k,exp} - y_{k,calc})^2}{\delta y_k^2} / (N - N_p), \quad (\text{A.3})$$

is minimized. Here, $y_{k,exp}$ and $y_{k,calc}$ are the k^{th} measured and calculated values, respectively, δy_k is the uncertainty of the k^{th} data point, N is the number of data points fitted, and N_p is the number of fit parameters. One can investigate the dependence of χ^2 on any parameter by exploring the χ^2 values about the χ^2 minimum (χ^2_{\min}) and allowing the other parameters to fit freely. The values $\chi^2_{\min} + 1$, $\chi^2_{\min} + 2$, $\chi^2_{\min} + 3$, etc. are estimates of the 1σ (68.3%), 2σ (95.4%), 3σ (99.7%), etc. confidence intervals. *chi2.m* accesses the best-fit parameters from *fl.m* and gives the user the option to explore the minimum about the best-fit for both P_H and f_H χ^2 -space directions. To do this, *chi2.m* sequentially calculates the minimum χ^2 value using the *fl.m* routine by holding either P_H or f_H fixed, and allowing the other parameter (and Y_{OB}) to vary. The functional flow chart is shown in [Figure A.10](#). Note that any uncertainty associated with the fitting of the rocking curve is neglected in this analysis, but due to the much lower uncertainty levels typical to R_B fitting, it is reasonable to assume that the yield data will be the dominant source for uncertainty.

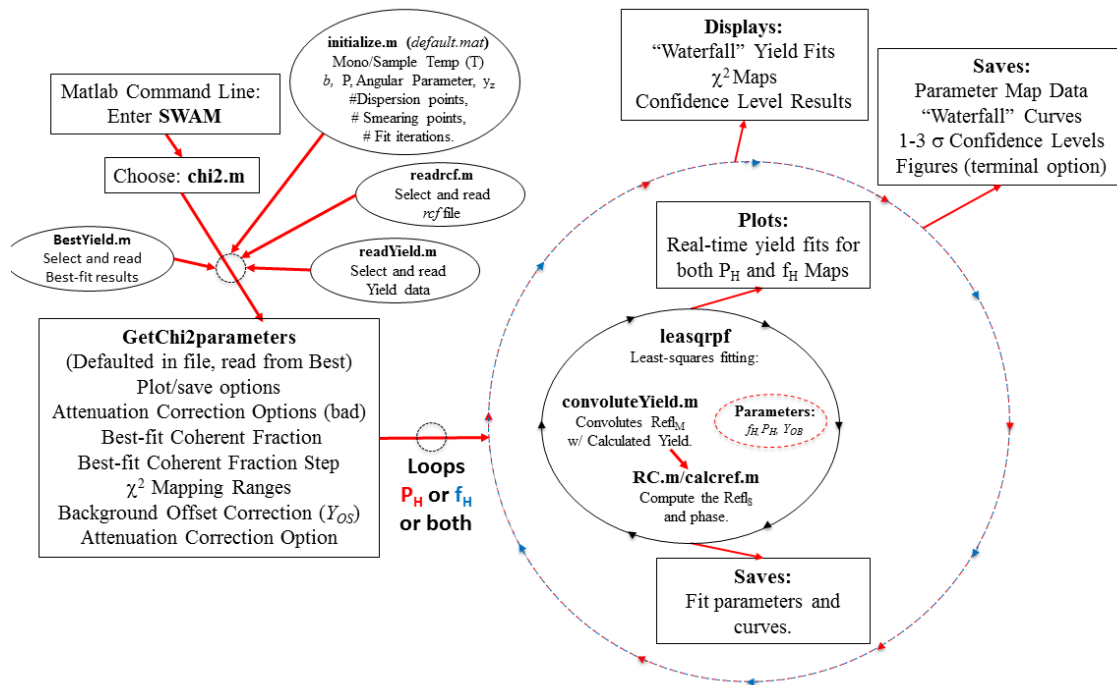


Figure A.10: Functional flow chart for *chi2.m*.

Upon selection of the *chi2.m* procedure in the SWAM Function Selector the user is requested to provide the experimental parameters provided for *r0.m*. Next, a series of browser windows require the selection of the *rcf* file (default filter **rcf**), the XSW Input file (default filter **XSW_Input**), and the best-fit file (default filter **XSW_Ouput**). After these have been selected, the user then selects the parameters for the χ^2 -mapping procedure on the input panel, shown in [Figure A.11\(a\)](#). The input parameters are defined as follows:

- **Parameters(s) to Map:** Select which XSW parameter the user would like to map: P_H and/or f_H .
- **File(s) to Save:** Select which output files are to be saved. Opting to save the *chi2* Results file will write the χ^2 values, Y_{OB} , Y_{OS} , P_H , f_H , and the attenuation correction option into a file suffixed with **_ChiMap*. Opting to save the Fitting Curves file will write all the simulated yield curves, which can be plotted in another program if desired. Opting to save the 1-sigma Params will output the parameter values at 1σ , 2σ , and 3σ confidence intervals.

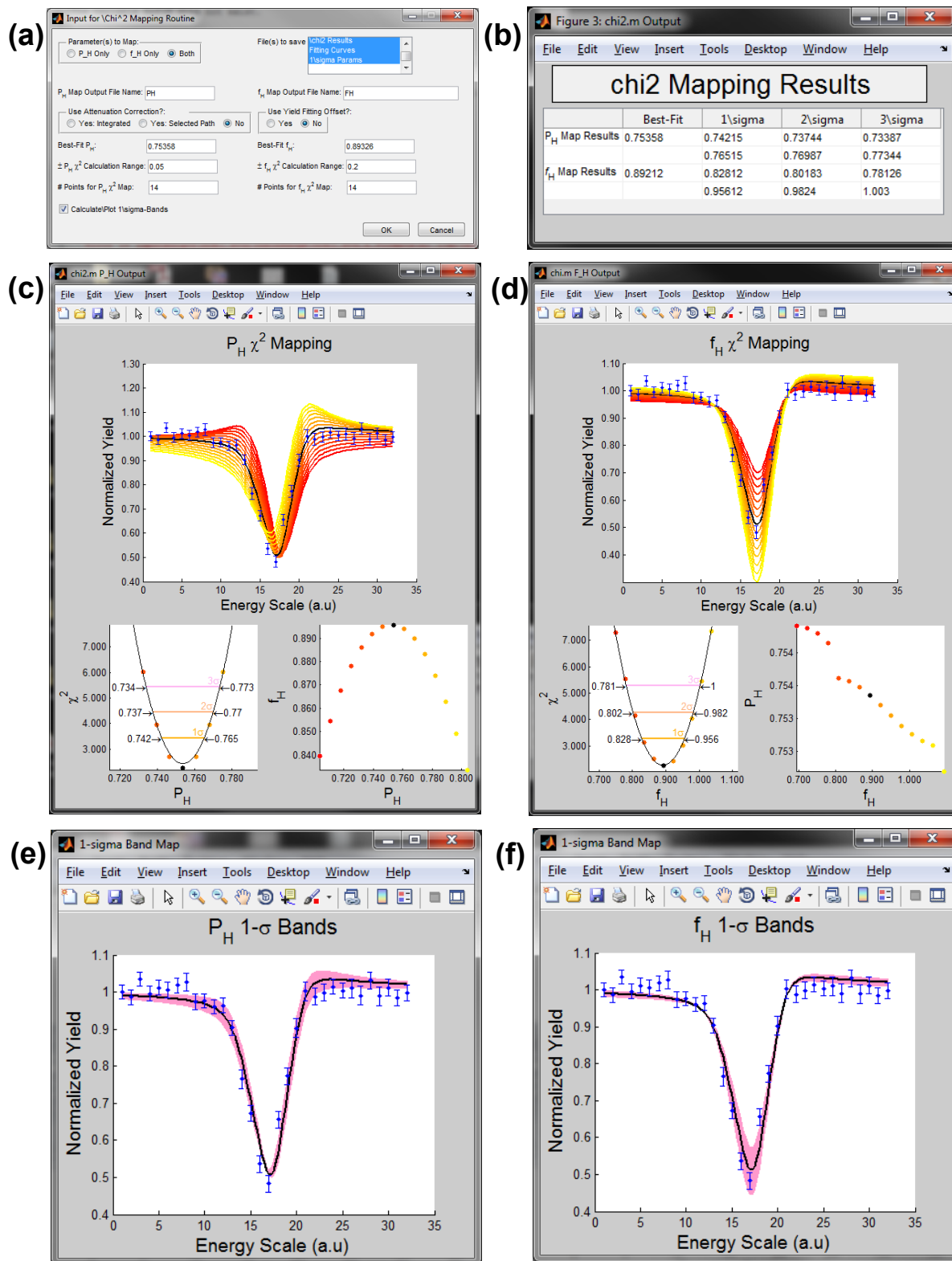


Figure A.11: Input and output panels for the χ^2 -mapping routine, *chi2.m*. (a) The input panel, (b) the 1-3 σ confidence levels, and (c)-(d) the χ^2 maps. (e) and (f) show the 1 σ confidence bands for the P_H and f_H fits, respectively.

- **Use Attenuation Correction?/Use Yield Fitting Offset?:** These fields are temporary, and in the future, should be read directly from the best-fit XSW output file. They enable the attenuation correction options discussed in [Section A.2.3](#).
- **Best-Fit P_H/f_H :** These values are the best-fit P_H and f_H acquired from the *fl.m* minimization procedure. They are loaded during the file selection routine.
- **P_H/f_H χ^2 Calculation Range:** This field dictates the range over which the χ^2 -map will be calculated. Currently, the values are defaulted at ± 0.05 and ± 0.20 , respectively, for P_H and f_H . There should be a way to infer a decent value for this from the best-fit parameters and their variances, but this functionality is not yet stable
- **# Points for P_H/f_H χ^2 -map:** This input defines the number of points in each map. With a 64-bit 2.67 GHz processor, each point takes ~ 30 seconds to calculate, so values of ~ 10 will create full parameter maps in ~ 5 minutes.
- **Calculate 1sigma-bands:** Activating this option will tell SWAM to find the P_H and f_H values at that χ^2+1 values and calculate the yield curves for these parameters. SWAM will then plot the yield curves about the best-fit value, as shown in [Figures A.11\(c\) and \(d\)](#). Take care to judiciously set the calculation range if this option is activated.

When the parameters are input, SWAM will immediately create a 3-panel figure ([Figures A.11\(c\) and \(d\)](#)) to display the analysis in real time. The largest plot displays the measured XSW data and the calculated yield curves. The calculated yield curves are displayed with an autumnal color scheme, progressing from red to yellow as the parameter is mapped from $- \rightarrow +$ displacement values. At the same time, the bottom two panels plot color-matched χ^2 -maps (bottom left) and $P_H - f_H$ maps (bottom right). When the mapping is complete the χ^2 -maps are fit with a 2nd-order polynomial which is used to subsequently used to estimate the 1σ , 2σ , and 3σ confidence values. These results are presented in an table, shown in [Figure A.11\(b\)](#), the cells of which are easily accessible copying to other programs. Finally, the user is presented with the option to save any of the displayed figures. A refit option then allows the user to continue to analyze additional yield sets using the same *rcf* file without reinitializing the entire analysis routine.

A.3: Major Changes to SWAM

As mentioned earlier, during the review of SWAM it became clear that the program required a major overhaul. General changes are noted in [Section A.1](#), many of which are cosmetic, correct minor errors, or improve the functionality and accessibility to the SWAM code itself. However, there were some major issues with early version of SWAM that have potential effects on the XSW results.

A.3.1: SWAM Extension to *E*-Scans

Prior to SWAMv3.0, the program was strictly limited to analysis of data acquired using angular θ -scans, as are typical for the Bedzyk group. However, experiments at ID32 at the ESRF, where the XSW data in this thesis were acquired, are generally performed using energy *E*-scans. Initial attempts by Feng in SWAM v2.1-2.4 were intended to extend the program to allow for the analysis of data acquired with *E*-scans. To do this, Feng established a network of conditional statements to account for differences in calculations between the two experimental modes. While Feng's modifications provided excellent groundwork for the extension of the routine, there existed no set of well-understood XSW data for testing at that time. This resulted in a series of errors in the calculation of y_z ([Eq. A.2](#)), which subsequently lead to errors in the calculated reflectivity and yield. Those errors have been corrected in the most recent version of SWAM and are documented throughout the script itself.

A.3.2: Convolution Correction

In early versions of SWAM the numerical convolution function was incorrectly coded. Namely, the routine was written so that the calculated monochromator emittance function is convoluted in such a way that the $j = 1$ point, (Figure A.12(a)), first encounters the $k = 1$ point of the sample crystal (Figure A.12(b)). Physically, this is not what occurs during a typical measurement. Regardless how the experiment is performed ($-\theta \rightarrow +\theta$, $+\theta \rightarrow -\theta$, $-E \rightarrow +E$, $+E \rightarrow -E$), if the monochromator design is non-dispersive then the α -branch of the reflection from one crystal will always encounter the β -branch of the other during the scan.

This error is observable only in certain experimental conditions. For example, XSW experiments performed by our group, the monochromator Darwin width is much typically much thinner than that of the sample crystal ($\omega_M \ll \omega_S$). In this case the measured rocking curve should be very close to that expected for the un-convoluted crystal, as the monochromator

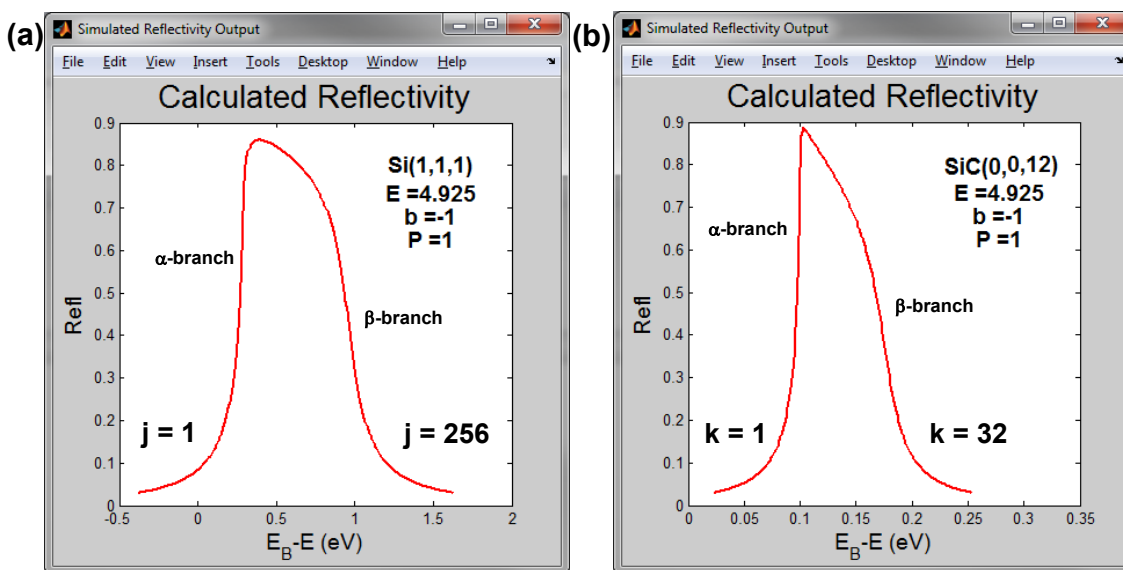


Figure A.12: Examples of simulated rocking curves for (a) Si(1,1,1) and (b) SiC(0,0,12) reflections at 4.925 keV. Previous SWAM versions incorrectly convoluted the two reflectivity curves, resulting in a “flipped” rocking curve in the case where $\omega_M \approx \omega_S$.

emittance function can be well-approximated with a δ -function. However, during the beamtimes at ID32 at the ESRF a measurement at $E = 4.925$ keV was performed in which the SiC(00012) reflection was much thinner than that of the Si(111) monochromator. During subsequent analysis the SWAM routine produced a rocking curve “flipped” on the E -axis due to the error in the convolution, greatly exasperating the effects of the error. This has been remedied in recent SWAM releases and documented in the routine script.

A.3.3: Data Weighting During Least-Squares Fitting

Early versions of SWAM failed to account for the weighting of data both in fitting of the rocking curve and yield data. For the *r0.m* function data points were not weighted, and for the *fl.m* routine the goodness-of-fit values were reporting using the “scaled χ^2 ” (χ_S^2) parameter, defined as

$\chi_S^2 = \sum (y_{x,exp} - y_{k,calc})^2 / N$. This analysis would typically produce fit values on the order of $\chi_S^2 \sim 10^{-4}$, a value that is hard to interpret and does not account for experimental uncertainty.

The current version of SWAM possesses weighting vectors defined by the calculated uncertainty values for each k^{th} data point and uses [Eq. A.3](#) for minimization. The χ^2 values output now provide give the user an excellent impression of the quality of fit and enable superior assessment of solution uncertainty.

A.4: Function Directory and Parameter Glossary

SWAM currently consists of one initialization function (*SWAM.m*), 4 main subroutines (*cr.m*, *r0.m*, *fl.m*, and *chi2.m*), and ~ 30 sub-functions. Also included in the SWAM directory are archival functions, default *.mat* arrays, *.ctl* files, and other reference libraries. The documents included in the latest version of SWAM include a selection of relevant XSW literature, SWAM

benchmarks and flowcharts, and a detailed SWAM Guide (derived from this Appendix) and Logbook to be shared between users.

A.4.1: Function Directory

A table of the SWAM functions names and objectives is shown in [Table A.1](#). Additional notes on each function are commented into the routines themselves. For complete function dependency information it is recommended to use the MATLAB Editor Tool *Show Dependency Report*. The *First-Tier Functions* in [Table A.1](#) are the main initialization scripts. The *Second-Tier Functions* are the functions critical to the calculations. The *Calculation* functions are those that are called by the *Second-Tier Functions* during calculations. The *Read/Write/Prompt* functions enable the user interface and the reading and writing of data files.

Table A.1: Function directory. Asterisked functions were acquired from the MATLAB Exchange.

First-Tier Functions		
	Function	Definition
1.)	<i>swam.m</i>	Initialization function
2.)	<i>cr.m</i>	Dynamical diffraction calculator (Section A.2.1)
3.)	<i>r0.m</i>	Fits rocking-curve data (Section A.2.2)
4.)	<i>fl.m</i>	Fits XSW yield data (Section A.2.3)
5.)	<i>chi2.m</i>	Performs χ^2 -mapping of P_H and f_H (Section A.2.4)
6.)	<i>convoluteRC.m</i>	Convolution of rocking curve calculation
7.)	<i>convoluteYield.m</i>	Convolution of yield calculation
8.)	<i>leasqpf.m</i>	Least-squares fitting procedure
9.)	<i>RC.m</i>	Calculation of single-bounce reflectivity
10.)	<i>RC2bounce.m</i>	Calculation of double-bounce reflectivity
Calculations		
11.)	<i>calcd.m</i>	Calculates $d_{hk\ell}$
12.)	<i>calcem.m</i>	Calculates e^{-M}
13.)	<i>calcf.m</i>	Calculates $F_0, F_H, F_{\bar{H}}$
14.)	<i>calcphix.m</i>	Calculates <i>phix</i> factors
15.)	<i>calcref.m</i>	Calculates $E_H:E_0$ ratio
16.)	<i>calcv.m</i>	Calculates $V_{u.c.}$
17.)	<i>cromer.mat.m</i>	Calculates f' and f''
18.)	<i>GaussianSmear.m</i>	Performs convolution of mono R_B with Gaussian

Read/Write/Prompt		
19.)	<i>ChiSave.m</i>	Displays save options for the <i>chi2.m</i> routine
20.)	<i>ExtractChi.m</i>	Extracts data from <i>chi2.m</i> figures
21.)	<i>filesave.m</i>	Save data into designated file
22.)	<i>GetChi2parameters.m</i>	Acquires user input for <i>chi2.m</i>
23.)	<i>GetcrParameters.m</i>	Acquires user input for <i>cr.m</i>
24.)	<i>Getflparameters.m</i>	Acquires user input for <i>fl.m</i>
25.)	<i>Getr0parameters.m</i>	Acquires user input for <i>r0.m</i>
26.)	<i>Initialize.m</i>	Acquires user input for basic experimental parameters
27.)	* <i>Inputsdlg.m</i>	Enables multifunctional dialog panels
28.)	* <i>MFquestdlg.m</i>	Flexible prompt dialog box
29.)	<i>rcfFileSave.m</i>	Saves the <i>rcf</i> file
30.)	<i>readBestFitFile.m</i>	Reads the best-fit <i>fl.m</i> output for <i>chi2.m</i> mapping
31.)	<i>readctl.m</i>	Reads the <i>ctl.m</i> file
32.)	<i>readdata.m</i>	Reads columnated data
33.)	<i>readrcf.m.m</i>	Reads <i>rcf</i> file
34.)	<i>readReflData.m</i>	Reads reflectivity data
35.)	<i>readYieldData.m</i>	Reads yield data
36.)	* <i>textbp.m</i>	Automatic textbox positioner
37.)	* <i>uipickfiles.m</i>	Interface for file selection

A.4.2: Parameter Glossary

[Table A.2](#) lists the critical parameters used in the SWAM routine and their handles. Parameters may be appended with an *S* or *M* within the code in order to distinguish sample values from monochromator values.

Table A.2: Parameter Glossary. Asterisked values are generally defined as global and apply across workspaces.

SWAM Crystal and Diffraction Parameters			
	Parameter/Hand	Definition	Equation
1.)	*Energy	Incident beam energy (keV)	-
2.)	<i>hc</i>	(Å keV)	-
3.)	* <i>lambda</i>	Incident beam wavelength (Å)	$hc/energy$
2.)	*Crystal	Crystal values, matches <i>.ctl</i>	-
3.)	* <i>hkl</i>	Miller Indices	-
4.)	* <i>b</i>	Crystal Asymmetric Factor	See Section A.2.1
5.)	* <i>P</i>	Polarization Factor	See Section A.2.1
6.)	* <i>yzRange</i>	Defines dimensionless η .	See Section A.2.1

7.)	<i>*T, Temp</i>	Crystal Temperature	-
8.)	<i>re</i>	Classical Electron Radius (Å)	See Chapter 3
9.)	<i>dspacing</i>	d-spacing	See <i>calcd.m</i>
10.)	<i>Vuc</i>	Unit Cell Volume reflectivity	See <i>calcv.m</i>
11.)	<i>eM</i>	Debye-Waller Factor	e^{-M}
12.)	<i>thB</i>	Geometrical Bragg Angle	$2d\sin(\theta_B) = n\lambda$
13.)	<i>gam</i>	Dimensionless Scale Factor	$\Gamma = -\frac{r_e \lambda^2}{\pi V_{u.c.}}$
14.)	<i>F0, Fh, Fhb</i>	Structure Factor	See Chapter 3
15.)	<i>ChiF0, ChiFh, ChiFhb</i>	Susceptibility	$\chi = -\Gamma F$
16.)	<i>g</i>	Imaginary numerator of η	$g = - P \frac{1 + b }{2\sqrt{ b }} \frac{\chi'_0}{ Re(\sqrt{\chi_H \chi_{\bar{H}}}) }$
17.)	<i>rkappa</i>	Imaginary denominator of η	$r_k = Im(\sqrt{\chi_H \chi_{\bar{H}}}) / Re(\sqrt{\chi_H \chi_{\bar{H}}})$
18.)	<i>eta</i>	Dimensionless angular/energy parameter	$\eta = -\frac{y_z + i g}{1 + i r_k}$
19.)	<i>omegaTh</i>	Angular Darwin Width (μrad)	$\omega_\theta = P \frac{1 + b }{2 b } \frac{\Gamma F'_0}{\sin(2\theta_B)}$
20.)	<i>omegaE</i>	Energy Darwin Width (eV)	$\omega_E = P \frac{1 + b }{2 b } \frac{\Gamma F'_0 / E}{\sin^2(\theta_B)}$
21.)	<i>AngOffset</i>	Angular Offset from θ_B	$\Delta\theta = \frac{1 + b }{2 b } \frac{\chi'_0}{\sin(2\theta_B)}$
22.)	<i>EnergyOffset</i>	Energy Offset from θ_B	$\Delta E = \frac{1 + b }{2 b } \frac{E \chi'_0}{\sin(2\theta_B)}$
23.)	<i>phi, p</i>	XSW phase	$\phi = \text{ArcTan}\left(Im\left(\frac{E_H}{E_0}\right) / Re\left(\frac{E_H}{E_0}\right)\right)$
24.)	<i>WAR</i>	Wave amplitude ratio	$\frac{E_H}{E_0} = -\frac{ P }{P} \sqrt{ b } \left(\frac{F_H}{F_{\bar{H}}}\right)^{\frac{1}{2}} (\eta \pm (\eta^2 - 1))^{1/2}$
25.)	<i>*RefIM, RefIS</i>	Mono and Sample Reflectivity	$R_B = \left \frac{E_H}{E_0}\right ^2$

A.5: Future Releases

While the current version of SWAM is certainly an improvement of previous versions, the program would benefit from a number of upgrades.

A.5.1: Dumond Diagram and Dispersion Surface Calculations

All the parameters necessary for the calculation of DuMond diagrams [342] and the dispersion surface are performed in *cr.m*. The simple extension of the routine to accommodate the production of diagrams would greatly assist in the conceptual understanding and visualization of the emittance and acceptance functions of the monochromator and the sample crystal, as well as the θ - E relationship with respect to the coupling between the incident and diffracted beams.

A.5.2: Model-Independent 3D Mapping and Global Fitting Routines

If three or more Fourier components are measured with XSW, it is possible to formulate an atomic density map via the summation of Fourier amplitudes and phases to create a model-independent normalized 3D atomic density distribution ($\rho(\mathbf{r})$). The relationship between this distribution and the sum of the measured H Fourier components is:

$$\rho(\mathbf{r}) = 1 + 2 \sum_{\substack{H \neq 0 \\ H \neq \bar{H}}} f_H \cos[2\pi(P_H - \mathbf{H} \cdot \mathbf{r})]. \quad (\text{A.4})$$

This approach is described in in Bedzyk's 2005 XSW Review [177]. Currently there exist no MATLAB routines that allow for the inversion of XSW data. However, one could envision the implementation of such a routine as an additional SWAM function that would read *fl.m* output, perform calculations, and plot the distribution $\rho(\mathbf{r})$ directly.

In addition to the integration of model-independent XSW imaging, a model-based global optimization routine is often used to more precisely determine the species' spatial distribution. This is possible by performing a global fit the results for all $H=hkl$ results using the relationship

$$f_H e^{2\pi i P_H} = \sum_i c_i e^{2\pi i \mathbf{H} \cdot \mathbf{r}_i}, \quad (\text{A.5})$$

where c_i and \mathbf{r}_i are the occupation and position of the species of interest at the i^{th} site. Currently, as described in both Anthony Escudro's and Zhenxing Feng's theses, the XSW global fitting procedure is an Igor Pro routine. In the future versions of SWAM, this routine should be consolidated with the other XSW analysis routines and can be added as the 5th analysis tool. MATLAB provides excellent optimization tools and this transition should be straightforward. Incorporation of both of these model-independent and model-dependent 3D imaging routines into SWAM would unite all routines into a central program, ultimately enabling the complete, streamlined analysis of XSW data into a single, centralized program.

A.5.3: Standing Wave Analysis GUI (SWAG)

In its current form, SWAM is a powerful tool for the analysis of XSW data. However, the dialog-box structure is inherently unwieldy and should ultimately be scrapped for a MATLAB-based Graphical User Interface (GUI). The dialog-box based program now used in SWAM highly limits program flexibility and requires tedious re-initialization of routines in order to modify parameters or change data sets. The event-driven programming afforded by the MATLAB GUI framework would allow the users to easily utilize multiple components of the program. SWAG itself is envisioned to replace the SWAM initialization function with a set of tabulated panels for each of the SWAM functions. This would replace the current model, which calls multiple objects

(dialog boxes, figures, file selection prompts, etc...) with an organized self-contained GUI. An example of the foundation for this program is shown in [Figure A.13](#). In this example there are three tabulated panels for each function *cr.m*, *r0.m*, and *fl.m*. On the *cr.m* tab, the Crystal Parameters tab includes a *.ctl* file browser and fields for crystal input parameters. Ideally this function would pass the necessary values to *cr.m* when *Execute Calculation* is pressed, and the output parameters would be printed in the right-hand panel. In reality, it was the initial goal of the SWAM upgrade project to construct this GUI. However, SWAM itself required a great deal more time and attention than originally thought, and therefore full implementation of the GUI must be left to future group members.

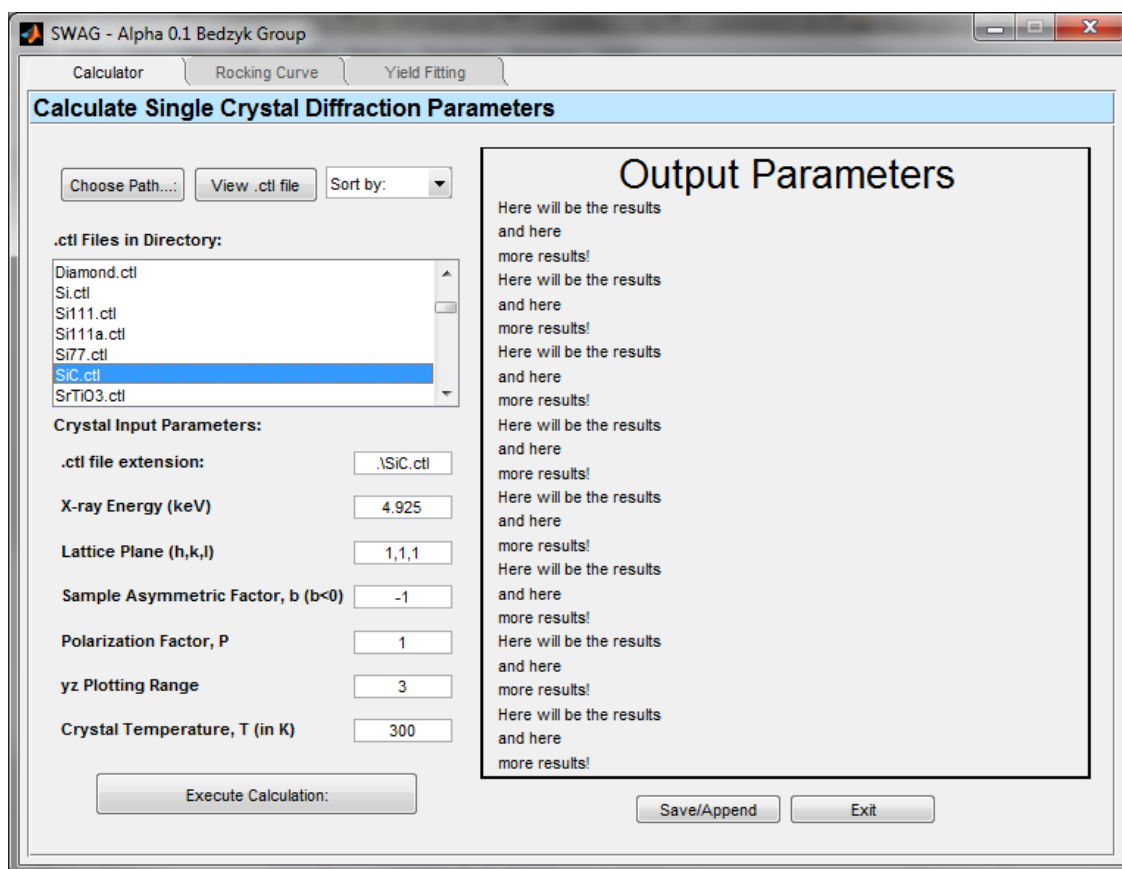


Figure A.13: The potential foundation of the SWAG program.

Appendix B: Alternate XSW-XPS Analysis

The peak-fitting models used to analyze the data in the main text (summarized in [Table 4.1](#)) differ greatly from those conventionally used in literature [24, 29]. However, we note that the model proposed by Emtsev and coworkers [24] can be well-fit by accounting for a small amount of graphene coverage and exchanging the intensity ratios for the S_1 and S_2 peaks ([Figure B.1](#)). Because zero-layer graphene is always found to coexist with a moderate percentage of graphene inclusions, our model, which accounts for $\sim 15\%$ of graphene coverage, may be a more accurate model. We observe that the data presented in the 2007 PRB work was also performed prior to the

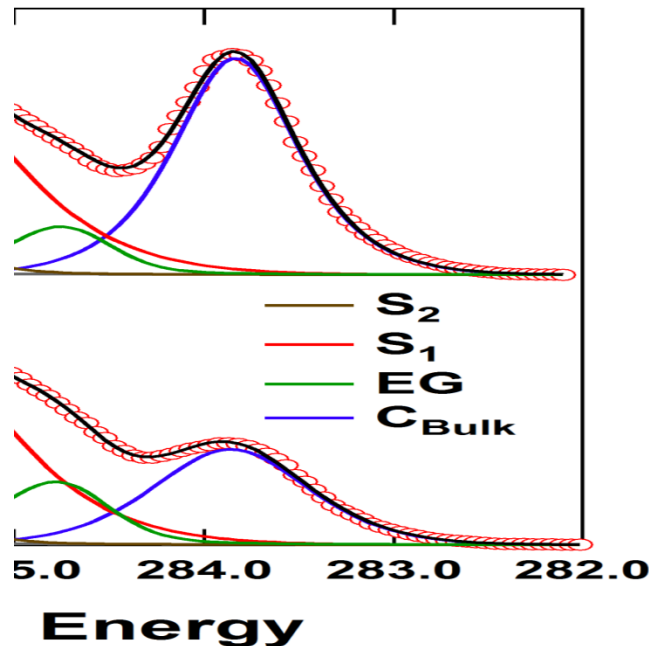


Figure B.1: Fits to data from nominal EG_0 -only graphene sample from Ref. [24]. In contrast to the interpretation of Emtsev *et al.* we fit the spectra accounting for a small coverage of EG (green), which is common in nominally EG_0 -only samples, and find an alternate model in which the relative intensities of the S_2 (brown) and S_1 (red) peaks are essentially reversed.

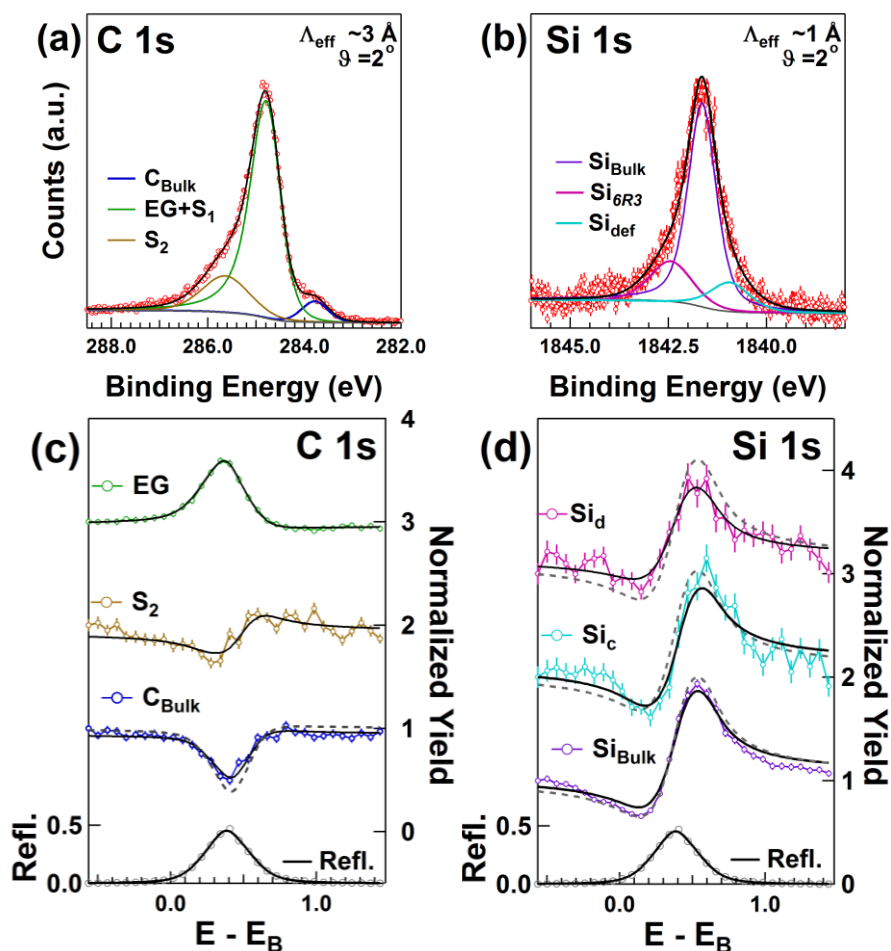


Figure B.2: XPS peak-fitting and consequent XSW data extracted using traditional peak-fitting parameters. The data presented in these figures are the same as that presented in [Figure 4.5](#) and [4.7](#). (a) The C 1s data in was fit with three peaks for XSW analysis because the S1 and EG peaks were experimentally inseparable. (b) The Si 1s peak fitting model now accounts for the possible presence of distinct EG_0 and defect core-shifted components. In (c) and (d) are the XSW results corresponding to the peak-fitting models in (a) and (b), respectively.

development of more well-controlled, homogenous EG/SiC(0001) produced by high-temperature Ar-growth [88]. The high step density common in UHV-grown would presumably lead to highly inhomogeneous graphene coverage and a contribution from those EG layers within the C 1s spectrum.

Similarly, Riedl *et al.* propose that the Si 2p spectrum be fit with a 3-peak model due to the presence of $6R3$ and “defect” species [30]. Although we do find that the intensity of the

wings of the Si 1s spectrum taken in the $\vartheta = 2^\circ$ geometry are increased in comparison to the spectra taken in the conventional geometry (Figure B.2) we find that this increase is marginal ($\sim \times 3$). Therefore, we suggest that the increased intensity at the wings are not likely surface-specific Si atoms with any distinct, chemical core-shifted components, but are rather caused by a distribution of bond-angles and bond-lengths induce at the strained interface. Because the covalent interaction of the top-most Si layer would place these strained Si in essentially SiC bulk configurations, the interpretation of strain broadening seems more likely than that of distinct core-level shifts. Finally, we note that in the work of Riedl *et al.* that both the $6R3$ and “defect” components disappear upon H-decoupling of the interface layer from the substrate, consistent with our interpretation.

Table B.1: XSW results based on Emtsevs C 1s and Riedl’s Si 2p XPS peak-fitting models. Reported uncertainties are 1σ confidence levels.

	Component, s	χ^2	P_s	z_s (Å)	f_s	σ_s (Å)
C 1s	Bulk C	1.30	0.76 ± 0.03	2.39 ± 0.13	0.85 ± 0.1	$0.23^{+0.07}_{-0.10}$
	EG + S_1	1.53	0.39 ± 0.03	N/A	0.22 ± 0.03	N/A
	S_2	2.94	0.83 ± 0.04	2.09 ± 0.10	0.65 ± 0.15	$0.37^{+0.10}_{-0.07}$
Si 1s	Bulk Si	4.85	1.00 ± 0.02	2.52 ± 0.05	0.88 ± 0.08	$0.21^{+0.06}_{-0.1}$
	Si_{6R3}	2.15	0.95 ± 0.06	2.42 ± 0.13	0.9 ± 0.3	$0.18^{+0.12}_{-0.08}$
	Si_{def}	0.79	0.97 ± 0.11	2.44 ± 0.25	0.6 ± 0.3	$0.4^{+0.2}_{-0.2}$

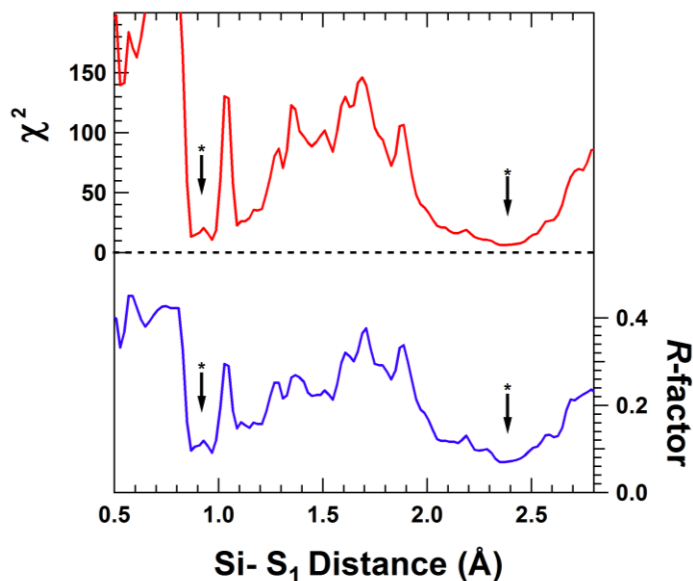


Figure B.3: Goodness-of-fit maps for the Si-S₁ distance with fixed S₂ position. The χ^2 map is in red on the left axis and the R -factor map is in blue, on the right axis. There exist two local minima, indicating possible solutions at Si-S₁ = 0.9 Å, and Si-S₁ = 2.4 Å, but both solutions appear unphysical.

Regardless, we provide parallel XSW analysis using the XPS peak-fitting models offered by Emtsev and Riedl. The C 1s and Si 1s spectra fit according to these models is shown in [Figure B.2\(a\) and \(b\)](#). Both spectra are easily fit based on the literature values. We note that in Emtsev's model the S₁ component and the EG component differ in binding energy by only ~0.1 eV. This greatly complicates the analysis of the EG and S₁ components. However, the S₂ component is practically isolated and can be analyzed in a straight-forward manner.

The XSW data and fits are presented in [Figure B.2\(c\) and \(d\)](#), and the results are summarized in [Table 4.1](#). Because the analysis of the EG + S₁ component proves impractical (there is one Fourier component comprised of as many as 4 distinct contributions), we explore Emtsev's model by position the S₂ species within its XSW-derived 1 σ confidence window ($2.0 \text{ \AA} < z_{S_1} < 2.2 \text{ \AA}$, see [Table S.2](#)) and mapping the goodness-of-fit χ^2 and R -factor as a function of z_{S_1} between $0.5 > z_{S_1} < 3.0$. The resulting χ^2 and R -factor maps are shown in [Figure B.3](#). There exist two distinct local minima in the map, indicating that there exist potential solutions for

Emtsev's model at $z_{S_1} \sim 0.9 \text{ \AA}$ $z_{S_2} \sim 2.4 \text{ \AA}$. The $z_{S_2} \sim 0.9 \text{ \AA}$ solution would indicate both unphysical Si-C and sp^2 C-C bonding distances, and the result actually requires significant electron density *between* the graphene sheets, for which there is no complimentary evidence. The $z_{S_1} \sim 2.4 \text{ \AA}$ solution produces an structure largely similar to the one presented in the main text, but places the Si-C-C₃ bonded atoms 0.3 \AA *above* the atoms in a graphene-like configuration, which makes little physical sense.

The XSW modulations resulting from the fits of the Si 1s spectrum was fit with the two additional core-shifted components are shown in [Figure B.2\(d\)](#). The XSW results for these 3 modeled components are practically indistinguishable within error ([Table B.1](#)). While this result could indicate the existence of small populations (<5% at surface) distinct chemical species in bulk-like SiC positions, it seems more likely that the interfacial strain broadens the Si 1s spectral distribution due to the increased variance in the distribution of Si-C bond lengths and angles of the top-most Si layers.

Vita

Jonathan D. Emery

Education

- Expected 2013 **Ph.D. in Materials Science and Engineering**
Northwestern University, Evanston, IL, USA
- 2007 **B.A. in Physics, Magna Cum Laude**
Carleton College, Northfield, IL, USA

Research Experience

- 2007 – Present Graduate Research Fellow
Northwestern University,
Dept. of Materials Science and Engineering
- 2006-2007 Undergraduate Research Assistant
Carleton College, Dept. of Physics
- 2006 Undergraduate Research Assistant
University of Minnesota, Twin Cities,
Dept. of Chemical Engineering and Materials Science

Awards and Honors

- 2012 Student Presentation Award
Northwestern Hilliard Symposium
- 2012 Advanced Photon Source Annual Report Highlighted Article
- 2008-2012 Materials Research Science and Engineering Center Fellowship,
Northwestern University
- 2011 Invited Seminar
UW-Milwaukee Physics Department

- 2011 Student Presentation Award
11th International Surface X-ray Neutron Scattering Conference
- 2009 Student Presentation Award
Advanced Photon Source Users' Meeting
- 2007 Awards of Distinction in Comprehensive Thesis and Major,
Carleton College
- 2005 Walter G. Andrews and Louise Seeger Andrews Award,
Carleton College

Publications

1. **J.D. Emery**, B. Detlefs, H.J. Karmel, L.O. Nyakiti D.K. Gaskill, M.C. Hersam, J. Zegenhagen, M. J. Bedzyk, "Chemically-resolved Interfacial Structure of Epitaxial Graphene on SiC(0001)", in preparation (2013).
2. **J.D. Emery**, V.D. Wheeler, B. Detlefs, M.B. McBriarty, S.S. Lee, P. Fenter, J. Zegenhagen, D. K. Gaskill, M. J. Bedzyk, "Interfacial Structure of H-intercalated Quasi-freestanding Epitaxial Graphene", in preparation (2013).
3. H.J. Karmel, J.J. Garramone, **J.D. Emery**, S. Kewalramani, M.J. Bedzyk, M.C. Hersam, "High-Stability Highly-Ordered Non-Covalent Graphene-Organic Interfaces", in preparation (2013).
4. D.E. Proffit, T. Philippe, **J.D. Emery**, Q. Ma, D.B. Buchholz, P.W. Voorhees, M.J. Bedzyk, R.P.H. Chang, T.O. Mason, "Thermal Stability of Amorphous Zn-In-Sn-O Films", in preparation (2013)
5. K. Everaerts, **J.D. Emery**, D.M. Jarwala, H.J. Karmel, V.K. Sangwan, P.L. Prabhumirashi, M.L. Geier, J.J. McMorrow, M.J. Bedzyk, A. Facchetti, M.C. Hersam, T.J. Marks, "Enhanced Chemical Cooperativity with Hafnia vs. Zirconia in Phosphonic Acid-based Low-Temperature, Solution-Processed Superlattice Gate Dielectrics", submitted (2013).
6. *J.M.P. Alaboson, C.-H. Sham, S. Kewalramani, **J.D. Emery**, J.E. Johns, A. Deshpande, T. Chien, M.J. Bedzyk, J.W. Elam, M.J. Pellin, M.C. Hersam. "Templating Sub-10 nm Atomic Layer Deposited Oxide Nanostructures on Graphene via One-Dimensional Organic Self-Assembled Monolayers," *Nano Letters*:10.1021/nl4000932 (2013).

7. J. Youn, S. Kewalramani, **J.D. Emery**, Y. Shi, S. Zhang, H-C Chang, Y-J Liang, C-M Yeh, C-Y Feng, H. Huang, C. Stern, L-H Chen, J-C Ho, M-C Chen, M.J. Bedzyk, A. Facchetti, and Tobin J. Marks, "Fused Thiophene Semiconductors: Crystal Structure-Film Microstructure-Transistor Performance Correlations," *Advanced Functional Materials*:10.1002/adfm.201203439, (2013).
8. A.L. Lipson, S. Chattopadhyay, H.J. Karmel, T.T. Fister, **J.D. Emery**, V.P. Dravid, M.M. Thackeray, P.A. Fenter, M.J. Bedzyk, M.C. Hersam. "Enhanced Lithiation of Doped 6H Silicon Carbide (0001) via High Temperature Vacuum Growth of Epitaxial Graphene," *The Journal of Physical Chemistry C* **116**(39) 20949-20957 (2012).
9. S. Chattopadhyay, A.L. Lipson, H.J. Karmel, **J.D. Emery**, T.T. Fister, P.A. Fenter, M.C. Hersam, M.J. Bedzyk. "In Situ X-ray Study of the Solid Electrolyte Interphase (SEI) Formation on Graphene as a Model Li-ion Battery Anode," *Chemistry of Materials* **24**(15) 3038-3043 (2012)
10. V.K. Sangwan, R.P. Ortiz, J.M.P. Alaboson, **J.D. Emery**, M.J. Bedzyk, L.J. Lauhon, T.J. Marks, M.C. Hersam. "Fundamental Performance Limits of Carbon Nanotube Thin-Film Transistors Achieved Using Hybrid Molecular Dielectrics," *ACS Nano* **6**(8) 7480-7488 (2012).
11. S.R. Walter, J. Youn, **J.D. Emery**, S. Kewalramani, J.W. Hennek, M.J. Bedzyk, A. Facchetti, T.J. Marks, F.M. Geiger. "In-Situ Probe of Gate Dielectric-Semiconductor Interfacial Order in Organic Transistors: Origin and Control of Large Performance Sensitivities," *Journal of the American Chemical Society* **134**(28) 11726-11733 (2012).
12. D.E. Proffitt, S.P. Harvey, A. Klein, R. Schafranek, **J.D. Emery**, D.B. Buchholz, R.P.H. Chang, M.J. Bedzyk, T.O. Mason. "Surface studies of crystalline and amorphous Zn-In-Sn-O transparent conducting oxides," *Thin Solid Films* **520**(17) 5633-5639 (2012).
13. J.M.P. Alaboson, Q.H. Wang, **J.D. Emery**, A.L. Lipson, M.J. Bedzyk, J.W. Elam, M.J. Pellin, M.C. Hersam. "Seeding Atomic Layer Deposition of High-k Dielectrics on Epitaxial Graphene with Organic Self-Assembled Monolayers," *ACS Nano* **5**(6) 5223-5232 (2011).
14. ***J.D. Emery**, Q.H. Wang, M. Zarrouati, P. Fenter, M.C. Hersam, M.J. Bedzyk. "Structural Analysis of PTCDA Monolayers on Epitaxial Graphene with Ultra-high Vacuum Scanning Tunneling Microscopy and High-resolution X-ray Reflectivity," *Surface Science* **605**(17-18) 1685-1693 (2011).

15. Y.G. Ha, **J.D. Emery**, M.J. Bedzyk, H. Usta, A. Facchetti, T.J. Marks. "Solution-Deposited Organic-Inorganic Hybrid Multilayer Gate Dielectrics. Design, Synthesis, Microstructures, and Electrical Properties with Thin-Film Transistors," *Journal of the American Chemical Society* **133**(26) 10239-10250 (2011).
16. M.D. Irwin, J.D. Servaites, D.B. Buchholz, B.J. Leever, J. Liu, **J.D. Emery**, M. Zhang, J.H. Song, M.F. Durstock, A.J. Freeman, *et al.* "Structural and Electrical Functionality of NiO Interfacial Films in Bulk Heterojunction Organic Solar Cells," *Chemistry of Materials* **23**(8) 2218-2226 (2011).

* denotes cover or highlighted article

Conference Presentations

1. "Synchrotron-based Structural Characterization of Epitaxial Graphene on SiC(0001)", 19th American Conference on Crystal Growth and Epitaxy, Invited Oral Presentation, Keystone, CO, July, 2013.
2. "Chemically-resolved Interfacial Structure of Epitaxial Graphene on SiC(0001)", Oral Presentation, American Vacuum Society 59th International Symposium, Tampa, FL, November, 2012.
3. "High-Resolution X-ray Reflectivity Studies of Functionalized Epitaxial Graphene", Oral Presentation, American Vacuum Society 59th International Symposium, Tampa, FL, November, 2012.
4. "Structural Analysis of PTCDA Monolayers on Epitaxial Graphene with UHV Scanning Tunneling Microscopy and High-Resolution X-ray Reflectivity", American Vacuum Society Prairie Chapter, Oral Presentation, Northwestern University, Evanston, IL August, 2011
5. "Structural Analysis of Chemically Functionalized Epitaxial Graphene with High-resolution X-ray Reflectivity", Poster Presentation, Materials Research Society Fall Meeting, Boston, MA, November, 2010.
6. "High-Resolution X-ray Reflectivity Studies of Chemically Functionalized Epitaxial Graphene", Oral Presentation, 6th Annual Minnesota Nanotechnology Conference, UM-Twin Cities, Minneapolis, MN, October, 2010.

7. **“Temperature-Dependent Structural Studies of Strained Epitaxial SrTiO₃ Ultrathin Films on Si(001)”*, Poster Presentation, The 11th International Conference on Surface X-ray and Neutron Scattering, Northwestern University, July, 2010
8. *“X-ray Surface Scattering Studies of Chemically Functionalized Epitaxial Graphene”*, Poster Presentation, Advanced Photon Source Users Meeting, Argonne, IL, May 2010.
9. *“Long-Period X-ray Standing Wave Studies of Self-assembled Nanoscale Dielectrics”*, Poster Presentation, Materials Research Society Fall Meeting, Boston, MA, November, 2009.
10. *“Long-Period X-ray Standing Wave Studies of Self-assembled Nanoscale Dielectrics”*, Poster Presentation, Advanced Photon Source Users Meeting, Argonne, IL, May 2009.
11. **“X-ray Characterization of Hybrid Nanoelectronic Materials”*, Poster Presentation, Advanced Photon Source Users Meeting, Argonne IL, May 2008.

*denotes best paper award